L. F. Greimann P.-S. Yang S. K. Edmunds A. M. Wolde-Tinsae

Final Report

# Design of Piles for Integral Abutment Bridges

Sponsored by the Iowa Department of Transportation, Highway Division,
and the Iowa Highway Research Board

August 1984

Iowa Department
of Transportation

Iowa DOT Project HR-252
ERI Project 1619
ISU-ERI-Ames 84286

report

College of
Engineering
Iowa State University

The opinions, findings, and conclusions expressed in this publication are those of the authors, and not necessarily those of the Highway Division of the Iowa Department of Transportation.

L.F. Greimann
P.-S. Yang
S.K. Edmunds
A.M. Wolde-Tinsae

Final Report

# Design of Piles for Integral Abutment Bridges

August 1984

Submitted to the Highway Division,
Iowa Department of Transportation

Iowa DOT Project HR-252
ERI Project 1619
ISU-ERI-Ames 84286

Department of Civil Engineering
Engineering Research Institute
Iowa State University, Ames

TABLE OF CONTENTS

# LIST OF TABLES

# LIST OF FIGURES

# ABSTRACT

More and more, integral abutment bridges are being used in place of the more traditional bridge designs with expansion releases. In this study, states which use integral abutment bridges were surveyed to determine their current practice in the design of these structures.

To study piles in integral abutment bridges, a finite element program for the soil-pile system was developed (1) with materially and geometrically nonlinear, two and three-dimensional beam elements and (2) with a nonlinear, Winkler soil model with vertical, horizontal, and pile tip springs. The model was verified by comparison to several analytical and experimental examples.

A simplified design model for analyzing piles in integral abutment bridges is also presented. This model grew from previous analytical models and observations of pile behavior. The design model correctly describes the essential behavioral characteristics of the pile and conservatively predicts the vertical load-carrying capacity.

Analytical examples are presented to illustrate the effects of lateral displacements on the ultimate load capacity of a pile. These examples include friction and end-bearing piles; steel, concrete, and timber piles; and bending about the weak, strong, and 45° axes for H piles. The effects of cyclic loading are shown for skewed and non-skewed bridges. The results show that the capacity of friction piles is not significantly affected by lateral displacements, but the capacity of end-bearing piles is reduced. Further results show that the longitudinal expansion of the bridge can introduce a vertical preload on the pile.

# 1. INTRODUCTION

Traditionally, a system of expansion joints, roller supports, and other structural releases has been provided on bridges to prevent damage caused by thermal expansion and contraction of the superstructure with annual temperature variations. Expansion joints usually increase the initial cost of a bridge and often do not function properly after years of service unless extensively maintained. Thus, integral abutment bridges, which have no expansion joints, provide a design alternative which potentially offers lower initial costs and lower maintenance costs. However, since the piles in an integral abutment bridge are the most flexible elements, they will be subjected to lateral movements as the bridge expands and contracts. Determining the maximum lateral displacement that does not cause a reduction in the load-carrying capacity of the piles (i.e., which does not alter the existing methods for designing the piles) is of primary importance in defining the maximum safe length for integral abutment bridges. Other factors to be considered in determining the allowable length for integral abutment bridges include the axial stresses induced in the superstructure caused by the partially restrained displacements of the abutments and the effects of the abutment movement on the integrity of the approach slab and fill. These two effects are not considered further in this study.

As part of this study, the highway departments using integral abutment bridges were surveyed to determine current design methods. Two analytical methods were developed to analyze embedded piles with

enforced horizontal displacements of the pile top: one based on a nonlinear finite element model and the other on a simplified collapse model. The finite element model is compared to experimental results and the simplified model to the finite element model. Both analytical models can be used to predict the effect of integral abutment bridge movements on the pile capacity. Various analytical examples are presented, representing skewed and nonskewed bridges.

# 2. DESIGN OF INTEGRAL BRIDGE ABUTMENTS

Responses to previous surveys concerning the use of integral abutments [2.1, 2.2] have indicated that most state highway departments have their own limitations and criteria in designing integral abutments. The bases of these limitations and criteria are shown to be primarily empirical.

The use of integral abutments in bridge design has so far been accepted by 28 state highway departments and the District Construction Office of Federal Highway Administration (FHWA), Region 15. This chapter summarizes the current thinking and practice in integral abutment design by those state highway departments and the District Construction Office, as obtained from a survey made as part of this study. A copy of the survey questionnaire is shown in the Appendix (Chapter 10).

Policies on several areas--integral abutment design, bridge movement, approach slabs, wingwall configurations and details, and general design details and guidelines--are discussed for the representative highway departments of Tennessee, New York, and California, as well as the FHWA. A summary on current practice by all the 28 states and the District Construction Office of FHWA, Region 15, is also given in the Appendix.

## 2.1. General Policy on Integral Abutment Design

### 2.1.1. Tennessee

Structures must be designed to accommodate the movements and stresses caused by thermal expansion and contraction. Bridge designers

should not accommodate these movements by using unnecessary bridge deck expansion joints and expansion bearings, because this solution creates more problems than it solves. Structural deterioration attributable to leaking expansion joints and frozen expansion bearings constitutes major bridge maintenance problems.

To eliminate the problems associated with leaking expansion joints and frozen expansion bearings, Tennessee's policy is to design and construct bridges with continuous superstructures, fixed or integral bearings at the piers and abutments, and no bridge deck expansion joints unless absolutely necessary. When expansion joints are necessary, they will be provided only at abutments [2.3].

### 2.1.2. New York

The New York Department of Transportation currently has tentative integral abutment guidelines that list the design parameters that must be satisfied by designers if they elect to use an integral abutment type structure. Integral abutments are allowed on structures with span lengths up to 300 ft, provided they satisfy the tentative guidelines. Span lengths between 300 and 400 ft are approved on an individual basis. To date (March 1983) New York has not constructed any over 300 ft.

The main concern regarding span length is the longitudinal movement and the large passive pressures that are generated as the structure expands against the compacted backfill. The general policy is to try to select a span arrangement and bearing types that result in approximately equal movements at each abutment. The 300-ft limitation results in movements that can safely be handled [2.4].

### 2.1.3. California

The end diaphragm is treated as an integral part of the bridge superstructure. Frequently this diaphragm is extended below the soffit of the superstructure to rest directly on piles or on a footing. This type of support is then called an "end diaphragm abutment." In California, an end diaphragm abutment may not be used where the roadway on the structure is designed to carry storm water [2.5].

### 2.1.4. Federal Highway Administration

The FHWA recommends that bridges with an overall length less than the following values should be constructed with continuous spans and, if unrestrained, have integral abutments. Greater values may be used when experience indicates such designs satisfactory [2.6].

| | |
|---|---|
| Steel | 300 ft |
| Cast-in-place concrete (CIP) | 500 ft |
| Pre- or post-tensioned concrete | 600 ft |

## 2.2. Provision for Bridge Movement

### 2.2.1. Tennessee

The total superstructure movement should be based on the following design parameters:

| Structure Type | Temp. Range | Coef. of Exp. | Total Movement |
|---|---|---|---|
| Concrete | 25° F - 95° F | 0.0000060 | 0.505 in./100 ft |
| Steel | 0° F -120° F | 0.0000065 | 0.936 in./100 ft |

The total movement per hundred feet is applicable to the structure length measured from the theoretical fixed center of the structure.

When the total anticipated movement at an abutment is less than 2 in. and the abutment is unrestrained against movement, no joint will be required and the superstructure and abutment beam will be constructed integrally. A construction joint shall be provided between the abutment backwall and the approach slab. (An unrestrained abutment is one that is free to rotate, such as a stub abutment on one row of piles or an abutment hinged at the footing with the axis of rotation being skewed between 60° and 90° to the direction of movement.)

When the total anticipated movement at an abutment is less than 1/4 in., the abutment may be constructed integrally with the superstructure regardless of the support conditions.

When the total movement is more than 1/4 in. and the abutment is restrained against movement and rotation, an expansion joint will be required.

When the total movement is greater than 1/4 in., the design drawings should show the total required movement for each joint and specify three proprietary strip seals for the contractor's selection. Alternate details may be submitted to the Engineer for approval [2.3].

2.2.2. New York

Since the approach slabs are connected to the bridge slab, the distance from end-to-end of the approach slab shall be considered the length for an integral abutment structure. The following guidelines apply:

1) Length 150 ft or less--no provision for expansion will be required.

2) Length over 150 ft and up to 300 ft--provision shall be made for expansion at the end of the approach slab. If at all possible, the span arrangement and interior bearing selection shall be such that approximately equal movements will occur at each abutment.

3) Length over 300 ft and up to 400 ft--lengths in this range shall be approved on an individual basis. Provision for expansion shall be made at the end of each approach slab.

4) Lengths over 400 ft--not recommended at this time [2.7].

2.2.3. California

Thermal movements are easily absorbed by integral abutments. Abutments of conventionally reinforced, continuous concrete bridges of over 400 ft in length have shown no evidence of distress even though the end diaphragms were supported on piles. However, movement of the abutments from shrinkage and temperature changes results in an opening at the paving notch allowing intrusion of water. Prestressed structures will amplify the intrusion problems because of the additional movement resulting from plastic shortening [2.5].

Movement of the abutments has caused maintenance problems attributable to settlement and erosion of the approach fill. Because of these problems, the use of the end diaphragm abutment shall be limited to the following values unless mitigating measures are used:

| Temp. Range | Steel | Reinf. Concrete | Precast Concrete | CIP/ Post Tension |
|---|---|---|---|---|
| 80 | 240 | 260 | 240 | 150 |
| 100 | 200 | 210 | 200 | 130 |
| 120 | 160 | 180 | 170 | 120 |

These data are based on a movement rating = 3/4 in.

### 2.2.4. Federal Highway Administration

Background. Thermal movements are predicted on the cold climate temperature ranges specified in the American Association of State Highway and Transportation Officials (AASHTO) bridge specifications, Article 1.2.15. State standards specifying other temperature ranges require adjustment of those values indicated [2.6].

1) For structural steel supported bridges, Article 1.2.15 specifies cold climate temperature range of 150° F with a thermal coefficient of 0.0000065, resulting in a total thermal movement of 1-1/4 in. (32 mm) of movement per 100 ft (30.5 m) of structure.
2) For concrete superstructures, AASHTO specifies a cold climate temperature range of 80° F, a thermal coefficient of 0.0000060 and a shrinkage factor of 0.0002. However, this shrinkage effect can be reduced provided the normal construction sequence allows the initial shrinkage to occur prior

to completion of the concrete operations. Based on an assumed shrinkage reduction of 50%, total allowance for thermal and shrinkage movement in a concrete structure would be approximately 3/4 in. (19 mm) per 100 ft (30.5 m).

3) For prestressed concrete structures, a somewhat smaller total movement will occur once the prestressing shortening has taken place. Movement of 5/8 in. (15.9 mm) per 100 ft (30.5 m) of structure would be a reasonable value. This allows for thermal movement and assumes no effect from shrinkage and long-term creep. This value has been substantiated in the field as reasonable for normal highway overcrossing structures.

4) In long pre- or post-tensioned concrete structures, long-term creep may occur but is normally insignificant insofar as provision for movement is concerned and, therefore, has not been included in 3) above.

5) The flexibility of individual substructure units will affect the distribution of the total movement between specified joints.

Recommendations

1) Cold climate conditions. Based on the above, consider adoption of Fig. 2.1 for determining the required provision for total movement under cold climate conditions.

2) Moderate climate conditions. In accordance with AASHTO Article 1.2.15 use temperature ranges of 120° F (steel) and 70° F (concrete) and a 20% reduction of the above values.

## 2.3. Approach Slab

### 2.3.1. New York

Approach slabs should be 20-ft-long maximum and the end of the approach slab shall be parallel to the skew (30° maximum skew angle).

A tight joint should be placed directly over the backwall between the approach slab and bridge slab. This will provide a controlled crack location rather than allowing a random crack pattern to develop. Epoxy coated dowels shall pass through the joint and shall be located near the bottom of the slab. This will keep the joint tight but still allow the approach slab to settle without causing tension cracking in the top of the slab.

There has been considerable discussion and no agreement on whether the joint should be formed or saw cut. A formed construction joint would provide positive assurance that the joint would wind up exactly where wanted and the approach slab would always be supported on the backwall. In many instances the approach slab is not as wide as the bridge slab. In those instances the joint is U-shaped and can be formed neatly and easily. The disadvantage to the formed joint is that it requires the approach slab to be poured separate from the bridge slab.

However, a saw cut joint would allow the bridge slab and approach slab to be cast in a single operation. Some concern arises as to how

vision for expansion indicate that there is a potential for future maintenance at these joints [2.7].

### 2.3.2. Federal Highway Administration

1) Approach slabs are needed to span the area immediately behind integral abutments to prevent traffic compaction of material where the fill is partially disturbed by abutment movement. The approach slab should be anchored with reinforcing steel to the superstructure and have a minimum span length equal to the depth of abutment (1-to-1 slope from the bottom of the rear face of the abutment) plus a 4-ft minimum soil bearing area. A practical minimum length of slab would be 14 ft. See Fig. 2.2 for details [2.6].
2) The design of the approach slab should be based on the AASHTO Specifications for Highway Bridges, Article 1.3.2(3) Case B, where design span "S" equals slab length minus 2 ft.
3) Positive anchorage of integral abutments to the superstructure is strongly recommended.
4) North Dakota provides a roadway expansion joint 50 ft from the end of the bridge to accommodate any pavement growth or bridge movement. This is considered desirable.

## 2.4. Wingwall Configurations and Details

### 2.4.1. Tennessee

This state uses No. 4 bars for 6-ft to 7-ft wingwalls, No. 5 bars for 7-ft to 10-ft wingwalls, and No. 6 bars for 10-ft to 12-ft wingwalls.

These values may be adjusted by individual design. For wingwall lengths greater than 12 ft, the designer will use a comprehensive analysis for each case [2.3].

2.4.2. New York

Wingwalls shall be in-line or flared. U-walls will not be allowed. U-walls were eliminated because of design uncertainty, backfill compaction difficulty, and the additional design and details that have to be worked out for the joint between the wingwalls and approach slab.

Wingwall lengths in excess of 10 ft should be avoided. Generally, the controlling design parameter is the horizontal bending in the wingwall at the fascia stringer, which is caused by the large passive pressure behind the wingwalls. When the wingwalls are longer than 10 ft, areas of steel greater than No. 11 bars at 6 in. may be required. The 10-ft dimension is a projected dimension and should be measured along a line perpendicular to the fascia stringer. Thus, flared wingwalls may be longer than 10 ft providing the projected length does not exceed 10 ft.

Stem thickness shall be 2 ft minimum. Wingwalls may be tapered to less than 2 ft in order to reduce vertical dead load [2.7].

On structures that have been designed to date, the controlling design parameter has been horizontal bending in the wingwall at the fascia girder caused by the large passive pressure behind the abutment. Since it is not certain what the horizontal pressure will be, the state has elected to use the maximum pressures that were obtained in the testing conducted by South Dakota State University for the South Dakota Department of Highways back in 1973. In their testing program they jacked against the backfill in 1/4-in. increments and measured

the corresponding passive pressures in the backfill material. To determine the horizontal pressure on the wingwall, the anticipated structure movement is calculated, and a corresponding passive pressure from South Dakota's test data is selected. This pressure is placed over the entire surface area of the abutment. Then the horizontal bending moment in the wingwalls caused by the passive pressure trying to bend the wingwalls about the fascia stringer is calculated [2.4].

## 2.5. General Design Details and Guidelines

### 2.5.1. New York

1) Foundation Type

All integral abutments shall be supported on piles. Steel H or CIP piles may be used for structure lengths 150 ft or less. Only steel H piles shall be used for structure lengths over 150 ft. All piles shall be in one single line and shall be oriented such that bending takes place about the weak axis of the pile. When steel H piles are used, the web of the pile shall be perpendicular to the center line of the stringer regardless of the skew.

2) Construction

- Steel or prestressed concrete superstructures may be used.
- Only straight stringers will be allowed. A curved superstructure will be allowed providing the stringers are straight. Curved stringers are eliminated to guard

against the possibility of flange buckling caused by the stringers trying to expand between the restraining abutments.

- Stringers shall be parallel to each other. The abutments shall also be parallel to each other.
- The maximum vertical curve gradient between abutments shall be 5%.
- Stage construction will not be allowed when integral abutments are used [2.7].

### 2.5.2. California

1) Restraining Forces

The values listed in Table 2.1 for resistance offered by various end conditions are applied at the base of the end diaphragm to determine the proper reinforcement. The values shown do not take into account the special situations where very long piles or small limber piles offer little resistance to longitudinal movement.

2) Earthquake Forces

Provide shear keys to resist transverse and longitudinal earthquake forces acting on the structure. These normally will be placed behind and at the ends of the abutment wall on narrow structures. On wide structures, additional keys may be located in the interior. One 1/2-in. expansion joint filler should be specified at the sides of all keys to minimize the danger of binding.

3) Drainage

- No pervious material collector or weep holes are required for flat slab bridges.
- Continuous pervious backfill material collector and weep holes may be used for abutments in fills or well-drained cuts and at sites where a 5-ft-level berm is specified.

| End Slope Treatment | Weep Hole Discharge |
|---|---|
| Unprotected berm | Directly on unprotected berm |
| Full slope paving | On spacer or groove in paved surface |

- Continuous permeable material and perforated steel pipe collector discharging into corrugated steel pipe overside drains should be used for all other abutments.
- Corrugated steel pipe overside drains must be coordinated with road plans. If there is no discharge system and no collector ditch, the outfall must be located away from the toe of slope to prevent erosion of the end slope.
- Abutment drainage systems should be coordinated with the slope paving.

4) Backfill Placement

Unless there are special soil conditions or unusual structure geometrics, the designer need not specify the method or timing of backfill placement. Passive resistance of soil in front of the end diaphragm offers little restriction to structure movement due to stressing. Nor will the active

pressure of backfill behind the end diaphragm materially alter the stress pattern even if the fill is completed at one abutment before being started at the other [2.5].

## 2.6. Summary and Conclusions

Previous surveys concerning the use of integral abutments [2.1, 2.2] have indicated that most state highway departments have their own limitations and criteria in designing integral abutments. The bases of these limitations and criteria are primarily empirical. Twenty-eight states and the District Construction Office of FHWA, Region 15, are known to use integral abutments. The current thinking and practice in integral abutment design by the 28 state highway departments and the District Construction Office of FHWA, Region 15, are summarized in Part 2 of the Appendix.

Iowa, South Dakota, and FHWA, Region 15, indicated that piling stresses due to lateral movement are calculated for integral abutment bridges. Alaska and Idaho indicated that such calculations are warranted only for integral abutment bridges that involve some unique feature. The remaining states neglected piling stresses due to lateral movement, although some states like California require some type of mitigating construction detail like driving the piles into predrilled holes.

Construction details vary widely from state to state. Pile head fixity conditions may be of the hinge, fixed, or partially restrained type. Pile caps may or may not be used. Approach slabs are in some

states tied to the abutment with dowels and move back and forth with the superstructure, while other states claim that an expansion joint between approach slab and bridge slab is needed to prevent possible maintenance problems. While granular material is the most widely used material as backfill, some states like New Mexico no longer use specified backfill. Wingwalls may be in-line or flared. Some states like New York do not allow U-walls because of design uncertainty, backfill compaction difficulty, and the additional design and details that have to be worked out for the joint between the wingwalls and approach slab. New York recommends avoiding wingwall lengths in excess of 10 ft. Tennessee requires the designer to use comprehensive analysis if wingwall lengths greater than 12 ft are to be used.

The maximum allowable lengths for bridges with integral abutments used by the different states are summarized in the Appendix. The length limitations have been set for the most part on the basis of experience and engineering judgment. Many of the states have been progressively increasing length limitations over the past 30 years, primarily as a result of the observance of satisfactory performance in actual installations. As of 1983, the length limitations for nonskewed integral abutment bridges had the following range: steel, 150 ft to 400 ft; concrete, 150 ft to 800 ft; prestressed concrete, 200 ft to 800 ft. Most states use the same length limitations for skewed integral abutment bridges.

# 3. SOIL CHARACTERIZATION

## 3.1. Introduction

The soil characteristics in the soil-pile problem can be described by three types of soil resistance-displacement curves: lateral resistance-displacement (p-y) curves; longitudinal load-slip (f-z) curves; and pile tip load-settlement (q-z) curves. The p-y curves represent the relationship between the lateral soil pressure against the pile (force per unit length of pile) and the corresponding lateral pile displacement. The f-z curves describe the relationship between skin friction (force per unit length of pile) and the relative vertical displacement between the pile and the soil. The q-z curves describe the relationship between the bearing stress at the pile tip and the pile tip settlement. The total pile tip force is q times the effective pile tip area. Figure 3.1 shows a typical soil resistance-displacement curve. All three types of curves assume the soil behavior to be nonlinear and can be developed from basic soil parameters.

The modified Ramberg-Osgood model (Sec. 3.2) will be used to approximate each of the three types of curves. The equations needed for calculating the constants used in this model are presented in Sec. 3.3 for lateral behavior and in Sec. 3.4 for vertical behavior. Numerical values for these constants are presented in Sec. 3.5 for six typical soils.

## 3.2. Model Idealization

### 3.2.1. Modified Ramberg-Osgood Model

The modified Ramberg-Osgood model, as shown in Eq. (3.1) in the form of a p-y curve, will be used to approximate the p-y, f-z, and q-z soil resistance-displacement curves.

$$p = \frac{k_h y}{\left[1 + \left|\frac{y}{y_u}\right|^n\right]^{1/n}} \tag{3.1}$$

$$y_u = \frac{p_u}{k_h} \tag{3.2}$$

in which

$k_h$ = initial lateral stiffness

$p$ = generalized soil resistance

$p_u$ = ultimate lateral soil resistance

$n$ = shape parameter

$y$ = generalized displacement

This model offers certain advantages over the other models and also includes the commonly used hyperbola as a special case [3.1]. Nonlinear behavior models for symmetrical or periodic loadings have been presented by a number of workers [3.2-3.6]. The constants needed in Eq. (3.1) can be determined from equations presented in Secs. 3.3 and 3.4. Figure 3.2 shows the modified Ramberg-Osgood curve for a typical p-y curve. Similar equations for a typical f-z curve (using $f_{max}$, the maximum shear

stress developed between the pile and soil, and $k_v$, the initial vertical stiffness) or a typical q-z curve (using $q_{max}$, the maximum bearing stress at the pile tip, and $k_q$, the initial point stiffness) will be used. Figure 3.3 shows the effect of the shape parameter n on the soil resistance-displacement behavior.

3.2.2. Cyclic Model

Because of annual temperature changes, a bridge superstructure undergoes expansion and contraction, which in turn causes the piles in integral abutment bridges to move back and forth. Thus, the modified Ramberg-Osgood model must accommodate loading and unloading of the pile during cyclic loading. The nonlinear behavior characteristics of piles and soils can be expressed by the concept of stress versus strain and soil resistance versus displacement, respectively, as shown in Figs. 3.4 and 3.5. A modified Ramberg-Osgood cyclic model for both symmetrical and irregular cyclic loadings is proposed

$$p = p_c + \frac{k_h(y - y_c)}{\left[1 + \left(\frac{1}{C}\left|\frac{y - y_c}{y_u}\right|\right)^n\right]^{1/n}} \tag{3.3}$$

where

$$C = \left|\pm 1 - \frac{p_c}{p_u}\right| \tag{3.4}$$

and also

$p_c$ = the soil resistance at the last reversal

$y_c$ = the soil displacement at the last reversal

The expression for the tangent modulus is obtained by differentiating Eq. (3.3) with respect to displacement y

$$k_{ht} = \frac{k_h}{\left[1 + \left(\frac{1}{C}\left|\frac{y - y_c}{y_u}\right|\right)^n\right]^{\frac{n+1}{n}}} \tag{3.5}$$

Figure 3.4 illustrates a typical example of this modified Ramberg-Osgood cyclic model. In this figure, hysteresis loops that appear to model the actual behavior of pile and soil quite well can then be readily constructed by adopting rules presented by Pyke [3.6]. These rules are stated as: 1) The tangent modulus on each loading reversal assumes a value equal to the initial tangent modulus for the initial loading curves, and 2) the shape of the unloading or reloading curves is the same as that of the initial loading curve, except that the scale is enlarged by a factor of c. This is indicated in Eq. (3.4) in which the first term is negative for unloading and positive for reloading; the maximum and minimum values of the stress or soil resistance are bounded by the ultimate (reference) stress or soil resistance.

As part of the finite element model to be presented in Chapter 4, the Ramberg-Osgood cyclic model will be required to track through several loading and unloading cycles. The determination of reversal values for loading and unloading of each load increment is obtained by adopting the flow chart in Table 3.1 (also illustrated in Fig. 3.5).

## 3.3. Lateral Behavior

The lateral resistance-displacement (p-y) curves are developed using the modified Ramberg-Osgood model (Eq. 3.1). The parameters needed for the modified Ramberg-Osgood equation are the initial lateral stiffness $k_h$, the ultimate lateral soil resistance $p_u$, and a shape parameter n. These parameters can be obtained using the equations in Table 3.2 and the soil parameters in Table 3.3 [3.7, 3.8].

For the design method to be developed in Chapter 5, the rather complicated variation of soil properties with depth will not be permitted. Simpler expressions for $k_h$ and $p_u$ are needed. For cohesive soils (clay), both $k_h$ and $p_u$ will be assumed to have a constant value for all depths [3.9, 3.10]

$$k_h = 67\ c_u \tag{3.6}$$

$$p_u = 9\ c_u B \tag{3.7}$$

For cohesionless soils (sand), both $k_h$ and $p_u$ will be assumed to vary linearly with depth [3.7, 3.9]

$$k_h = n_h x \tag{3.8}$$

$$n_h = \frac{J\gamma}{1.35} \tag{3.9}$$

$$p_u = (3\gamma B k_p)x \tag{3.10}$$

The value $n_h$ is the constant of subgrade reaction. The other constants used in the above equations are defined in Table 3.3.

## 3.4. Vertical Behavior

The load-slip (f-z) and pile tip load-settlement (q-z) curves are developed using the modified Ramberg-Osgood model (Eq. 3.1). The parameters needed for Eq. (3.1) for the f-z curve are the initial vertical stiffness $k_v$, the maximum shear stress $f_{max}$, and the shape parameter n. These parameters can be obtained using Table 3.4 [3.7, 3.9, 3.12]. The parameters needed for the modified Ramberg-Osgood equation for the q-z curve are the initial point stiffness $k_q$, the maximum bearing stress $q_{max}$, and the shape parameter n. These parameters can be calculated from the equations in Table 3.5 [3.7, 3.8].

The factor $\alpha$ in Fig. 3.6 is used to obtain the soil/pile adhesion, given the soil cohesion. Various curves have been presented in the literature for this value [3.9]. The curve in Fig. 3.6 is not the same as that used in previous work [3.7]. The lower curve in Fig. 3.6 is recommended for steel H piles over the one previously used [3.12].

## 3.5. Typical Soils

Soil properties and Ramberg-Osgood curve parameters are given for six typical soil types in Tables 3.6 to 3.11 [3.7].

# 4. THREE-DIMENSIONAL FINITE ELEMENT PILE MODEL

## 4.1. Introduction

A state-of-the-art mathematical model that can be used to help evaluate the safety of piles in skewed bridges with integral abutments is described herein. Normally, for a skewed bridge with integral abutments subjected to a change in temperature, thermal movements caused by temperature changes in most cases include biaxial behavior in the pile. Thus, a three-dimensional behavior of soil-pile interaction is to be considered for all components of the system, with compatibility and equilibrium enforced throughout.

The mathematical model developed in this investigation was limited to defining the behavior of soil-pile interaction. A combination of a one-dimensional idealization for the piles (beam column) and an equivalent spring idealization for the soil, which includes vertical springs, lateral springs, and a point spring, are shown in Fig. 4.1.

## 4.2. Three-dimensional Beam Finite Element

Basically, two different approaches have been pursued in incremental, nonlinear finite element analysis. In the first, static and kinematic variables are referred to Eulerian (convected) coordinates in each load step (Fig. 4.2). This procedure is generally called the Eulerian, convected, or moving coordinate formulation. In this approach the geometry of the continua is updated, and the deformations are assumed to be infinitesimal; hence, the linear relations can be used. The incremental governing equations are obtained by applying the principle

of virtual work or other equivalent theorems to the continuum using its configuration and stress at the previous step as the initial configuration and stress [4.1].

In the second approach, which is generally called the Lagrangian, stationary Lagrangian, or total Lagrangian formulation, all static and kinematic variables are referred to the original configuration (Fig. 4.2). The advantage of the total Lagrangian formulation is the ease with which it handles the boundary conditions and nonhomogeneities. For large displacement problems, the construction of shape functions for flexural problems is quite difficult and complex if the convergence conditions of the finite element method are to be met [4.1]. As the rotations become large, a component originally along the coordinate axis of the beam is no longer along that axis. Therefore, the assumed shape functions in the axial (linear) and transverse (cubic) directions are not compatible. This effect restricts the rotations to moderate values.

An updated Lagrangian formulation, which reduces the efforts in computation for problems where the nonlinearities arise from material nonlinearity and finite displacement and rotation, is presented here [4.1]. In the updated Lagranian formulation, the coordinates rotate and translate with the body but do not deform with it (Fig. 4.2). If the strains are small, this formulation linearizes the strain-displacement relations in terms of the deformation displacements relative to the element moving chord. The large displacement effects are treated by transformations of displacement and force components between the Eulerian and updated Lagrangian coordinates. Strictly speaking, the

updated Lagrangian formulation is a mixed procedure of the Eulerian and total Lagrangian formulations.

Derivations of the beam-column element with geometrically and materially nonlinear stiffness equations have been presented by several investigators [4.2-4.20]. A condensed description of this approach is given here to clarify the notation and approach used in the report. The following assumptions have been used in this derivation:

- The beam elements are assumed to be initially straight.
- Plane sections remain plane after deformation.
- The cross section of the beam is constant and has at least one plane of symmetry.
- Shear deformation is not considered.
- The effect of torsional deformation on normal strain is negligible (unrestrained warping).
- The beam-column element can undergo large rotations, but the deformation within each element from the chord is restricted to be small.

4.2.1. Coordinate Systems

In order to describe the system, three types of coordinate systems will be defined here:

1) A fixed, global set of coordinates (X, Y, Z).
2) Nodal coordinates ($\bar{x}$, $\bar{y}$, $\bar{z}$)--a set of nodal coordinates associated with each node that coincides with $\vec{b}_1$, $\vec{b}_2$, and $\vec{b}_3$ (the orthogonal base vectors), respectively, for each node. The initial orientations of the vectors $\vec{b}_i$ are chosen to

coincide with the principal directions of the cross section, and since the vectors rotate with the node, they remain aligned with the principal directions.

3) Element or local coordinates (x, y, z)--a set of element coordinates associated with each element. The element coordinates rotate and translate with the end points of the element. The x, y, and z axes are associated with the orthogonal base unit vectors $\vec{e}_1$, $\vec{e}_2$, and $\vec{e}_3$, respectively, for each element. These are the updated Lagrangian coordinates described in the introduction to this chapter and illustrated in Fig. 4.2.

These coordinate systems are illustrated in Fig. 4.3. The unit vectors $\vec{b}_i$ and $\vec{e}_i$ immediately define the rotational transformation for any vector components between the coordinate systems. Thus, for a vector $\vec{V}$ with global components ($V_X$, $V_Y$, $V_Z$), nodal coordinate components ($V_{\bar{x}}$, $V_{\bar{y}}$, $V_{\bar{z}}$), and element coordinate components ($V_x$, $V_y$, $V_z$), the transformation between global and nodal components is given by

$$\{V_N\} = \begin{Bmatrix} V_{\bar{x}} \\ V_{\bar{y}} \\ V_{\bar{z}} \end{Bmatrix} = \begin{bmatrix} \ell'_1 & m'_1 & n'_1 \\ \ell'_2 & m'_2 & n'_2 \\ \ell'_3 & m'_3 & n'_3 \end{bmatrix} \begin{Bmatrix} V_X \\ V_Y \\ V_Z \end{Bmatrix} = [T_{NG}] \{V_G\} \qquad (4.1)$$

where $\ell'_i$, $m'_i$, and $n'_i$ are the global components of the nodal base vector $\vec{b}_i$. Similarly

$$\{V_E\} = \begin{Bmatrix} V_x \\ V_y \\ V_z \end{Bmatrix} = \begin{bmatrix} \ell_1 & m_1 & n_1 \\ \ell_2 & m_2 & n_2 \\ \ell_3 & m_3 & n_3 \end{bmatrix} \begin{Bmatrix} V_X \\ V_Y \\ V_Z \end{Bmatrix} = [T_{EG}]\{V_G\} \qquad (4.2)$$

Because of the orthogonality of the transformation matrices, their inverse is equal to the transpose, so

$$\{V_G\} = [T_{NG}]^T \{V_N\} \qquad (4.3)$$

$$\{V_G\} = [T_{EG}]^T \{V_E\} \qquad (4.4)$$

4.2.2. Strain-Displacement and Deformation Displacements

In the updated Lagrangian formulation, displacements are subdivided into rigid body displacements, which cause no strains, and deformation displacements. The rigid body displacements correspond exactly to the translation and rotation of the element coordinate system. The additional displacements needed to bring the element into its deformed configuration are the deformation displacements. Consider a generic beam-column element with node I and J (or 1 and 2) as shown in Fig. 4.4. The element has six degree of freedoms per node: three displacements and three rotations. The nodal displacement vectors in global and element coordinates are designated as $D_1$ to $D_{12}$ and $d_1$ to $d_{12}$, respectively (see Fig. 4.4). The positive directions are given by the righthand rule. Figure 4.5 shows the three-dimensional beam-column element with global, nodal, and element coordinates before and after being deformed. The element coordinate system (x, y, z) for the

beam-column element is defined so that the x axis is and remains coincident with a line joining the endpoints of the element, while the y and z axes can be defined by a third node which lies in the positive x-y plane (K node). In general, the third node translates as the average of the two end nodes. In addition, it rotates about the local axis of the beam (x axis) an amount equal to the average of the twisting rotations at the ends [4.21]. The deformation nodal displacements are given by

$$\left\{ d^d \right\}^T = \left\{ \Delta_{IJ},\ \theta^x_{IJ},\ \theta^y_I,\ \theta^z_I,\ \theta^y_J,\ \theta^z_J \right\} \tag{4.5}$$

where

$\Delta_{IJ}$ = elongation

$\theta^x_{IJ}$ = torsional deformation rotation

$\theta^y_I,\ \theta^z_I,\ \theta^y_J,\ \theta^z_J$ = bending deformation rotation at ends I and J

The elongation is directly determined by

$$\Delta_{IJ} = \left(\vec{x}^t_J - \vec{x}^t_I\right) - \left(\vec{x}^0_J - \vec{x}^0_I\right)$$

$$= \frac{1}{(\ell^t + \ell^0)} \left[ 2\left( X^0_{JI} D_{71} + Y^0_{JI} D_{82} + Z^0_{JI} D_{93} \right) \right.$$

$$\left. + (D_{71})^2 + (D_{82})^2 + (D_{93})^2 \right] \tag{4.6}$$

where

$\vec{X}_I^t$ = position vector of node I at time t

$\vec{X}_I^0$ = position vector of node I at time 0

$\ell^0$, $\ell^t$ = the length of the element at time 0 and t, respectively.

$X_{JI}^0 = X_J^0 - X_I^0$, $D_{71} = D_7 - D_1$, etc.

In static analysis, the times 0 and t are used to represent the initial stage and the current stage and not real time.

For the purpose of computing the relative rotations at time t, $\theta_I^y$, $\theta_I^z$, $\theta_J^y$, $\theta_J^z$, and $\theta_{IJ}^x$, nodal unit vectors for node I and J are defined by $\vec{b}_{Ii}^t$, $\vec{b}_{Ji}^t$, respectively (i = 1, 3). Element unit vectors (x, y, z) are denoted by $\vec{e}_i^t$. Since the nodal vectors $\vec{b}_{Ii}^t$ and $\vec{b}_{Ji}^t$ rotate with the nodes, the angle between $\vec{b}_{Ii}^t$ and $\vec{e}_i^t$ indicates the magnitude of the deformation at node I. For example, the cross product of the two vectors $\vec{e}_1^t$ and $\vec{b}_{I1}^t$ is a vector perpendicular to the plane which contains these two vectors. The magnitude of this vector is equal to the sine of the angle between $\vec{e}_1^t$ and $\vec{b}_{I1}^t$. With the assumption of small deformation within the updated coordinate system, the bending deformation rotation $\theta_I^y$ can be obtained by projecting this vector $(\vec{e}_1^t \times \vec{b}_{I1}^t)$ on the current y axis. This is illustrated in Fig. 4.5 and the mathematical expressions are given below.

$$\theta_I^y = (\vec{e}_1^t \times \vec{b}_{I1}^t) \cdot \vec{e}_2^t \tag{4.7}$$

$$\theta_I^z = (\vec{e}_1^t \times \vec{b}_{I1}^t) \cdot \vec{e}_3^t \tag{4.8}$$

$$\theta_J^y = (\vec{e}_1^t \times \vec{b}_{J1}^t) \cdot \vec{e}_2^t \tag{4.9}$$

$$\theta_J^z = (\vec{e}_1^t \times \vec{b}_{J1}^t) \cdot \vec{e}_3^t \tag{4.10}$$

The torsional deformation is found by taking the cross product of $\vec{b}_{I2}^t$ and $\vec{b}_{J2}^t$ and projecting this vector on the current axis of the beam (x axis). This yields

$$\theta_{IJ}^x = (\vec{b}_{I2}^t \times \vec{b}_{J2}^t) \cdot \vec{e}_1^t \tag{4.11}$$

The method of updating the nodal and element unit vectors $\vec{b}_{Ii}^t$, $\vec{b}_{Ji}^t$, and $\vec{e}_i^t$ will be discussed later.

The neutral axis deformation displacement for the beam-column element is given by cubic shape functions to describe bending deformations and linear shape functions to specify axial and torsional deformations as

$$\begin{Bmatrix} u_{na}^d \\ v_{na}^d \\ w_{na}^d \\ \phi_{na}^d \end{Bmatrix} = \begin{bmatrix} \xi & 0 & 0 & 0 & 0 & 0 \\ 0 & 0 & 0 & \ell^t(\xi-2\xi+\xi^3) & 0 & \ell^t(-\xi^2+\xi^3) \\ 0 & 0 & \ell^t(-\xi+2\xi^2-\xi^3) & 0 & \ell^t(\xi^2-\xi^3) & 0 \\ 0 & \xi & 0 & 0 & 0 & 0 \end{bmatrix} \begin{Bmatrix} \Delta_{IJ} \\ \theta_{IJ}^x \\ \theta_I^y \\ \theta_I^z \\ \theta_J^y \\ \theta_J^z \end{Bmatrix}$$

$$= [N] \{d^d\} \tag{4.12}$$

where

$$\xi = x/\ell^t \tag{4.13}$$

The $u^d_{na}$, $v^d_{na}$, $w^d_{na}$ neutral axial deformation displacements do not include rigid body motion and, hence, are with respect to the element coordinate system in Fig. 4.2 (i.e., the moving chord which connects the end points).

Following the usual Euler-Bernoulli beam assumptions that normals to the midline remain straight and normal, the deformation displacement at each point of the beam element may be written as

$$u^d_p = u^d_{na} - y\frac{\partial v^d_{na}}{\partial x} - z\frac{\partial w^d_{na}}{\partial x} \tag{4.14}$$

$$v^d_p = v^d_{na} - z\phi^d_{na} \tag{4.15}$$

$$w^d_p = w^d_{na} + y\phi^d_{na} \tag{4.16}$$

From the previous assumptions, the effect of torsional deformation on normal strain is neglected and shear deformation is not considered. The relationship between the beam normal strains and the displacements is

$$\varepsilon = \frac{\partial u^d_p}{\partial x} + \frac{1}{2}\left(\frac{\partial v^d_p}{\partial x}\right)^2 + \frac{1}{2}\left(\frac{\partial w^d_p}{\partial x}\right)^2 \tag{4.17}$$

The equation is valid as long as $(\partial v_p^d/\partial x)^2$ and $(\partial w_p^d/\partial x)^2$ are large compared to $(\partial u_p^d/\partial x)^2$. Although this condition is similar in appearance to that of moderate rotation theories, it is far less restrictive because $v_p$ and $w_p$ are the displacements relative to the updated element coordinate x. By reducing the size of the element, $v_p^d$ and $w_p^d$ can be made as small as necessary [4.22].

From Eqs. (4.12) to (4.17), the strain and displacement can be related as

$$\varepsilon = ([B_L] + \frac{1}{2}[B_{NL}])\{d^d\} \tag{4.18}$$

where

$$[B_L] = [1/\ell^t,\ 0,\ \rho(6\xi - 4),\ -\eta(6\xi - 4),\ \rho(6\xi - 2)\ -\eta(6\xi - 2)] \tag{4.19}$$

$$[B_{NL}] = \{d^d\}^T([G_z]^T[G_z] + [G_y]^T[G_y]) \tag{4.20}$$

$$[G_z] = [0,\ -\rho,\ 0,\ \psi_1(\xi),\ 0,\ \psi_2(\xi)] \tag{4.21}$$

$$[G_y] = [0,\ \eta,\ -\psi_1(\xi),\ 0,\ -\psi_2(\xi),\ 0] \tag{4.22}$$

$$\psi_1(\xi) = 1 - 4\xi + 3\xi^2 \tag{4.23}$$

$$\psi_2(\xi) = -2\xi + 3\xi^2 \tag{4.24}$$

$$\eta = \frac{y}{\ell^t}\ ,\ \rho = \frac{z}{\ell^t} \tag{4.25}$$

For general nonlinear problems, the solution algorithm (Newton-Raphson method) is based upon the application of a small load increment. For

this technique, it is necessary to relate the rate of change of force with displacement, that is, the tangent stiffness. From Eq. (4.18) that rate of strain $\Delta\varepsilon$ can be found as

$$\Delta\varepsilon = ([B_L] + [B_{NL}])\{\Delta d^d\} \tag{4.26}$$

or

$$\Delta\varepsilon = [B]\{\Delta d^d\} \tag{4.27}$$

Once the strains are known, the stresses are computed by the constitutive laws [4.23]. The nonlinear stress-strain relationship of the beam material will be approximated by the modified Ramberg-Osgood cyclic model (see Sec. 3.2.2). The incremental stress-strain relationship of the beam-column element is expressed as

$$\Delta\sigma = E_T\ \Delta\varepsilon \tag{4.28}$$

where $E_T$ is the tangent modulus of elasticity of the stress-strain curve. If the thermal strains are considered, Eq. (4.28) is modified to

$$\Delta\sigma = E_T(\Delta\varepsilon - \Delta\varepsilon_T) \tag{4.29}$$

$$\Delta\varepsilon_T = \alpha\Delta T \tag{4.30}$$

in which

$\Delta T$ = temperature above an arbitrary reference temperature

$\alpha$ = coefficient of thermal expansion

4.2.3. Nodal Forces Computation

Using the principle of minimum potential energy [4.23], the deformation nodal forces are found as

$$\{f^d\} = \int_V [B]^T \sigma \, dV \tag{4.31}$$

where V is the volume of the element. The deformation nodal forces are conjugate to the deformation nodal displacements in the sense that their scalar product yields work, so that from Eq. (4.5) it follows that

$$\{f^d\}^T = \{f_{IJ}, m_{IJ}, m_I^y, m_I^z, m_J^y, m_J^z\} \tag{4.32}$$

The integral for the nodal forces, Eq. (4.31), is evaluated numerically. The following definitions are made in order to obtain the deformation nodal forces:

$$P_i = \int_A \sigma \, dA \tag{4.33}$$

$$M_i^y = \int_A \sigma z dA \tag{4.34}$$

$$M_i^z = -\int_A \sigma y dA \tag{4.35}$$

$$M_i = \frac{1}{\ell^t} \int_A \sigma(y^2 + z^2) dA \tag{4.36}$$

where i = I and J denotes $\xi = 0$ and 1, respectively, and A refers to the beam cross-sectional area. The quantities obtained from Eqs. (4.33) to Eq. (4.36) are assumed to be linear functions of $\xi$; for example,

$$P(\xi) = (P_J - P_I)\xi + P_I \tag{4.37}$$

$$M^y(\xi) = (M_J^y - M_I^y)\xi + M_I^y \tag{4.38}$$

$$M^z(\xi) = (M_J^z - M_I^z)\xi + M_I^z \tag{4.39}$$

$$M(\xi) = (M_J - M_I)\xi + M_I \tag{4.40}$$

The integrals in Eqs. (4.33) to (4.36) must be evaluated numerically since the cross section may be partially plastic. Numerical methods are introduced to calculate the strains and stresses (which are functions of $\xi$, $\eta$, and $\rho$) at different points of the cross section. The cross-sectional area is correspondingly divided into a number of subelements over the depth and width as shown in Fig. 4.6. The number of layers used in two directions must be sufficient to describe the variation of material properties and stresses over the depth and width. Each subelement is assumed to have uniform material properties, and the strain is evaluated at the centroid of the subelement. The stress is assumed constant and equal to the stress calculated at the centroid of the subelement.

The deformation nodal forces in Eq. (4.31) can be computed by introducing [B] from Eq. (4.27) and Eqs. (4.33) through (4.40) to obtain

$$\{f^d\} = \int_V [B]^T \sigma dA = [A_L] + [A_{NL}] \tag{4.41}$$

where

$$[A_L] = \begin{bmatrix} 1/2(P_I + P_J) \\ M_{IJ} \\ M_I^y \\ M_I^z \\ M_J^y \\ M_J^z \end{bmatrix} \tag{4.42}$$

$$[A_{NL}] = \begin{bmatrix} 0 \\ \left(\frac{1}{2} M_I + \frac{1}{2} M_J\right) \theta_{IJ}^x + \frac{1}{12}\left(M_J^z - M_I^z\right)\left(\theta_J^y - \theta_I^y\right) + \frac{1}{12}\left(M_J^y - M_I^y\right)\left(\theta_I^z - \theta_J^z\right) \\ \frac{-1}{12}\left(M_J^z - M_I^z\right)\theta_{IJ}^x + \frac{\ell^t}{60}(6P_I + 2P_J)\theta_I^y + \frac{\ell^t}{60}(-P_I - P_J)\theta_J^y \\ \frac{1}{12}\left(M_J^y - M_I^y\right)\theta_{IJ}^x + \frac{\ell^t}{60}(6P_I + 2P_J)\theta_I^z + \frac{\ell^t}{60}(-P_I - P_J)\theta_J^z \\ \frac{1}{12}\left(M_J^z - M_I^z\right)\theta_{IJ}^x + \frac{\ell^t}{60}(-P_I - P_J)\theta_I^y + \frac{\ell^t}{60}(2P_I + 6P_J)\theta_J^y \\ \frac{-1}{12}\left(M_J^y - M_I^y\right)\theta_{IJ}^x + \frac{\ell^t}{60}(-P_I - P_J)\theta_I^z + \frac{\ell^t}{60}(2P_I + 6P_J)\theta_J^z \end{bmatrix} \tag{4.43}$$

The first term on the righthand side of Eq. (4.41) is the linear approximation to the nodal forces and, hence, is not dependent on the deformation. The second term introduces the additional contribution as a result of a deformation. The linear term

$$M_{IJ} = \frac{GJ}{\ell^t}\,\theta^x_{IJ} \tag{4.44}$$

has been added to Eq. (4.42), even though it does not result from the normal axial stress, in which G is the shearing modulus, and J is a torsional constant expressed as a function of the element cross section [4.20].

The nodal forces $\{f\}$ in the updated element coordinate system can be obtained from the deformation nodal forces $\{f^d\}$ by equilibrium as

$$\{f\} = [R_L]^T \{f^d\} \tag{4.45}$$

in which

$$[R_L] = \begin{bmatrix} -1 & 0 & 0 & 0 & 0 & 0 & 1 & 0 & 0 & 0 & 0 & 0 \\ 0 & 0 & 0 & -1 & 0 & 0 & 0 & 0 & 0 & 1 & 0 & 0 \\ 0 & 0 & \frac{-1}{\ell^t} & 0 & 1 & 0 & 0 & 0 & \frac{1}{\ell^t} & 0 & 0 & 0 \\ 0 & \frac{1}{\ell^t} & 0 & 0 & 0 & 1 & 0 & \frac{-1}{\ell^t} & 0 & 0 & 0 & 0 \\ 0 & 0 & \frac{-1}{\ell^t} & 0 & 0 & 0 & 0 & 0 & \frac{1}{\ell^t} & 0 & 1 & 0 \\ 0 & \frac{1}{\ell^t} & 0 & 0 & 0 & 0 & 0 & \frac{-1}{\ell^t} & 0 & 0 & 0 & 1 \end{bmatrix} \tag{4.46}$$

### 4.2.4. Tangent Stiffness Matrix in Element Coordinate System

The incremental deformation displacements can be related to the incremental displacements in element coordinates by the linearized equation

$$\{\Delta d^d\} = [R_L]\ \{\Delta d\} \tag{4.47}$$

which, with Eq. (4.45), establishes the principle of contragradience.

As the chord (convected coordinates) rotates as shown in Fig. 4.2, the transformation matrix $[R_L]$ changes. That is, the transformation from the deformation coordinates, which are based on the rotating chord, to the temporarily stationary updated coordinates changes. Using the first term of a Taylor Series, the incremental form of Eq. (4.45) is

$$\{\Delta f\} = [\Delta R]^T\ \{f^d\} + [R]^T\ \{\Delta f^d\} \tag{4.48}$$

in which [R] is the changing transformation matrix. Now, since the increments are small, [R] is approximately $[R_L]$ and

$$\{\Delta f\} = [\Delta R]^T\ \{f^d\} + [R_L]^T\ \{\Delta f^d\} \tag{4.49}$$

Equation (4.45) with $[R_L]$ remains valid for the total force transformation during the entire displacement increment, if the increment is small. Since the assumed deformation shape functions are with respect to the chord (which moves with respect to the updated Lagrangian coordinates), the rate of change of the matrix $[\Delta R]$ is nonzero. If the assumed shape functions had included the rigid body motion (i.e., polynomials with respect to the updated coordinates), $[\Delta R]$ would have been equal to zero.

The second term on the righthand side of Eq. (4.49) can be expressed by

$$[R_L]^T \{\Delta f^d\} = [R_L]^T \int_V [\Delta B]^T \sigma dV + [R_L]^T \int_V [B]^T \Delta\sigma dV \tag{4.50}$$

The following definitions are introduced

$$[R_L]^T \int_V [B]^T \Delta\sigma dV = ([k_0] + [k_L]) \{\Delta d\} \tag{4.51}$$

$$[R_L]^T \int_V [\Delta B]^T \sigma dV = [k_{G1}] \{\Delta d\} \tag{4.52}$$

where

$$[k_0] = [R_L]^T \int_V [B_L]^T E_T [B_L] dV [R_L] \tag{4.53}$$

$$[k_L] = [R_L]^T \left[ \int_V ([B_L]^T E_T [B_{NL}] + [B_{NL}]^T E_T [B_L] + [B_{NL}]^T E_T [B_{NL}]) dV \right] [R_L] \tag{4.54}$$

$$[\Delta B]^T = ([G_z]^T [G_z] + [G_y]^T [G_y]) [R_L] \{\Delta d\} \tag{4.55}$$

The first term on the righthand side of Eq. (4.49) can be expressed by

$$[\Delta R]^T \{f^d\} = [k_{G2}] \{\Delta d\} \tag{4.56}$$

and will be considered later.

The matrix $[k_O]$ is the conventional stiffness matrix; $[k_{G1}]$ and $[k_{G2}]$ are the initial stress matrix (or the geometric stiffness matrix), which depend linearly on the deformation nodal displacements; and $[k_L]$ represents the large displacement stiffness matrix, which depends on quadratic terms of the deformation nodal displacements. The updated Lagrangian strain approach makes the strains and rotations in the element system small enough (for reasonably small element sizes) that $[k_L]$ can be omitted [4.18]. Equation (4.49) can then be reduced to

$$\{\Delta f\} = ([k_O] + [k_G])\{\Delta d\}$$
$$= [k]_T\{\Delta d\} \tag{4.57}$$

where

$$[k_G] = [k_{G1}] + [k_{G2}] \tag{4.58}$$

The following definitions are made in order to obtain the expressions for $[k_O]$, $[k_G]$

$$(EA)_{Ti} = \int_A E_T dA \tag{4.59}$$

$$(EK^y)_{Ti} = \int_A E_T z dA \tag{4.60}$$

$$(EK^z)_{Ti} = \int_A E_T y dA \tag{4.61}$$

$$(EI^y)_{Ti} = \int_A E_T z^2 dA \tag{4.62}$$

$$(EI^{z})_{Ti} = \int_{A} E_T y^2 dA \tag{4.63}$$

$$(EI^{yz})_{Ti} = \int_{A} E_T yz dA \tag{4.64}$$

where i = I and J denotes $\xi = 0$ and 1, respectively. The quantities obtained from Eqs. (4.59) to (4.64) are assumed to be linear functions of $\xi$ [similar to Eqs. (4.37) to (4.40)].

The conventional matrix stiffness is obtained by evaluating the integral [see Eq. (4.53)]

$$[k_0] = [R_L]^T [k_0^d] [R_L] \tag{4.65}$$

$$[k_0^d] = \int_{V} [B_L]^T E_T [B_L] dV \tag{4.66}$$

Using the definition of Eqs. (4.59) to (4.64) gives Eq. (4.67) (see following page). The linear term $(GJ)_T/\ell^t$ has been inserted into Eq. (4.67), even though it does not result from axial (normal) strain. It should be noted that for a conventional stiffness matrix this term is used to resist the applied torsion.

The geometric (initial stress) stiffness matrix $[k_{G1}]$ is obtained by evaluating the integral of Eq. (4.52) with the definition in Eqs. (4.33) to (4.36) and (4.59) to (4.64):

$$[k_{G1}] = [R_L]^T [k_{G1}{}^d] [R_L] \tag{4.68}$$

The explicit form of $[k_G]$ (= $[k_{G1}]$ + $[k_{G2}]$) will be shown later.

$$
[k_0^d] = \begin{bmatrix}
\frac{1}{\ell^t}\left(\frac{1}{2}(EA)_{TI} + \frac{1}{2}(EA)_{TJ}\right) & 0 & \frac{-1}{\ell^t}(EK^y)_{TI} & \frac{1}{\ell^t}(EK^z)_{TI} & \frac{1}{\ell^t}(EK^y)_{TJ} & \frac{-1}{\ell^t}(EK^z)_{TJ} \\
 & \frac{(GJ)_T}{\ell^t} & 0 & 0 & 0 & 0 \\
 & & \frac{1}{\ell^t}\left(3(EI^y)_{TI} + (EI^y)_{TJ}\right) & \frac{-1}{\ell^t}\left(3(EI^{yz})_{TI} + (EI^{yz})_{TJ}\right) & \frac{1}{\ell^t}\left((EI^y)_{TI} + (EI^y)_{TJ}\right) & \frac{-1}{\ell^t}\left((EI^{yz})_{TI} + (EI^{yz})_{TJ}\right) \\
 & \text{sym} & & \frac{1}{\ell^t}\left(3(EI^z)_{TI} + (EI^z)_{TJ}\right) & \frac{-1}{\ell^t}\left((EI^{yz})_{TI} + (EI^{yz})_{TJ}\right) & \frac{1}{\ell^t}\left((EI^z)_{TI} + (EI^z)_{TJ}\right) \\
 & & & & \frac{1}{\ell^t}\left((EI^y)_{TI} + 3(EI^y)_{TJ}\right) & \frac{-1}{\ell^t}\left((EI^{yz})_{TI} + 3(EI^{yz})_{TJ}\right) \\
 & & & & & \frac{-1}{\ell^t}\left((EI^z)_{TI} + 3(EI^z)_{TJ}\right)
\end{bmatrix} \qquad (4.67)
$$

The geometric (initial stress) stiffness matrix $[k_{G2}]$, as shown in Eq. (4.56), is evaluated as follows. By the chain rule, since [R] changes with the displacements {d},

$$[\Delta R]^T \{f^d\} = \sum_{i=1}^{12} \left[\frac{\partial R}{\partial d_i}\right]^T \Delta d_i \{f^d\} \tag{4.69}$$

For the purpose of evaluating the derivative in this equation, write

$$[R] = [R_L] [R_N] \tag{4.70}$$

in which $[R_N]$ is a transformation matrix due to the small rigid body motion between the chord and the updated coordinates. From Eqs. (4.45) and (4.70), Eq. (4.69) becomes

$$[\Delta R]^T \{f^d\} = \sum_{i=1}^{12} \left[\frac{\partial R_N}{\partial d_i}\right]^T \Delta d_i [R_L]^T \{f^d\}$$

$$= \sum_{i=1}^{12} \left[\frac{\partial R_N}{\partial d_i}\right]^T \Delta d_i \{f\} \tag{4.71}$$

Only two terms in Eq. (4.71) will be presented here; the others will follow a similar derivation. Consider only the terms $[\partial R_N/\partial d_2]^T \Delta d_2$ and $[\partial R_N/\partial d_8]^T \Delta d_8$. Consider the matrix $[r_N]$, which forms a 3 × 3 submatrix on the diagonal of $[R_N]$ [similar to Eq. (4.4)]. For a displacement $d_2$, the transformation between the chord and the updated coordinates is (see Fig. 4.7).

$$[r_N^2] = \begin{bmatrix} 1 & -\frac{d_2}{\ell} & 0 \\ \frac{d_2}{\ell} & 1 & 0 \\ 0 & 0 & 1 \end{bmatrix} \tag{4.72}$$

Similarly, for a displacement $d_8$,

$$[r_N^8] = \begin{bmatrix} 1 & \frac{d_8}{\ell} & 0 \\ -\frac{d_8}{\ell} & 1 & 0 \\ 0 & 0 & 1 \end{bmatrix} \tag{4.73}$$

If $d_2$ and $d_8$ are small, $[r_N]$ is the sum of these two matrices. Substituting the sum of Eqs. (4.72) and (4.73) into Eq. (4.71) (i = 2 and 8 only) gives

$$[\Delta R]^T \{f^d\} = [R_o]^T \{f\} \{Q_o\} \{\Delta d\} \tag{4.74}$$

where

$$[R_o]^T = \begin{bmatrix} [r_o] & & & \\ & [r_o] & & \\ & & [r_o] & \\ & & & [r_o] \end{bmatrix}^T \tag{4.75}$$

$$[r_o] = \begin{bmatrix} 0 & 1 & 0 \\ -1 & 0 & 0 \\ 0 & 0 & 0 \end{bmatrix} \tag{4.76}$$

$$[Q_o] = \begin{bmatrix} 0 & \frac{-1}{\ell} & 0 & 0 & 0 & 0 & 0 & \frac{1}{\ell} & 0 & 0 & 0 & 0 \end{bmatrix} \tag{4.77}$$

Similarly, for i = 3 and 9 (see Fig. 4.7), one obtains

$$[r_1] = \begin{bmatrix} 0 & 0 & 1 \\ 0 & 0 & 0 \\ -1 & 0 & 0 \end{bmatrix} \tag{4.78}$$

$$[Q_1] = \begin{bmatrix} 0 & 0 & \frac{-1}{\ell} & 0 & 0 & 0 & 0 & 0 & \frac{1}{\ell} & 0 & 0 & 0 \end{bmatrix} \tag{4.79}$$

for i = 4 and 10 (see Fig. 4.7). The average twist angle is taken as the rigid body rotation about the x axis, which gives

$$[r_2] = \begin{bmatrix} 0 & 0 & 0 \\ 0 & 0 & 1 \\ 0 & -1 & 0 \end{bmatrix} \tag{4.80}$$

$$[Q_2] = \begin{bmatrix} 0 & 0 & 0 & \frac{1}{2} & 0 & 0 & 0 & 0 & 0 & \frac{1}{2} & 0 & 0 \end{bmatrix} \tag{4.81}$$

The rate of change of $[r_N]$ with respect to $d_1$, $d_5$, $d_6$, $d_7$, $d_{11}$, and $d_{12}$ is zero. By substituting Eqs. (4.75) to (4.81), Eq. (4.71) now becomes

$$\begin{aligned} [\Delta R]^T\{f^d\} &= \left( [R_o]^T\{f\}[Q_o] + [R_1]^T\{f\}[Q_1] + [R_2]^T\{f\}[Q_2] \right)\{\Delta d\} \\ &= [k_{G2}]\{\Delta d\} \end{aligned} \tag{4.82}$$

The explicit form of $[k_G]$ which can be obtained by combining $[k_{G1}]$ and $[k_{G2}]$ is given by Eq. (4.83) (see following page).

$$[k_G] = \frac{1}{\ell^t}$$

$$\begin{bmatrix}
0 & B1 & -B_2 & 0 & 0 & 0 & 0 & -B_1 & B_2 & 0 & 0 & 0 \\
0 & C_1 + B_3 & 0 & \frac{\ell^t}{2} B_2 & 0 & C_2 & 0 & -C_1 - B_3 & 0 & \frac{\ell^t}{2} B_2 & 0 & C_3 \\
0 & 0 & C_1 + B_3 & \frac{\ell^t}{2} B_1 & -C_2 & 0 & 0 & 0 & -C_1 - B_3 & \frac{\ell^t}{2} B_1 & -C_3 & 0 \\
0 & B_4 & B_5 & C_4 & C_5 & -C_6 & 0 & -B_4 & -B_5 & -C_4 & -C_5 & C_6 \\
0 & B_6 & -C_2 & C_5 - \frac{\ell^t B_5}{2} & C_7 & 0 & 0 & -B_6 & C_2 & -C_5 - \frac{\ell^t B_5}{2} & -C_8 & 0 \\
0 & C_2 & B_6 & -C_6 + \frac{\ell^t B_4}{2} & 0 & C_7 & 0 & -C_2 & -B_6 & C_6 + \frac{\ell^t B_4}{2} & 0 & -C_8 \\
0 & -B_1 & B_2 & 0 & 0 & 0 & 0 & B_1 & -B_2 & 0 & 0 & 0 \\
0 & -C_1 - B_3 & 0 & \frac{-\ell^t B_2}{2} & 0 & -C_2 & 0 & C_1 + B_3 & 0 & \frac{-\ell^t B_2}{2} & 0 & -C_3 \\
0 & 0 & -C_1 - B_3 & \frac{-\ell^t B_1}{2} & C_2 & 0 & 0 & 0 & C_1 + B_3 & \frac{-\ell^t B_1}{2} & C_3 & 0 \\
0 & B_7 & B_8 & -C_4 & -C_5 & C_6 & 0 & -B_7 & -B_8 & C_4 & C_5 & -C_6 \\
0 & -B_6 & -C_3 & -C_5 + \frac{\ell^t B_8}{2} & -C_8 & 0 & 0 & B_6 & C_3 & C_5 + \frac{\ell^t B_8}{2} & C_9 & 0 \\
0 & C_3 & -B_6 & C_6 + \frac{\ell^t B_7}{2} & 0 & -C_8 & 0 & -C_3 & B_6 & -C_6 + \frac{\ell^t B_7}{2} & 0 & C_9
\end{bmatrix} \tag{4.83}$$

where

$$C_1 = \frac{1}{60}(6P_I + 6P_J) \qquad B_1 = \frac{1}{\ell^t}\left(m_I^z + m_J^z\right)$$

$$C_2 = \frac{\ell^t}{60}(5P_I + P_J) \qquad B_2 = \frac{1}{\ell^t}\left(m_I^y + m_J^y\right)$$

$$C_3 = \frac{\ell^t}{60}(P_I + 5P_J) \qquad B_3 = f_{IJ} = \frac{1}{2}(P_I + P_J)$$

$$C_4 = \left(\frac{1}{2}M_I + \frac{1}{2}M_J\right) \qquad B_4 = m_I^y$$

$$C_5 = \frac{\ell^t}{12}\left(M_J^z - M_I^z\right) \qquad B_5 = m_I^z \qquad (4.84)$$

$$C_6 = \frac{\ell^t}{12}\left(M_J^y - M_I^y\right) \qquad B_6 = m_{IJ}$$

$$C_7 = \frac{(\ell^t)^2}{60}(6P_I + 2P_J) \qquad B_7 = m_J^y$$

$$C_8 = \frac{(\ell^t)^2}{60}(P_I + P_J) \qquad B_8 = m_J^z$$

$$C_9 = \frac{(\ell^t)^2}{60}(2P_I + 6P_J)$$

in which the quantities $C_i$ (i = 1, 9) and $B_i$ (i = 1, 8) result from $[k_{G1}]$ and $[k_{G2}]$, respectively.

Not all terms of the initial matrix represented in Eq. (4.83) are of equal importance. The terms which correspond to a change in the axial force due to the presence of initial transverse forces $B_1$

and $B_2$ during a rotation relative to the element system have been neglected. The transverse forces are generally quite small compared to the axial stiffness, so a small axial displacement will compensate for these changes in axial force caused by rotation of shear forces.

The stiffness matrix $[k_G]$ is not symmetric. The unsymmetric terms arise in $[k_{G2}]$ due to the twist and bending of the member $B_4$ - $B_8$ and the presence of an initial bending moment $\ell^t B_1/2$, $\ell^t B_2/2$, $\ell^t B_4/2$, $\ell^t B_5/2$, $\ell^t B_7/2$, and $\ell^t B_8/2$. During a moderate rotation in the updated system, these unsymmetric terms will contribute very little to the total stiffness. After these terms are neglected, Eq. (4.83) becomes Eq. (4.85) (see following page).

4.2.5. Coordinate Updating and Three-dimensional Transformation Matrix

The beam-column element formulations are based on the general incremental updated Lagrangian continuum mechanics equations, which are briefly summarized in the previous sections. Consider the motion of a beam-column element in a fixed Cartesian coordinate system (global system) as shown in Fig. 4.8. In Eq. (4.48) the incremental equilibrium equations of a beam-column element were derived by first evaluating the finite element matrices corresponding to the element coordinate system (see Fig. 4.8), and then transforming the resulting matrices to the global Cartesian coordinate axes prior to the element assemblage process [4.1]. The finite element matrices corresponding

$$[k_G] = \frac{1}{\ell^t}\begin{bmatrix}
0 & 0 & 0 & 0 & 0 & 0 & 0 & 0 & 0 & 0 & 0 & 0 \\
C_1 + B_3 & 0 & 0 & 0 & C_2 & 0 & -C_1 - B_3 & 0 & 0 & 0 & C_3 \\
 & C_1 + B_3 & 0 & -C_2 & 0 & 0 & 0 & -C_1 - B_3 & 0 & -C_3 & 0 \\
 & & C_4 & C_5 & -C_6 & 0 & 0 & 0 & -C_4 & -C_5 & C_6 \\
 & & & C_7 & 0 & 0 & 0 & C_2 & -C_5 & -C_8 & 0 \\
 & & & & C_7 & 0 & -C_2 & 0 & C_6 & 0 & -C_8 \\
 & \text{sym} & & & & 0 & 0 & 0 & 0 & 0 & 0 \\
 & & & & & & C_1 + B_3 & 0 & 0 & 0 & -C_3 \\
 & & & & & & & C_1 + B_3 & 0 & C_3 & 0 \\
 & & & & & & & & C_4 & C_5 & -C_6 \\
 & & & & & & & & & C_9 & 0 \\
 & & & & & & & & & & C_9
\end{bmatrix} \tag{4.85}$$

to the element coordinate axes are obtained by measuring all static and kinematic quantities in the element coordinate system. Thus, the transformation matrix $[T^t]$, which relates displacements measured in the element system at the current configuration (at time t) to the displacements measured in the global coordinate system, can be obtained by a simple vector transformation between the element and global coordinate system.

As mentioned before, the unit vectors $\vec{e}_i^t$, $\vec{b}_{Ii}^t$, and $\vec{b}_{Ji}^t$ $(i = 1,3)$ must be updated for each incremental load in order to track the element and nodal coordinate systems. For the purpose of tracking the unit vectors $\vec{e}_i^t$, $\vec{b}_{Ii}^t$, and $\vec{b}_{Ji}^t$ at the current stage, start from the initial stage (at time 0) when the unit vectors $\vec{e}_i^0$, $\vec{b}_{Ii}^0$, and $\vec{b}_{Ji}^0$ are the same. After the first incremental load is applied, the incremental displacements $\{\Delta D^t\}$ are obtained in the global coordinate system

$$\{\Delta D^t\} = \begin{Bmatrix} \{\Delta D_{TI}^t\} \\ \{\Delta D_{\theta I}^t\} \\ \{\Delta D_{TJ}^t\} \\ \{\Delta D_{\theta J}^t\} \end{Bmatrix} \tag{4.86}$$

where

$\{\Delta D_{TI}^t\}$ = translation at node I in X, Y, and Z directions

$\{\Delta D_{\theta I}^t\}$ = rotation at node I in X, Y, and Z directions

At the initial stage, the third node K is defined as a point in the positive x-y plane as shown in Fig. 4.8. At the current stage, node I and J are displaced to the new position $\vec{X}_I^t$ and $\vec{X}_J^t$, respectively.

$$\vec{X}_I^t = \vec{X}_J^0 + \Delta\vec{D}_{TI}^t \tag{4.87}$$

$$\vec{X}_J^t = \vec{X}_J^0 + \Delta\vec{D}_{TJ}^t \tag{4.88}$$

The third node (K node) translates as the average of the two end nodes. In addition, it rotates about the axis of the beam on the average of the twisting rotations. Since the incremental displacements $\{\Delta D^t\}$ are assumed to be small, the new position of the K node is obtained as

$$\vec{X}_K^t = \vec{X}_{TK}^t + \Delta\vec{D}_{\theta K}^t \times \left(\vec{X}_{TK}^t - \vec{X}_M^t\right) \tag{4.89}$$

where

$$\vec{X}_{TK}^t = \vec{X}_K^0 + \frac{1}{2}\left(\Delta\vec{D}_{TI}^t + \Delta\vec{D}_{TJ}^t\right) \tag{4.90}$$

is the translation term. The small rotation about the beam axis is

$$\Delta\vec{D}_{\theta K}^t = \left[\frac{1}{2}\left(\Delta\vec{D}_{\theta I}^t + \Delta\vec{D}_{\theta J}^t\right) \cdot \vec{e}_1^t\right]\vec{e}_1^t \tag{4.91}$$

The last quantity in Eq. (4.89), in which

$$\vec{X}_M^t = \frac{1}{2}\left(\vec{X}_I^t + \vec{X}_J^t\right) \tag{4.92}$$

is the radius vector from the midpoint M to K.

The direction cosines for the updated element unit vectors $\vec{e}_i^t$ (Eq. 4.2) can now be determined by vector mechanics as follows:

$$\vec{e}_1^t = \frac{\vec{X}_{IJ}^t}{\left|\vec{X}_{IJ}^t\right|} = \ell_1^t\vec{I} + m_1^t\vec{J} + n_1^t\vec{K} \tag{4.93}$$

$$\vec{e}_3^t = \frac{\vec{X}_{IJ}^t \times \vec{X}_{IK}^t}{\left|\vec{X}_{IJ}^t \times \vec{X}_{IK}^t\right|} = \ell_3^t\vec{I} + m_3^t\vec{J} + n_3^t\vec{K} \tag{4.94}$$

$$\vec{e}_2^t = \vec{e}_3^t \times \vec{e}_1^t = \ell_2^t\vec{I} + m_2^t\vec{J} + n_2^t\vec{K} \tag{4.95}$$

where $\vec{I}$, $\vec{J}$, $\vec{K}$ are unit vectors in the global coordinate system and

$$\vec{X}_{IJ}^t = \vec{X}_J^t - \vec{X}_I^t \text{ , etc.} \tag{4.96}$$

Each element is associated with an element coordinate system (x,y,z), which is rotated relative to the global coordinates (X,Y,Z) by a rigid body motion. Incremental nodal displacements in the element and global coordinates are related by an orthogonal transformation

$$\{\Delta d\} = [T]\{\Delta D\} \tag{4.97}$$

where

$$[T] = \begin{bmatrix} [T_{EG}] & & & \\ & [T_{EG}] & & \\ & & [T_{EG}] & \\ & & & [T_{EG}] \end{bmatrix} \tag{4.98}$$

and $[T_{EG}]$ is presented in Eq. (4.2).

Now, for the nodal coordinate system, the unit vectors $\vec{b}_{Ii}^t$ and $\vec{b}_{Ji}^t$ must be updated since they rotate with the nodes. From the assumption

that the incremental rotations $\{\Delta D^t_{\theta I}\}$ and $\{\Delta D^t_{\theta J}\}$ are small, the incremental vectors can be obtained by taking the cross product of the two vectors, $\Delta\vec{D}^t_{\theta I}$ and $\vec{b}^0_{Ii}$, and updating

$$b^{\rightarrow t}_{Ii} = \vec{b}^{\,0}_{Ii} + \Delta\vec{D}^t_{\theta I} \times \vec{b}^0_{Ii} \tag{4.99}$$

$$b^{\rightarrow t}_{Ji} = b^{\rightarrow 0}_{Ji} + \Delta\vec{D}^t_{\theta J} \times \vec{b}^0_{Ji} \tag{4.100}$$

These current updated vectors must be normalized to obtain the direction cosines for the current updated unit vectors (Eq. 4.1). For the next increment, t = 0 refers to the previous increment.

4.2.6. Tangent Stiffness Matrix in Global Coordinate System

The nodal forces and displacement in the global system can be related to the current system as follows:

$$\{F\} = [T]^T\{f\} \tag{4.101}$$

$$\{d\} = [T]\{D\} \tag{4.102}$$

The incremental nodal forces in the global system can be found as

$$\{\Delta F\} = [T]^T\{\Delta f\} \tag{4.103}$$

Substituting Eqs. (4.57) and (4.97) into Eq. (4.103) yields the tangent stiffness of the beam-column element in the global coordinate system as

$$\{\Delta F\} = [K]_T\{\Delta D\} \tag{4.104}$$

where

$$[K]_T = [T]^T[k]_T[T] \tag{4.105}$$

## 4.3. Soil Spring Finite Element

### 4.3.1. Soil Model Description

The basic assumptions employed for the treatment of the three-dimensional soil model are as follows:

(1) Torsional soil resistance is not considered in the soil-pile interaction [4.24].

(2) There is no coupling between the axial and lateral soil resistance. That is, the deformation modes for an isolated soil spring are independent of each other. Parker and Reese [4.25] have reported that the relationship between axial load and displacements of the soil is not significantly affected by the presence of lateral deflections of the soil, and vice versa. Soil behavior can thus be divided into axial and lateral parts as described in Secs. 3.3 and 3.4.

(3) The behavior of the soil at a particular depth is independent of the soil behavior at another depth [4.26].

(4) The lateral soil behavior is assumed to be independent in the two orthogonal lateral directions. That is, the soil resistance in the y direction is not affected by the soil resistance in the z direction. Two independent lateral springs will be placed in the y and z directions, respectively.

The soil displacements and forces are calculated on the basis of the displacements in the element coordinate system as shown in Fig. 4.9.

4.3.2. Soil Springs

If nonlinear behavior is considered, the soil spring stiffness is not a constant and instead is a function of displacement. Only the lateral spring element in the y direction will be discussed here, since the other soil spring would follow the same derivations. As discussed in the previous section, the soil resistance directly opposes the lateral displacement in the y direction. The lateral soil resistance per unit length of the pile p is assumed to be linearly distributed along the pile element (Fig. 4.9). A set of p-y curves is represented by the modified Ramberg-Osgood cyclic model (see Sec. 3.2.2). In this figure, p, y, and $k_{yt}$ (the lateral soil tangent stiffness) are in the updated element y direction. The relationship between incremental soil resistance and displacement can be expressed following Eq. (3.5) as

$$\Delta p_y = k_{yt} \Delta y \tag{4.106}$$

The quantities $\Delta y$, $k_{yt}$, and $p_y$ are assumed to be a linear function of $\xi$,

$$\Delta y = [1 - \xi, \ \xi] \begin{Bmatrix} \Delta d_2 \\ \Delta d_8 \end{Bmatrix} = [N_s]\{\Delta d\} \tag{4.107}$$

$$k_{yt} = [1 - \xi, \ \xi] \begin{Bmatrix} k_{ytI} \\ k_{ytJ} \end{Bmatrix} \tag{4.108}$$

$$p_y = [1 - \xi, \ \xi] \begin{Bmatrix} p_{yI} \\ p_{yJ} \end{Bmatrix} \tag{4.109}$$

By the principle of virtual work

$$\{\Delta f\} = [k_y]_T\{\Delta d\} \tag{4.110}$$

where

$$[k_y]_T = \int_o^{\ell} [N_s]^T k_{yt} [N_s] dx \tag{4.111}$$

The explicit form of soil lateral tangent stiffness for y motions is

$$[k_y]_T = \ell^t \begin{bmatrix} 1/4\ k_{ytI} + 1/12\ k_{ytJ} & 1/12\ k_{ytI} + 1/12\ k_{ytJ} \\ \text{sym} & 1/12\ k_{ytI} + 1/4\ k_{ytJ} \end{bmatrix} \tag{4.112}$$

The total nodal forces {f} can be obtained by using the principle of virtual work as

$$\{f\} = \int_0^{\ell} [N_s]^T p_y\ dx \tag{4.113}$$

or, explicitly, since degree-of-freedom 2 and 8 are for the y displacements of the beam element,

$$\begin{Bmatrix} f_2 \\ f_8 \end{Bmatrix} = \ell^t \begin{Bmatrix} 1/3\ P_{yI} + 1/6\ p_{yJ} \\ 1/6\ p_{yI} + 1/3\ p_{yJ} \end{Bmatrix} \tag{4.114}$$

The tangent stiffness of the nonlinear springs for the other cases (lateral z spring, vertical spring, and point spring) can be obtained

in a similar manner (see Fig. 4.1). The matrix $[k_s]_T$ represents the tangent stiffness for the soil model, which is added to the beam stiffness $[k]_T$ to form the tangent stiffness of the soil-pile interaction model.

### 4.3.3. Backwall Soil Model

Figure 4.10 shows the backwall soil model which is considered in integral bridge abutments. Longitudinal bridge movements may cause parts of the backwall to come into contact with or separate from the soil. In the idealized backwall soil model, it can be assumed that the backwall soil is attached to the backwall, so that the soil spring properties of the backwall soil can be treated the same as the soil springs attached to the pile.

## 4.4. Basic Nonlinear Solution Techniques

In previous sections the finite element model which is used to predict the nonlinear behavior of pile-soil interaction has been described. The general incremental tangent stiffness equations for the beam column and soil spring elements are the major results. In this section these equations become the basis from which a general incremental nonlinear solution procedure is formulated.

### 4.4.1. The Incremental Load Technique

The conditions of equilibrium for a given structure are satisfied by solving the structural stiffness equations for the unknown generalized (global) displacements given a known applied loading. In a linear analysis environment this solution procedure is straightforward because all of the stiffness parameters are constant, that is, independent of

displacement and expressed in closed form. This is not the case in a nonlinear analysis environment where the stiffness parameters are themselves dependent on the state of total displacement, total stress, and material properties, and may not be conveniently expressed in closed form. In this case the most suitable approach to analysis is by applying the total load in a series of small finite-sized increments. For each load increment the resulting increment of displacement is determined from the incremental stiffness equations where the stiffness parameters are evaluated to reflect the instantaneous state of the total displacement, total stress, and material characteristics that exist just prior to the application of the load increment. The total displacement after the load increment has been applied is evaluated by adding the computed displacement increment to the total displacement that exists prior to the application of the load increment.

This type of solution is a piecewise linear solution, a physical representation of which is illustrated in Fig. 4.11. This figure shows three load-displacement (F - d) curves for a single degree-of-freedom system. Curve A represents the linear behavior which would result by solving the governing stiffness equation for the total load applied in one increment; curve B is the piecewise linear solution which would result by applying the total load in several increments; and curve C represents the exact nonlinear behavior. It is clear that as the size of the load increment approaches zero (or the number of load increments approaches infinity), the piecewise linear curve approaches the true curve. Since load increments of infinitesimal order are impossible to

achieve, a reasonable number of moderately sized load increments will be applied.

4.4.2. Newton-Raphson Iteration Method

As indicated in Fig. 4.11, it is desirable for the structure solution procedure to come as close to curve C with as few load increments as possible to obtain the desired analytical accuracy. This can be achieved by employing the Newton-Raphson method to iteratively satisfy equilibrium.

This approach is characteristic of the tangent stiffness technique where, in a given load increment, the Newton-Raphson iteration method is applied so that the element nodal displacements are successively corrected until joint equilibrium is satisfied. These displacement corrections are computed using element tangent stiffness matrices, which are successively computed to reflect the most current state of total displacement, total stress, and material properties.

The basic characteristics of this technique are illustrated in Fig. 4.12 for a single degree-of-freedom system which is characterized by the following parameters:

$\sigma$ = element stress

f = element force

F = applied external load

d = element displacement (in this case for a single degree-of-freedom, this is the same as the global displacement D)

$E_T$ = element material property parameter--the instantaneous slope of the element stress-strain relationship

$k_T = k_T(d, \sigma, E_T)$ the tangent stiffness--a function of total element displacement d, total element stress $\sigma$, and the state of the element material property parameter $E_T$.

At a particular level of applied load, given by $F_j$, the total element stress is given by $\sigma_j$, the total element force is given by $f_j$, the total element displacement is given by $d_j$, and the current tangent stiffness is given by $k_{Tj}$. This state, which is indicated by point 1 on Fig. 4.12, is reached after the application of several load increments.

At this level of applied load $F_j$, the description of the Newton-Raphson iteration begins with the application of an increment of external load $\Delta F$. To satisfy equilibrium, the following relationship must be true:

$$f_j + (k_{Tj})\ \Delta d = F_j + \Delta F \tag{4.115}$$

Equation (4.115) is a representation of the linearized incremental analysis wherein the structure is assumed to behave linearly during the application of an incremental load $\Delta F$. Equation (4.115) also establishes the analysis at point 2 of Fig. 4.12. This increment of displacement $\Delta d_j^1$, which results from the application of $\Delta F$, is computed by rearranging Eq. (4.115) and solving for $\Delta d_j^1$ as follows:

$$\Delta d_j^1 = k_{Tj}^{-1}\ (F_j + \Delta F - f_j) \tag{4.116}$$

The increment of displacement is added to the previous total displacement $d_j$ to form the new total displacement

$$d_j^1 = d_j + \Delta d_j^1 \tag{4.117}$$

where

$d_j^1$ = the new total displacement

Note that the subscript denotes the load increment number and the superscript denotes the iteration number within this load step.

The analysis is still at point 2 on Fig. 4.12, where a new material property parameter $E_{Tj}^1$ and a new state of element stress $\sigma_j^1$ are computed in order to reflect the new displacement $d_j^1$. Since the element stiffness $k_T$ is dependent on $\sigma$, d, and $E_T$, it is recomputed to reflect $\sigma_j^1$, $d_j^1$, and $E_{Tj}^1$ as follows:

$$k_{Tj}^1 = k_T\left(\sigma_j^1,\ d_j^1,\ E_{Tj}^1\right) \tag{4.118}$$

The stiffness parameter $k_{Tj}^1$ is the tangent stiffness at point 3 on the actual load-displacement curve of Fig. 4.12.

The internal force due to the new displacement $d_j^1$ and the new state of element stress $\sigma_j^1$ is computed in the following manner:

$$f_j^1 = f(\sigma_j^1,\ d_j^1) \tag{4.119}$$

where

$f_j^1$ = the new total internal force

Equation (4.119) establishes the analysis at point 3 of Fig. 4.12. At this point, equilibrium is satisfied if and only if the following relationship is true:

$$F_j + \Delta F - f_j^1 = 0 \tag{4.120}$$

However, because of nonlinear behavior, it is clear that equilibrium at point 3 is not satisfied exactly by Eq. (4.120) because $\Delta d_j^1$ and $d_j^1$ were computed on the basis of the previous tangent stiffness $k_{Tj}$, while $f_j^1$ was computed on the basis of the new state of $\sigma_j^1$ and $d_j^1$. This established the need for a solution technique like the Newton-Raphson method, which attempts to modify $f_j^1$ in such a way as to satisfy the equilibrium equation (Eq. 4.120) at the new applied load level $F_j + \Delta F$.

Since Eq. (4.120) is not satisfied, it is more suitably expressed in the following form:

$$\Delta F_j^1 = F_j + \Delta F - f_j^1 \tag{4.121}$$

where $\Delta F_j^1$ is called the residual or unbalanced force, which results from the changing stiffness. The Newton-Raphson method thus attempts to find an equilibrium solution for an increment of external load $\Delta F$, by forcing the residual $\Delta F_j^1$ to be as close to zero as possible through a series of iterations.

The next step in the iteration method is to attain a new equilibrium solution by assuming that the residual is applied as an external load

$$\Delta d_j^2 = \left(k_{Tj}^1\right)^{-1} \left(F_j + \Delta F - f_j^1\right) \tag{4.122}$$

$$= \left(k_{Tj}^1\right)^{-1} \left(\Delta F_j^1\right)$$

where $\Delta d_j^2$ represents a new displacement increment, which is a displacement correction to $d_j^1$, in order to adjust equilibrium to compensate for the residual. The analysis is now at point 4 of Fig. 4.12. This $\Delta d_j^2$ is added to $d_j^1$ and a new total displacement $d_j^2$ is obtained. Following the same procedures, one computes $\sigma_j^2$, $E_{Tj}^2$, $k_{Tj}^2$, and $f_j^2$. If this iteration is convergent, then this new residual is smaller than the previous residual and the true equilibrium solution is approached. Solution of the displacement for the next load increment can proceed by the same processes as before.

4.4.3. Convergence Criteria

If the equilibrium is ultimately satisfied for a particular load increment, this method must result in a series of residuals which tend toward zero. It will be assumed that the iteration converges and equilibrium is satisfied when the most recently computed displacement increment and/or residual is less than or equal to some user-prescribed tolerance [4.17]. The convergence criterion used herein for a single degree-of-freedom is

$$\frac{\left|\Delta d_j^{i+1}\right|}{\left|d_j^i\right|} \leq \text{tolerance} \qquad (4.123)$$

where $\Delta d_j^{i+1}$ is the most recently computed displacement increment and $d_j^i$ is the current state of total displacement just before $\Delta d_j^{i+1}$ is added to form a new total displacement. If Eq. (4.123) is satisfied, then the convergence is indicated, equilibrium is sufficiently satisfied, the iteration stops, and the analysis proceeds to the next

increment of applied load. This stage of the analysis is indicated by point 6 of Fig. 4.12.

In the event that convergence is not satisfied, it may be that the displacement increments are diverging, which indicates that the iteration process cannot find an equilibrium solution for the given increment of applied load. Divergence can be caused by a numerical instability because of the stiffness changing too rapidly within the load increment. In the event of such behavior, a smaller load increment may produce more stable behavior.

On the other hand, if the load increment is already reasonably small, divergence may signify that the structural stiffness is tending toward zero, which indicates instability of the structure. In any case, if divergence is detected, the Newton-Raphson process and the total analysis are terminated.

The Newton-Raphson process and the total analysis are terminated on the basis of one additional mechanism. It is a safety mechanism and is employed in order to prevent excessive iterations. Thus, the iterative process is terminated and the total analysis is terminated if the number of iterations exceeds a user-specified maximum.

### 4.4.4. The Complete Solution Procedure in Detail

The basic properties of load incrementation and Newton-Raphson iteration described in the previous sections are combined to form the basis of the total nonlinear solution procedure. In this nonlinear solution procedure the most current information available concerning the structure is used to calculate the incremental quantities at any step. In other words, the tangent stiffness matrix at the start of

each iteration is used to estimate the next incremental quantities. It requires the formation of the element tangent stiffness transformed into global coordinates at the start of each iteration.

Suppose that current $\left\{\varepsilon_j^i\right\}$, $\left\{\sigma_j^i\right\}$, $\left\{P_j^i\right\}$, $\left\{M_j^i\right\}$, $\left\{M_j^{yi}\right\}$, $\left\{M_j^{zi}\right\}$, $\left\{f_j^i\right\}$, $\left\{F_j^i\right\}$, $\left\{X_j^i\right\}$, $\left\{b_j^i\right\}$, $\left\{e_j^i\right\}$, $\left\{D_j^i\right\}$, $\left\{d_j^i\right\}$, $\left\{A_{L_j}^i\right\}$, and $\left\{A_{NL_j}^i\right\}$ are given at the jth increment and the ith iteration. The condition i = 1 and j = 1 is the initial stage in the nonlinear problem. Thus, except for $X_1^1$, $\left\{b_1^1\right\}$, and $\left\{e_1^1\right\}$, the above vectors are null. To generate the i + 1 iteration by the updated Lagrangian method, the following steps will be followed:

Step 1: Calculate the current unbalanced forces in the global system

$$\left\{\Delta F_j^{i+1}\right\} = \left\{F_{j+1}\right\} - \left\{F_j^i\right\} \tag{4.124}$$

where

$\left\{F_{j+1}\right\}$ = forces for j + 1 load increment

$\left\{F_j^i\right\}$ = forces from previous iteration i

Step 2: Establish the current element coordinates $\left\{x_j^i\right\}$ for the element at hand by formulating the transformation matrix $\left\{T_j^i\right\}$ from the current global coordinates $\left\{X_{Ij}^i\right\}$, $\left\{X_{Jj}^i\right\}$, and $\left\{X_{Kj}^i\right\}$.

Step 3: Generate the structural tangent stiffness in current coordinates $\left\{X_j^i\right\}$

(a) Establish $E_T$ at each integration point through the cross section (with current strain deformation); that is, Eq. (3.5) is used to calculate $E_T$ for static and cyclic loading.

(b) Perform $(EA)_T$, $(EK^y)_T$, $(EK^z)_T$, $(EI^y)_T$, $(EI^z)_T$, and $(EI^{yz})_T$ integrals at each end from Eqs. (4.59) to (4.64).

(c) Determine $\left[k^i_{Oj}\right]$ [from Eq. (4.65)]; also with current $\left\{P^i_j\right\}$, $\left\{M^i_j\right\}$, $\left\{M^{yi}_j\right\}$, and $\left\{M^{zi}_j\right\}$ [from Eqs. (4.33) to (4.36)] find $\left[k^i_{Gj}\right]$ from Eq. (4.85).

(d) Generate $\left[k^i_j\right]_T$ by adding $\left[k^i_{sj}\right]_T$ (from Eq. (4.112)).

(e) Transform $\left[k^i_j\right]_T$ into global coordinates through the transformation matrix $\left[T^i_j\right]$ (Eq. 4.98) to get $\left[K^i_j\right]_T$ (Eq. 4.105).

(f) Assemble $\left[K^i_j\right]_T$ into the structural tangent stiffness $\Sigma\left[K^i_j\right]_T$.

Step 4: Solve for the incremental displacements with the current unbalanced forces

$$\left\{\Delta D^{i+1}_j\right\} = \Sigma\left[K^i_j\right]_T{}^{-1}\left\{\Delta F^{i+1}_j\right\} \tag{4.125}$$

Step 5: Update coordinates and formulate $\left[T^{i+1}_j\right]$

(a) Update coordinates for node I, J, and K from Eqs. (4.87) to (4.88).

(b) Update displacements, $\left\{D^{i+1}_j\right\} = \left\{D^i_j\right\} + \left\{\Delta D^{i+1}_j\right\}$.

(c) Update nodal unit vectors $\left\{b^{i+1}_j\right\}$ from Eqs. (4.99) to (4.100).

(d) From the updated coordinates in (a), find the unit vectors $\left\{e_j^{i+1}\right\}$ in element coordinate system from Eqs. (4.93) to (4.95) to formulate $\left[T_j^{i+1}\right]$.

Step 6: Calculate updated strains and stresses

(a) Use the unit vectors $\left\{b_{Ij}^{i+1}\right\}$ , $\left\{b_{Jj}^{i+1}\right\}$ , and $\left\{e_j^{i+1}\right\}$ to find $\left\{d_j^{di+1}\right\}$ from Eqs. (4.6) to (4.11).

(b) Compute $\left\{\varepsilon_j^{i+1}\right\}$ from Eq. (4.18).

(c) Compute $\left\{\sigma_j^{i+1}\right\}$ from Eq. (3.3).

Step 7: Compute element nodal forces in the element system

(a) Perform numerical integration from Eqs. (4.33) to (4.36) and use Eqs. (4.42) and (4.43) to find $\left[A_{Lj}^{i+1}\right]$ and $\left[A_{NLj}^{i+1}\right]$ .

(b) Compute $\left\{f_j^{d\ i+1}\right\}$ from Eq. (4.41).

(c) Compute $\left\{f_j^{i+1}\right\}$ from Eq. (4.45).

Step 8: Find the equilibrium external nodal forces in global coordinates

$$\left\{F_j^{i+1}\right\} = \Sigma\left[T_j^{i+1}\right] \left\{f_j^{i+1}\right\} \tag{4.126}$$

Step 9: Test for convergence. If not satisfied, return to step 1. Otherwise, store these stresses and strains and go to the next increment load $\{F_{j+2}\}$. Each step of this algorithm is tangent to the load-versus-displacement curve, as suggested before. The process is interpreted graphically in Fig. 4.13.

## 4.5. Analytical Verification

Based on the theory outlined above, two computer programs (IAB2D and IAB3D) have been developed to solve the nonlinear pile-soil interaction problems for both two- and three-dimensional cases. A number of examples have been analyzed to establish its reliability. Three sample problems were analyzed with the three-dimensional program: (a) large deflection analysis of a shallow arch; (b) large displacement, three-dimensional analysis of a 45° bend; (c) a simple soil problem to check soil nonlinearity and cyclic behavior.

### 4.5.1. Large Deflection Analysis of a Shallow Arch

The clamped circular arch with a single static load at the apex was analyzed for buckling using the beam-column element, as shown in Fig. 4.14. The material of the arch was assumed to be isotropic linear elastic. One half of the arch was idealized using six equal beam-column elements.

This arch was also analyzed by Bathe and Bolourchi, who used 6, 12, and 18 equal beam elements and 8 six-node isoparametric elements with 2 × 2 Gauss integration [4.1]. Mallet and Berke used 4 "equilibrium-based" elements [4.27]. Dupuis et al. [4.28] analyzed the same arch using curved beam elements. In addition, the experiment results given by Gjelsvik and Bodner [4.29] are also shown in Fig. 4.14.

Figure 4.14 shows the predicted load-deflection curve of the arch obtained by using IAB3D. In this analysis the use of beam-column elements is quite effective, and the numerical results match the experimental results.

### 4.5.2. Large Displacement Three-dimensional Analysis of a 45° Bend

The large displacement response of a cantilevered 45° bend beam subjected to a concentrated end load, as shown in Fig. 4.15, was calculated. The concentrated tip load is applied in the positive Y direction. The material was assumed to be linearly elastic.

The linear and nonlinear solution of this curved beam subjected to a tip load was given by Bathe and Bolourchi [4.1] by using 8 equal straight beam elements and 16 sixteen-node, three-dimensional solid elements. Figure 4.15 shows the tip deflection predicted by ADINA using the two finite element models [4.30]. The ADINA solution, obtained with a large number of elements and load steps, should be regarded as the most correct answer.

The numerical results obtained by using the IAB3D computer program with eight equal, straight beam-column elements is also shown in Fig. 4.15. The predicted tip deflections match with ADINA solutions. Figure 4.16 also shows the deflected shapes of the bend at various load levels.

### 4.5.3. Soil Problems

Several soil problems were analyzed to check the soil material nonlinearity and cyclic behavior. Since the vertical, lateral, and point springs are assumed to be similar and uncoupled, only the lateral springs are considered here. For example, suppose an HP14×73 pile was embedded below the ground as shown in Fig. 4.17. The soil responses can then be observed by specifying loads and displacements in the Y and Z directions. Theoretical displacements and soil resistance follow the p-y curve path. For a specified load the displacement will be obtained from the Newton-Raphson solution algorithm. For a specified cyclic load and displacement,

the soil response will follow the modified Ramberg-Osgood cyclic curves. Figures 4.18 to 4.19 show the soil response for specified cyclic loads in Y, Z, and YZ directions, respectively.

## 4.6. Two-dimensional Version

### 4.6.1. Specialization from the Three-dimensional Model

The general features of the two-dimensional program IAB2D are similar to the three-dimensional program IAB3D, except it is specifically written for two-dimensional problems, and, hence, more efficient than using IAB3D for those problems. The two-dimensional version is different in several ways from the program developed in the previous report [4.24]; for example,

(1) The soil properties are assumed linearly distributed along the element instead of the step-wise distribution.

(2) The modified Ramberg-Osgood cyclic model is introduced in order to model cyclic behavior.

(3) Beam and spring elements can be arbitrarily oriented.

(4) Thermal strain is introduced into the stress-strain relationship of the beam-column element to permit the thermal expansion and contraction.

(5) Geometric boundary conditions are permitted to change between load steps.

As discussed in Sec. 4.2.1 and 4.2.2, three different coordinate systems are required for three-dimensional update Lagrangian formulation. In the two-dimensional case, only two coordinate systems are needed, that is, only element and global coordinate systems. The deformation displacements, $\{d^d\}^T = \{\Delta_{IJ}, \theta_I^z, \theta_J^z\}$, can be found as follows [4.24]:

$$\Delta_{IJ} = \frac{1}{(\ell^0 + \ell^t)} \left[ 2X_{JI}^0 D_{41} + 2Y_{JI}^0 D_{52} + (D_{41})^2 + (D_{52})^2 \right] \quad (4.127)$$

$$\alpha = \sin^{-1} \frac{D_{52} X_{21}^0 - D_{41} Y_{21}^0}{\ell^0 \ell^t} \quad (4.128)$$

$$\theta_I^z = D_3 - \alpha \quad (4.129)$$

$$\theta_J^z = D_6 - \alpha$$

where

$\alpha$ = rigid body rotation in the X-Y plane.

4.6.2. Analytical Verification

Several numerical example problems are solved using the two-dimensional computer program IAB2D. At the same time, these problems were also solved with IAB3D to confirm the validity of the three-dimensional computer problem. As mentioned in the previous report [4.24], a beam-column problem and a short, thick column problem were first used to check geometric and material nonlinearity, respectively. Additional problems were introduced, such as: (a) snap-through problem, (b) Williams' toggle problem, (c) two-dimensional frame problem, (d) thermal problem, and (e) soil problem.

#### 4.6.2.1. Snap-through Problem

Figure 4.20 shows a simple symmetric truss with a concentrated load at the top. This type of problem can be solved by incrementing the deflections (rather than loads). The load-deflection curve is shown in Fig. 4.20. Several positions can be used to check the results. When the truss has a deflection where $\Delta$ equals -1.2 in. (the truss is in the horizontal position), the truss resists no load. If the truss has a deflection where $\Delta$ equals -2.4 in. (the truss is below horizontal by 1.2 in.), the strain is zero and, hence, the bar forces are zero. If $\Delta$ is greater than -2.4 in., the truss members are in tension and the load increases.

#### 4.6.2.2. Williams' Toggle Problem

The toggle shown in Fig. 4.21, having E = 29000 ksi and A = 1 sq in., was first analyzed and tested by Williams [4.31]. The load-deflection curve can be obtained by using specified load or displacement as shown in Fig. 4.21.

#### 4.6.2.3. Two-dimensional Frame Problem

A two-dimensional square portal frame subjected to two vertical loads and a small horizontal load is shown in Fig. 4.22. The theoretical buckling loads for the side-sway mode are: $P_{cr}$ (fixed base) 4605 kips, and $P_{cr}$ (hinged base) 1170 kips [4.32]. The horizontal load is quite small (0.001 P) but is sufficient to initiate geometrically nonlinear behavior. The load-deflection curves for both cases (fixed base and hinged base) are shown in Fig. 4.22. The numerical results show that the critical load for the fixed base is 4600 kips and for the hinged base is 1150 kips.

#### 4.6.2.4. Thermal Problems

Several thermal problems were used to check thermal strain caused by temperature changes: (a) cantilever beam, subjected to uniform and gradient temperature changes; and (b) fixed-end beam, subjected to uniform and gradient temperature changes. The results, although not shown here, compared exactly with theoretical solutions.

#### 4.6.2.5. Soil Problems

Soil models were also tested in the two-dimensional computer program, and the results are close to the theoretical answers and the numerical results obtained in IAB3D.

### 4.6.3. Experimental Verification

#### 4.6.3.1. Load Transfer in End-bearing Steel H Piles

In Ref. [4.33], the increase in the load-carrying capacity of an end-bearing pile due to load transferred to the surrounding soil by friction was experimentally studied. Site conditions, pile driving, and instrumentation were examined. The strain-gage readings were analyzed to determine the distribution of the load transferred along the piles. The piles were loaded and unloaded in increments to 150 kips, 300 kips, 450 kips, and 600 kips. A plot of pile load as a function of depth is shown in Fig. 4.23. From these curves, the true elastic shortening can be obtained, and the total displacements at each point of the pile can be calculated by adding the accumulated elastic shortening to the observed tip displacements as shown in Fig. 4.24. Two sets of f-z and q-z curves (one set for each pile) can be constructed [4.24]. Since all the pile load tests were held at the same site, the final set of f-z curves was taken as the average of the f-z curves from HP

14×89 and HP14×117. Soil parameters for the modified Ramberg-Osgood cyclic curves are obtained by approximately fitting the irregular shape of the average f-z curves and q-z curves. The pile is subdivided into eight elements of unequal length in order to correspond to the experimental data given in Fig. 4.23. The load-settlement curves for HP14×117, both observed and predicted values, are plotted in Fig. 4.25. The results calculated from the computer solution (IAB2D) are a fairly good approximation to the results obtained in the experiment.

4.6.3.2. Lateral Load Tests on Drilled Piers in Stiff Clay

Two drilled piers were selected from the laterally loaded pile tests conducted by Bhushan et al. [4.34]. (These piles were analyzed during the previous project [4.24] by YANG5 and are repeated here using the current program.) Measurements of horizontal ground line displacements were made for two piers. Soil properties, as determined by borings at each test site, are summarized in Table 4.1. The two piers (1 and 2 in Table 4.1) were constructed with a spacing of about 20 ft and were loaded by jacking between them. Displacements of the piers were measured by the dial gauges located 1 ft above ground surface. The properties of Table 4.1 are consistent with a very stiff clay in Table 3.11. Thus, an n = 2, Ramberg-Osgood curve, was used to approximate the p-y curve. (An n = 1 curve was used in the first project, [4.24].) The displacements at the top of the pier are plotted in Fig. 4.26 (Pier No. 1) and Fig. 4.27 (Pier No. 2). A comparison between the predicted values obtained from IAB2D and the experimental results shows that the results are adequate, certainly within limits usually expected with this type of analysis. The error in the initial

stiffness in these figures is caused by the approximation of the initial slope of the p-y curves.

4.6.3.3. Lateral Load Tests on Instrumented Timber Piles

Lateral load tests were conducted by Alizadeh [4.35] on four instrumented, Class B timber piles at two sites approximately 1000 ft apart. The two piles at each test site were 7 ft apart.

The soils at Test Site 1 consisted of 4 ft of sand and gravel underlain by layers of clay. The soils at Test Site 2 consisted of a layer of "fat clay" over layers of silt and "lean clay." At both sites the clay soils had a soft to medium consistency and an average shear strength of about 600 psf [4.35]. The timber piles used were 43-ft long and were slightly tapered. The diameter of the embedded portion of the piles ranged from just over 1 ft near the ground surface to approximately 0.8 ft near the pile tip. The modulus of elasticity of each pile was determined from calibration tests (Table 4.2) [4.35].

Each of the piles was instrumented with strain gauges. The two piles at each test site were tested at the same time by jacking the piles apart. The loads were applied at the ground surface in increments of 5 kips up to a maximum load of 20 kips. The pile displacements were measured at the ground surface.

For the analysis of the piles using the finite element program, the foundation soils were taken to be a combination of the six typical soil types presented in Sec. 3.5 of this report. The clay and silt soils at both test sites were assumed to be soft clay with average undrained cohesion values of 620 psf at Test Site 1 and 670 psf at Test Site 2. The sand and gravel layer at Test Site 1 was assumed to be medium sand.

A constant pile diameter, equal to the average diameter of the upper half of the embedded portion of the pile, was used. The ultimate strength of the timber was estimated to be 7230 psi [4.36].

The experimental results and the results obtained with the finite element program are compared in Figs. 4.28 to 4.30. For the smaller loads, the results from the program for piles 1-A and 1-B are close to the experimental values but for the 20 kip applied load, there is quite a difference (Figs. 4.28 and 4.30). The computed results were not as close to the experimental results for piles 2-A and 2-B. The discrepancies are probably because of inadequate modeling of the soil, which had not been quantitatively described in Ref. [4.24].

4.6.3.4. Pile Response to Axial and Lateral Loading

Combined axial and lateral load tests were conducted on three pile groups and on a single pile by Stevens et al. [4.37]. The experimental data for the single pile will be compared to values predicted by the finite element program. The soil profile at the test sight is shown in Fig. 4.31. The piles are installed primarily in alluvial sands. The friction angle, as determined from triaxial compression tests, ranged from 38° to 41°. The blow count varied from 5 to 40 blows/ft and the dry unit weight ranged from 103 to 115 pcf [4.37]. The groundwater table during the tests was maintained at 1 ft below the ground surface by a dewatering system.

A schematic diagram of the pile is also shown in Fig. 4.31. The piles used in the test were untreated green Douglas fir piles. The modulus of elasticity and ultimate strength of the timber were taken to be 2000 ksi and 3615 psi, respectively [4.36]. The piles had initial

lengths of 43 to 45 ft, butt diameters of 12 to 14 in., and tip diameters of 8.5 to 10 in. The piles were installed by jetting and driving to the prescribed tip elevation [4.37].

The pile groups and the single piles were subjected to four types of tests: cyclic preloading, pile driving effects, axial load testing, and combined load testing. The results of the axial and combined load tests on the single piles will be presented here. For the axial load tests the loads were applied in 60 kip increments until failure. For the combined load test an axial load of 60 kips was first applied to the pile. Then a lateral load was applied to the pile 28 in. above the ground surface in increments of 12 kips until failure. The lateral deflection was measured 33 in. above the ground surface.

For determining input for the finite element program, the 20-ft-thick layer of sand near the surface was assumed to be medium sand. The silty clay and sandy silt layers were modeled as stiff clay, and the layer of sand near the bottom of the pile was assumed to be dense sand. The curve parameters for each layer were determined from the equations in Tables 3.2, 3.4, and 3.5. A constant pile diameter of 11.75 in. was used for the computer analysis. This constant diameter is equal to the average diameter of the upper half of the embedded portion of the pile. The boundary conditions used in the computer analysis are shown in Fig. 4.31. The loads on the pile were applied using hydraulic jacks. The pile was assumed to be pinned at the top of the vertical hydraulic jack. The pile cap and hydraulic jacks were modeled as a single rigid element.

The results of the experimental tests and the computer analysis are shown in Figs. 4.32 and 4.33. These figures show that the results obtained using the finite element program are close to the observed values, although the finite element program does predict a lower ultimate load for the axial load test.

4.6.4. Guidelines for Program Usage

The basic philosophy of the finite element method is to analyze a piecewise approximation to the structure. Specifically, the structure or body is divided into finite elements; simple functions, usually polynomials, are assumed to approximate the displacements within each element. The greater the number of terms included in the approximation, the more closely the exact solution is represented [4.23]. For example, in the beam-column element the displacement functions (shape functions) are assumed to be a linear polynomial in the longitudinal direction and a cubic polynomial in the transverse direction.

In the region of high curvature gradients, a finer mesh is necessary to obtain satisfactory solutions. For a beam on an elastic foundation, 4 to 8 elements in a one-half wave of the deflected slope will provide satisfactory results. For elastic problems the length of one-half wave is $\pi/\beta$ [4.38] where

$$\beta^4 = \frac{k_y \ell^4}{EI} \tag{4.130}$$

where

$k_y$ = the lateral stiffness of the soil

$\ell$ = length of the pile

EI = the flexural rigidity of the pile

For inelastic problems, high curvature gradients occur in the region of a plastic hinge and a finer mesh is required to achieve comparable accuracy. The experience of the authors indicates that the change in curvature between elements should be no more than 0.0001 rad./in. Also, the mesh must be sufficiently fine to model changing soil and pile properties.

Load step sizes are controlled by the relative amount of nonlinear behavior. For example, convergence can become a numerical problem in the plastic region due to the difference between loading and unloading moduli. This problem can usually be overcome by reducing the load or displacement increment.

Mesh size and convergence problems are encountered in all types of finite element analysis. Usually, these problems can be analyzed by reducing the mesh (or load increment) size until no significant change in the answer occurs.

# 5. DESIGN METHOD

## 5.1. Introduction

One of the objectives of this study was to develop a simplified design method for analyzing piles in integral abutment bridges. The design method could then be used to determine the maximum allowable length for an integral abutment bridge. In the following sections a design model will be presented and the axial, lateral, and combined axial-lateral behavior of the model analyzed. From this information the design method will be formulated, and examples illustrating the use of the design method will be presented.

## 5.2. Design Model

The model used to describe the soil-pile system is shown in Fig. 5.1(a). The model consists of only one pile. Lateral loading group effects can be ignored if the spacing of the piles perpendicular to the direction of loading is greater than 2.5 to 3 times the pile diameter or width [5.1, 5.2]. The pile is idealized as a beam column with an elastic, perfectly plastic, moment-curvature relationship, as shown in Fig. 5.1(b). The boundary conditions at the top of the pile are assumed to provide lateral restraint and either zero (pinned condition) or complete (fixed condition) moment restraint. The tip of the pile is assumed to be free.

The soil is idealized as three sets of springs: lateral springs, vertical springs, and a point spring. The soil resistance-displacement relationships for the springs are shown in Fig. 5.1(c). The design

model assumes these relationships are bilinear, as opposed to the finite element model which assumes the relationships are in the form of the Ramberg-Osgood curves presented in Chapter 3. The soil parameters (the ultimate soil resistance and the initial stiffness) used in each model can be obtained from the equations in Chapter 3. The behavior of the present model will be analyzed in the following sections and will be compared with results from the finite element program described in Chapter 4.

## 5.3. Axial Behavior

The assumed axial behavior of the soil-pile system can be approximated by the bilinear load-displacement curve in Fig. 5.2. The parameters required to describe the axial behavior are the axial stiffness $K_a$ and the ultimate axial load $V_u$. Equations for determining the axial stiffness are given in Sec. 5.3.1, while equations for determining the ultimate axial load are given in Sec. 5.3.2.

### 5.3.1. Axial Stiffness

The axial stiffness of the soil-pile system depends on the stiffness of the vertical springs $k_v$, the stiffness of the point spring $k_q$, and the axial stiffness of the pile AE/L. The axial stiffness $K_a$ can be obtained by analyzing a differential element of an axially loaded pile, as shown in Fig. 5.3(b). From this figure the following differential equation can be written:

$$dV = k_v \, u \, dx \tag{5.1}$$

where V is the axial load on the pile, u is the displacement of a point on the pile, and x is the depth below the ground surface. The general solution of this equation is

$$u = c_1 e^{\sqrt{\frac{k_v}{AE}}\, x} + c_2 e^{\sqrt{\frac{k_v}{AE}}\, x} \tag{5.2}$$

with the boundary conditions

$$\text{at } x = 0 \qquad AE \frac{du}{dx} = -V$$

$$\text{at } x = L \qquad AE \frac{du}{dx} = -k_q A_e u$$

The value A is the cross-sectional area of the pile, $A_e$ is the effective pile tip area, and E is the modulus of elasticity of the pile material. For an H pile, $A_e$ is the rectangular area formed by the section depth and the flange width. The values $c_1$ and $c_2$ are constants determined from the boundary conditions. From the above equations the axial stiffness of the soil-pile system $K_a$ is obtained

$$K_a = \frac{\sqrt{k_v AE}\,(k_q A_e s + \sqrt{k_v AE}\, r)}{k_q A_e r + \sqrt{k_v AE}\, s} \tag{5.3}$$

$$K_a = \sqrt{k_v AE} \qquad (\text{for } \ell' > 2) \tag{5.4}$$

The values r and s in Eq. (5.3) are coefficients from Fig. 5.4, L is the embedded length of the pile, and $\ell' = \sqrt{k_v/AE}\, L$. A different method of determining the load-settlement curves is presented in Ref. [5.3].

### 5.3.2. Ultimate Axial Load

There are two types of axial failure mechanisms: the slip mechanism and the lateral mechanism. The slip mechanism occurs when the soil fails and the pile slips through the soil. The pile remains essentially undeformed. The lateral mechanism occurs when the pile deflects laterally and mobilizes the lateral soil springs. The ultimate axial load $V_u$ is the load associated with the mechanism which forms first.

#### 5.3.2.1. Slip Mechanism

The load capacity of the pile for the slip mechanism is equal to the sum of the load carried by skin friction along the length of the pile and the load carried by end bearing at the pile tip, as shown in Fig. 5.3(a). This load can be calculated from Eq. (5.5).

$$\begin{aligned} V_u &= \text{skin friction capacity} + \text{end-bearing capacity} \\ &= f_{max}\, L + q_{max}\, A \end{aligned} \tag{5.5}$$

Expressions for calculating $f_{max}$ and $q_{max}$ are given in Chapter 3.

#### 5.3.2.2. Lateral Mechanism

Failure of the soil-pile system can also be associated with lateral movement of the pile. If geometric instability was the only collapse consideration (i.e., no material yielding), the ultimate load would equal the elastic buckling load $V_{cr}$. If collapse was due to plasticity effects only (i.e., no geometric instability), the ultimate load $V_p$ would occur when a plastic hinge(s) forms and produces a plastic mechanism. In general, both geometric instability and plasticity effects are present, and collapse occurs as an interaction of these two effects. The resulting lateral mechanism load, sometimes called inelastic

buckling, is lower than either the elastic buckling load or the plastic mechanism load $V_p$.

This concept will be illustrated using the schematic example of a pile shown in Fig. 5.5(a). The pile is loaded with an eccentrically applied axial load and has a lateral restraint, representing the abutment, at the pile head. Idealized material properties for the perfectly elastic case and the rigid, perfectly plastic case are shown in Fig. 5.5(b). The failure modes and load-displacement curves for each case are illustrated in Figs. 5.5(c) and (d). The failure load for the perfectly elastic case is equal to the elastic buckling load for a concentrically loaded pile. The eccentricity e of the load produces the beam-column-type behavior as illustrated in Fig. 5.5(d). The failure load for the rigid, perfectly plastic case is equal to the load required to form a plastic hinge in the pile. The moment at the top $M_p'$ is the full plastic moment capacity of the pile reduced by axial load effects. Fig. 5.5(e) shows the load-displacement curves for both of the idealized cases. As mentioned earlier, both geometric and material effects interact such that the actual load-displacement behavior is similar to that illustrated in Fig. 5.5(e). The objective of the finite element approach described in Chapter 4 is to predict this behavior. The design methods described in this chapter are not intended to have the capability of predicting this complete curve. However, a reasonable, and conservative, estimate to the ultimate load $V_u$ can be obtained using the Rankine equation [5.3, 5.4].

$$\frac{V_u}{V_{cr}} + \frac{V_u}{V_p} = 1.0 \qquad (5.6)$$

This equation combines both geometric and material instabilities (inelastic buckling).

5.3.2.3. Elastic Buckling Load

The elastic buckling load for a pile $V_{cr}$ can be calculated using nondimensional graphs developed by Davisson [5.5], Reddy and Valsangkar [5.6], and Toakley [5.7]. The design model (Fig. 5.1a) will be approximated by the models shown in Fig. 5.6(a) and (b) for which the nondimensional solutions were developed. These models are laterally supported by elastic springs with a stiffness $k_h$.

Figure 5.6(a) represents an initially straight pile along which no vertical load transfer occurs; that is, there are no vertical springs along the pile and the pile axial load is constant. For this case Figs. 5.7 and 5.8 can be used to obtain nondimensional buckling coefficients V' and U', from which the buckling load can be calculated. For soils with a constant lateral stiffness $k_h$ the buckling load is given by

$$V_{cr} = \frac{U'EI}{R^2} \qquad (5.7)$$

where I is the moment of inertia of the pile and

$R$ = relative stiffness factor

$$= \sqrt[4]{\frac{EI}{k_h}}$$

$$\ell_{max} = \frac{L}{R}$$

For soils with a linearly varying $k_h$, the buckling load is given by

$$V_{cr} = \frac{V'EI}{T^2} \tag{5.8}$$

where

$T$ = relative stiffness factor

$$= \sqrt[5]{\frac{EI}{n_h}}$$

$$z_{max} = \frac{L}{T}$$

The boundary conditions used in this section are illustrated in Fig. 5.9. Even though the bottom of the pile could conceivably be idealized as laterally free, a laterally restrained boundary condition seems to better describe the elastic buckling case. Analyses with the finite element program and Ref. [5.5] suggest that this is so because the controlling buckling lobe forms near the top of the pile, in the region of the eccentricity. The theoretical elastic buckling solution implies that a free bottom will displace laterally; this was not observed in any cases. For the top of the pile, either the pinned case or the fixed, no translation case will be appropriate for an integral abutment bridge. Figures 5.7 and 5.8 show the effect that boundary conditions at the head of the pile have on the elastic buckling load. Considering that there is uncertainty in the buckling analysis and that no curves are given for the fixed, no translation case, it is appropriate to use the following approximations in place of Figs. 5.7 and 5.8:

| | U' | V' |
|---|---|---|
| Pinned head | 2.0 | 2.3 |
| Fixed head | 2.5 | 4.15 |

(5.9)

The values for the fixed head are taken from Fig. 5.10 for the constant axial load case ($\psi = 0$) and apply only for piles where $z_{max}$ or $\ell_{max}$ are greater than four.

The assumption that the axial load is constant along the pile is only true for short piles or for stiff end-bearing piles [5.3]. For other piles vertical load transfer occurs along the pile as illustrated in Fig. 5.6(b) and, therefore, the axial load varies with depth. This nonlinear variation of axial load is schematically illustrated in Fig. 5.6(c). The linear variation which is assumed in order to solve the governing buckling equations is also shown in Fig. 5.6(c) and given by the equation

$$V_x = V\left(1 - \psi\left(\frac{x}{L}\right)\right) \tag{5.10}$$

where $V_x$ is the axial load at any depth x, V is the axial load at the pile head, and $\psi$ is a coefficient which represents the rate of decrease in axial load between the pile head and pile tip. The linear approximation matches the actual only at the top and bottom. Other variations could have been chosen, for instance, a linear variation which is tangent to the actual variation at the pile head. However, the assumed linear variation should give conservative results for the elastic buckling load. From Eq. (5.10) the axial load at the pile tip is equal to $V(1 - \psi)$. Following the analysis in Sec. 5.3.1, the axial load at

the pile tip is equal to the force in the point spring, that is, $k_q$ times the pile tip displacement from Eq. (5.2) for x = L. Equating these two expressions for the axial load at the pile tip gives

$$(1 - \psi)V = \frac{k_q A_e}{k_q A_e s + \sqrt{k_v AE}\ r} V$$

or, $\psi$ can be obtained by

$$\psi = 1 - \frac{k_q A_e}{k_q A_e s + \sqrt{k_v AE}\ r} \tag{5.11}$$

Figure 5.10 is used to obtain a set of nondimensional buckling coefficients which take into account the axial load transfer along the pile. These coefficients are used in Eqs. (5.7) and (5.8), as before. Figure 5.10 can only be used for piles where $z_{max}$ or $\ell_{max}$ are greater than or equal to four. As discussed for the uniform axial load case, the pinned-bottom condition is appropriate. The elastic buckling load is increased substantially by considering axial load transfer.

5.3.2.4. Plastic Mechanism Load

In order to calculate the ultimate load using the Rankine equation [Eq. (5.6)], the plastic mechanism load $V_p$ must also be determined. This is the load at which the pile collapses due to the formation of a sufficient number of plastic hinges to create a mechanism. For example, the plastic mechanism load for the pile in Fig. 5.5(c) is given by

$$V_p = \frac{M'_p}{e} \tag{5.12}$$

The plastic moment capacity $M_p$ is reduced to $M_p'$ because of the presence of the compressive axial load. The value of $M_p'$ depends on the cross section of the pile. For a rectangle, $M_p'$ is given by [5.8]:

$$M_p' = M_p \left(1 - \left(\frac{V}{V_y}\right)^2\right) \tag{5.13}$$

where V is the compressive axial load in the pile, $V_y$ is the yield load of the pile ($F_y A$), and $F_y$ is the yield stress of the pile material.

For H-shaped sections the following approximate expressions apply [5.9]:

Strong axis bending:

$$M_p' = M_p \qquad V \leq 0.15\ V_y \tag{5.14}$$

$$M_p' = 1.18 M_p \left(1 - \frac{V}{V_y}\right) \qquad V_y \geq V \geq 0.15\ V_y \tag{5.15}$$

Weak axis bending:

$$M_p' = M_p \qquad V \leq 0.4\ V_y \tag{5.16}$$

$$M_p' = 1.19\ M_p \left(1 - \left(\frac{V}{V_y}\right)^2\right) \qquad V_y \geq V \geq 0.4\ V_y \tag{5.17}$$

The plastic mechanism load will vary for each situation depending on the boundary conditions, geometry, and properties of the pile, and on the properties of the soil.

5.3.3. Calibration--Axial Behavior

Example problems will be presented in this section to compare the results obtained from the design method and the finite element program

for problems involving the axial behavior of the soil-pile system. For all the examples an HP10×42 pile was used. The pile was bent about the weak axis and had a modulus of elasticity of 29000 ksi and a yield stress of 50 ksi.

The ultimate vertical load $V_u$ is determined from a load-displacement diagram using the following procedures. For piles whose load-displacement curves exhibit a definite maximum load, this maximum load is taken as the ultimate load. For all other piles, a line with a slope of AE/L is drawn through the origin of the load-displacement curve. A second line, which intersects the settlement axis at (0.15 + 0.1b) inches, is drawn parallel to the first line. The value b is the diameter or width of the pile in feet. The intersection of the second line and the load-displacement curve gives the ultimate vertical load [5.10, 5.11].

To illustrate the slip mechanism, a 40-ft-long, axially loaded pile was used. The properties of the soil are listed in Fig. 5.11 and are typical values from Chapter 3 for stiff clay. The load-displacement curve for this pile is also shown in Fig. 5.11. The axial stiffness and ultimate vertical load calculated using the design method, Eqs. (5.4) and (5.5), agree quite well with the finite element results.

The lateral mechanism, as predicted by the Rankine equation, was checked using the 40-ft-long, eccentrically loaded pile shown in Fig. 5.12. Figure 5.12(a) shows the pile with a vertical pinned support at the pile tip and with lateral springs only (no vertical springs). This configuration was used with values of e of 1 in. and 2 in. In Fig. 5.12(b) vertical springs were added and the vertical support at

the pile tip removed. For this case, e was taken as 2 in. The soil properties that were used are given in Table 5.1. Even though the soil types with parameters 1/5 the values of soft clay and loose sand are somewhat unrealistic, they were used in order to check the Rankine equation for a greater range of values. Note that clay is approximated as having a uniform lateral soil stiffness, whereas sand is approximated as linearly varying. A large value for $f_{max}$ was used for all clay soils to insure that the slip mechanism would not occur in Fig. 5.12(b). Table 5.2 gives the finite element results for $V_u$, as well as the values of $V_p$ and $V_{cr}$ from the design method (Eqs. 5.7, 5.8, 5.9, and 5.12), for selected combinations of soil types (Table 5.1) and support conditions (Fig. 5.12). Typical load-displacement curves for the case with vertical springs are shown in Fig. 5.13. These curves were obtained by specifying vertical displacements at the pile head and exhibit a typical beam-column-type behavior. The shape of the curves is as described in Fig. 5.5(e). Notice that the descending branch of the curves falls most rapidly for the softest soil. The Rankine equation and the finite element results are compared in Fig. 5.14. In this figure the curve for the pile with vertical springs crosses the curves for the other cases, not because $V_u$ is less, but because $V_{cr}$ increases more rapidly for this case. The Rankine equation gives conservative results, even for the clay with parameters 1/5 those of soft clay. However, unconservative results were obtained when a soil type with parameters 1/50 those of soft clay was used. From Fig. 5.14 it can be seen that plasticity effects tend to dominate the behavior of piles in realistic soil types and that elastic buckling is unlikely to occur;

that is, the points tend to be in the upper left of the figure. In this region the finite element results are above the Rankine equation because the finite element program uses the average axial load in the top element and not the axial load at the top node.

## 5.4. Lateral Behavior

The lateral behavior of the soil-pile system will be approximated by a bilinear load-displacement curve similar to the one shown in Fig. 5.2 for axial behavior. The two parameters required to describe the lateral behavior are the lateral stiffness $K_L$ and the ultimate lateral load $H_u$. Methods for determining these parameters will be presented in Sec. 5.4.1 and 5.4.2, respectively.

### 5.4.1. Lateral Stiffness

The response of a pile to lateral loads can be described by the differential equation

$$EI \frac{d^4\Delta_h}{dx^4} = - p \tag{5.18}$$

in which $\Delta_h$ represents the lateral deflection of the pile, and p represents the soil reaction on the pile (force per unit length). The relationship between the soil reaction and the lateral deflection is given by

$$p = k_h\Delta_h \tag{5.19}$$

For this study, $k_h$ will be assumed to be either constant with depth or linearly varying with depth. Substituting Eq. (5.19) into Eq. (5.18) yields the differential equation for the deflection of a laterally loaded pile.

$$EI \frac{d^4\Delta_h}{dx^4} + k_h\Delta_h = 0 \tag{5.20}$$

Various solutions for Eq. (5.20) have been obtained for free-headed (zero moment) and fixed-headed piles, and for soil with either a constant $k_h$ or a linearly varying $k_h$. From these solutions, the lateral stiffness at the pile head $K_L$ can be determined. For soil with a constant $k_h$ the following two equations apply [5.12, 5.13]:

For a free-headed pile

$$K_L = \frac{EI}{Y_{\ell q}R^3} \tag{5.21}$$

For a fixed-headed pile

$$K_L = \frac{EI}{I_p R^3} \tag{5.22}$$

where $Y_{\ell q}$ and $I_p$ are nondimensional coefficients from Fig. 5.15 and $\ell_{max} = L/R$. For values of $\ell_{max}$ greater than five, use $\ell_{max}$ equal to five. For soil with a linearly varying $k_h$, the following apply [5.14]:

For a free-headed pile

$$K_L = \frac{EI}{A_y T^3} \tag{5.23}$$

For a fixed-headed pile

$$K_L = \frac{EI}{F_y T^3} \tag{5.24}$$

where $A_y$ and $F_y$ are nondimensional coefficients from Fig. 5.16 and $z_{max} = L/T$. For values of $z_{max}$ greater than ten, use $z_{max}$ equal to ten.

5.4.2. *Ultimate Lateral Load*

The ultimate lateral load $H_u$ on the pile depends on the plastic moment capacity of the pile $M_p$, the ultimate lateral soil resistance $p_u$, the eccentricity of the load above the ground surface e, the embedded length of the pile L, and the boundary conditions. The five lateral failure modes that the pile can undergo are illustrated in Figs. 5.17 and 5.18. The soil reaction distributions shown in these figures are based on the assumption that the pile moments are sufficient to develop fully the ultimate soil resistance $p_u$ [5.3]. Given the soil reaction distributions, expressions for determining the maximum lateral load can be derived from statics.

Relatively short piles fail in a soil failure mode as shown in Fig. 5.17(a) for free-headed piles (no restraints), and in Fig. 5.18(a) for fixed-headed piles (moment restraint). For these piles, the soil along their entire length fails, while moments in the pile remain less than the plastic moment. For the free-headed case, $H_u$ can be determined from

$$H_u = -p_u(L + 2e) + p_u \sqrt{(L + 2e)^2 + L^2} \tag{5.25}$$

$$H_u = 0.414\, p_u L \qquad (e = 0) \tag{5.26}$$

for a constant $p_u$ and from

$$H_u = \frac{L^2 \, p_{uL}}{6(e + L)} \tag{5.27}$$

for a linearly varying $p_u$. The value $p_{uL}$ represents the value of $p_u$ at a depth L below the surface. For the fixed-headed case, $H_u$ is given by

$$H_u = p_u L \tag{5.28}$$

$$\leq \frac{2Mp}{L}$$

for a constant $p_u$ and by

$$H_u = \frac{1}{2} L \, p_{uL} \tag{5.29}$$

$$\leq \frac{1.5Mp}{L}$$

for a linearly varying $p_u$. Intermediate length piles with a fixed head fail in a combined soil and pile failure mode, as can be seen in Fig. 5.18(b). In this case the soil fails along the entire length of the pile and a plastic hinge forms at the pile head. Expressions for determining $H_u$ are, for constant and linearly varying $p_u$, respectively

$$H_u = -p_u L + \sqrt{2p_u{}^2 L^2 + 4p_u M_p} \tag{5.30}$$

$$H_u = \frac{M_p}{L} + \frac{1}{6} L \, p_{uL} \tag{5.31}$$

Longer piles fail in a pile failure mode. Figure 5.17(b) illustrates this failure mode for a free-headed pile. At failure, a plastic hinge

has formed in the pile, and all the soil above the hinge has failed. Soil below the hinge is not activated in the rigid, perfectly plastic mechanism. $H_u$ is given by

$$H_u = -p_u e + \sqrt{p_u^2 e^2 + 2\, p_u M_p} \tag{5.32}$$

$$H_u = \sqrt{2 p_u M_p} \qquad (e = 0) \tag{5.33}$$

for the constant $p_u$ case and by

$$H_u = \left(-0.75\, p_{uL_2} e + \sqrt{(0.75\, p_{uL_2} e)^2 + 3\, p_{uL_2} M_p}\right) \Big/ 2 \tag{5.34}$$

$$H_u = \frac{1}{2}\sqrt{3\, p_{uL_2} M_p} \qquad (e = 0) \tag{5.35}$$

for the linear $p_u$ case, where $L_2 = 2H_u/p_{uL_2}$. Equations (5.34) and (5.35) must be solved iteratively using the definition of $L_2$. The value $p_{uL_2}$ represents the value of $p_u$ at a depth $L_2$ below the surface. Fig. 5.18(c) represents the pile failure mode for a fixed-headed pile. Two plastic hinges form in the pile and the soil between the hinges has failed. $H_u$ is determined from

$$H_u = 2\sqrt{p_u M_p} \tag{5.36}$$

for a constant $p_u$ and from

$$H_u = \sqrt{\frac{3}{2}\, p_{uL_2} M_p} \tag{5.37}$$

for a linearly varying $p_u$.

5.4.3. Calibration--Lateral Behavior

Examples comparing the results from the design method with results from the finite element program will be given in this section. The pile type and pile material properties are as given in Sec. 5.3.3. The soil properties are typical values from Chapter 3 for medium sand and stiff clay and are given in Fig. 5.19 through 5.24. The length of the pile will be varied to illustrate the different failure modes described above.

Of the lateral failure modes given in Sec. 5.4.2, the two pile failure modes (Fig. 5.17b and 5.18c) will control for almost all practical cases. Results for these two modes are presented in Figs. 5.19 and 5.20. These figures show load-displacement curves for a 40-ft-long laterally loaded pile, bending about the weak axis, for both fixed-headed and free-headed cases. Figure 5.19 represents the case where $p_u$ is a constant, while Fig. 5.20 has a linearly varying $p_u$. The lateral stiffness of the soil-pile system is also shown in both figures. As can be seen from the figures, there is good agreement between the design method results and the finite element results in Fig. 5.19. However, in Fig. 5.20 the design method gives smaller values for the lateral stiffness and lower ultimate loads than the finite element program. These differences are caused by the stepwise variation of $k_h$ and $p_u$ used in the finite element program, whereas the design method assumes a linear variation. For both cases shown in Fig. 5.20 the design method does give conservative results. Notice that large lateral displacements are required to fully develop the ultimate lateral load.

Load-displacement curves for the other lateral failure modes are given in Fig. 5.21 through 5.24. Results for the soil and pile failure

mode (Fig. 5.18b) for an 80-in.-long pile are shown in Fig. 5.21(a) for a constant $p_u$ and in Fig. 5.23(a) for a linearly varying $p_u$. Results for the soil failure mode (Figs. 5.17a and 5.18a) for a 40-in.-long pile and a constant $p_u$ are presented in Fig. 5.21(b) for the free-headed condition, and in Fig. 5.22 for the fixed-headed condition. The soil failure mode with a linearly varying $p_u$ is illustrated in Fig. 5.23(b) for the free-headed condition and in Fig. 5.24 for the fixed-headed condition. These four figures all show reasonably good agreement between the design method results and the finite element results. As before, the agreement for the cases with a constant $k_h$ and $p_u$ is better than the agreement for the cases with linearly varying parameters.

## 5.5. Combined Behavior

In the previous sections the effects of separately applied axial and lateral loads and displacements on the design model have been discussed. Equations for stiffness and ultimate load have also been presented. Now, the behavior due to the combined application of these effects will be analyzed. Specifically, the behavior due to a lateral displacement and a vertical load at the pile head will be discussed. As an example, consider the pile in Fig. 5.25. Note that the slip mechanism is eliminated here by the bottom support. The pile is first given a horizontal displacement $\Delta_h$ to simulate the movement of the bridge superstructure due to a temperature change. If this movement is sufficiently large, a plastic hinge may form near the top of the pile at a distance $L_2$ from the ground surface. An axial load V, representing the

live load on the bridge, is then applied to the pile. As V increases, a plastic hinge eventually will form in the pile even for soft soils. The moment at the plastic hinge becomes smaller as the axial load increases. The plastic moment $M_p'$ can be calculated from Eqs. (5.13) through (5.17). The load-displacement behavior of the pile is illustrated schematically in Fig. 5.5(e). The figure, which was originally developed for a pile with an eccentrically applied axial load, shows the actual curve bounded by the curves for $V_p$ and $V_{cr}$. This suggests that the same relationship used to relate $V_u$, $V_p$, and $V_{cr}$ for axial loading might also be used for piles with combined loading. This is the approach that will be taken in the next section to determine the ultimate load of a pile.

5.5.1. Ultimate Load for Combined Behavior

The combined behavior of the pile is similar to the axial behavior described in Sec. 5.3.2 in that the pile can fail either by slipping through the soil or by deflecting laterally. The slip mechanism again occurs due to failure of the soil, while the pile remains relatively undeformed. The ultimate load for the slip mechanism is the same as before and is given by Eq. (5.5). The lateral mechanism occurs when the pile deflects laterally due to the interaction of geometric instability and plasticity effects. Consistent with the procedure used in Sec. 5.3.2.2, the Rankine equation (Eq. 5.6) will be used to estimate the ultimate load for the lateral mechanism. Values for the elastic buckling load and the plastic mechanism load, which are required for the Rankine equation, can be determined from the following two sections.

### 5.5.2. Elastic Buckling Load

The elastic buckling load for initially bent columns approaches the elastic buckling load for straight columns, providing the initial imperfections are relatively small [5.4]. Following this same rationale, the elastic buckling load for a pile with a lateral pile head displacement will be calculated using the expressions presented in Sec. 5.3.2.3 for straight piles. An example demonstrating the validity of this assumption is shown in Fig. 5.26. A 40-ft-long pile, as in Fig. 5.25, with elastic pile and soil properties was analyzed using the finite element program with values of $\Delta_h$ of 1 and 2 in. As can be seen from the figure, the displacements of the two piles differ somewhat, but the critical load $V_{cr}$ is the same.

### 5.5.3. Plastic Mechanism Load

The plastic mechanism load $V_p$ is the load which causes a complete mechanism to form assuming rigid, perfectly plastic behavior. The value $V_p$ will be derived using the pile shown in Fig. 5.27. The pile head in this figure is first displaced from point a to point b because of the expansion/contraction of the bridge superstructure. This movement causes a plastic hinge to form at a depth $L_2$ below the surface. (Remember, the pile is rigid, and perfectly plastic!) When the vertical load V is applied, the pile head moves to point c. This results in a second hinge forming at a distance $L_1$ below the first hinge. It is important to note that two plastic hinges must form when rigid, perfectly plastic behavior is assumed. This does not mean that two hinges form in the real pile at the ultimate load. In general, the second hinge forms only at a very large displacement.

The change in external work and internal energy caused by the pile head moving from b to c can be expressed in the following equation for a soil with a constant $p_u$:

$$V\delta = M'_p\left(\theta_1 + M'_p \quad \theta_1 + \theta_2 - \frac{\Delta_h}{L_2}\right) + p_u L_2\left(\frac{y}{2}\right) + p_u L_1\left(\frac{y}{2}\right) \qquad (5.38)$$

Simplifying and solving for V gives

$$V = \frac{M'_p\left(\frac{4}{L_1} - \frac{2}{\ell}\right) + p_u L_2}{\left(\frac{y}{L_1} + \frac{2\Delta_h}{\ell}\right)} \qquad (5.39)$$

where $\ell = L_1 + L_2$. The mechanism begins at y equal zero, which corresponds to the point $V_p$ in Fig. 5.5(e)

$$V_p = \frac{M'_p}{\Delta_h}\left(1 + \frac{2L_2}{L_1}\right) + \frac{p_u}{2\Delta_h} L_2(L_1 + L_2) \qquad (5.40)$$

The location of the plastic hinges, that is, $L_1$ and $L_2$, are, in a typical problem of this type, selected to minimize the mechanism load. This leads to a negative value of $L_2$ which is a physically unattractive solution (a plastic hinge occurring at a pinned end.) In lieu of this approach, each term on the right of Eq. (5.40) will be bounded by a conservative estimate. In the first term, $L_1$ is taken as much larger than $L_2$. This is a small approximation since $L_2$ is usually small. In the second term, $L_1$ will be assumed to be small with respect to $L_2$. This is not true but is certainly conservative; that is, it gives a lower bound to the second term. Next, $L_2$ will be assumed to be

$\sqrt{2M'_p/p_u}$, which is the depth to the plastic hinge when there is no axial load as for Eq. (5.33). Equation (5.40) thereby reduces to

$$V_p = \frac{2M'_p}{\Delta_h} \tag{5.41}$$

Similar derivations can be made for piles with linearly varying $p_u$. Due to the simplifying approximation made, $p_u$ drops out of these equations for $V_p$. Therefore, $V_p$ for pinned-headed piles with either constant or linearly varying $p_u$ is given by Eq. (5.41). Similarly, for all fixed-headed piles the following equation can be derived:

$$V_p = \frac{4M'_p}{\Delta_h} \tag{5.42}$$

The effect of vertical springs on $V_p$ can be accounted for by using a reduced value of V in the expressions for $M'_p$ (Eqs. 5.13 through 5.17). The value of V at the hinge location, for example, at $L_2$, could be used from Eqs. (5.10) and (5.11). This will result in a larger value of $M'_p$ at the plastic hinges and reduce some of the conservatism in the design method.

5.5.4. Calibration--Combined Behavior

The examples run to check the combined behavior have configurations identical to those in Fig. 5.12, except that the pile head is now given a lateral displacement $\Delta_h$ instead of having an eccentrically applied load. Also, one case is run with the pile head fixed against rotation. As before, a 40-ft-long HP10x42 pile, bent about the weak axis with a modulus of elasticity of 29000 ksi and a yield stress of 50 ksi, is

used. The soil properties used are given in Table 5.1. Table 5.3 gives the finite element results for $V_u$, as well as the design method results for $V_p$ and $V_{cr}$ (Eqs. 5.7, 5.8, 5.9, 5.41, and 5.42). The $V_u$ values for 1/5 soft clay are very unstable. This occurs because of the rapidly descending branch of the load-displacement curve after the ultimate load is reached. The Rankine equation and the finite element results are compared in Fig. 5.28. As was true for the axial load only examples, the Rankine equation gives conservative results, although there is a much wider scatter of points than for the axial load case. As described in Sec. 5.5.3, the plastic mechanism load is conservative because of the conservative estimates used in bounding Eq. (5.40) to obtain the simplified Eq. (5.41). The method is particularly conservative for the case with vertical springs, that is, when the axial load varies along the pile length. As noted in Sec. 5.5.3, the reduced axial load at the hinge locations would increase the plastic moment capacity. This correction was not used in Fig. 5.28.

## 5.6. Applications of the Design Method

The bridge superstructure will expand and contract with changes in temperature. Methods for determining the change in temperature are presented in Sec. 5.6.1 along with equations for calculating the lateral pile head displacement and the maximum bridge length. Sec. 5.6.2 presents a summary of the design method developed in this chapter.

### 5.6.1. Actual Temperature Changes

The lateral displacement of a pile due to a change in temperature can be determined from

$$\Delta_h = \alpha \, \Delta T \, L_b/2 \tag{5.43}$$

where $\alpha$ is the coefficient of thermal expansion for the material in the bridge superstructure, $L_b$ is the length of the bridge, and $\Delta T$ is the average temperature change. The AASHTO code gives values of $\alpha$ and $\Delta T$ as

$\alpha$ = 0.000006/°F normal weight concrete

= 0.0000065/°F structural steel

$\Delta T_{ave}$ = 60° F moderate climate, metal structures

= 75° F cold climate, metal structures

= 35° F moderate climate, concrete structures

= 40° F cold climate, concrete structures

For concrete bridges in climates similar to Iowa's, a possibly better estimate of $\Delta T$ is to calculate the change in length from dawn on the coldest day of the year to dawn on the hottest day of the year and then add the estimated change in length during the hottest day of the year. This temperature change is given in the following equation [5.17].

$$\Delta T = T_1 - T_2 + (T_3 - T_1)/3 \tag{5.44}$$

where $T_1$ is the air temperature at dawn on the hottest day of the year, $T_2$ is the air temperature at dawn on the coldest day of the year, and $T_3$ is the maximum air temperature on the hottest day of the year. Another method for determining $\Delta T$, which is based on extensive empirical data, is given in Ref. [5.18]. The maximum length of the bridge can now be determined from Eq. (5.43)

$$L_b = \frac{2\Delta_h}{\alpha \Delta T} \tag{5.45}$$

where $\Delta_h$ is the largest lateral displacement which does not cause a reduction in the ultimate vertical load of the pile.

5.6.2. Summary of the Design Method

In the previous sections of this chapter a simplified design method has been presented for analyzing piles in integral abutment bridges. The purpose for developing this method was to predict the change in the ultimate load capacity of a pile due to lateral pile head displacements, and, thereby, determine the maximum allowable length for bridges with integral abutements. Two failure mechanisms are possible: the slip mechanism and the lateral mechanism. The ultimate load for the slip mechanism can be determined from Eq. (5.5) and does not depend on the lateral displacement of the pile. The ultimate load for the lateral mechanism can be determined from Eq. (5.6). This load does depend on the lateral displacement, since $V_p$ (Eqs. 5.41, 5.42) decreases with increasing $\Delta_h$. The ultimate load for the pile is the smaller of the two mechanism loads. The slip mechanism will tend to control for friction piles with relatively small $\Delta_h$ values. The lateral mechanism will tend to control for end-bearing piles and for friction piles with large $\Delta_h$ values. As long as the slip mechanism controls, the ultimate load in the piles will be unaffected by the $\Delta_h$. If the lateral mechanism controls, then the design of the piles may need to be modified in order to use integral abutments. Anticipated values for $\Delta_h$ can be calculated from equations in Sec. 5.6.1.

# 6. PILE BEHAVIOR IN INTEGRAL ABUTMENT BRIDGES

## 6.1. Steel Piles in Nonskewed Bridges

### 6.1.1. Friction and End-bearing Piles

In the previous report the ultimate load-carrying capacity of friction piles embedded in typical Iowa soils was studied [6.1]. In the present work these cases have been reinvestigated with an improved representation of the real soil-pile interaction. As discussed in Sec. 3.4, the parameter $\alpha$ used to construct the f-z curves has been changed (see Fig. 3.6). For very stiff clays the factor $\alpha$, which is used to obtain the soil-pile adhesion from the given soil cohesion, has been reduced by almost one-half. This is, presumably, more suitable for steel H piles [6.2]. The soil and pile models used in the previous work [6.1] did not include cyclic behavior. In the soil-pile interaction problem, the pile will take a shape similar to the solid line in Fig. 6.1, as the pile is subjected to the specified lateral displacement $\Delta_h$. As the vertical load V is applied, the pile deflects as illustrated by the dashed line. As can be seen, some of the soil springs will be subjected to load reversals (cyclic loading). Similarly, some of the pile moments are reversed during this loading history. With these changes, it was decided to recalculate the pile capacities studied in the previous work.

A typical pile (HP10×42) in an integral abutment bridge with bending about the weak axis will be analyzed by first applying a lateral displacement (to simulate induced thermal expansion or contraction) and no rotation (since the bridge is much stiffer than the pile) at the

pile top. Then a vertical load V (to simulate the bridge load) will be applied until failure occurs. In this manner, the effect of the horizontal pile top displacement on the pile capacity can be observed. Two different piles are investigated: friction piles and end-bearing piles. The point spring resistance in the end-bearing piles is taken to be large to simulate stiff rock. In the IAB2D program, the total displacement $\Delta_h$ is applied in increments of 0.5 in., while V is held equal to zero. Once the total $\Delta_h$ is achieved (0, 1, 2, or 4 in.), V is increased in increments of 5 kips or 10 kips until the vertical capacity of the pile is reached.

Results obtained by running the IAB2D program will be presented here to show the behavior of a steel H pile embedded in Iowa soils. (Chapter 3 summarizes the soil properties.) Sets of vertical load-settlement curves with specified lateral displacements (see Fig. 6.1) for a friction pile in very stiff clay and end-bearing piles in soft clay and loose sand are shown in Figs. 6.2 through 6.4, respectively. These are typical of the other cases. The ultimate loads are defined by the tangent offset method described in Sec. 5.3.3. The nondimensional forms of the ultimate pile load ratio $V_u/V_{uo}$ versus the specified lateral displacement $\Delta_h$ for friction piles and end-bearing piles in different types of Iowa soils are shown in Figs. 6.5 and Fig. 6.6, respectively. The value $V_{uo}$ represents the ultimate load when there is no induced lateral displacement.

Figure 6.5 shows that a lateral movement of up to 4 in. has no effect on the vertical load capacity of friction piles. These results are different from the results obtained in the previous report [6.1].

Two primary reasons explain this difference. First, since the $\alpha$ factor (adhesion/cohesion) has been reduced in the present study (Sec. 3.4), the pile capacity, as limited by friction, has been reduced. Hence, this slip mode will tend to control even though $\Delta_h$ may be large. The slip mode is not affected by lateral displacements. Second, since the cyclic model was introduced into the pile stress-strain relation, the moment-curvature relations of the pile are no longer path independent.

Figure 6.7(a and b) shows the moment-curvature relation and path for loading and unloading of the noncyclic [6.1] and cyclic model (current work), respectively. The unloading paths are significantly different, that is, different tangent stiffnesses and moment vs. curvature results. The load-deflection curves will be significantly different for these two cases.

Figure 6.8 shows the load-settlement curves for the cyclic and noncyclic model in very stiff clay with a specified lateral displacement of 1 in. Notice that the collapse load for very stiff clay is nearly the same for both cases even though the two models travel different load-displacement curves. This observation fits a more general theorem of plastic design which states that the mechanism collapse load of a frame is independent of any residual stresses which may be present in the unloaded structure, whether these are caused by welding, imperfect fit of members, or support settlement. In all of these cases, a complete mechanism will be formed eventually [6.3]. The theorem assumes the system has unlimited ductility. However, as illustrated by Fig. 6.8, the mechanism may form at quite different levels of displacement. Hence, if the offset method is used to determine the

ultimate load (Sec. 5.3.3), a significantly different value is obtained from the cyclic model than the noncyclic model. This difference was not anticipated in the previous work. Since the cyclic model and the reduced $\alpha$ more realistically represent the pile and soil behavior, the present conclusion is valid; that is, lateral displacements do not affect the capacity for friction piles in the Iowa soils.

In the end-bearing piles the failure mode is dominated by the yield load of the pile. The slip mechanism does not occur. Figure 6.6 (a and b) shows that the ultimate load-carrying capacity of the pile is reduced in soft clay and loose sand. Since the lateral stiffness of the soil in soft clay and loose sand is relatively small, the pile is permitted to deflect laterally under vertical load and the lateral failure mode eventually develops. For the stiff soils, the full yield load of the pile is developed before lateral motions are permitted.

Results obtained using the design method developed in Chapter 5 are also presented in Fig. 6.5 and 6.6. As can be seen in Fig. 6.5, for friction piles the design method concurs with results from the finite element program and predicts no reduction in the ultimate vertical load for values of $\Delta_h$ up to 4 in. For end-bearing piles in clay (Fig. 6.6a) and sand (Fig. 6.6b) both the finite element program and the design method predict some reduction in load-carrying capacity. Agreement between the two methods is good with the design method results being slightly conservative. Besides predicting a greater relative reduction in capacity due to $\Delta_h$, as illustrated by the nondimensional plots in Fig. 6.5 and 6.6, the design method also gives

conservative magnitudes of the capacity (Fig. 5.28). The design method and the finite element program use slightly different expressions for determining the lateral stiffness and ultimate lateral strength of the soil (Sec. 3.3). This may account for some of the differences between the results. The design method will also tend to give conservative results because the equation for $M_p'$ does not take into consideration the reduction in axial load along the pile (see Sec. 5.5.3). Additionally, conservative approximations are used to reduce Eq. (5.40) to Eq. (5.41).

6.1.2. Effect of Cyclic Lateral Displacements

Two cases are presented here to illustrate the effect of cyclic lateral displacements on pile capacity: friction piles in very stiff clay and end-bearing piles in soft clay. These are the cases most likely to be affected by cyclic loading. The specified lateral displacement is cyclically applied; for example, $\Delta_h$ is cycled from +1.0 in. to -1.0 in. to +1.0 in. The vertical load V is then applied.

The resultant set of vertical load-settlement curves after the specified cyclic lateral displacements for a friction pile in very stiff clay and end-bearing pile in soft clay are identical to those shown in Figs. 6.2 and Fig. 6.3, respectively. These results show that the vertical load capacity is not significantly affected by the cyclic lateral displacements. The effects of cyclic behavior are not included in the design method.

6.1.3. Effect of Pinned Pile Top

The condition at the pile top, which is embedded in the concrete abutment, depends on the relative stiffness of the superstructure and

the abutment. The top of the pile can be assumed to be (a) fully restrained without rotation (fixed pile head), (b) partially restrained allowing some degree of rotation, or (c) pinned, allowing complete rotation freedom (pinned pile head). Section 6.1.1 has discussed the friction and end-bearing piles with fixed pile heads in very stiff clay and soft clay. The friction and end-bearing piles with pinned pile heads in very stiff clay and soft clay will be presented here. Figure 6.9 shows the nondimensional forms of ultimate vertical load ratio versus lateral specified displacements of friction and end-bearing piles with pinned pile heads in very stiff clay and soft clay. A comparison of Fig. 6.5 and Fig. 6.9(a) shows that the load capacity of the friction pile is not affected by the boundary condition on the pile top. In both cases, the failure mechanism is controlled by the slip mechanism. This is not true in the case of the end-bearing pile with fixed and pinned pile heads. The load capacity is reduced more in soft clay than in very stiff clay (Fig. 6.6a and Fig. 6.9b). The failure mechanism in both cases is controlled by the lateral mechanism, which is affected by the number of plastic hinges (two for the fixed case, one for the pinned) and the lateral soil resistance. The reduced lateral resistance of soft clay more easily permits the lateral mode.

Figure 6.9 also shows results obtained using the design method. Both the finite element method and the design method predict no reduction in load-carrying capacity for friction piles for values of $\Delta_h$ up to 3 in. The design method does, however, predict a small reduction for $\Delta_h$ values greater than 3 in. Figure 6.9(b) for end-bearing piles shows similar reductions in ultimate load for both the finite element

program and the design method. One difference is that the design method predicts a greater reduction in load capacity for piles in very stiff clay than for piles in soft clay, whereas the finite element program sometimes shows a greater reduction for piles in soft clay.

## 6.2. Nonskewed Bridge Example

### 6.2.1. Bridge Studied

A nonskewed bridge located at State Avenue over U.S. 30, Story County, Ames, Iowa, was chosen to investigate the behavior of an integral abutment bridge subjected to thermal expansion and contraction. Plan and elevation views of the bridge are shown in Fig. 6.10. It is a 245-ft-long, prestressed concrete bridge with integral abutments and piers. There are no expansion joints on the bridge; however, expansion joints are located in the approach slab about 20 ft from each end of the bridge.

A section through the bridge deck is shown in Fig. 6.11. Pretensioned, prestressed concrete beams were used to support a poured-in-place concrete deck. The beams and deck were designed to act as a monolithic unit, even over the piers. The steel piles, pier cap, diaphragm, concrete beam, and concrete deck were all reinforced to behave as a single unit. A section through the abutment is shown in Fig. 6.12. The pile is oriented with its strong axis along the roadway center line (bending about the weak axis) and is reinforced within the abutment cap and diaphragm to transmit the full plastic moment of the pile (HP10×42). More details about the State Avenue bridge can

be found in Iowa Department of Transportation design sheets, File No. 22616 and Design No. 267.

### 6.2.2. Mathematical Model of the Bridge

The proposed mathematical model of the State Avenue bridge is shown in Fig. 6.13(a). Two types of prestressed concrete beams, C30-50 and C80, are used in this bridge. A simplified two-dimensional model of the bridge, which contains one concrete beam, a section of the abutment and pile cap, and one pile as shown in Fig. 6.13(b), was used. The cross-sectional properties have been calculated based upon this idealization. Note also that the bridge was assumed to be symmetrical about the midlength. Figure 6.14 shows the section through the abutment and the soil profile. The granular backfill is considered as dense sand. The abutment pile was driven in an 8-ft deep, oversized hole through the fill. Voids around the pile are assumed to still be empty. The finite element model is shown in Fig. 6.15. Six beam-column elements, each 20-ft long, are used to represent the concrete beam; two beam-column elements, each 3.75-ft long, are used to represent the abutment and pile cap; and 12 elements with unequal length are used to represent the pile. There are no vertical soil springs along the abutment and the predrilled oversized hole. No lateral soil springs are attached within the predrilled oversized hole. Soil properties based on the Iowa soils are calculated. The temperature change is taken as -60° F to +60° F from the construction temperature (see Eq. 5.44).

### 6.2.3. Numerical Results

Several cases have been investigated in order to fully understand the behavior of the integral abutment bridges with thermal expansion

and contraction. These are: (a) no thermal changes, (b) with +60° F temperature changes, (c) without backfill, with +60° F temperature changes, (d) with a complete cycle of temperature changes (-60° F to +60° F), and (e) without concrete bridge model, but with specified lateral displacements equal to the displacements in case (b). After each of these loadings, a vertical load is applied at the top of the pile until failure (Fig. 6.15).

Vertical load-settlement curves obtained by running the IAB2D program are shown in Fig. 6.16. Case (e) is actually a single pile with an abutment attached to it, very similar to the cases in Sec. 6.1. It fails by the slip mechanism when the applied load exceeds the friction force of the soil springs. The rest of the cases do not fail at this level, since the pile is part of the bridge model. As the pile moves downward, the concrete bridge beams carry some load as a cantilever type structure. Cases (a) and (b) have noticeably different load-settlement curves. In case (b) the +60° F temperature change expands the beams and activates the passive soil pressure behind the abutment. (See diagram in Fig. 6.17.) Since the beam and abutment are not co-linear, a moment M and subsequent shear $V_s$ are introduced into the concrete beam. The shear $V_s$, equal to about 20 kips in this case, is applied to the pile. In other words, the pile is subjected to a 20-kips downward load before the vertical live load is applied. From Fig. 6.16, cases (a) and (b) do have a 20-kips difference in ultimate load. This is also confirmed by case (c), which is identical to case (b) except the backfill is removed. In this case, the initial 20-kip pile load is not introduced and the load-settlement curve is about the same

as case (a). A comparison of cases (b) and (d) shows that there is no difference in load-settlement curves for cyclic and noncyclic thermal changes.

## 6.3. Steel Piles in Skewed Bridges

As illustrated in Fig. 6.18, pile orientations for steel H piles in integral abutment, skewed bridges can be classified into four types: the web of the pile perpendicular (Type 1) or parallel (Type 2) to the roadway center line, and the web of the pile parallel (Type 3) or perpendicular (Type 4) to the center line of the abutment. In addition, some states use circular piles (Type 5) in integral abutments on skewed bridges. In each of these types the pile is bending about its weak axis, strong axis, or a combination of both. Bending of piles about the weak axis was discussed in Sec. 6.1. Before proceeding to an actual bridge, individual piles displaced laterally about the strong axis and at 45° to the strong and weak axis will be studied.

### 6.3.1. Bending about the Strong Axis

For H piles bent about the strong axis (displaced along the weak axis), the analysis procedure is the same as in Sec. 6.1.1, except the pile cross-sectional properties are rotated 90°. The two-dimensional program IAB2D can still be used for this case. A set of nondimensional curves of the ultimate pile load ratio ($V_u/V_{uo}$) versus the specified lateral displacement ($\Delta_h$, in the direction of the weak axis), for friction and end-bearing piles in different types of Iowa soils, are shown in Figs. 6.19 and 6.20, respectively. The pile heads are fixed against rotation in these figures.

Figure 6.19 shows that a lateral movement of up to 4 in. has no effect on the vertical load capacity for friction piles. This is not true for end-bearing piles, since the failure mode is dominated by the yield load of the pile. The slip mechanism does not occur. Figure 6.20(a) shows that end-bearing piles with a fixed pile head and bending about the strong axis have a significantly reduced ultimate load capacity in very stiff clay.

Figure 6.21 shows the vertical load-settlement curves of end-bearing piles with fixed pile head displaced 4 in. laterally for soft clay, stiff clay, and very stiff clay. These curves show that the peak load (point of zero slope) for very stiff clay is greater than for stiff clay, which is greater than for soft clay. As mentioned in Sec. 6.1.1, the peak load is not affected by the residual stress effects, in this case, plastic hinges formed by the lateral motion. However, as Fig. 6.21 clearly shows, residual stresses do affect the load-settlement curve. For the very stiff clay displaced 4 in. laterally, two plastic hinges formed in the pile. For soft clay and stiff clay only one plastic hinge formed. This plastic hinge formation does significantly affect the load-settlement curve of the very stiff clay pile; the tangent stiffness is noticeably reduced at point A in Fig. 6.21. Hence, the ultimate load for the very stiff clay case, as determined by the offset displacement, is less than for soft clay and stiff clay.

Results from the design method, which are also shown in Figs. 6.19 and 6.20, give conservative results, as discussed in Sec. 6.1.

### 6.3.2. Friction and End-bearing Piles Bending about the 45° Axis

If pile orientations of types 3 and 4 are adopted for construction convenience, the thermal expansion or contraction along the roadway center can be divided into components parallel and perpendicular to the pile web (see Fig. 6.18). Thus, the piles in integral abutment skewed bridges will be subjected to biaxial bending resulting from thermal movement. Piles displaced at 45° from the major axes will be analyzed in this section to illustrate the effect of biaxial bending. The same loading procedure is used as in Sec. 6.3.1, except that the specified lateral displacement $\Delta_h$ is measured in a direction 45° from the principal axes (see Fig. 4.17). The three-dimensional computer program IAB3D is used to calculate the load capacities of friction and end-bearing piles.

For friction piles, results obtained from the IAB3D program show that the load capacity of friction piles is not affected by applying the specified lateral displacement $\Delta_h$ (0, 1, 2, or 4 in.) in the 45° direction for all Iowa soils, since failure is controlled by the slip mechanism. This agrees with the results obtained from the previous sections.

The ultimate vertical load ratio for end-bearing piles with specified displacement $\Delta_h$ (0, 1, 2, or 4 in.) in the direction of 45° axis is shown in Fig. 6.22. In this case, the load capacity of end-bearing piles is affected by the specified movements at the top, since failure is controlled by the lateral mechanism. It is interesting to note that the load capacity of end-bearing piles bent about the 45° axis is between the load capacity of end-bearing piles bent about the weak and strong axis (Sec. 6.1 and 6.3.1). The upper bound and lower bound

on the load capacity of end-bearing piles can be estimated from the weak or strong axis bending. As an expedient solution, analysis can be accomplished by a simplified two-dimensional analysis.

The design method was not developed for the biaxial bending case.

### 6.3.3. Effect of Pinned Pile Top

In this section, the effect of a pin at the pile top on friction and end-bearing piles bent about the strong axis will be demonstrated. Piles in very stiff clay and soft clay will be studied. Results obtained from the IAB2D show that the load capacity of the friction piles is not affected by the boundary condition at the pile top. In both cases (fixed and pinned), the failure mechanism is controlled by the slip mechanism. This is not true in the case of an end-bearing pile (compare Figs. 6.20(a) and Fig. 6.23). For pinned piles displaced 4 in. laterally, the tangent stiffness of the load-settlement curve in very stiff clay is not reduced as significantly as it was at point A in Fig. 6.21 for fixed piles. Hence, the vertical load capacity, as determined by the offset method, is not noticeably reduced.

Also shown in Fig. 6.23 are curves developed using the design method. Behavior similar to that described in Sec. 6.1 occurs. Again the design method gives conservative answers.

## 6.4. Skewed Bridge Example

In this section a skewed bridge with integral abutments is used to investigate the behavior of the piles under temperature changes. The bridge in Sec. 6.2 is used as a skewed bridge in which the skew

angle is 30° (see Fig. 6.24). The pile orientations are classified into four different types as mentioned in Sec. 6.2. These four different types of pile orientations, as shown in Fig. 6.18, will be discussed here.

Since the same bridge is used in this example, the properties of prestressed concrete beams, abutments, piles, and soil profiles are the same as in Sec. 6.2. The mathematical model for this skewed bridge is also similar to the one used in Sec. 6.2, except that a three-dimensional model is required to account for the effect of the skew. This three-dimensional model includes a concrete beam, abutment, and pile. Only one-half of the bridge in this model is analyzed by taking advantage of the symmetry about the midline of the bridge. The global coordinates as shown in Fig. 6.24 are selected to impose the symmetry requirement. Rotations about the global X-axis at the abutments and piers are considered to be restrained because of the diaphragm underneath the concrete beam.

Four types of pile orientations in the abutment are considered and are loaded with the following cases: (a) without thermal changes, (b) with +60° F temperature changes, and (c) without bridge beam and with $\Delta_h$ for +60° F temperature changes. Results obtained from the IAB3D program show that there is no significant difference in the load-settlement curves for different pile orientations, that is, the load-settlement curves will not be affected by the pile orientations (see Fig. 6.25). This agrees with the results in the previous sections which indicate that bending about weak, strong, and 45° axes do not affect the vertical load capacity of friction piles which fail by the

slip mechanism. As in the two-dimensional case, as the applied load exceeds the pile friction resistance, the excess load will be carried by the concrete beams as a cantilever type structure. Hence, case (a) continues to carry an increasing load beyond case (c). Cases (a) and (b) have a noticable difference because of the pile pre-load induced by the thermal expansion, as illustrated in Fig. 6.17.

The deflected shape of the skewed bridge (in the plan view) after thermal expansion is also shown in Fig. 6.24. If the soil springs acting on the abutment in the tangential direction, which represent the friction resistance of the backfill, did not exist, the bridge would move toward the upper right.

## 6.5. Timber and Concrete Piles

Piles are available in a variety of sizes, shapes, and materials to suit many special requirements, including economic competition. Piles can be classified by the principal materials of which they consist, for example, timber, concrete, and steel piles. Steel H piles have been discussed in Secs. 6.1 and 6.3. Circular timber and concrete piles will be investigated in this section.

Timber piles are probably the most commonly used type. Under many circumstances, they provide dependable, economical foundations. Their length is limited by the height of available trees; piles 20- to 40-ft long are common, but longer ones cannot be obtained economically in all areas.

Since concrete piles were initially used shortly before 1900, several types of concrete piles have been devised. Today an engineer

may choose those best suited to a particular project. Concrete piles may be divided into two principal categories, cast-in-place and precast piles. The cast-in-place piles may be further divided into cased and uncased piles.

A Douglas fir timber pile and a cast-in-place concrete pile, both 1-ft diameter and 20-ft long, will be investigated here. Table 6.1 shows the material properties of timber and concrete piles [6.4]. The stress-strain relationship of the timber pile can be represented by the modified Ramberg-Osgood cyclic model. For concrete piles, reinforcing bars are used to resist the tensile force for the internal moment. The beam element in the current program does not have the capability of modeling the post-cracking behavior of reinforced concrete piles. The representation at the bond/anchorage/cracking behavior of reinforced concrete is a complex phenomenon which has not been completely solved by state-of-the-art methods. The scope of this project did not permit incorporation of such behavior. In addition, since the pile is predominately in axial compression, the compression characteristics of the material will dominate. The compression stress-strain relation of the concrete pile is idealized by the modified Ramberg-Osgood cyclic model.

Using the same procedure as in Sec. 6.1.1, results indicate that the vertical load capacity of timber and concrete friction piles with fixed pile heads in six types of Iowa soils is not reduced by a lateral movement of up to 2 in. The failure for both timber and concrete friction piles with vertical loads is by the slip mechanism. Point bearing timber and concrete piles are not analyzed. The results obtained using

the design method also show no reduction in load capacity for timber and concrete friction piles with lateral displacements of up to 2 in.

As described above, these analyses are based upon a Ramberg-Osgood representation of the timber and concrete materials, which implies unlimited ductility. This is not necessarily true. Hence, the above conclusion that the capacity of a friction pile is unaffected by lateral displacements of up to 2 in. will be true only if the pile has the ductility to develop a full plastic moment and, subsequently, to behave as a plastic hinge for the required rotations. The results of the finite element analysis indicate that, for a 2 in. lateral displacement, the plastic hinge rotation required at the top of a pile is approximately 0.04 radians over a 24-in. length in timber and over a 12-in. length in concrete.

# 7. SUMMARY, CONCLUSIONS, AND RECOMMENDATIONS FOR FURTHER STUDY

## 7.1. Summary

The states which use integral abutments in bridge design and the District Construction Office of the FHWA, Region 15, were surveyed to determine their current thinking and practice in integral abutment design. In Chapter 2 various policies are discussed for representive highway departments, and a summary of current practice by all the states and the FHWA is given in the Appendix. For most states the length limitations for integral abutment bridges have been set on the basis of past experience and have been increasing over the years as a result of satisfactory performance in actual installations. There is not a common set of design details used to implement integral abutment bridges.

The parameters needed to describe the behavior of the soil are given in Chapter 3. Three types of soil resistance-displacement curves were developed: lateral, vertical, and pile tip. The parameters needed for each curve are the initial stiffness, the ultimate soil resistance, and a shape factor. Each of these curves was approximated using a modified Ramberg-Osgood model. This model was expanded to include cyclic loadings. Simpler expressions for the soil parameters are presented for use with the design method in Chapter 5. Six typical Iowa soils were identified.

An algorithm based upon a nonlinear finite element procedure was developed to study the soil-pile interaction in integral abutment bridges. The finite element idealization consists of a one-dimensional

idealization for the pile and nonlinear springs for the foundation. Incremental finite elements with an updated Lagrangian formulation and material nonlinearities were used. For the purposes of treating arbitrary large rotations, node orientations were described by unit vectors. Deformations were defined by the orientation of these vectors relative to a rigid body element coordinate system which is along the beam chord. The total deformation nodal forces were evaluated by numerical integration through the cross section. Explicit forms of the tangent stiffness in the element coordinate system are presented. Updating of the element coordinates in three dimensions is also described. The numerical techniques available for the solutions of the nonlinear equations are reviewed, and the incremental and iterative techniques used in the study are discussed in detail. Two computer programs (IAB3D and IAB2D) have been developed to solve the nonlinear soil-pile interaction problems for both three- and two-dimensional cases. A number of experimental and analytical examples have been analyzed to establish their reliability.

A simplified design model for analyzing piles in integral abutment bridges is presented in Chapter 5. This model grew from previous analytical models and observations of pile behavior. The pile is described in terms of its axial behavior, lateral behavior, and combined axial-lateral behavior. The axial behavior was controlled by one of two failure mechanisms: the slip mechanism which occurred when the soil failed with the pile slipping through the soil and the lateral mechanism which occurred when the pile deflected laterally under vertical load. Several types of lateral behavior could occur, depending upon the

size of pile, the soil properties, the length of the pile, and the boundary conditions. For the combined behavior, either the slip mechanism or the lateral mechanism would again control. The slip mechanism was not affected by lateral displacements. The Rankine equation, which utilized the elastic buckling load and the rigid, perfectly plastic mechanism load, was used to determine the ultimate load for the lateral mechanism. The design model was compared with the finite element model results. The design model correctly describes the essential behavioral characteristics of the pile and conservatively predicts the vertical load-carrying capacity. One limitation of the design model was that only one type of soil could be used throughout the pile depth; that is, layered soils could not be used.

In Chapter 6 many analytical examples are presented in which a pile was given a lateral displacement to simulate the bridge expansion. A vertical load was then applied until failure occurred. These examples showed that for the cases studied in Iowa soils, friction H piles experienced no decrease in load-carrying capacity for lateral displacements up to 4 in. This was true whether the pile was bent about the strong axis, weak axis, or 45° from either axis. This was also true for timber and concrete piles displaced up to 2 in. All of these cases failed by the slip mechanism. However, end-bearing piles did show significant reductions in load-carrying capacity for similar lateral displacements and for bending about all three axes. These cases failed by the lateral mechanism. Other examples showed that the cyclic behavior had no effect. Examples with skewed and nonskewed bridges showed no effect on the pile capacity since these piles were friction piles. However, the longi-

tudinal expansion of the bridges introduced a preload on the pile which reduced the effective pile capacity.

## 7.2. Conclusions

The ultimate load capacity for friction piles was not affected by lateral displacements of up to 4 in. for H piles and up to 2 in. for timber and concrete piles. This conclusion differs from that obtained in the previous study because a smaller value for the soil-pile adhesion was used, and because cyclic effects were included. However, the ultimate load capacity was significantly reduced for lateral displacements greater than 2 in. for end-bearing H piles.

A vertical preload was introduced on the pile by the thermal expansion of the bridge as it pushed the abutment against the backfill. The load capacity of the pile was thus effectively reduced.

The maximum allowable length for bridges with integral abutments thus depends on whether the piles are friction or end bearing, as well as on the properties of the soil and piles. Methods for determining the allowable length are presented in this report. These methods showed that the current length limitation of 265 ft for bridges with integral abutments is conservative.

It is important to note that the allowable lengths determined using the design method were based on the structural integrity of the piles only. Other factors, notably the effects of the abutment movement on the approach slab and fill and the effects of the induced axial stresses in the superstructure, must also be considered. While

these factors have a relatively small effect on shorter bridges, as longer bridges with integral abutments are built these problems will become of greater importance.

## 7.3. Recommendations for Further Study

1) A scale model of a pile in an integral abutment bridge could be set up and tested in the laboratory. The experimental results can be compared to the results obtained from the analytical and simplified design methods.
2) An actual bridge could be instrumented to monitor thermal movements and piling stresses during temperature changes.
3) A study of the backfill and the approach slab under cyclic thermal movements would determine the most suitable type of approach slab to be used with the integral abutment type of bridges.
4) The design method could be refined by including the effects of axial load transfer and differing soil types in the calculation of the plastic mechanism load.
5) A study of the effects of the pile preload caused by the thermal expansion of the bridge is needed.
6) The effects of the abutment movement on the approach slab and fill and the effects of the induced axial stresses in the superstructure need further consideration.

## 8. ACKNOWLEDGMENT

The study presented in this report was conducted by the Engineering Research Institute of Iowa State University and was sponsored by the Iowa Department of Transportation, Highway Division, through the Iowa Highway Research Board.

The authors wish to extend sincere appreciation to Charles A. Pestotnik, Henry Gee, and Vernon Marks, from the Iowa DOT; Bruce Johnson from the Federal Highway Administration; and Wallace W. Sanders, Jr. from Iowa State University.

# 9. REFERENCES

## Chapter 2

2.1. Greimann, L. F., Wolde-Tinsae, A. M., and Yang, P. S., "Skewed Bridges with Integral Abutments," Bridges and Culverts, Transportation Research Record 903, Transportation Research Board, National Academy of Sciences, 1983.

2.2. Wolde-Tinsae, A. M., Greimann, L. F., and Johnson, B. V., "Performance of Integral Bridge Abutments," Journal of the International Association for Bridge and Structural Engineering, IABSE Proceedings P-58/83, Feb. 1983, pp. 17-34.

2.3. "Tennessee Structures Memorandum-045," State of Tennessee, SM045-01/07, Feb. 1982.

2.4. Hourigan, E. V., Deputy Chief Engineer (Structures), New York State Department of Transportation, 1220 Washington Avenue, State Campus, Albany, New York, Correspondence, April 1983.

2.5. Hood, G. A., and Mancarti, G. D., "Memo to Designers," Department of Transportation, Sacramento, Calif., Feb. 1983.

2.6. "Integral, No-Joint Structures and Required Provisions for Movement," U.S. Department of Transportation, Federal Highway Administration, T5140.13, Jan. 28, 1980.

2.7. "Tentative Integral Abutment Guidelines," New York State Department of Transportation, 1220 Washington Avenue, State Campus, Albany, New York, Feb. 10, 1983.

## Chapter 3

3.1. Desai, C. S., and Wu, T. H., "A General Function for Stress-Strain Curves," in Numerical Methods in Geomechanics, ASCE, 1976.

3.2. Duncan, J. M., and Chang, C.-Y., "Nonlinear Analysis of Stress and Strain in Soils," Journal of Soil Mechanics and Foundation Division, ASCE, Vol. 96, No. SM5, Proc. Paper 7513, Sept. 1970, pp. 1629-1653.

3.3. Finn, W. D., Lee, K. W., and Martin, G. R., "An Effective Stress Model for Liquefaction," Journal of the Geotechnical Engineering Division, ASCE, Vol. 103, No. GT6, Proc. Paper 13008, June 1977, pp. 517-533.

3.4. Martin, P. P., "Nonlinear Methods for Dynamic Analysis of Ground Response," Ph.D. Thesis, University of California at Berkeley, 1975.

3.5. Streeter, V. L., Wylie, E. B., and Richart, F. E., Jr., "Soil Motions Computations by Characteristic Methods," Journal of the Geotechnical Engineering Division, ASCE, Vol. 100, No. GT3, Proc. Paper 10410, March 1974, pp. 247-263.

3.6. Pyke, R., "Nonlinear Soil Models for Irregular Cyclic Loadings," Journal of the Geotechnical Engineering Division, ASCE, Vol. 105, No. GT6, Proc. Paper 14642, June 1977, pp. 715-726.

3.7. Wolde-Tinsae, A. M., Greimann, L. F. and Yang, P. S., Nonlinear Pile Behavior in Integral Abutment Bridges, Final Report, DOT Project HR-227, ISU-ERI-Ames 82123, Feb. 1982.

3.8. Ha, N. B., and O'Neill, M. W., "Field Study of Pile Group Action," Federal Highway Administration, Technical Report No. FHWA/RD-81/003, 1981.

3.9. Poulos, H. G., and Davies, E. H., Pile Foundation Analysis and Design, John Wiley and Sons, Inc., New York, 1980.

3.10. Davisson, M. T., "Lateral Load Capacity of Piles," Transportation Research Record 333, 1970.

3.11. Tomlinson, M. J., "The Adhesion of Piles Driven in Clay Soils," Proceedings, 4th International Conference on Soil Mechanics and Foundation Engineering, Vol. 2, 1957, p. 66.

3.12. Highway Structures Design Handbook, Vol. 1, United States Steel Corp., 1965.

## Chapter 4

4.1. Bathe, K. J., and Bolourchi, S., "Large Displacement Analysis of Three-Dimensional Beam Structures," International Journal for Numerical Methods in Engineering, Vol. 14, 1979, pp. 961-986.

4.2. Argyris, J. H., Dunne, P. C., and Scharpf, D. W., "On Large Displacement-Small Strain Analysis of Structures with Rotational Degree of Freedom," Computer Methods in Applied Mechanics and Engineering, Vol. 14, 1978, pp. 401-451.

4.3. Besseling, J. F., "Nonlinear Analysis of Structures by the Finite Element Method as a Supplement to a Linear Analysis," Computer Methods in Applied Mechanics and Engineering, Vol. 3, 1974, pp. 173-194.

4.4. Oden, J. T., and Neighbors, A., "Network-Topological Formulation of Analyses of Geometrically and Materially Nonlinear Space Frame," Space Structures, John Wiley and Sons, Inc., New York, 1967.

4.5. Johnson, D., and Brotton, D. M., "A Finite Deflection Analysis for Space Structures," Space Structures, John Wiley and Sons, Inc., New York, 1967.

4.6. Belytschko, T., and Hsieh, B. J., "Nonlinear Transient Finite Element Analysis with Convected Co-ordinates," International Journal of Numerical Methods in Engineering, Vol. 7, 1973, pp. 255-271.

4.7. Belytschko, T., Schwer, L., and Klein, M. J., "Large Displacement, Transient Analysis of Space Frames," International Journal of Numerical Methods in Engineering, Vol. 11, 1977, pp. 65-84.

4.8. Orean, C., "Tangent Stiffness in Plane Frames," Journal of the Structural Division, ASCE, Vol. 99, No. ST6, June 1973, pp. 973-985.

4.9. Orean, C., "Tangent Stiffness in Space Frames," Journal of the Structural Division, ASCE, Vol. 99, No. ST6, June 1973, pp. 987-1001.

4.10. Rajasekaran, S., and Murray, D. W., "Finite Element Solution of Inelastic Beam Equations," Journal of the Structural Division, ASCE, Vol. 99, No. ST6, June 1973, pp. 1025-1041.

4.11. Bavant, Z. P., and Nimeiri, M. E., "Large-Deflection Spatial Buckling of Thin-Walled Beams and Frames," Journal of the Engineering Mechanics Division, ASCE, Vol. 99, No. EM6, Dec. 1973, pp. 1259-1281.

4.12. Murray, D. W., and Wilson, E. L., "Finite Element Large Deflection Analysis of Plates," Journal of the Engineering Mechanics Division, ASCE, Vol. 95, No. EM1, Feb. 1969, pp. 143-165.

4.13. Oden, J. T., Clough, R. W., and Yamamoto, Y., Advances in Computational Methods in Structural Mechanics and Design, UAH (The University of Alabama in Huntsville) Press, Huntsville, Ala., 1972.

4.14. Gallagher, R. H., Yamada, Y., and Oden, J. T., Recent Advances in Matrix Methods of Structural Analysis and Design, UAH Press, Huntsville, Ala., 1969.

4.15. Wunderlich, W., Stein, E., and Bathe, K. J., Nonlinear Finite Element Analysis in Structural Mechanics, Springer-Verlag, Berlin-Heidelberg-New York, 1981.

4.16. Belytschko, T., Osias, J. R., and Marcal, P. V., Finite Element Analysis of Transient Nonlinear Structural Behavior, The American Society of Mechanical Engineers, 1975.

4.17. Cook, R. D., Concepts and Applications of Finite Element Analysis, 2nd Edition, John Wiley and Sons, Inc., New York, 1981.

4.18. Zienkiewicz, O. C., The Finite Element Method, 3rd Edition, McGraw-Hill Book Co., New York, 1977.

4.19. Przemieniecki, J. S., Theory of Matrix Structural Analysis, McGraw-Hill Book Co., New York, 1968.

4.20. Beaufait, F. W., Rowan, W. H., Jr., Hoadley, P. G., and Hackett, R. M., Computer Methods of Structural Analysis, 3rd Edition, Department of Civil Engineering, Vanderbilt University, Nashville, Tenn., 1975.

4.21. Kohnke, P. C., Engineering Analysis System Theoretical Manual, ANSYS, Swanson Analysis System, Inc., Houston, Penn., 1984.

4.22. Argyvis, J. H., Hilpert, O., Malejannakis, G. A., and Scharpf, D. W., "On the Geometrical Stiffness of a Beam in Space," Computer Methods in Applied Mechanics and Engineering, Vol. 20, 1979, pp. 105-131.

4.23. Desai, C. S., and Abel, J. F., Introduction to the Finite Element Method, Van Nostrand Reinhold Co., New York, 1972.

4.24. Wolde-Tinsae, A. M., Greimann, L. F., and Yang, P. S., Nonlinear Pile Behavior in Integral Abutment Bridges, Final Report, DOT Project HR-227, ISU-ERI-Ames 82123, Feb. 1982.

4.25. Parker, F., Jr., and Reese, L. C., "Experimental and Analytical Studies of Behavior of Single Piles in Sand under Lateral and Axial Loading," Research Report 117-2, Center for Highway Research, The University of Texas at Austin, Nov. 1970.

4.26. Desai, C. S., and Christian, J. T., Numerical Methods in Geotechnical Engineering, 1st Edition, McGraw-Hill Book Company, New York, 1977.

4.27. Mallet, R. H., and Berke, L., Automated Method for the Large Deflection and Instability Analysis of Three-Dimensional Truss and Frame Assemblies, AFFDL-TR-66-102, Dec. 1966.

4.28. Dupuis, G. A., Hibbitt, H. D., McNamara, S. F., and Marcal, P. V., "Nonlinear Material and Geometric Behavior of Shell Structures," Computer and Structure, Vol. 1, 1971, pp. 223-239.

4.29. Gjelsvik, A., and Bodner, S. R., "The Energy Criterion and Snap Buckling of Arches," Journal of the Engineering Mechanics Division, ASCE, Vol. 88, No. EM5, May 1962, pp. 87-134.

4.30. Bathe, K. J., "ADINA- A Finite Element Program for Automatic Dynamic Incremental Nonlinear Analysis," Report 82448-1, Acoustics and Vibration Lab., Mechanical Engineering Dept., Massachusetts Institute of Technology, 1977.

4.31. Williams, F. W., "An Approach to the Nonlinear Behavior of the Members of a Rigid Jointed Plane Framework with Finite Deflections," Quarterly Journal of Mechanics and Applied Mathematics, Vol. 17, 1964, pp. 451-469.

4.32. Chajes, A., Principles of Structural Stability Theory, Prentice-Hall, Inc., Englewood Cliffs, N.J., 1974.

4.33. D'Appolonia, E., and Romualdi, J. D., "Load Transfer in End-Bearing Steel H-Pile," Journal of the Soil Mechanics and Foundations Division, ASCE, Vol. 89, No. SM2, March 1963, pp. 1-25.

4.34. Bhushan, K., Haley, S. C., and Fong, P. T., "Lateral Load Tests on Drilled Piers in Stiff Clays," Journal of the Geotechnical Engineering Division, ASCE, Vol. 105, No. GT8, Aug. 1979, pp. 969-985.

4.35. Alizadeh, M., "Lateral Load Tests on Instrumented Timber Piles," Performance of Deep Foundations, ASTM STP444, American Society for Testing and Materials, 1969, pp. 379-394.

4.36. Bodig, J. B., and Jayne, B. A., Mechanics of Wood and Wood Composites, Van Nostrand Reinhold Company, New York, 1982.

4.37. Stevens, J. B., Holloway, D. M., Moriwaki, Y., and Demsky, E. C., "Pile Group Response to Axial and Lateral Loading," in Symposium on Deep Foundations, Ed. by F. Fuller, New York, ASCE, 1979, pp. 396-419.

4.38. Heténgi, M., Beams on Elastic Foundation, The University of Michigan Press, Ann Arbor, Mich., 1946.

## Chapter 5

5.1. Davisson, M. T., "Lateral Load Capacity of Piles," Transportation Research Record 333, 1970.

5.2. Prakash, S., "Behavior of Pile Groups Subjected to Lateral Loads," Ph.D. Thesis, University of Illinois, Urbana, 1962.

5.3. Poulos, H. G., and Davies, E. H., Pile Foundation Analysis and Design, John Wiley and Sons, Inc., New York, 1980.

5.4. Chajes, A., Principles of Structural Stability Theory, Prentice-Hall, Inc., Englewood Cliffs, N.J., 1974.

5.5. Davisson, M. T., "Estimating Buckling Loads for Piles," Proceedings, Second Pan American Conference on Soil Mechanics and Foundation Engineering, Vol. 1, 1963, pp. 351-71.

5.6. Reddy, A. S., and Valsangkar, A. J., "Buckling of Fully and Partially Embedded Piles," Journal of the Soil Mechanics and Foundation Division, ASCE, Vol. 96, SM6 1970, pp. 1951-1965.

5.7. Toakley, A. Raymond, "Buckling Loads for Elastically Supported Struts," Journal of the Engineering Mechanics Division, ASCE, Vol. 91, EM3, 1965, pp. 205-231.

5.8. Neal, B. G., The Plastic Methods of Structural Analysis, 2nd Edition, John Wiley & Sons, Inc., New York, 1963.

5.9. Commentary on Plastic Design in Steel, ASCE Manual of Engineering Practice, No. 41, 1961.

5.10. Wolde-Tinsae, A. M., Greimann, L. F. and Yang, P. S., Nonlinear Pile Behavior in Integral Abutment Bridges, Final Report, DOT Project HR-227, ISU-ERI-Ames 82123, Feb. 1982.

5.11. Peck, R. B., Hanson, W. E., and Thornburn, T. H., Foundation Engineering, John Wiley and Sons, Inc., New York, 1974.

5.12. Davisson, M. T., and Gill, H. L., "Laterally Loaded Piles in a Layered Soil System," Journal of the Soil Mechanics and Foundations Division, ASCE, Vol. 89, SM3, 1963, pp. 63-94.

5.13. Barber, E. S., Discussion of Paper by S. M. Gleser, Symposium on Lateral Load Tests on Piles, ASTM Special Technical Publication No. 154, 1953.

5.14. Reese, L. C., and Matlock, H., "Non-Dimensional Solutions for Laterally Loaded Piles with Soil Modulus Assumed Proportional to Depth," Proceedings, Eighth Texas Conference on Soil Mechanics and Foundation Engineering, Bureau of Engineering Research, University of Texas at Austin, 1956, pp. 1-41.

5.15. Broms, B. B., "Lateral Resistance of Piles in Cohesive Soils," Journal of the Soil Mechanics and Foundations Division, ASCE, Vol. 90, SM2, 1964, pp. 27-63.

5.16. Broms, B. B., "Lateral Resistance of Piles in Cohesionless Soils," Journal of the Soil Mechanics and Foundations Division, ASCE, Vol. 90, SM3, 1964, pp, 123-156.

5.17. Jorgenson, James L., "Behavior of Abutment Piles in an Integral Abutment Bridge," North Dakota State Highway Department, Fargo, N.D., Nov. 1981.

5.18. Emerson, Mary, "Thermal Movements of Concrete Bridges: Field Measurement and Methods of Prediction," Joint Sealing and Bearing Systems for Concrete Structures, ACI SP-70, 1981, pp. 77-102.

## Chapter 6

6.1. Wolde-Tinsae, A. M., Greimann, L. F. and Yang, P. S., Nonlinear Pile Behavior in Integral Abutment Bridges, Final Report, DOT Project HR-227, ISU-ERI-Ames 82123, Feb. 1982.

6.2. Highway Structures Design Handbook, Vol. 1, United States Steel Corp., 1965.

6.3. Neal, B. G., The Plastic Methods of Structural Analysis, 2nd Edition, John Wiley and Sons, Inc., New York, 1963.

6.4. Bodig, J. B., and Jayne, B. A., Mechanics of Wood and Wood Composites, Van Nostrand Reinhold Company, New York, 1982.

# 10. APPENDIX

Part 1. Integral Abutment Bridge Questionnaire

Part 2. Summary of Design Assumptions and Recommendations by the Different States

PART 1. INTEGRAL ABUTMENT BRIDGE QUESTIONNAIRE

1. Do you routinely calculate the change in the load-carrying capacity of the piles due to lateral movement of the integral abutment? Are the piling stresses due to the lateral movement calculated? Please explain the method(s) you use.

2. How do you determine what maximum length to use for bridges with integral abutments?

3. Do you have a design manual or design example for integral abutment bridges that we could study? (If so, we would appreciate receiving one copy.)

4. Please include any other information you have concerning the analysis and design of integral abutment bridges in your state.

Please note that the intent of the survey is to document current procedures and not to criticize any one method. If any information pertaining to design examples or manuals is wished to remain confidential, please let us know.

Please return to: Lowell Greimann
416 Town Engineering
Iowa State University
Ames, Iowa 50011

Part 2. Summary of Design Assumptions and Recommendations by the Different States

| State | Design Consideration: Piling Stresses Due to Lateral Movement are Calculated | Design Consideration: Criteria for Maximum Length for Bridges with Integral Abutments | Design Assumptions and Details: Pile Head | Pile Cap | Approach Slab | Back Fill | Comments |
|---|---|---|---|---|---|---|---|
| Alaska | Only for long bridges | On the basis of experience<br>Steel: ≤ 300 ft<br>Concrete: ≤ 400 ft<br>Prestressed: ≤ 416 ft | Hinge | --- | No | Granular material | Bridges with integral abutments may be constructed with spread footing or pilings. As longer bridges without expansion joints are found to be without problems, the length limit has increased to 400 ft for concrete bridges. |
| Arizona | No | On the basis of experience<br>Steel: ≤ 253 ft<br>Concrete: ≤ 330 ft<br>Prestressed: ≤ 404 ft | Hinge | No | Tied to abutment with dowels and moves back and forth with superstructure | Cohesive material | |
| California | Piles are driven into pre-drilled holes, and stresses due to lateral movement are neglected | On the basis of experience<br>Steel: ≤ 240 ft<br>Concrete: ≤ 260 ft<br>Prestressed: ≤ 150 ft | Partially restrained | | --- | Pervious | |
| Colorado | No | On the basis of experience<br>Steel: ≤ 200 ft<br>Concrete: ≤ 400 ft<br>Prestressed: ≤ 400 ft | Hinge | No | For bridge length > 200 ft, use approach slab | Granular | No problem in skew; use predrilled oversized hole. |
| Connecticut | No | On the basis of experience<br>Steel: ≤ 200 ft<br>Concrete: ≤ ---<br>Prestressed: ≤ --- | Fixed | --- | | --- | As of May 1983, only one integral abutment has been designed and constructed. The design of this 245-ft-long two-span continuous bridge was based upon information received from the South Dakota Department of Transportation. |
| Georgia | No | Based on total anticipated lateral movement of ≤ 2 in.<br>Steel: ≤ 300 ft<br>Concrete: ≤ 600 ft<br>Prestressed: ≤ --- | Free translation, free rotation, roller | No | Expansion joint between approach slab and bridge slab | Roadway fill | Integral abutments have been used only at sites where steel H Piles are suitable. The steel H Piles are placed such that they bend about their weak axis. |

Part 2. Continued.

| State | Design Consideration: Piling Stresses Due to Lateral Movement are Calculated | Design Consideration: Criteria for Maximum Length for Bridges with Integral Abutments | Design Assumptions and Details: Pile Head | Design Assumptions and Details: Pile Cap | Design Assumptions and Details: Approach Slab | Design Assumptions and Details: Back Fill | Comments |
|---|---|---|---|---|---|---|---|
| Idaho | Only for those that involve some unique feature that would warrant such calculations | Based upon FHWA guidelines and the state's own experience<br>Steel: ≤ 200 ft<br>Concrete: ≤ 400 ft<br>Prestressed: ≤ 400 ft | Hinge | Rigid pile cap | Expansion joint specified between rigid pavement and approach slab; no special treatment specified for flexible pavement | Free draining granular material | Assume that passive earth pressure at abutments tends to restrain movement and reduce deflections from calculated values. Skewed three-span steel girder bridge with integral abutment was built; rotational forces from lateral earth presence on end wall caused failure in pier anchor bolts on exterior girder. |
| Indiana | No | Steel: ≤ ---<br>Concrete: ≤ 150 ft<br>Prestressed: ≤ --- | Hinge | Embed piles only 1 ft into the cap | 20-ft. approach slab integrally attached to bridge | Select granular fill | Only vertical piles are used with integral abutments. When bridge skew > 30°, length limit for concrete bridges is ≤ 100 ft. Integral abutments have been used for many years with no adverse experiences. On longer bridges the integral connection is eliminated, substituting a neoprene bearing pad or expansion device, use alternating vertical and battered piles in the cap and still neglect lateral forces on the piles. |
| Iowa | Yes | Based on an allowable bending stress of 55% of yield plus a 30% overstress. Moment in pile found by a rigid frame analysis considering relative stiffness of the superstructure and the piling. Assume piles to be 10.5 ft and neglect soil resistance. Analysis showed that allowable pile deflection was about 3/8 in.<br>Steel: ≤ ---<br>Concrete: ≤ 265 ft<br>Prestressed: ≤ 265 ft | Fixed | Neglect | Neglect | Roadway fill | Conservative design. |

Part 2. Continued.

| State | Design Consideration: Piling Stresses Due to Lateral Movement are Calculated | Design Consideration: Criteria for Maximum Length for Bridges with Integral Abutments | Design Assumptions and Details: Pile Head | Design Assumptions and Details: Pile Cap | Design Assumptions and Details: Approach Slab | Design Assumptions and Details: Back Fill | Comments |
|---|---|---|---|---|---|---|---|
| Kansas | No | Based on experience<br>Steel: ≤ 250 ft-300 ft<br>Concrete: ≅ 500 ft<br>Prestressed: ≤ --- | Hinge | Pile caps not used | Use slab support at backwall and pavement rests on slab with about 30 ft from end of wearing surface | Backfill compaction has settlement just off end of bridge | Have used integral abutments for cast-in-place bridge structures for many years and have encountered no difficulties. Expect to increase length limits in the future. |
| Kentucky | No | Steel: ≤ ---<br>Concrete: ≤ 300 ft<br>Prestressed: ≤ 300 ft | Fixed or partially restrained | --- | No special treatment with flexible pavement | Special granular backfill specified | Piles are placed in holes prebored for a distance of 8 ft below bottom of pile cap. |
| Missouri | No | Based on experience of Missouri and other states (mainly Tennessee)<br>Steel: ≤ 400 ft<br>Concrete: ≤ 400 ft<br>Prestressed: ≤ 500 ft | Hinge | On extreme skews (±40°), use shear key on bottom of pile cap to prevent lateral movement of pile cap | --- | Roadway fill | Require a minimum of 15 ft pile length to permit flexure of pile. |
| Montana | No | Based on experience and engineering judgment<br>Steel: ≤ 300 ft<br>Concrete: ≤ 350 ft<br>Prestressed: ≤ 300 ft | Hinge | --- | Not fixed to abutment | Granular material | ≤ 30° skew |
| North Dakota | No | Steel: ≤ 350 ft | Fixed | Abutment wall is pile cap and is reinforced to resist bending below superstructure | Assume approach slab has no effect | Select granular material | ≤ 30° skew |

Part 2. Continued.

| State | Design Consideration: Piling Stresses Due to Lateral Movement are Calculated | Design Consideration: Criteria for Maximum Length for Bridges with Integral Abutments | Design Assumptions and Details: Pile Head | Design Assumptions and Details: Pile Cap | Design Assumptions and Details: Approach Slab | Design Assumptions and Details: Back Fill | Comments |
|---|---|---|---|---|---|---|---|
| Nebraska | No | Based primarily on past experience and recommendations from other agencies<br>Steel: ≤ 200 ft<br>Concrete: ≤ 300 ft<br>Prestressed: ≤ 300 ft | Hinge | --- | --- | Select granular fill | ≤ 15° skew<br>Procedures for determining piling numbers are the same as for conventional abutments. The pilings are rotated to provide bending about weak axis. Presently only steel H piles are used in integral abutments and also substantial anchorage between the girder and the abutment are provided. Wings on integral abutments are not attached to the abutment in order to reduce resistance to rotation. This is accomplished by using a bond breaker between the abutment and wing and designing the wing as a stand-alone structure. |
| New Mexico | No | --- | Partially restrained or fixed | --- | Used on some bridges and not on others | Do not use specified backfill anymore | Have built bridges with up to 15° skew; skew angle neglected. |
| New York | No | Steel: ≤ 300 ft<br>Concrete: ≤ ---<br>Prestressed: ≤ 400 ft | --- | --- | Approach slab should be 20 ft long maximum and the end of the approach slab shall be parallel to the skew. Construction joint provided between approach slab and bridge slab | Granular fill behind backwall and wingwalls | New York State has tentative integral abutment bridge design guidelines that list the design parameters that must be satisfied. |
| Ohio | No | Based on experience and engineering judgment<br>Steel: ≤ 300 ft<br>Concrete: ≤ 300 ft<br>Prestressed: ≤ 300 ft | Hinge | Pile cast in pile cap 2 ft | Tie approach slab to abutment | Granular material | Oil country pipelines not used in integral abutments because they are stiffer than H piles about weak axis. Integral abutment bridges built only with zero skews. |

Part 2. Continued.

| State | Design Consideration: Piling Stresses Due to Lateral Movement are Calculated | Design Consideration: Criteria for Maximum Length for Bridges with Integral Abutments | Design Assumptions and Details: Pile Head | Pile Cap | Approach Slab | Back Fill | Comments |
|---|---|---|---|---|---|---|---|
| Oklahoma | No | Based on allowable lateral movement of 0.5 in.<br>Steel: ≤ 200 ft<br>Concrete: ≤ 200 ft<br>Prestressed: ≤ 200 ft | Partially restrained | --- | --- | --- | Integral abutments only with zero skews. |
| Oregon | No | Based on engineering judgment. Length varies depending on location in state.<br>Steel: ≤ ---<br>Concrete: ≤ 350 ft<br>Prestressed: ≤ 350 ft | Hinge | Pile cast in pile cap 1 ft | Approach slab tied to pile cap | Granular | --- |
| South Dakota | Yes | --- | Fixed | --- | Tied to bridge to prevent erosion of shoulder | Granular | --- |
| Tennessee | No | Based on experience<br>Steel: ≤ 400 ft<br>Concrete: ≤ 800 ft<br>Prestressed: ≤ 800 ft | Hinge | --- | Construction joint between abutment backwall and approach slab | Granular | No bridge deck expansion joints are to be provided unless absolutely necessary. |
| Utah | No | Steel: ≤ 300 ft<br>Concrete: ≤ ---<br>Prestressed: ≤ 300 ft | Hinge | --- | Expansion joint between approach slab and bridge slab | Granular | Steel piles used primarily through granular material over bed rock. |
| Virginia | No | Steel: ≤ 242 ft<br>Concrete: ≤ ---<br>Prestressed: ≤ 454 ft | Hinge or fixed | Uniform width and parallel to bridge skew | No approach slab | Use 1.5 ft of porous backfill with 0.5 in. diameter pile underdrain | Max skew, 10°; relatively small movement at each abutabutment (± 3/8 in.). |

Part 2. Continued.

| State | Design Consideration: Piling Stresses Due to Lateral Movement are Calculated | Design Consideration: Criteria for Maximum Length for Bridges with Integral Abutments | Design Assumptions and Details: Pile Head | Design Assumptions and Details: Pile Cap | Design Assumptions and Details: Approach Slab | Design Assumptions and Details: Back Fill | Comments |
|---|---|---|---|---|---|---|---|
| Vermont | No | Steel: ≤ 150 ft<br>Concrete: ≤ ---<br>Prestressed: ≤ --- | Partially restrained or fixed | Rigid pile cap | Approach slab anchored to abutment | No special treatment | ≤ 30° skew |
| Washington | No | Mainly based on past experience<br>Steel: ---<br>Concrete: ≤ 400 ft<br>Prestressed: ≤ 400 ft | Hinge | Designed as cross beam on simple supports | Approach slab attached to abutment with allowance for expansion | Granular backfill, earth pressure applied normal to abutment | --- |
| Wisconsin | No | Steel: ≤ 200 ft<br>Concrete: ≤ 300 ft<br>Prestressed: ≤ 300 ft | Fixed | Designed as reinforced continuous beam over pilings | Designed for vertical load only | Granular | ≤ 30° skew for slabs;<br>≤ 15° skew for prestressed or steel girders |
| Wyoming | No | Based on various studies, reports, etc.<br>Steel: ≤ 300 ft<br>Concrete: ≤ 500 ft<br>Prestressed: ≤ 500 ft | Plastic hinge | Assumed to be a mass attached to end of girder | --- | Granular | --- |
| FHWA, Region 15 | Yes | Steel: ≤ ---<br>Concrete: ≤ 270 ft<br>Prestressed: ≤ 300 ft | Hinge or partially restrained | Pile cast in pile cap 1 ft | --- | Pervious | --- |

# 11. TABLES

Table 2.1. Design restraining forces.

| Abutment Type | Design Longit. Force (Service Level) |
|---|---|
| End Diaphragm on Cast In Drilled Hole Piles | *25 kips per pile |
| End Diaphgram on Concrete Driven Piles | *20 kips per pile |
| End Diaphragm on 45-Ton Steel Piles | *15 kips per pile |
| End Diaphragm on Neoprene Strip or Pads | 15% of dead load |
| End Diaphragm on Rollers | 5% of dead load |

*These values are for the design of end diaphragm only.

Table 3.1. Flow chart for determining the reversal values of loading and unloading.

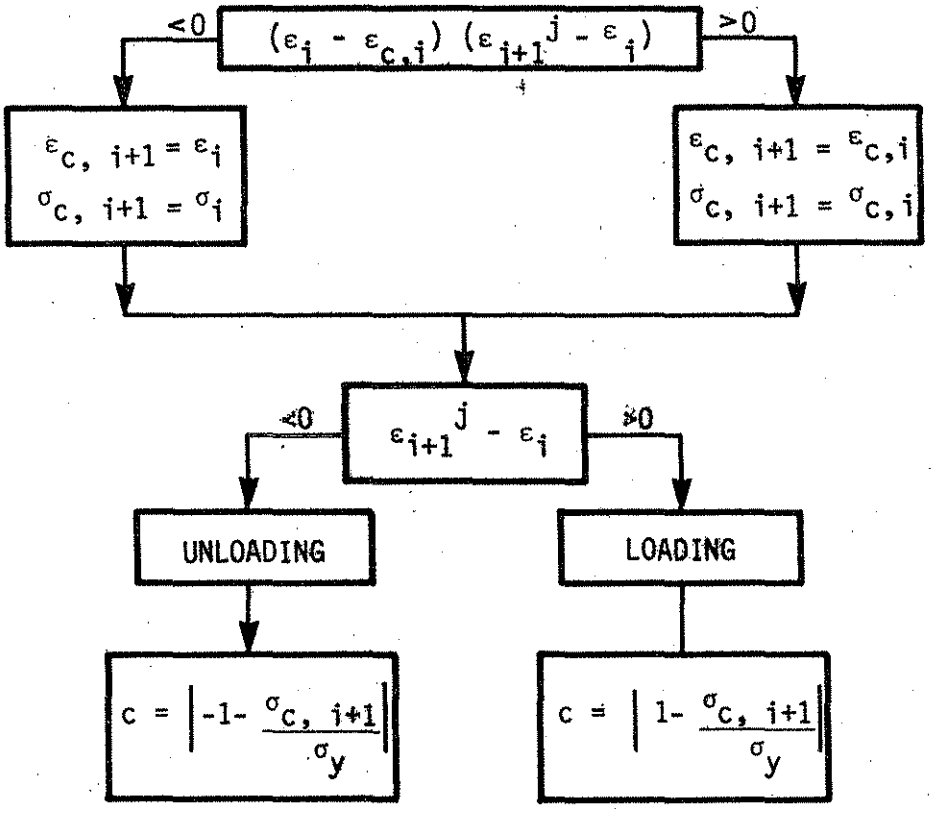


$\varepsilon_i$ = THE CONVERGED STRAIN OF THE PREVIOUS INCREMENT i,
$\sigma_i$ = THE CONVERGED STRESS OF THE PREVIOUS INCREMENT i,
$\varepsilon_{c,i}$ = THE REVERSAL STRAIN OF THE PREVIOUS INCREMENT i,
$\sigma_{c,i}$ = THE REVERSAL STRESS OF THE PREVIOUS INCREMENT i,
$\varepsilon_{i+1}^{j}$ = THE UPDATED STRAIN OF THE CURRENT INCREMENT i+1,
$\sigma_{i+1}^{j}$ = THE UPDATED STRESS OF THE CURRENT INCREMENT i+1,
$\varepsilon_{c,i+1}$ = THE UPDATED REVERSAL STRAIN OF THE CURRENT INCREMENT i+1
$\sigma_{c,i+1}$ = THE UPDATED REVERSAL STRESS OF THE CURRENT INCREMENT i+1,

Table 3.2. Parameters for p-y curve.

| Case | n | $p_u$ (use lesser value) | $k_h$ |
|---|---|---|---|
| Soft clay (Static load) | 1.0 | $p_u = 9c_uB$ | |
| | | $p_u = \left(3 + \frac{\gamma}{c_u}x + \frac{0.5}{B}x\right)c_uB$ | $\frac{p_u}{y_{50}}$ |
| Stiff clay (Static load) | 1.0 | $p_u = 9c_uB$ | |
| | | $p_u = \left(3 + \frac{\gamma}{c_u}x + \frac{0.5}{B}x\right)c_uB$ | $\frac{p_u}{y_{50}}$ |
| Very stiff clay (Static load) | 2.0 | $p_u = 9c_uB$ | |
| | | $p_u = \left(3 + \frac{\gamma}{c_u}x + \frac{2.0}{B}x\right)c_uB$ | $\frac{p_u}{2y_{50}}$ |
| Sand (Static load) | 3.0 | $p_u = \gamma x\left[B(k_p - k_a) + xk_p\tan\alpha\tan\beta + xk_o\tan\beta(\tan\phi - \tan\alpha)\right]$ | $\frac{J\gamma x}{1.35}$ |
| | | $p_u = \gamma x\left[k_p^3 + 2k_p^2k_o\tan\phi - k_a\right]B$ | |

Note: For notations refer to Table 3.3.

Table 3.3. Soil parameters for Table 3.2.

| Parameter | Evaluation |
|---|---|
| $\varepsilon_{50}$ | From laboratory triaxial test, or use<br>= 0.02 for soft clay<br>= 0.01 for stiff clay<br>= 0.005 for very stiff clay<br>(Axial strain at 0.5 times peak stress difference) |
| $c_u$ | Undrained cohesion indicated for an unconsolidated, undrained laboratory test |
| B | Pile width |
| $\gamma$ | Effective unit soil weight |
| x | Depth from soil surface |
| $\phi$ | Angle of internal friction |
| $k_p$ | $= \tan^2 (45° + \frac{\phi}{2})$ |
| $k_a$ | $= \tan^2 (45° - \frac{\phi}{2})$ |
| $k_o$ | $= 1 - \sin\phi$ |
| $\alpha$ | $= \frac{\phi}{2}$ for dense or medium sand |
| | $= \frac{\phi}{3}$ for loose sand |
| $\beta$ | $= 45° + \frac{\phi}{2}$ |
| J | = 200 for loose sand |
| | = 600 for medium sand |
| | = 1500 for dense sand |
| $y_{50}$ | Displacement at one-half ultimate soil reaction |
| | $= 2.5 B\varepsilon_{50}$ for soft and stiff clay |
| | $= 2.0 B\varepsilon_{50}$ for very stiff clay |

Table 3.4. Parameters for f-z curve.

| Case | n | $f_{max}$ | | $k_v$ |
|---|---|---|---|---|
| | | H Piles | Others | |
| Clay (Static load) | 1.0 | The least of: | The lesser of: | $\frac{10f_{max}}{z_c}$ |
| | | $2(d+b_f)c_u$ | $\ell_g c_a$ | |
| | | $2(d+2b_f)c_a$ | $\ell_g c_u$ | |
| | | $2(dc_u+b_f c_a)$ | | |
| Sand (Static load) | 1.0 | $0.02N(2(d+2b_f))$ (klf) | $0.04N\ell_g$ (klf) | $\frac{10f_{max}}{zc}$ |

$\alpha$ = Shear strength reduction factor (see Fig. 3.6)

$c_u$ = Undrained cohesion of the clay soil

= 97.0N + 114.0 (psf)

$c_a$ = Adhesion between soil and pile

= $\alpha c_u$ (psf)

N = Average standard penetration blow count

$z_c$ = Relative displacement required to develop $f_{max}$

= 0.4 in. (0.033 ft) for sand

= 0.25 in. (0.021 ft) for clay

$\ell_g$ = Gross perimeter of the pile (ft)

d = Section depth of H pile or diameter of pipe pile (ft)

$b_f$ = Flange width of H pile (ft)

Table 3.5. Parameters for q-z curve.

| Case | n | $q_{max}$ | $k_q$ |
|---|---|---|---|
| Clay (Static case) | 1.0 | $9c_u$ | $\frac{10q_{max}}{z_c}$ |
| Sand (Static case) | 1.0 | $8N_{corr}$ (ksf) | $\frac{10q_{max}}{z_c}$ |

$N_{corr}$ = Corrected standard penetration test (SPT) blow count at depth of pile tip

= N (uncorrected) if $N \leq 15$

= 15 + 0.5(N-15) if $N > 15$

$c_u$ = Undrained cohesion of the clay soil

= 97.0N + 114.0 (psf)

$z_c$ = Relative displacement required to develop $q_{max}$

= 0.4 in. (0.033 ft) for sand

= 0.25 in. (0.021 ft) for clay

N = Average standard penetration blow count

Table 3.6. Soil properties and curve parameters for loose sand.

| | Range of Values | | Typical Value |
|---|---|---|---|
| | Lower Bound | Upper Bound | |
| **Soil Properties:** | | | |
| Blow count, N | 4 | 10 | 5 |
| Unit weight, $\gamma$ (pcf) | 90 | 125 | 110 |
| Angle of friction, $\phi$ | 28° | 30° | 30° |
| **p-y Curve Parameters:** | | | |
| n | 3.0 | 3.0 | 3.0 |
| $p_u$ (klf) | $0.10x^2 + 0.22Bx$ for $x \leq 21B$<br>$2.3Bx$ for $x > 21B$ | $0.16x^2 + 0.33Bx$ for $x \leq 23B$<br>$4.0Bx$ for $x > 23B$ | $0.14x^2 + 0.29Bx$ for $x \leq 23B$<br>$3.5Bx$ for $x > 23B$ |
| $k_h$ (ksf) | 13x | 19x | 16x |
| **f-z Curve Parameters:** | | | |
| n | 1.0 | 1.0 | 1.0 |
| $f_{max}$ (klf)* | 0.4 | 1.0 | 0.5 |
| $k_v$ (ksf)* | 120 | 300 | 150 |
| **q-z Curve Parameters:** | | | |
| n | 1.0 | 1.0 | 1.0 |
| $q_{max}$ (ksf) | 32 | 80 | 40 |
| $k_q$ (kcf) | 9700 | 24,000 | 12,000 |

*These values are for a HP10×42 pile.

B = pile width (ft).

x = depth from soil surface (ft).

Table 3.7. Soil properties and curve parameters for medium sand.

| | Range of Values | | Typical Value |
|---|---|---|---|
| | Lower Bound | Upper Bound | |
| **Soil Properties:** | | | |
| Blow count, N | 10 | 30 | 15 |
| Unit weight, $\gamma$ (pcf) | 110 | 130 | 120 |
| Angle of friction, $\phi$ | 30° | 35° | 35° |
| **p-y Curve Parameters:** | | | |
| n | 3.0 | 3.0 | 3.0 |
| $p_u$ (klf) | $0.18x^2 + 0.29Bx$ for $x \leq 18B$ | $0.33x^2 + 0.44Bx$ for $x \leq 21B$ | $0.31x^2 + 0.41Bx$ for $x \leq 21B$ |
| | $3.5Bx$ for $x > 18B$ | $7.6Bx$ for $x > 21B$ | $7.0Bx$ for $x > 21B$ |
| $k_h$ (ksf) | 49x | 58x | 53x |
| **f-z Curve Parameters:** | | | |
| n | 1.0 | 1.0 | 1.0 |
| $f_{max}$ (klf)* | 1.0 | 3.0 | 1.5 |
| $k_v$ (ksf)* | 300 | 900 | 450 |
| **q-z Curve Parameters:** | | | |
| n | 1.0 | 1.0 | 1.0 |
| $q_{max}$ (ksf) | 80 | 180 | 120 |
| $k_q$ (kcf) | 24,000 | 55,000 | 36,000 |

*These values are for a HP10×42 pile.

Table 3.8. Soil properties and curve parameters for dense sand.

| | Range of Values | | Typical Value |
|---|---|---|---|
| | Lower Bound | Upper Bound | |
| **Soil Properties:** | | | |
| Blow count, N | 30 | 50 | 30 |
| Unit weight, $\gamma$ (pcf) | 110 | 140 | 130 |
| Angle of friction, $\phi$ | 35 | 40 | 40 |
| **p-y Curve Parameters:** | | | |
| n | 3.0 | 3.0 | 3.0 |
| $p_u$ (klf) | $0.28x^2 + 0.38Bx$ for $x \leq 21B$ | $0.55x^2 + 0.61Bx$ for $x \leq 27B$ | $0.51x^2 + 0.57Bx$ for $x \leq 27B$ |
| | $6.4Bx$ for $x > 21B$ | $15Bx$ for $x > 27B$ | $14Bx$ for $x > 27B$ |
| $k_h$ (ksf) | 120x | 160x | 140x |
| **f-z Curve Parameters:** | | | |
| n | 1.0 | 1.0 | 1.0 |
| $f_{max}$ (klf)* | 3.0 | 5.0 | 3.0 |
| $k_v$ (ksf)* | 900 | 1500 | 900 |
| **q-z Curve Parameters:** | | | |
| n | 1.0 | 1.0 | 1.0 |
| $q_{max}$ (ksf) | 180 | 260 | 180 |
| $k_q$ (kcf) | 55,000 | 79,000 | 55,000 |

*These values are for a HP10×42 pile.

Table 3.9. Soil properties and curve parameters for soft clay.

| | Range of Values | | Typical Value |
|---|---|---|---|
| | Lower Bound | Upper Bound | |
| **Soil Properties:** | | | |
| Blow count, N | 2 | 4 | 3 |
| Unit weight, $\gamma$ (pcf) | 90 | 110 | 100 |
| Undrained cohesion, $c_u$ (psf) | 375 | 750 | 405 |
| **p-y Curve Parameters:** | | | |
| n | 1.0 | 1.0 | 1.0 |
| $p_u$ (klf) (use lesser value) | 3.4B or 1.1B+0.09Bx+0.19x | 6.8B or 2.3B+0.11Bx+0.38x | 3.6B or 1.2B+0.10Bx+0.20x |
| $k_h$ (ksf) (use lesser value) | 67.5 or 23+1.8x+3.8x/B | 135 or 45+2.2B+7.5x/B | 73 or 24+2x+4.1x/B |
| **f-z Curve Parameters:** | | | |
| n | 1.0 | 1.0 | 1.0 |
| $f_{max}$ (klf)* | 1.24 | 2.26 | 1.34 |
| $k_v$ (ksf)* | 590 | 1080 | 640 |
| **q-z Curve Parameters:** | | | |
| n | 1.0 | 1.0 | 1.0 |
| $q_{max}$ (ksf) | 3.4 | 6.8 | 3.6 |
| $k_q$ (kcf) | 1600 | 3200 | 1700 |

*These values are for a HP10×42 pile.

Table 3.10. Soil properties and curve parameters for stiff clay.

| | Range of Values | | Typical Value |
|---|---|---|---|
| | Lower Bound | Upper Bound | |
| **Soil Properties:** | | | |
| Blow count, N | 5 | 17 | 15 |
| Unit weight, γ (pcf) | 115 | 135 | 120 |
| Undrained cohesion, $c_u$ (psf) | 1500 | 3000 | 1569 |
| **p-y Curve Parameters:** | | | |
| n | 1.0 | 1.0 | 1.0 |
| $p_u$ (klf) (use lesser value) | 14B or 4.5B+0.12Bx+0.75x | 27B or 9.0B+0.14Bx+1.5x | 14B or 4.7B+0.12Bx+0.78x |
| $k_h$ (ksf) (use lesser value) | 540 or 180+4.6x+30x/B | 1080 or 360+5.4x+60x/B | 560 or 190+4.8x+31x/B |
| **f-z Curve Parameters:** | | | |
| n | 1.0 | 1.0 | 1.0 |
| $f_{max}$ (klf)* | 3.71 | 3.73 | 3.86 |
| $k_v$ (ksf)* | 1770 | 1780 | 1850 |
| **q-z Curve Parameters:** | | | |
| n | 1.0 | 1.0 | 1.0 |
| $q_{max}$ (ksf) | 14 | 27 | 14 |
| $k_q$ (kcf) | 6400 | 13,000 | 6700 |

*These values are for a HP10×42 pile.

Table 3.11. Soil properties and curve parameters for very stiff clay.

| | Range of Values | | Typical Value |
|---|---|---|---|
| | Lower Bound | Upper Bound | |
| **Soil Properties:** | | | |
| Blow count, N | 18 | 50 | 50 |
| Unit weight, $\gamma$ (pcf) | 120 | 140 | 130 |
| Undrained cohesion, $c_u$ (psf) | 3000 | 6000 | 5000 |
| **p-y Curve Parameters:** | | | |
| n | 2.0 | 2.0 | 2.0 |
| $p_u$ (klf) (use lesser value) | 27B or 9B+0.12Bx+6x | 54B or 18B+0.14Bx+12x | 45B or 15B+0.13Bx+10x |
| $k_h$ (ksf) (use lesser value) | 1350 or 450+6x+300x/B | 2700 or 900+7x+600x/B | 2250 or 750+6.5x+500x/B |
| **f-z Curve Parameters:** | | | |
| n | 1.0 | 1.0 | 1.0 |
| $f_{max}$ (klf)* | 3.73 | 7.47 | 6.22 |
| $k_v$ (ksf)* | 1780 | 3560 | 2960 |
| **q-z Curve Parameters:** | | | |
| n | 1.0 | 1.0 | 1.0 |
| $q_{max}$ (ksf) | 27 | 54 | 45 |
| $k_q$ (kcf) | 13,000 | 26,000 | 21,000 |

*These values are for a HP10×42 pile.

Table 4.1. Soil characteristics.

| Pier No. | Site No. | Soil Type | Total Unit Wt.--lbs/ft$^3$ | Avg. Undrained Shear Strength lbs/ft$^2$ | $\varepsilon_{50}$ % | Depth ft |
|---|---|---|---|---|---|---|
| 1 | A | Sandy Clay (CL - CH) | 130 | 5500 | 0.96 | 0 ~ 9 |
| 2 | B | Sandy Clay (CL) | 130 | 4750 | 0.72 | 0 ~16 |

Table 4.2. Modulus of elasticity for timber piles.

| Test Site | Pile | Average Modulus of Elasticity, E(ksi) |
|---|---|---|
| 1 | 1-A | 2000 |
| | 1-B | 2500 |
| 2 | 2-A | 1900 |
| | 2-B | 2000* |

*Assumed, as no calibration test was made on this pile.

Table 5.1. Soil properties used to check the lateral mechanism (see *Chapter 3 for notation*).

| Soil Types | $k_h$ (ksi) | $p_u$ (k/in) | $k_v$ (ksi) | n (p-y) | n (f-z) |
|---|---|---|---|---|---|
| Very stiff clay | 15.6 | 3.75 | 20.06 | 2.0 | 1.0 |
| Soft clay | 0.5 | 0.24 | 4.10 | 1.0 | 1.0 |
| 1/5 Soft clay | 0.1 | 0.05 | 0.82 | 1.0 | 1.0 |
| Dense sand | 0.0840x | 0.0104x | - | 3.0 | 1.0 |
| Loose sand | 0.0095x | 0.0058x | - | 3.0 | 1.0 |
| 1/5 Loose sand | 0.0019x | 0.0012x | - | 3.0 | 1.0 |

Table 5.2. Tabulated values for the plastic mechanism load $V_p$, the elastic buckling load $V_{cr}$, and the ultimate load from finite element results $V_u$.

| | Soil Types | $V_p$ (k) | $V_{cr}$ (k) | $V_u$(k) (finite element) |
|---|---|---|---|---|
| e = 1" (see Fig. 5.12(a)) | very stiff clay | 480.5 | 11352 | 534 |
| | soft clay | 480.5 | 2036 | 477 |
| | 1/5 soft clay | 480.5 | 909 | 350 |
| e = 2" (Fig. 5.12(a)) | very stiff clay | 384.8 | 11352 | 446 |
| | soft clay | 384.8 | 2036 | 396 |
| | 1/5 soft clay | 384.8 | 909 | 285 |
| | dense sand | 384.8 | 5260 | 441 |
| | loose sand | 384.8 | 2201 | 415 |
| | 1/5 loose sand | 384.8 | 1156 | 373 |
| e = 2" (w/vertical springs) (Fig. 5.12(b)) | very stiff clay | 384.8 | 18787 | 478 |
| | soft clay | 384.8 | 3370 | 421 |
| | 1/5 soft clay | 384.8 | 1504 | 320 |

Table 5.3. Tabulated values for the plastic mechanism load $V_p$, the elastic buckling load $V_{cr}$, and the ultimate load $V_u$ for combined loading.

| | Soil Types | $V_p$ (k) | $V_{cr}$ (k) | $V_u$(k) (finite element) |
|---|---|---|---|---|
| $\Delta_h$ = 1 in. (see Fig. 5.25) | very stiff clay | 539.6 | 11352 | 580 |
| | soft clay | 539.6 | 2036 | 537 |
| | 1/5 soft clay | 539.6 | 909 | 437 |
| $\Delta_h$ = 2 in. (see Fig. 5.25) | very stiff clay | 480.5 | 11352 | 564 |
| | soft clay | 480.5 | 2036 | 483 |
| | 1/5 soft clay | 480.5 | 909 | 357 |
| | dense sand | 480.5 | 5260 | 590 |
| | loose sand | 480.5 | 2201 | 548 |
| | 1/5 loose sand | 480.5 | 1156 | 485 |
| $\Delta_h$ = 2 in. (see Fig. 5.25 w/fixed pile head) | very stiff clay | 539.6 | 14190 | 602 |
| | soft clay | 539.6 | 2545 | 538 |
| | 1/5 soft clay | 539.6 | 1136 | 458 |
| $\Delta_h$ = 2 in. (w/vertical springs, no support at pile tip) | very stiff clay | 480.5 | 18787 | 740 |
| | soft clay | 480.5 | 3370 | 584 |
| | 1/5 soft clay | 480.5 | 1504 | 500 |

Table 6.1. Material properties of timber and concrete piles.

| Piles | Modulus of Elasticity ksi | Yield Stress ksi |
|---|---|---|
| Douglas fir timber pile | 2000 | 7.5 |
| Concrete pile | 4300 | 4.0 |

# 12. FIGURES

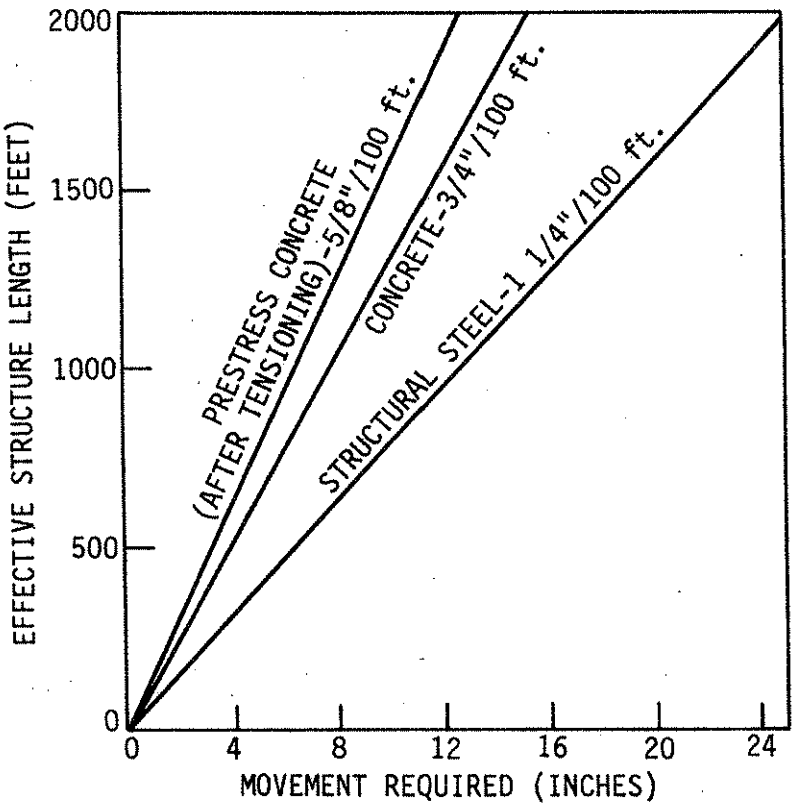


Fig. 2.1. Effective structure length versus movement required for cold climate conditions.

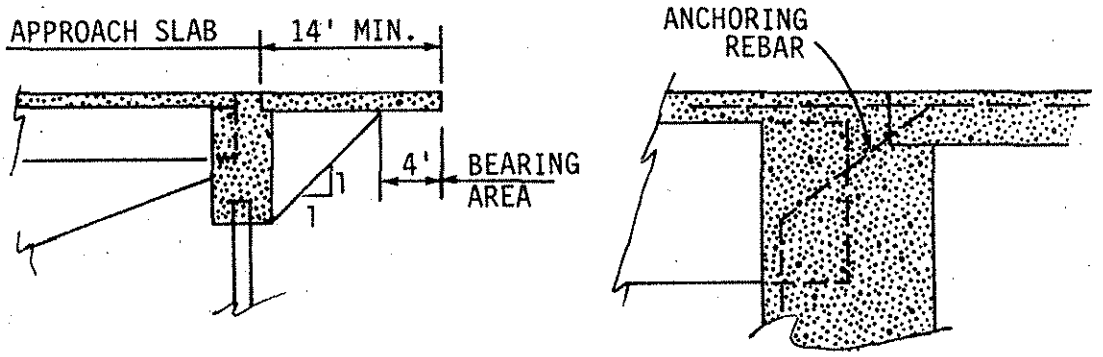


Fig. 2.2. Approach slab detail (FHWA).

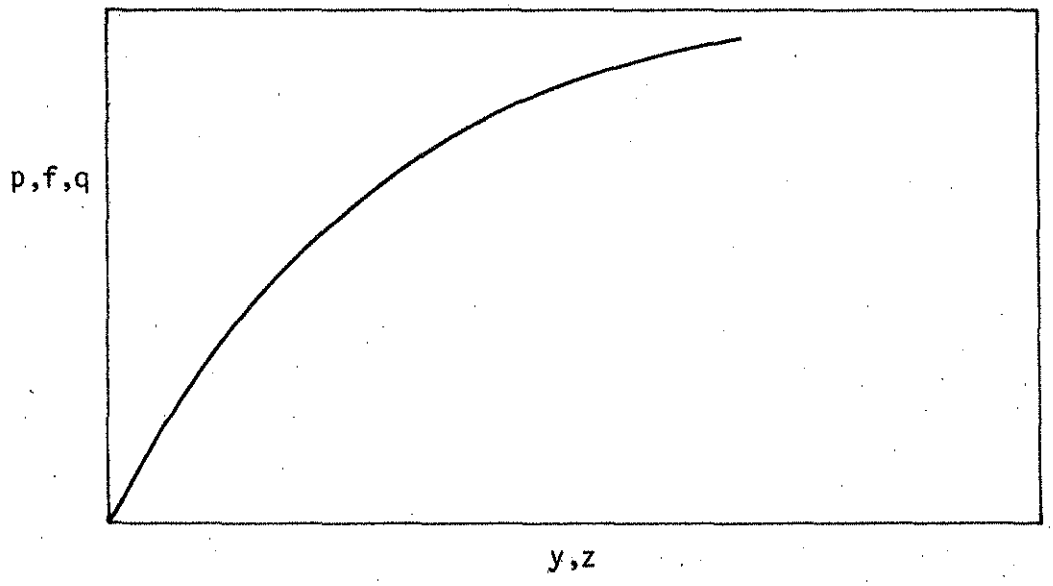


Fig. 3.1. Typical soil resistance-displacement curve.

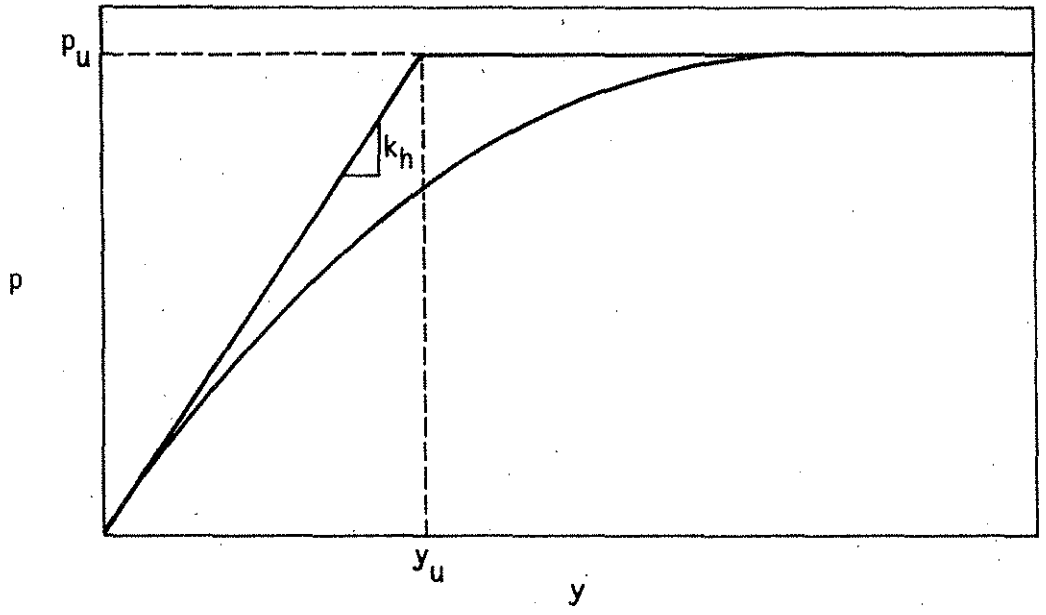


Fig. 3.2. Typical p-y curve with Ramberg-Osgood constants.

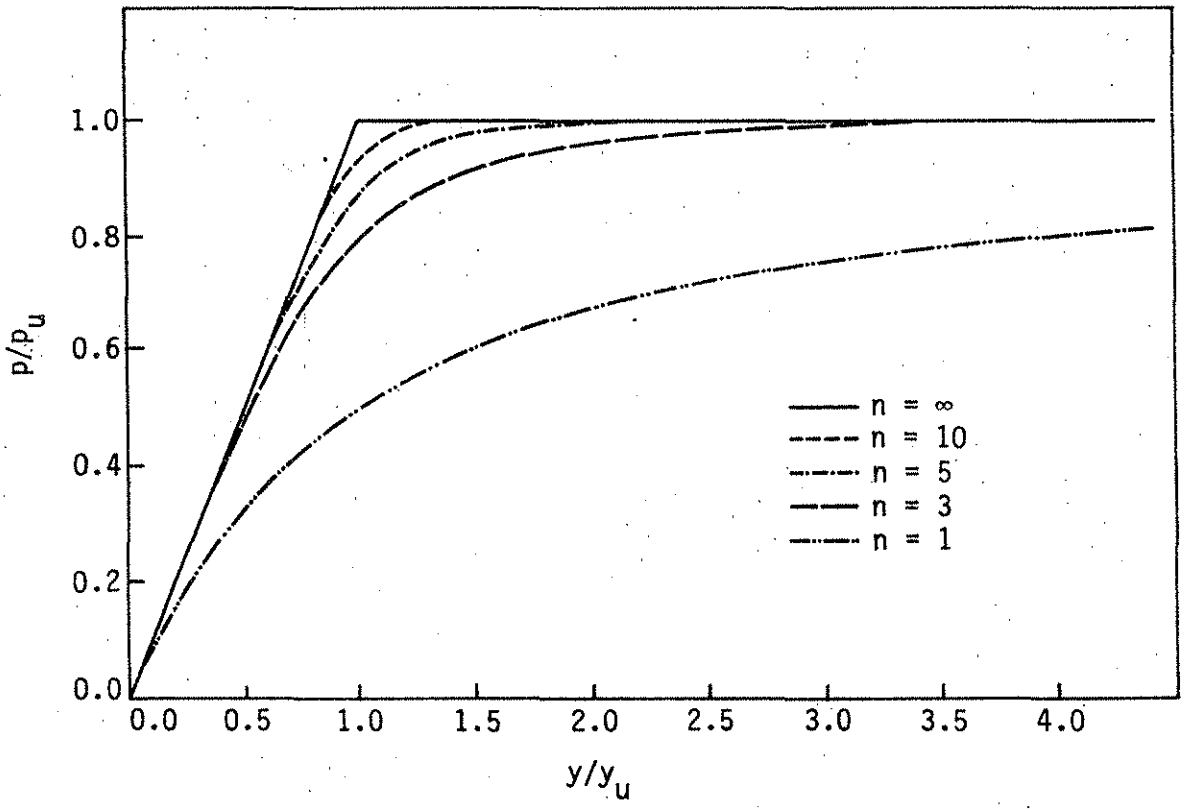


Fig. 3.3. Nondimensional form of the modified Ramberg-Osgood equation.

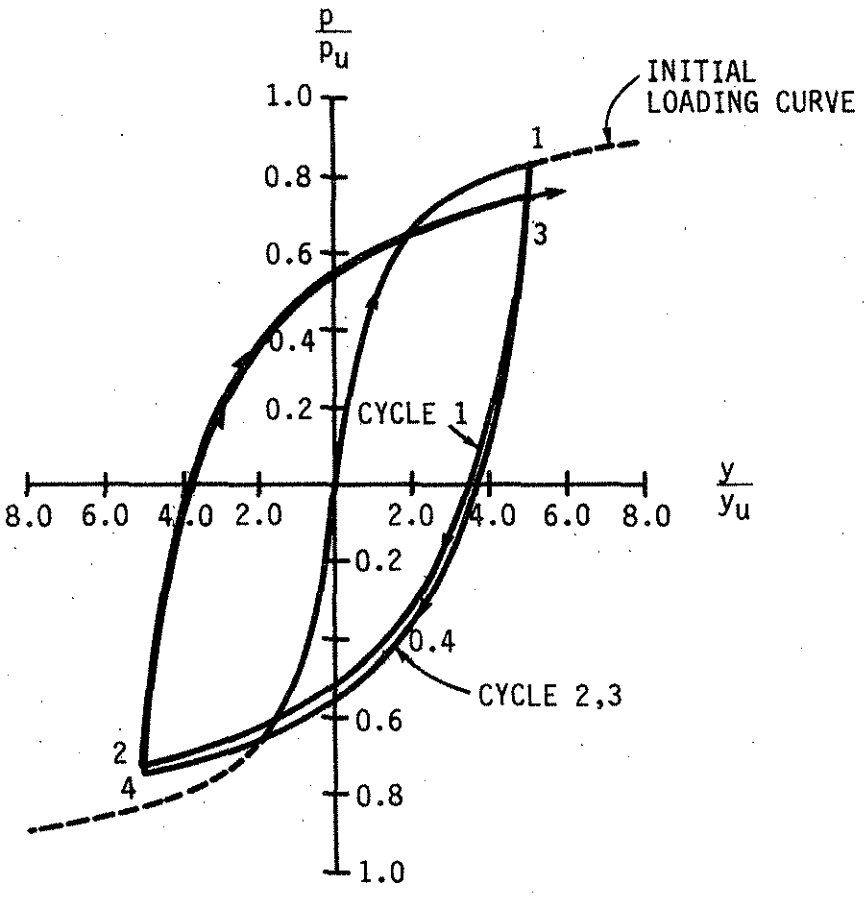


Fig. 3.4. Hysteresis loops in accordance with modified Ramberg-Osgood cyclic model with n = 1.0.

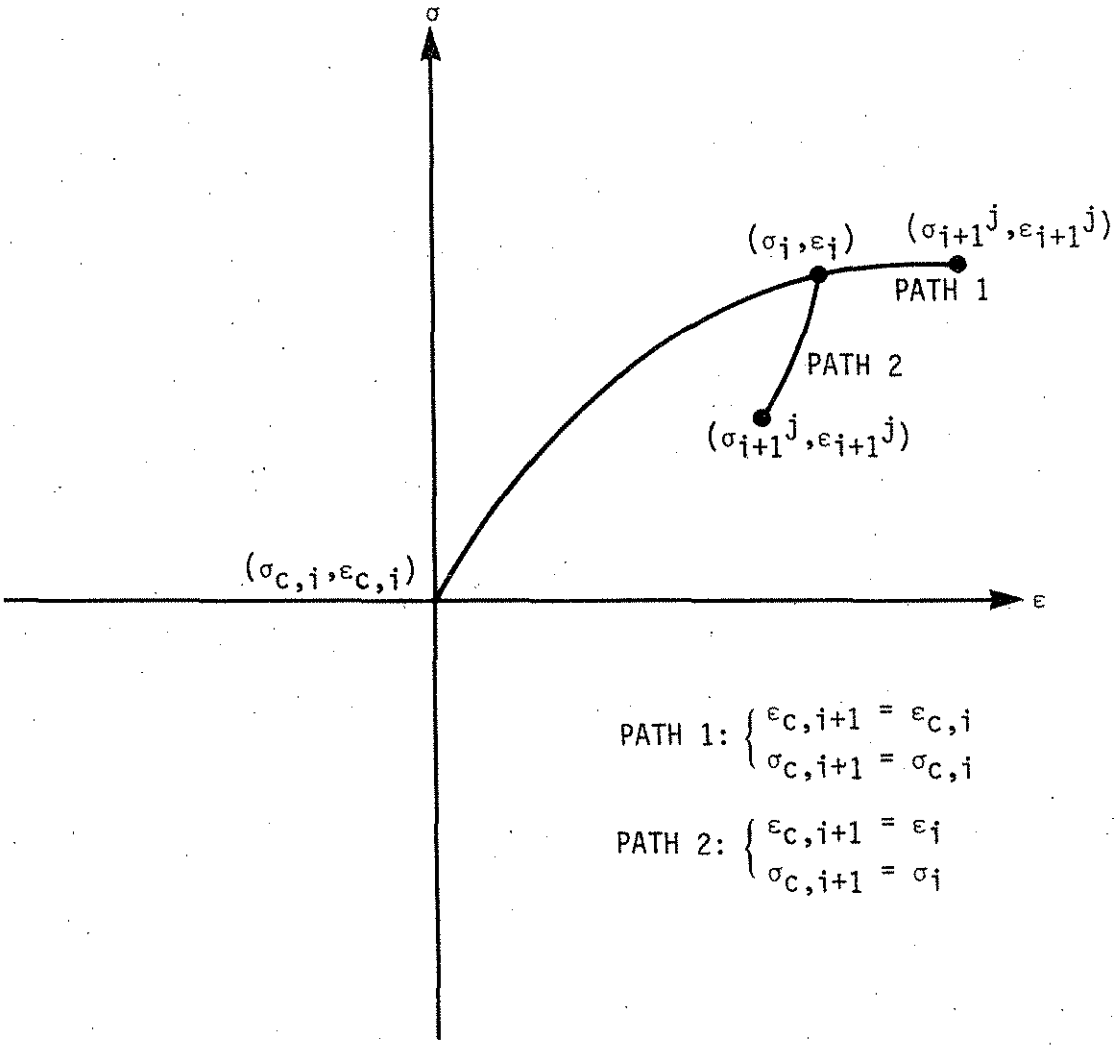


Fig. 3.5. The determination of reversal values for loading and unloading.

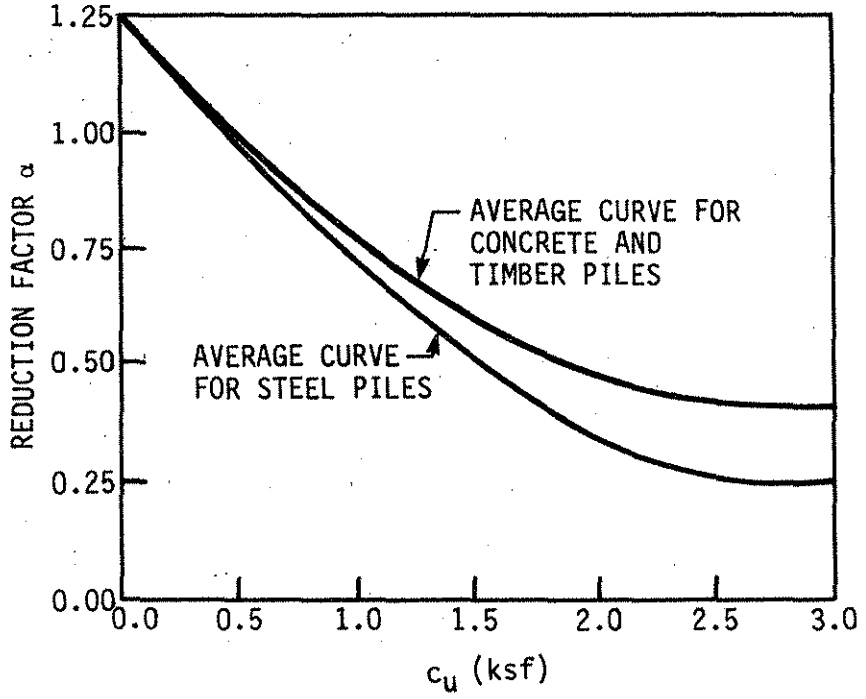


Figure 3.6. Reduction factor α [3.11].

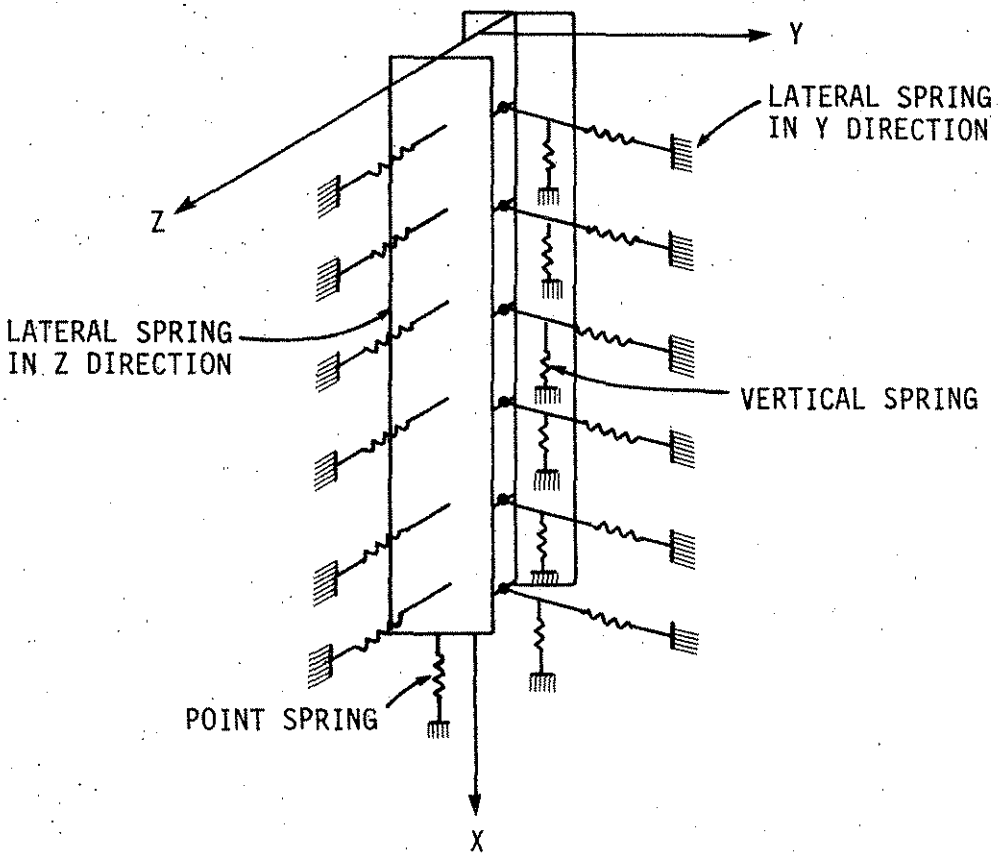


Fig. 4.1. A combination of a one-dimensional idealization for the piles and an equivalent nonlinear spring idealization for the soil.

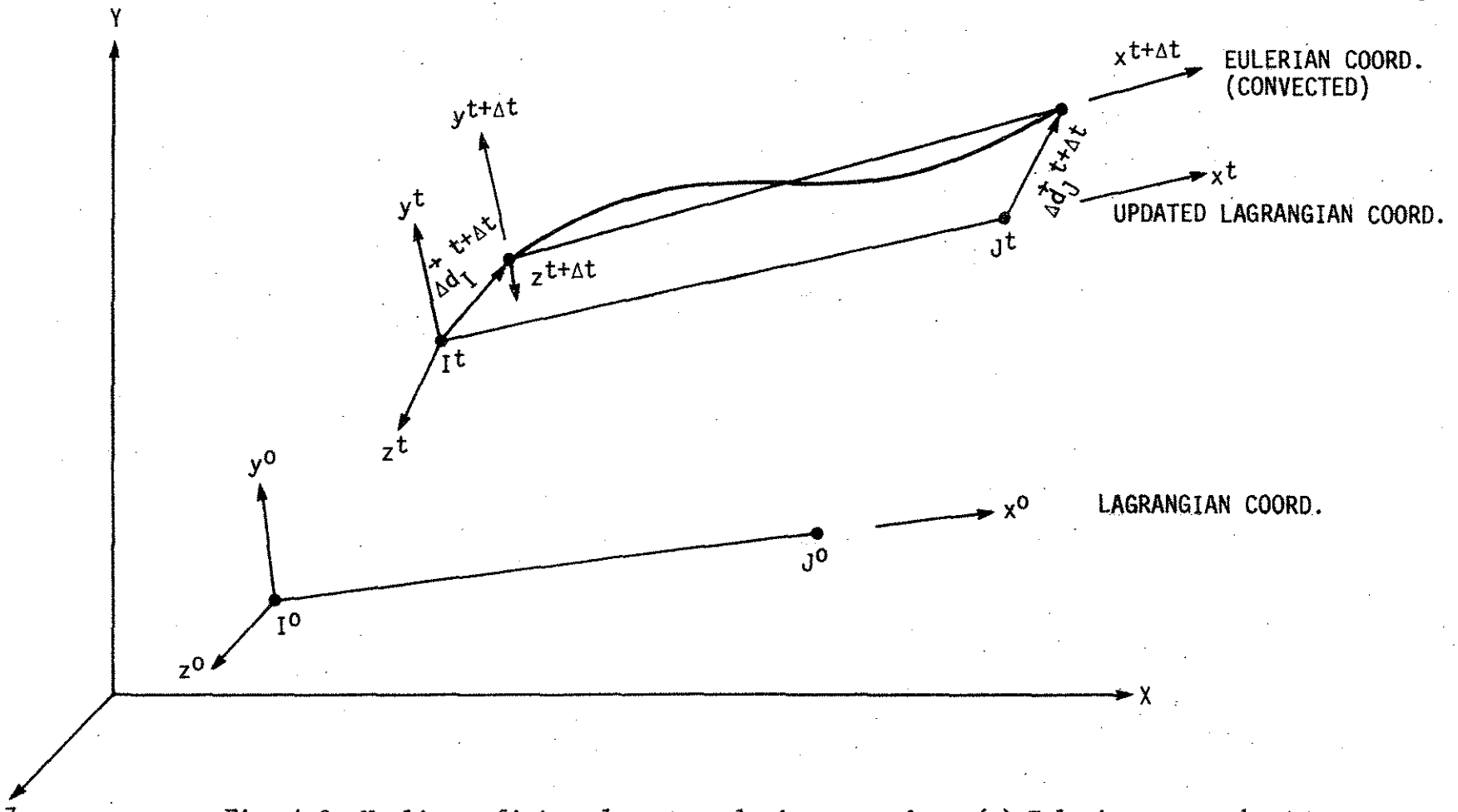


Fig. 4.2. Nonlinear finite element analysis approaches: (a) Eulerian approach, (b) Lagrangian approach, (c) updated Lagrangian approach.

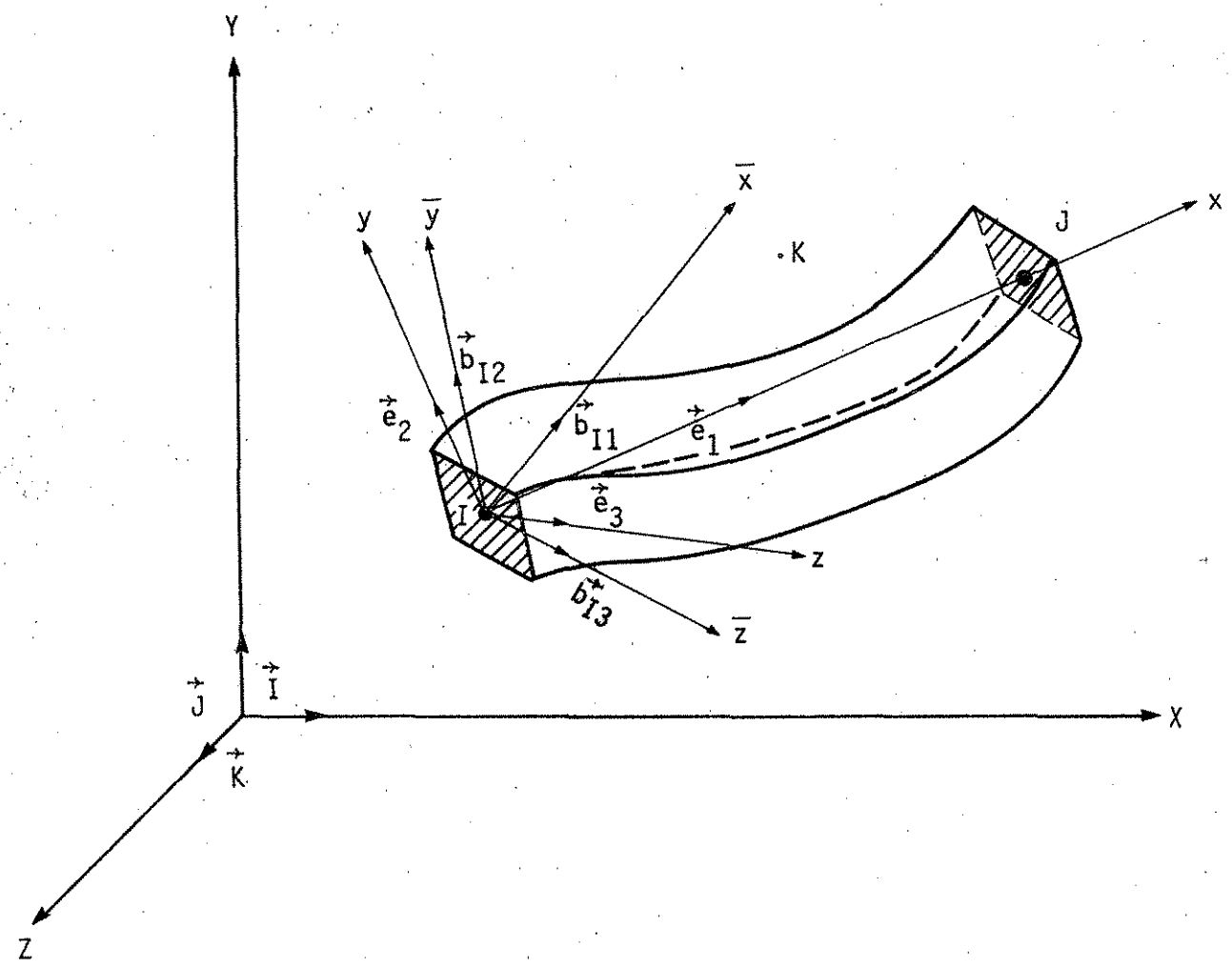


Fig. 4.3. Coordinate systems and nomenclature.

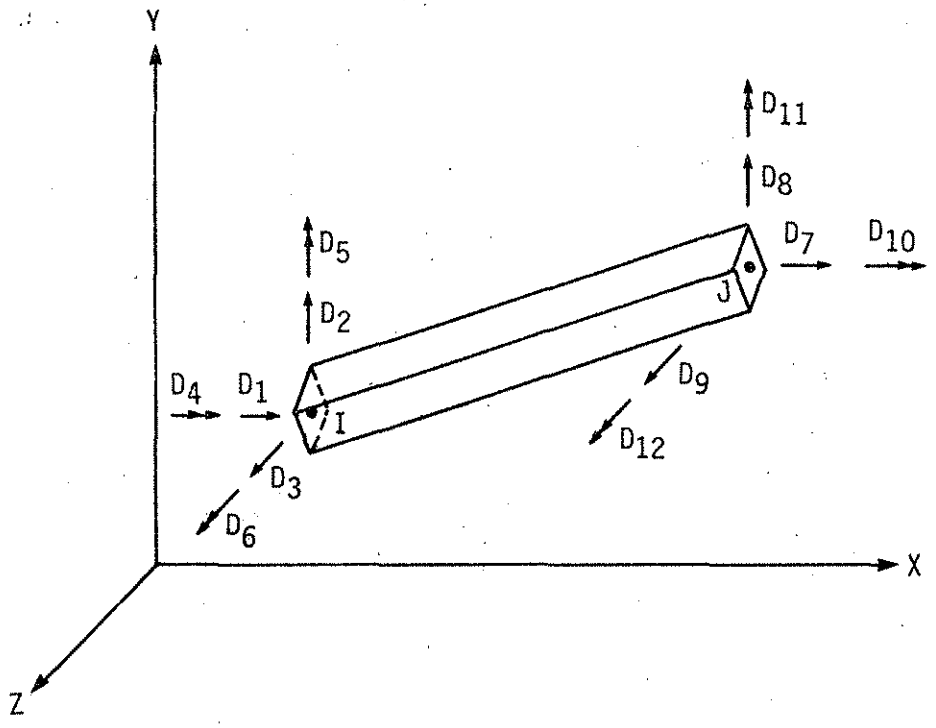


Fig. 4.4.(a). Three-dimensional beam-column element, global degrees of freedom.

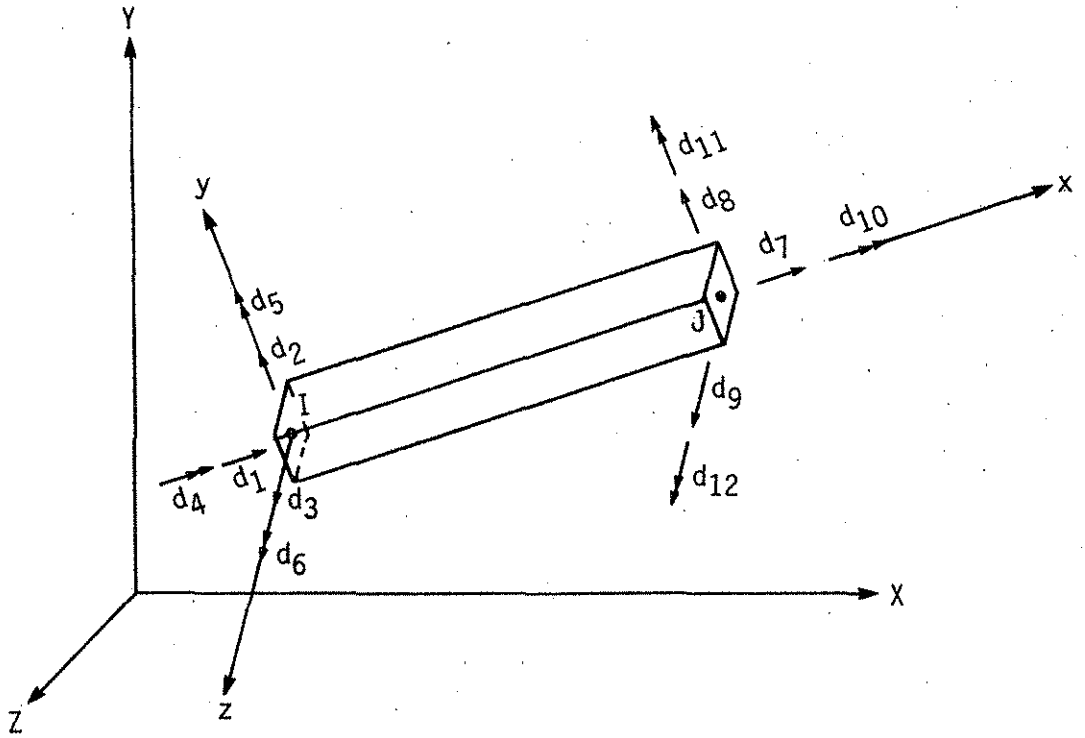


Fig. 4.4.(b). Three-dimensional beam-column element, element (local) degrees of freedom.

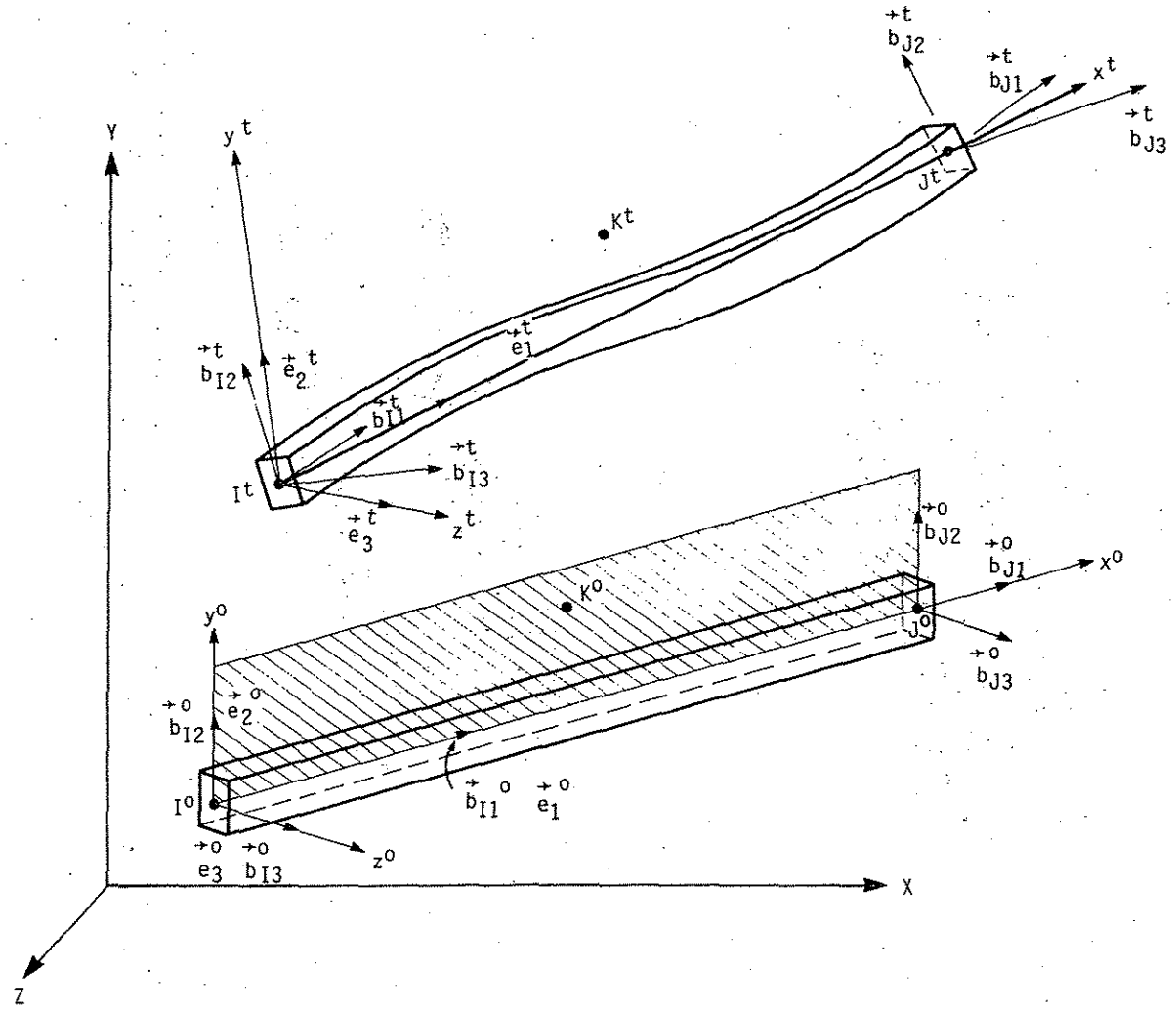


Fig. 4.5. Three-dimensional beam-column element before and after being deformed.

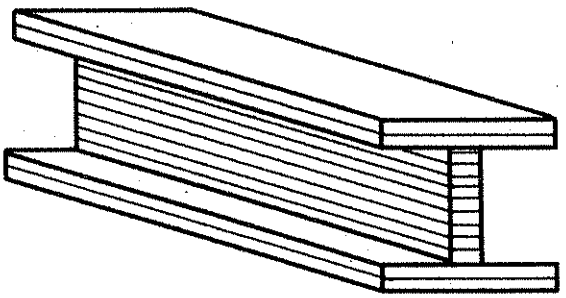

(a)

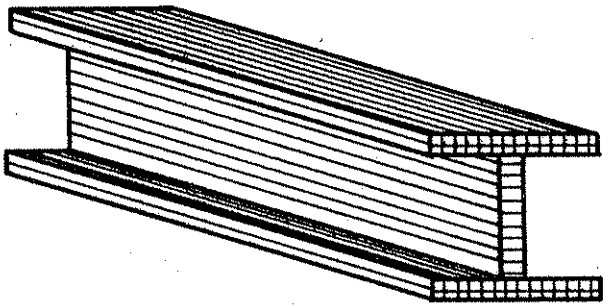

(b)

Fig. 4.6 (a). Element layering for two-dimensional analysis.
(b). Element layering for three-dimensional analysis.

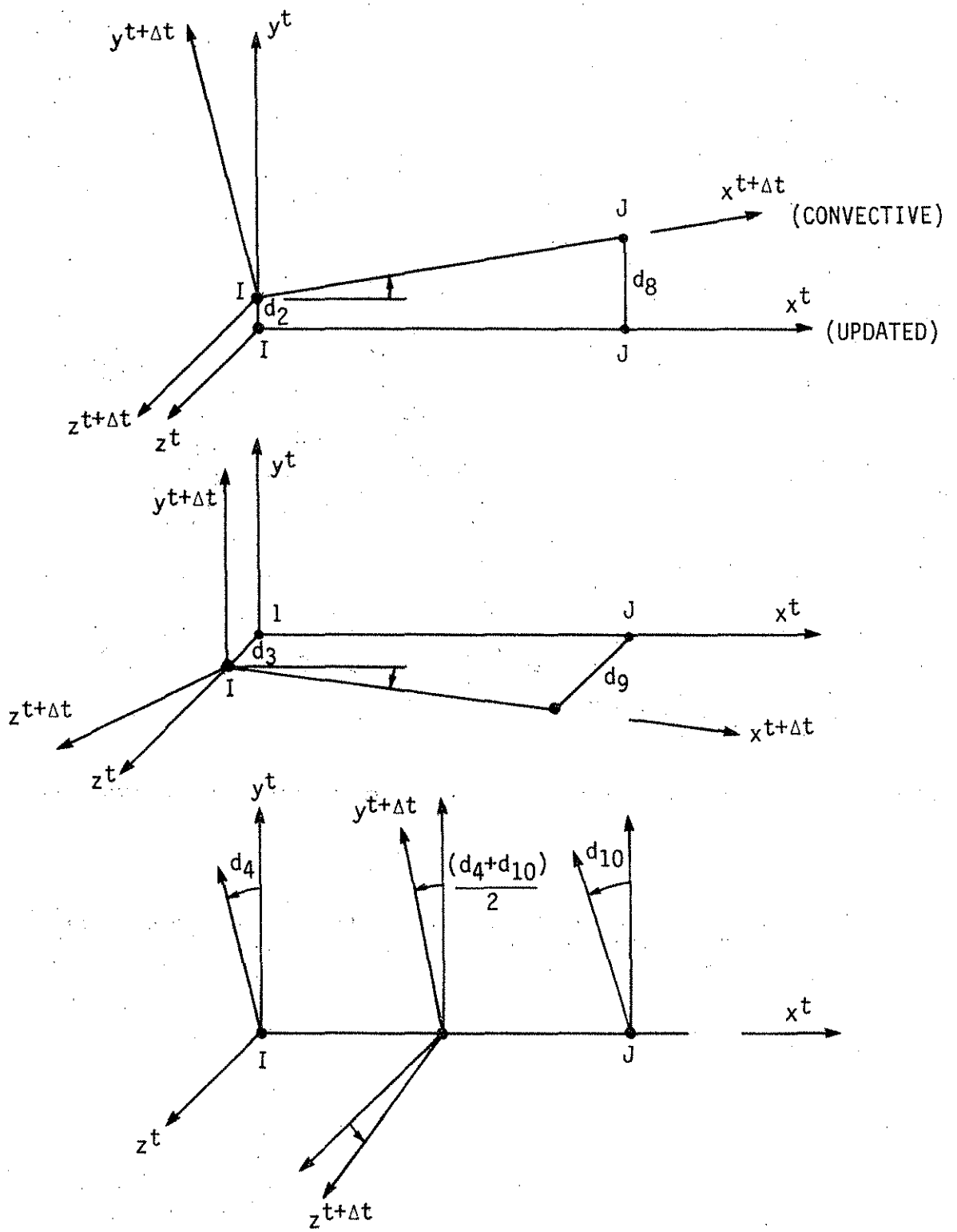


Fig. 4.7. The rate of change of the transformation matrix with respect to the nodal displacements {d}.

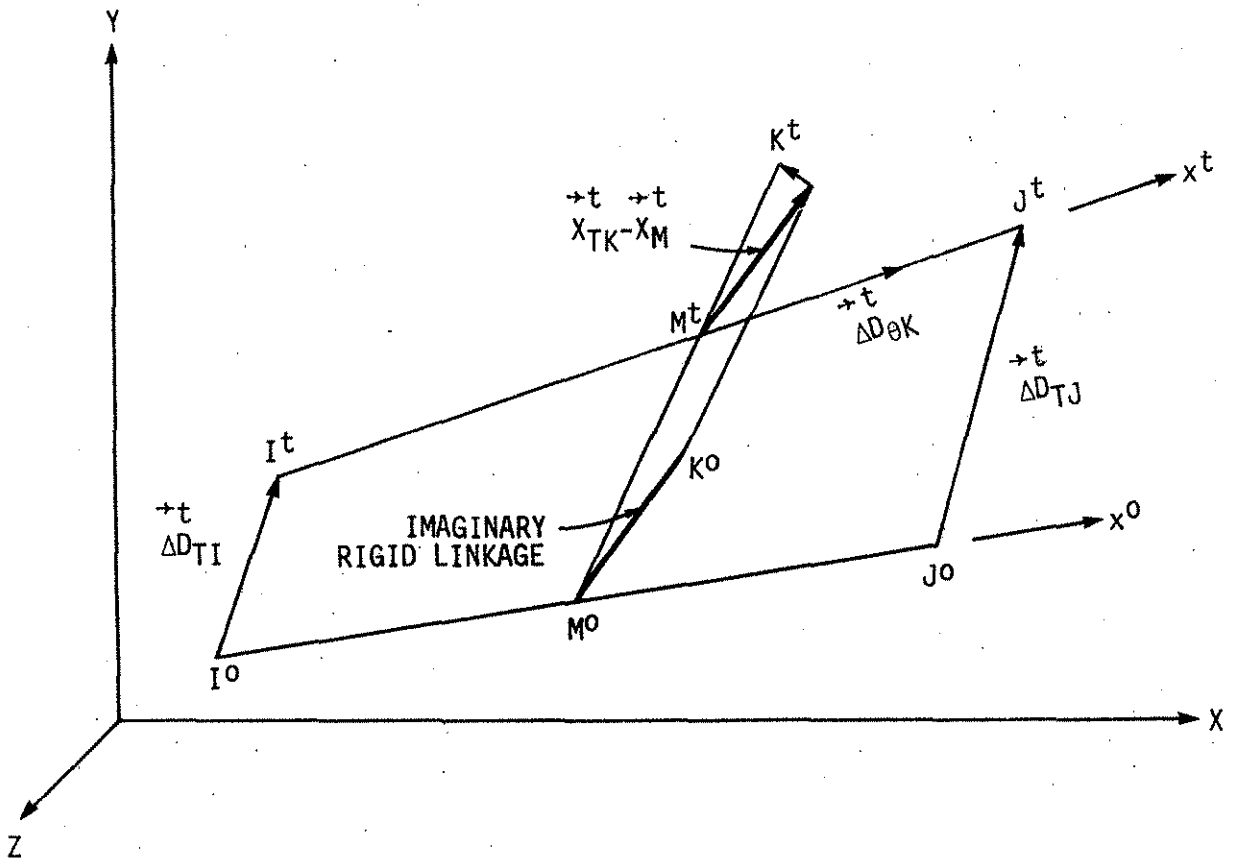


Fig. 4.8. The coordinate updating of K node in three-dimensional beam-column element.

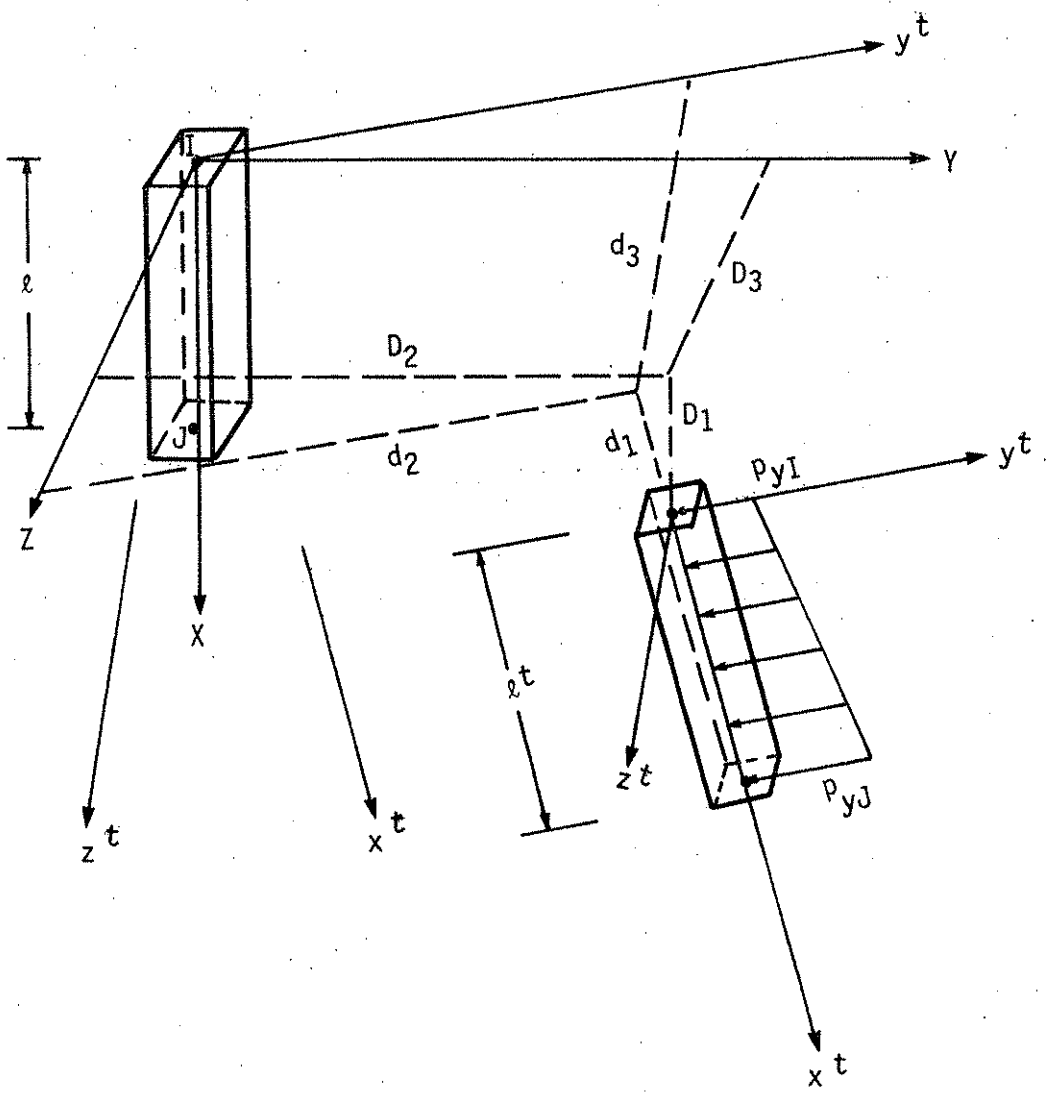


Fig. 4.9. External and internal forces and displacements acting on the pile element.

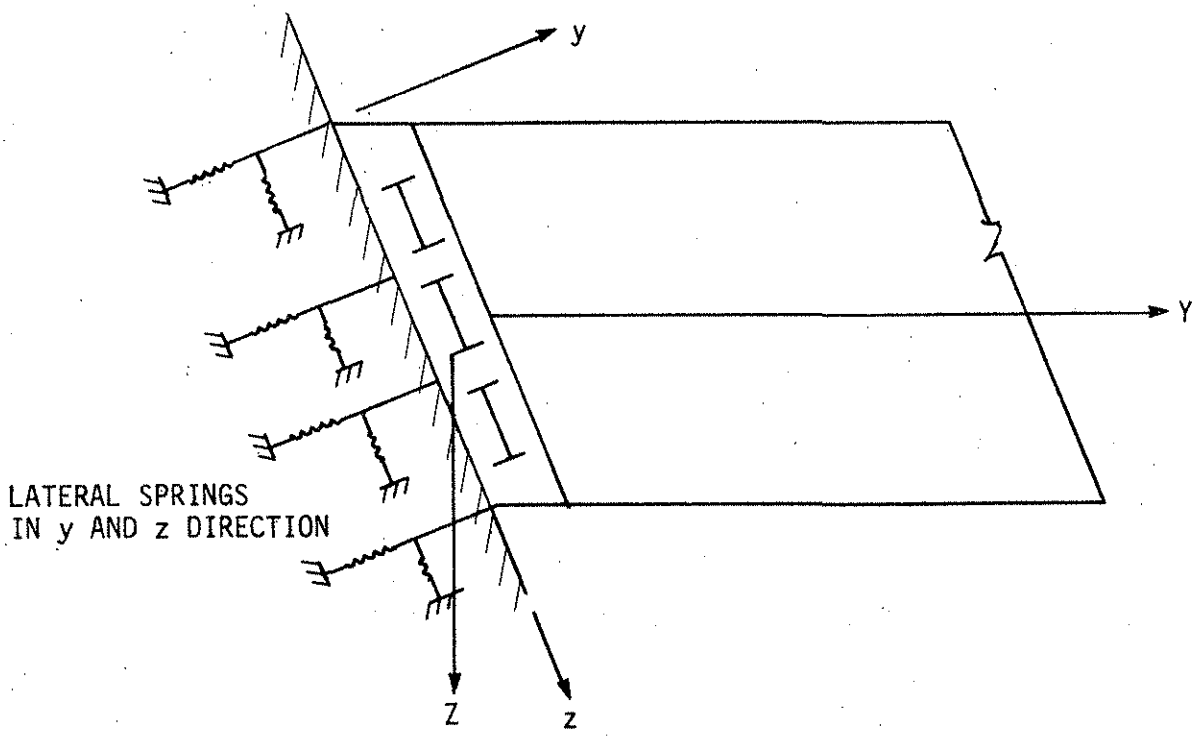


(a)

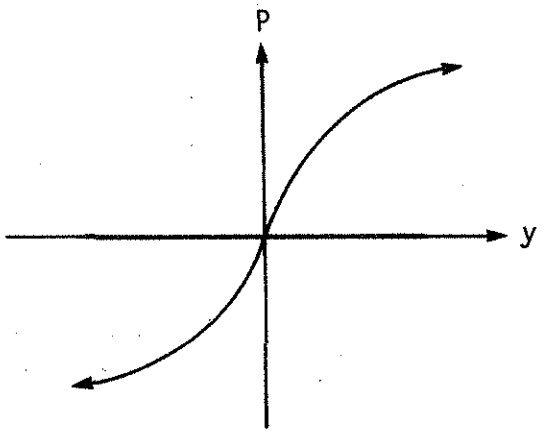


(b)

Fig. 4.10 (a). Idealized backwall soil model in integral bridge abutments.
(b). p-y curve for backwall soil model in element y direction.

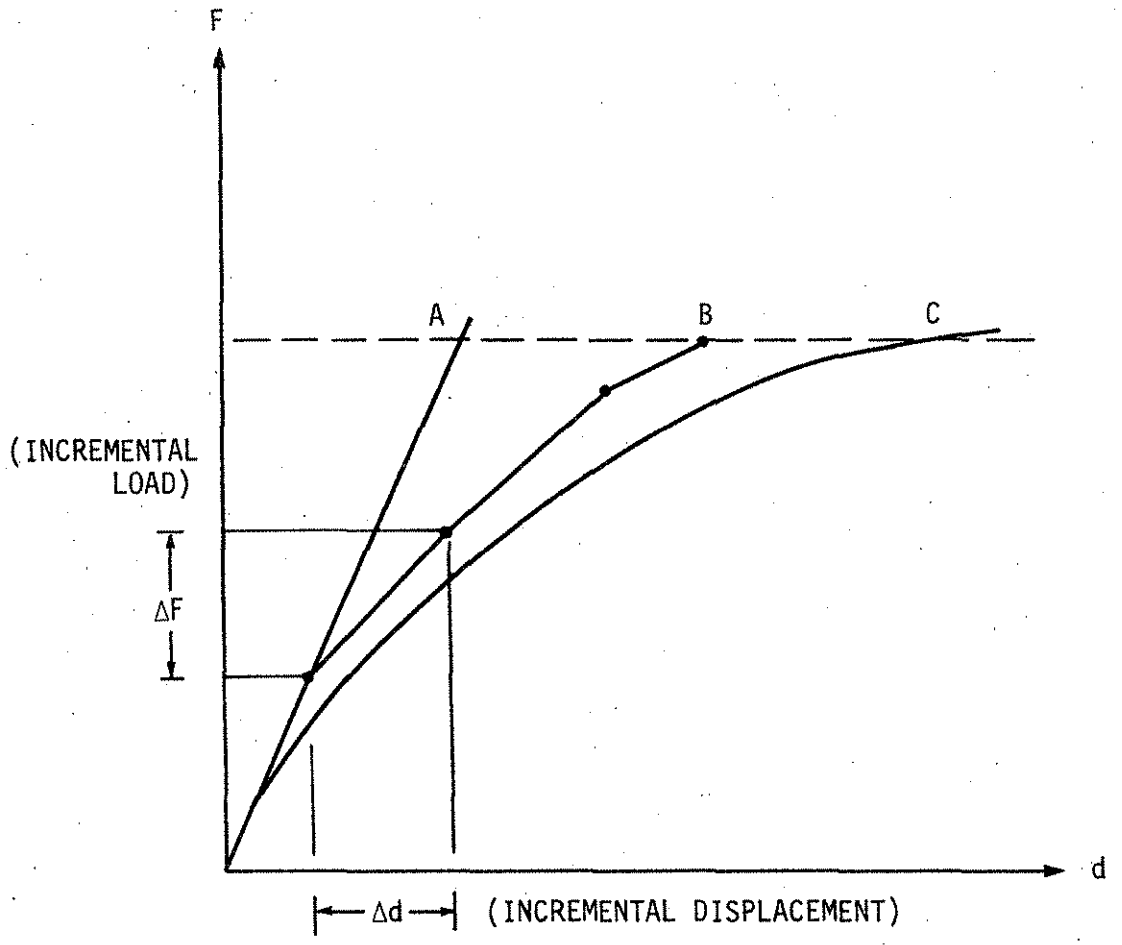


Fig. 4.11. Piecewise linear solution for a single degree-of-freedom system.

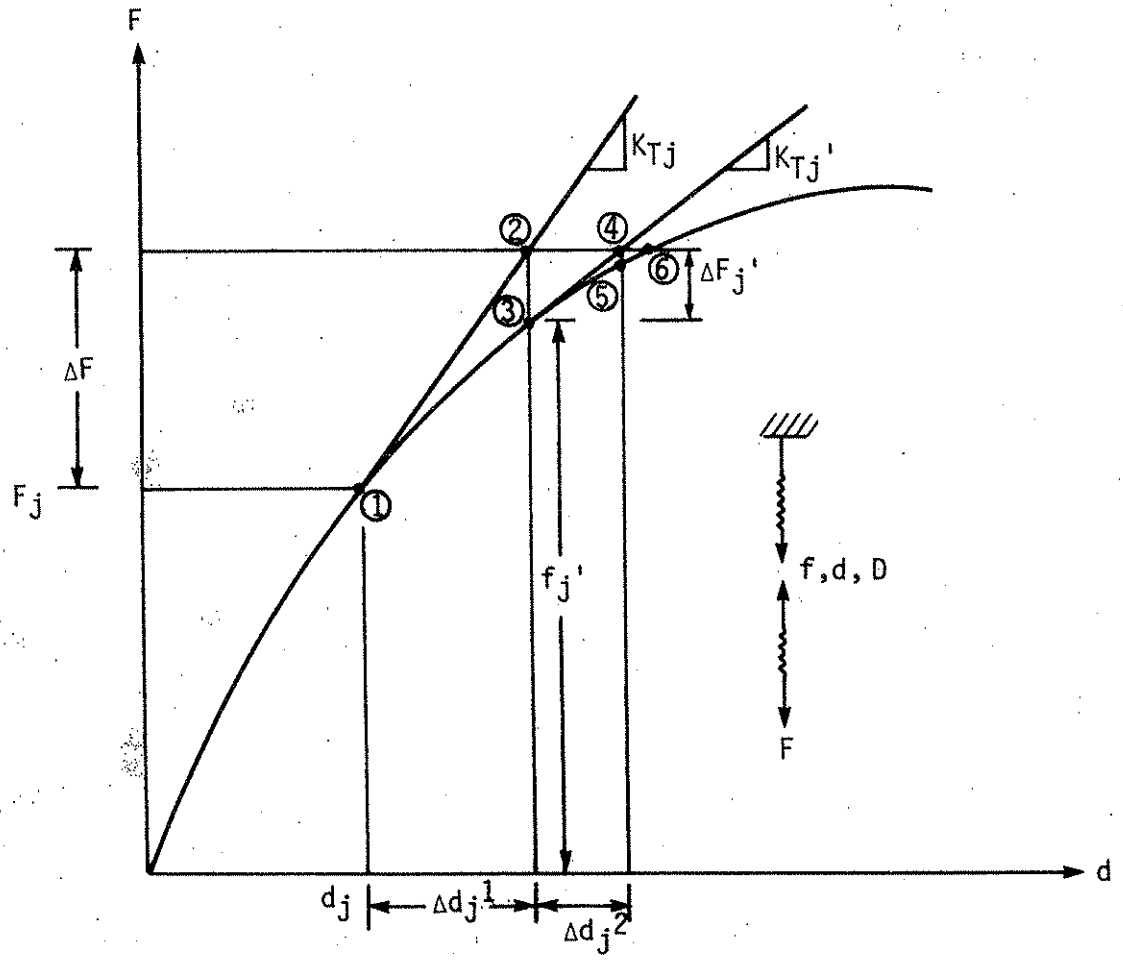


Fig. 4.12. Characteristics of Newton-Raphson iteration in a simple one-degree-of-freedom.

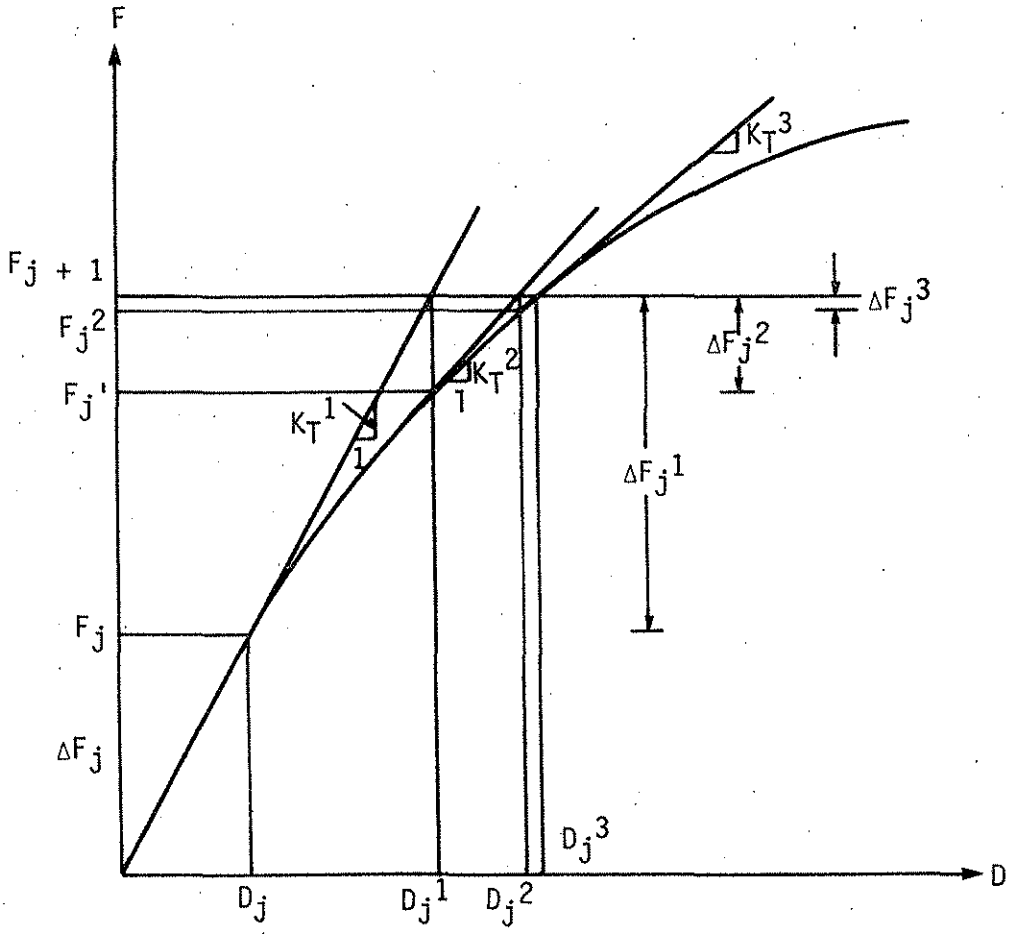


Fig. 4.13. Increment-iteration or mixed procedure in a multi-degree-of-freedom structure (Newton-Raphson solution of the equation F = f(D)).

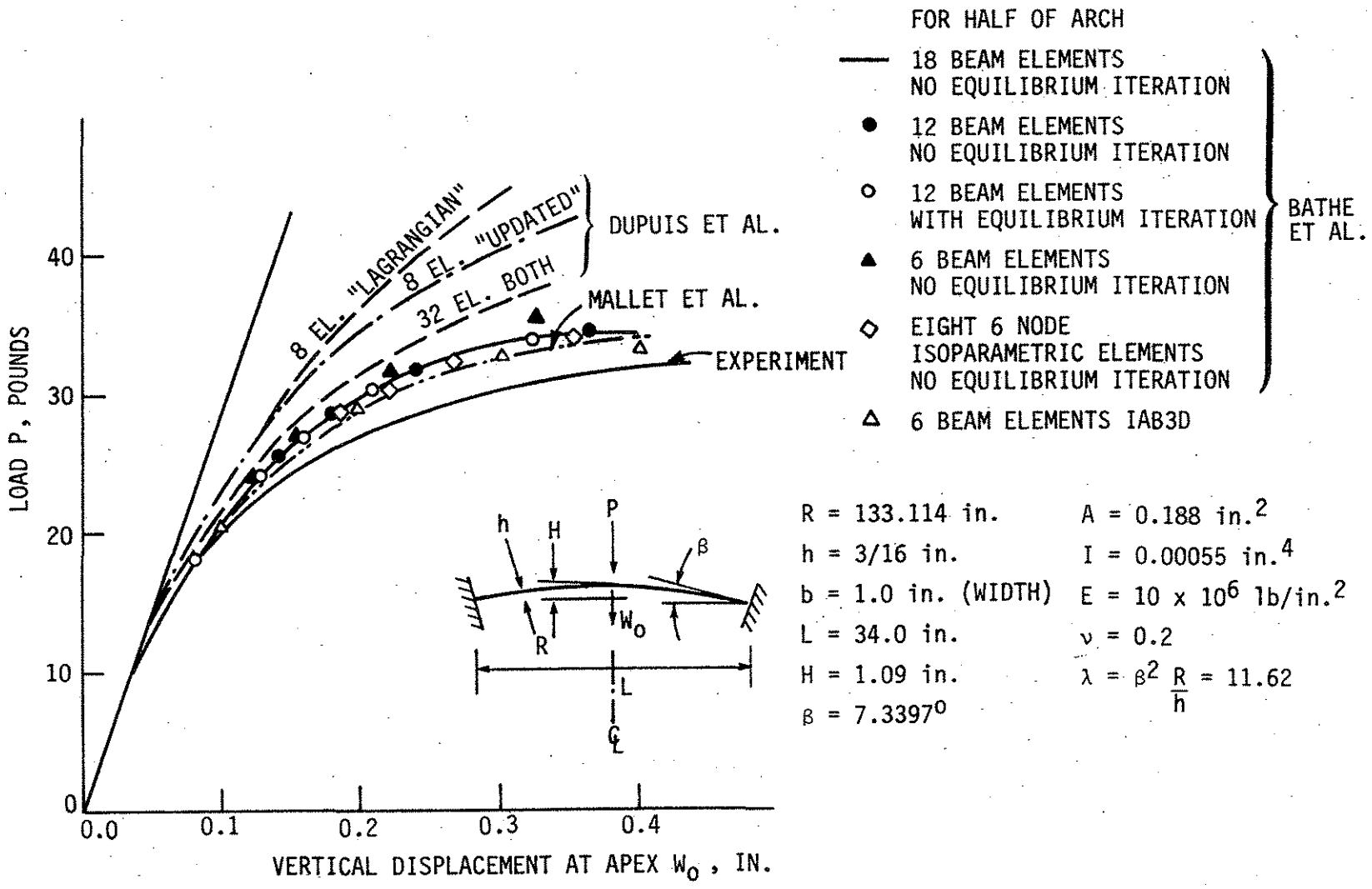


Fig. 4.14. Large deflection analysis of shallow arch under concentrated load.

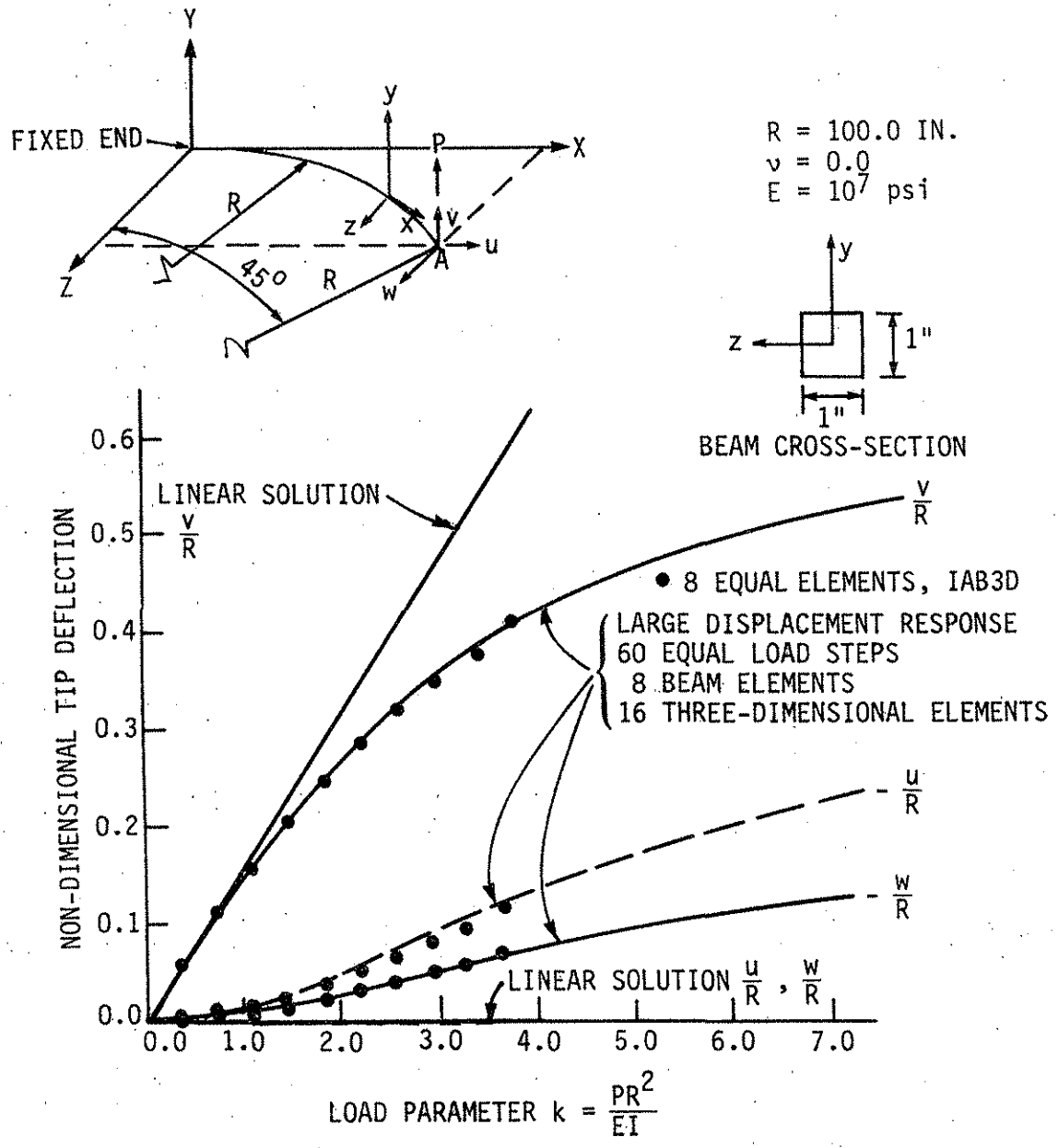


Fig. 4.15. Three-dimensional large deflection analysis of a 45° circular bend.

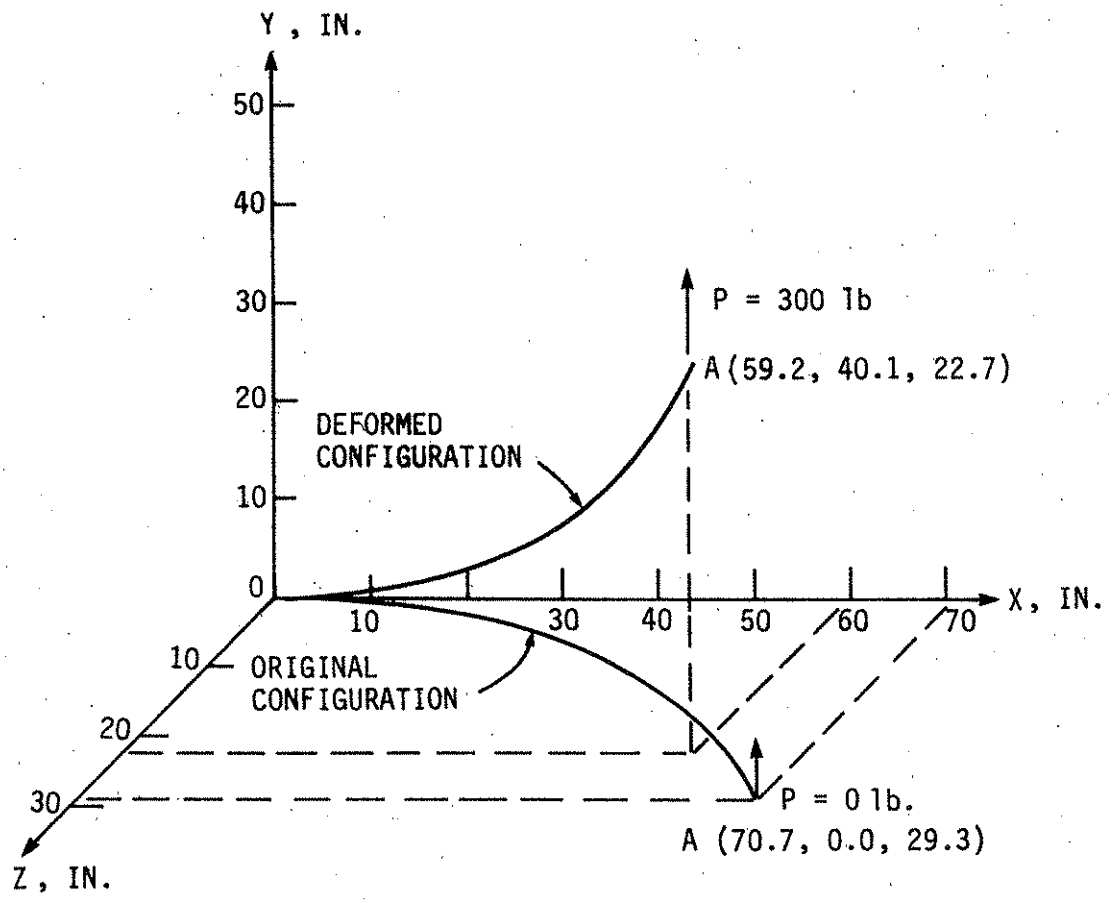


Fig. 4.16. Deformed configuration of a 45° circular bend.

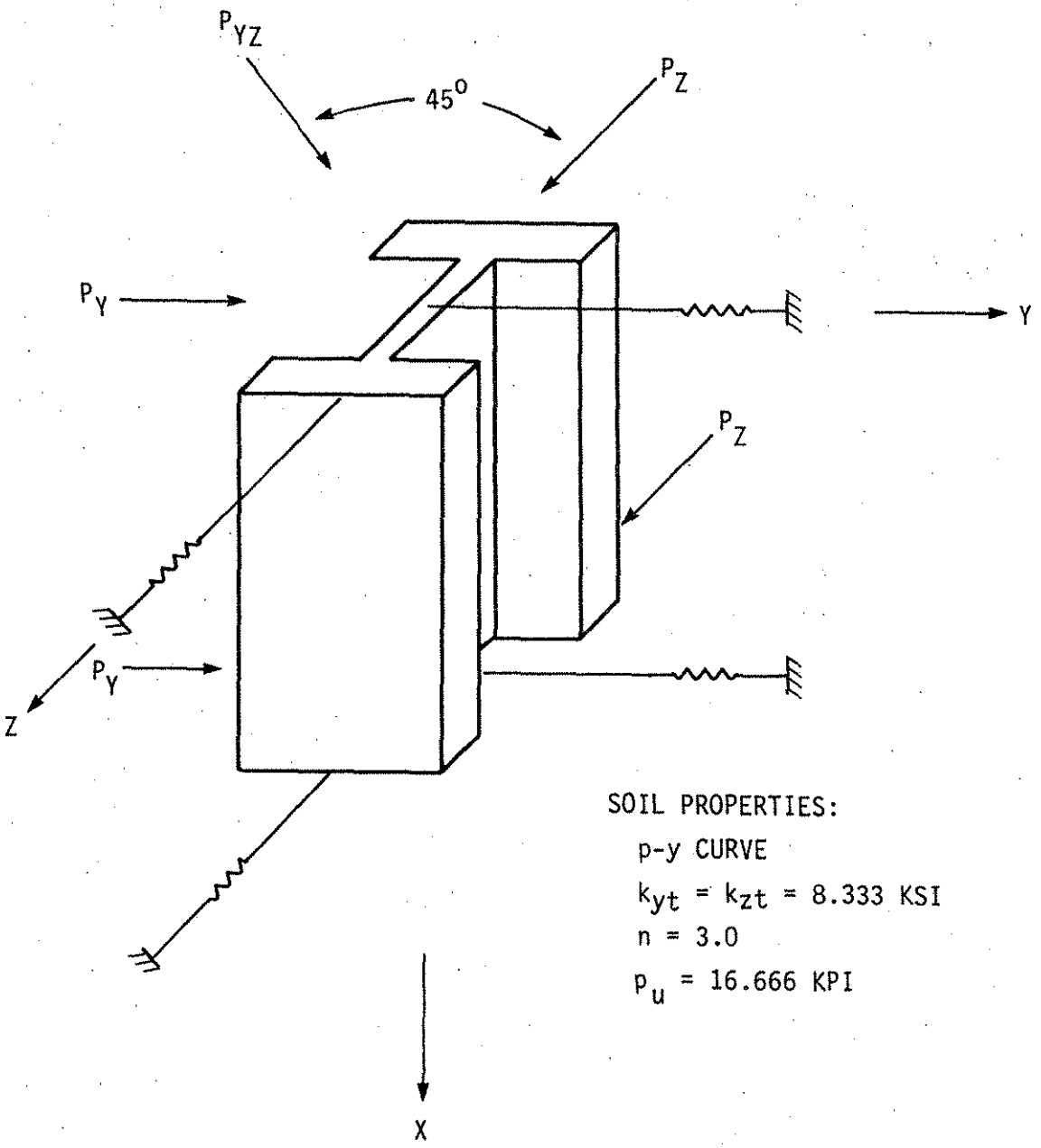


Fig. 4.17. HP14x73 pile used to check soil response.

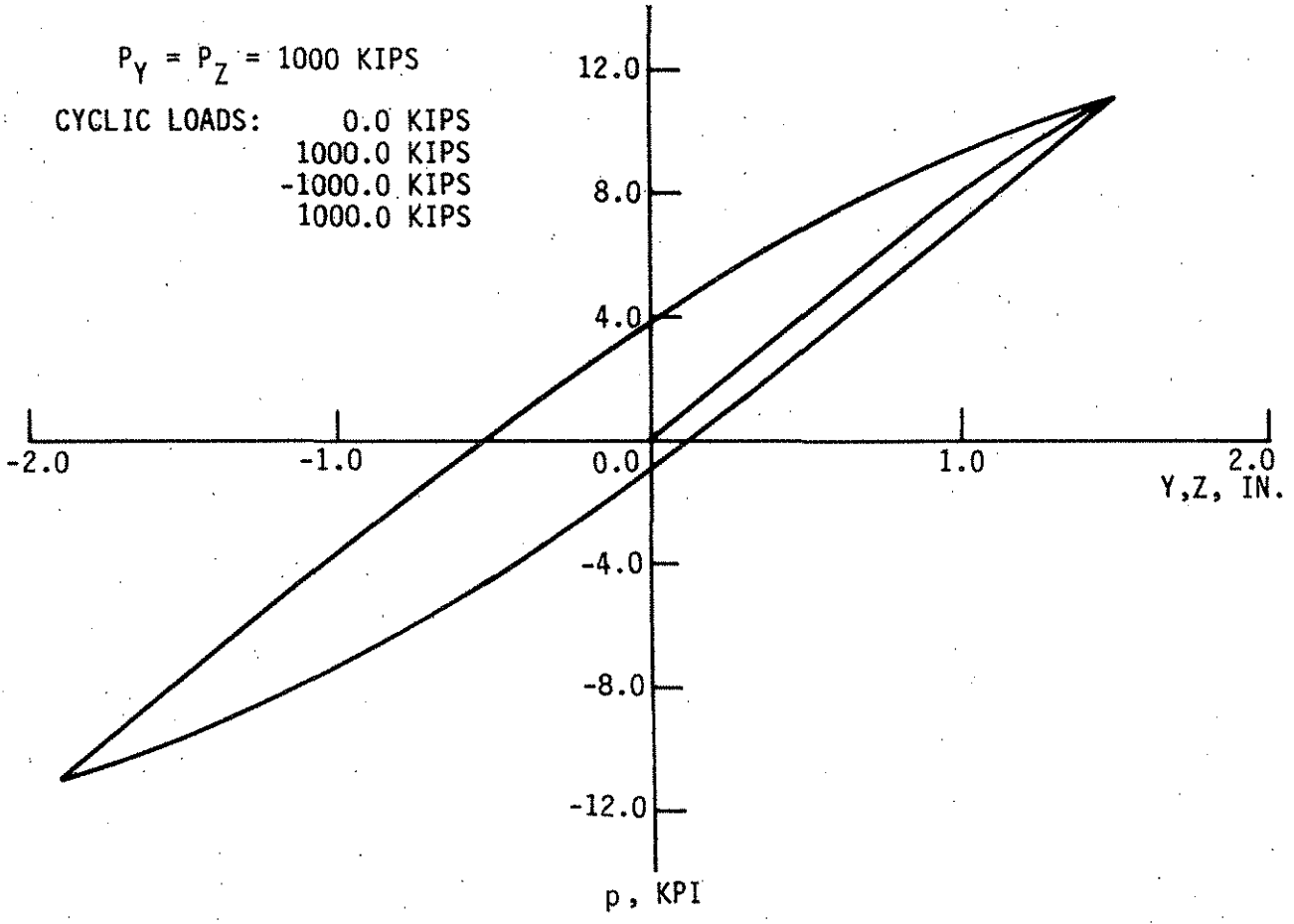


Fig. 4.18. Soil response for cyclic loads in Y, Z directions.

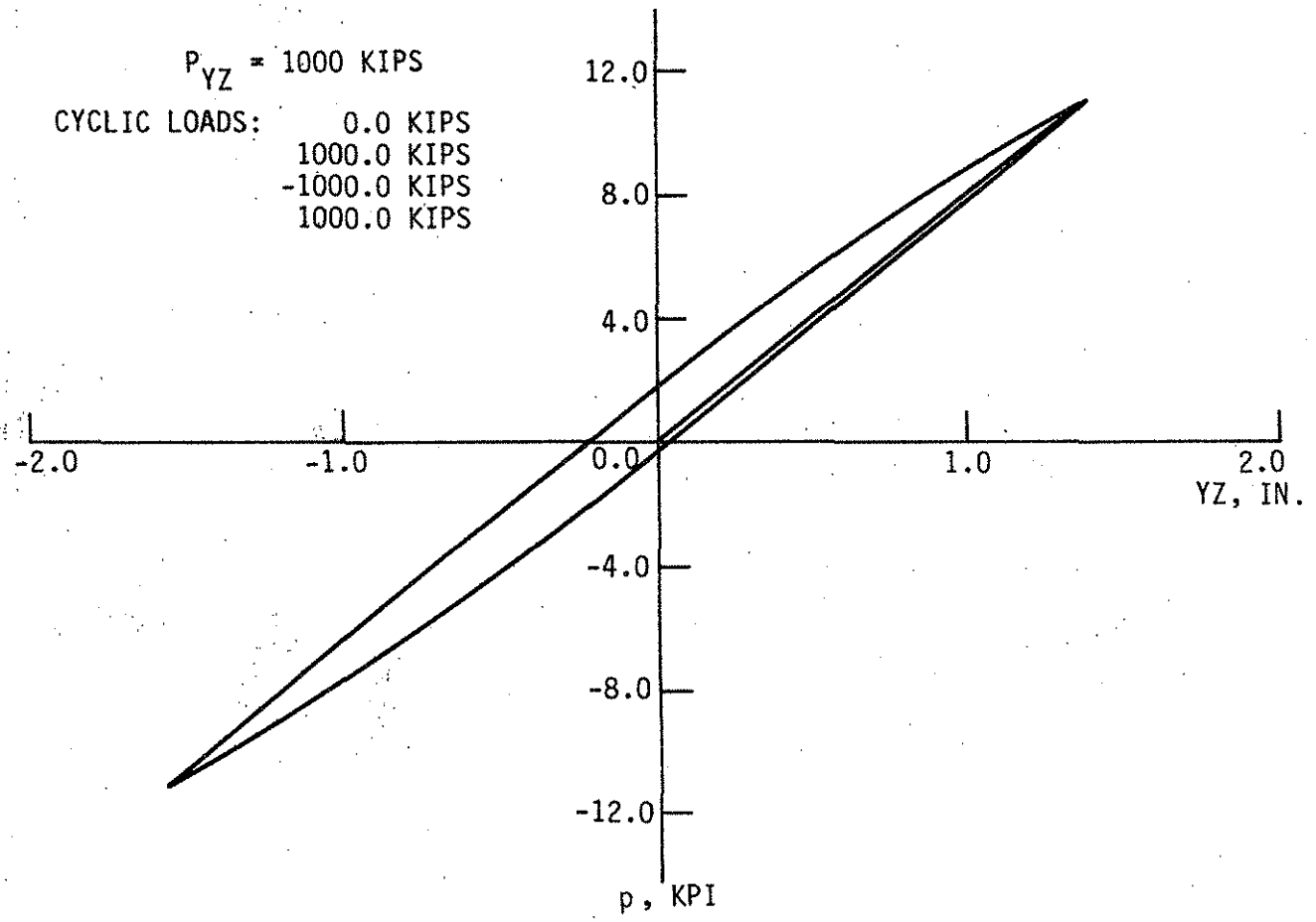


Fig. 4.19. Soil response for cyclic loads in YZ direction.

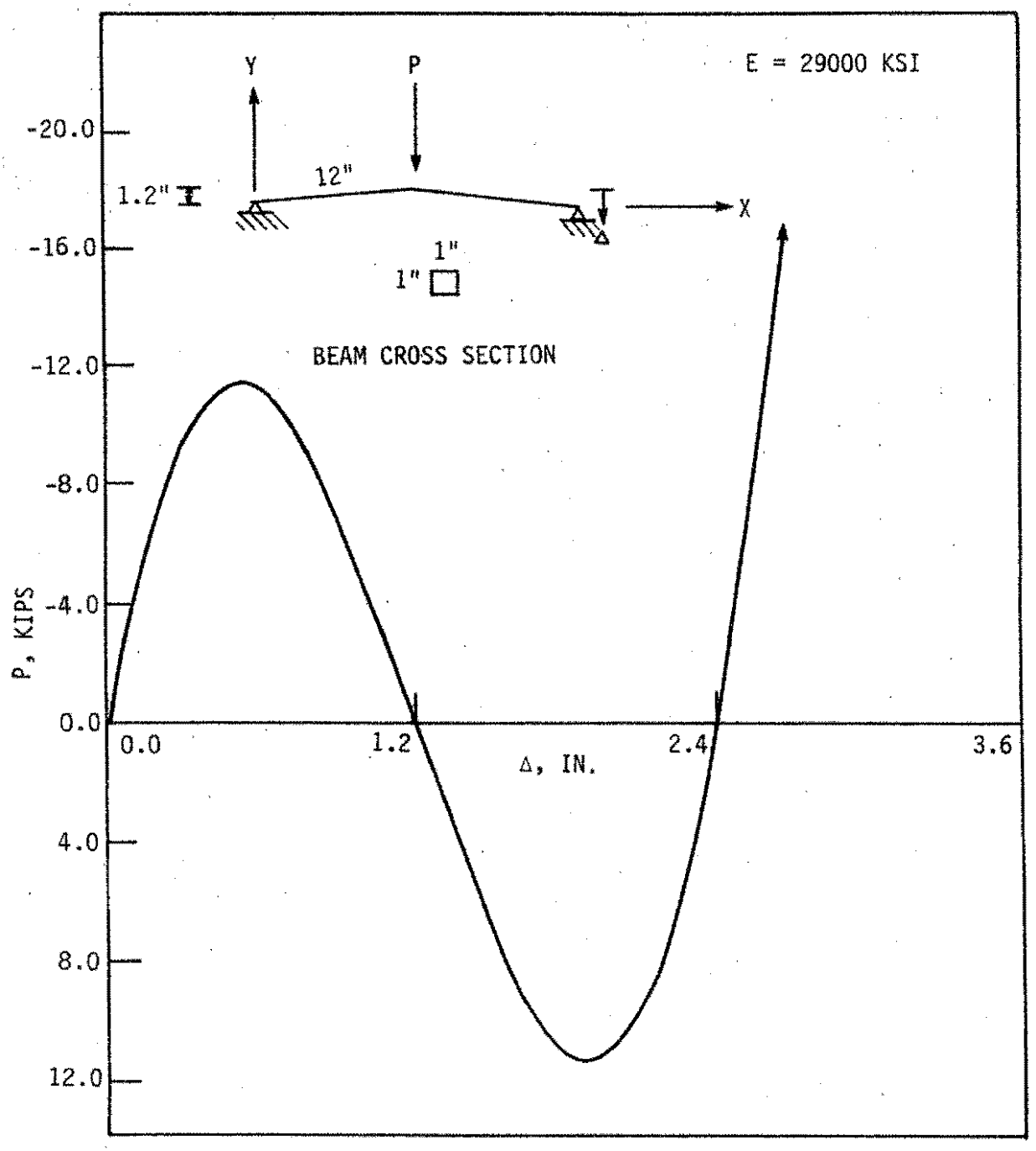


Fig. 4.20. Load-deflection characteristics of snap-through problem.

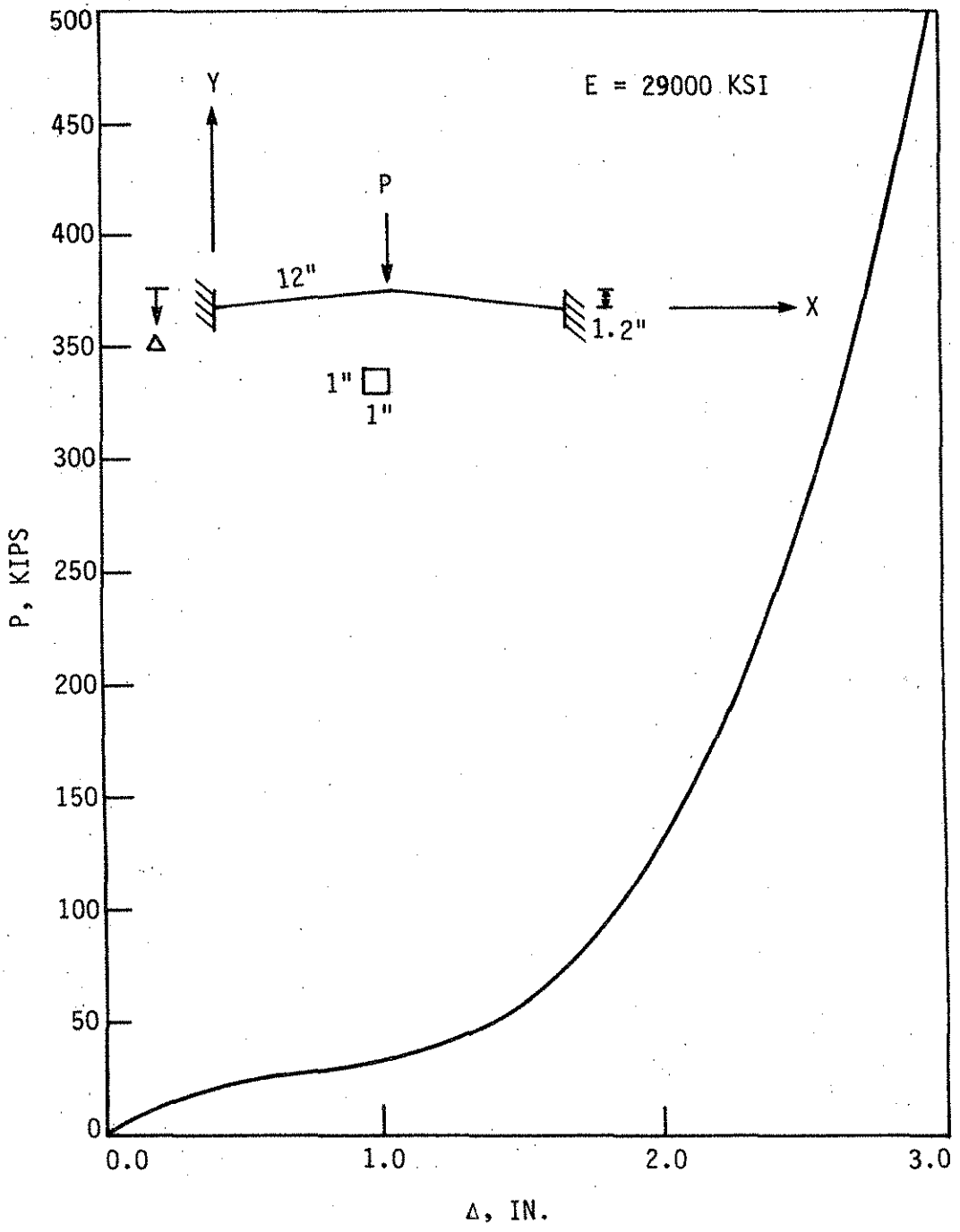


Fig. 4.21. Load-deflection characteristics of toggle.

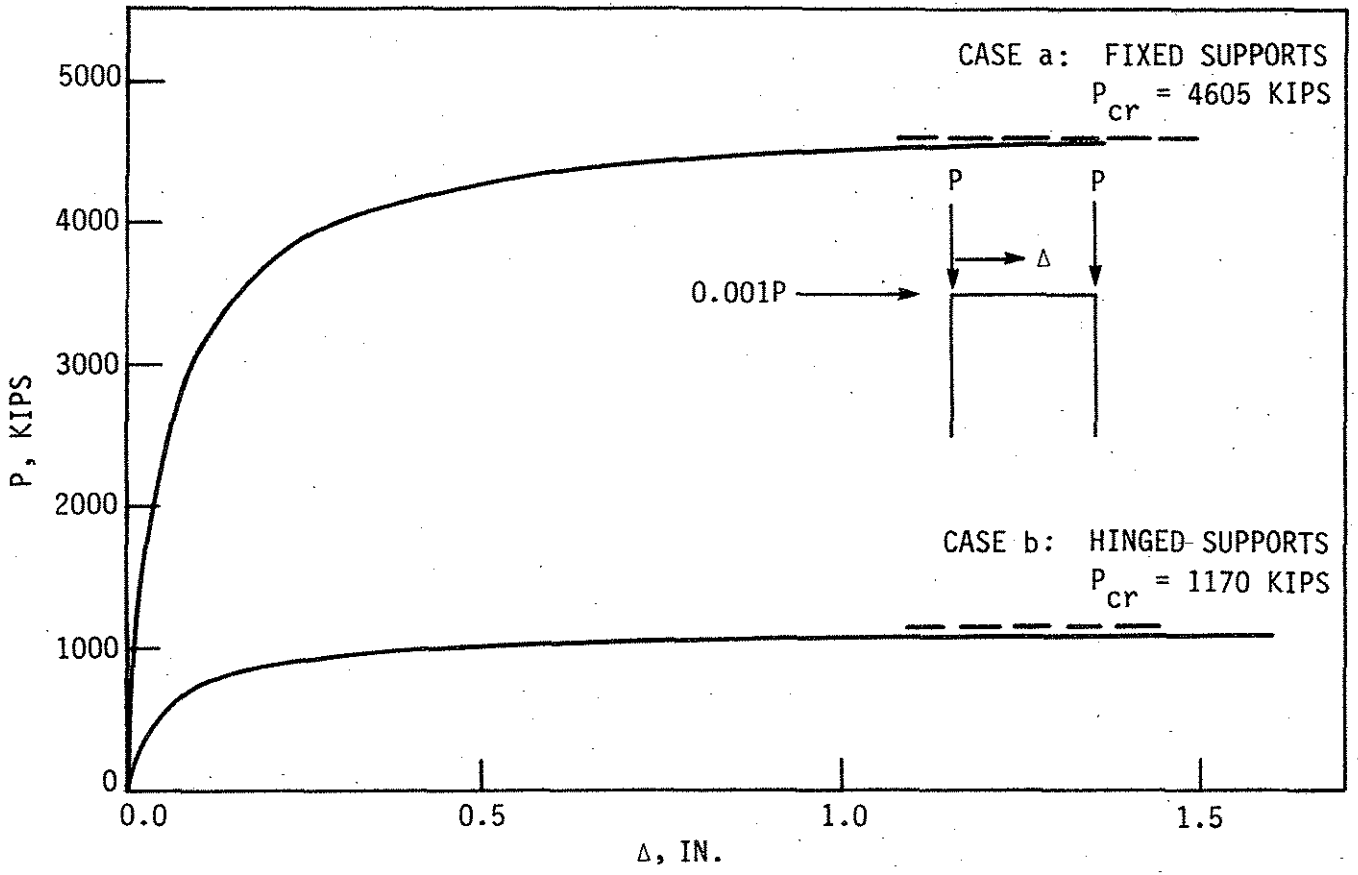


Fig. 4.22. Load-deflection characteristics of two-dimensional portal frame with fixed base and hinged base.

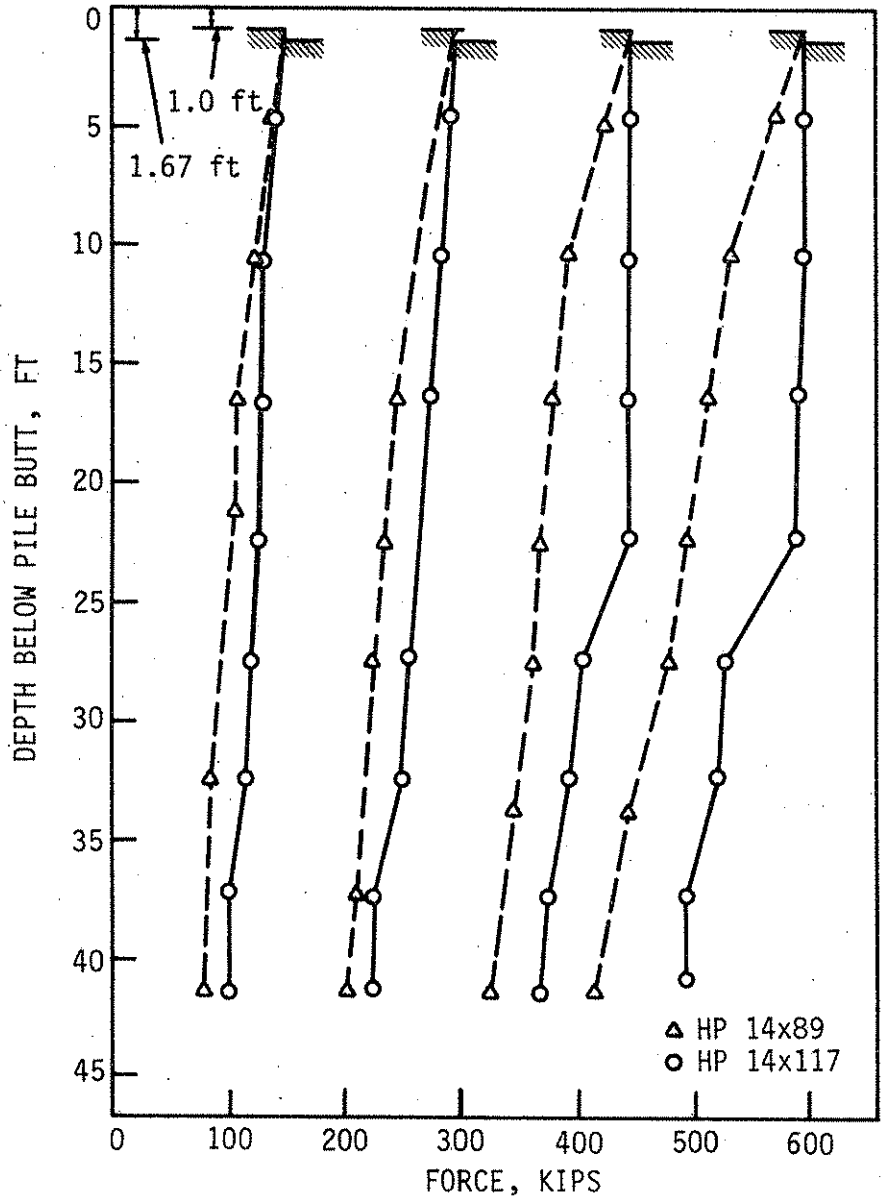


Fig. 4.23. Force in pile as a function of depth.

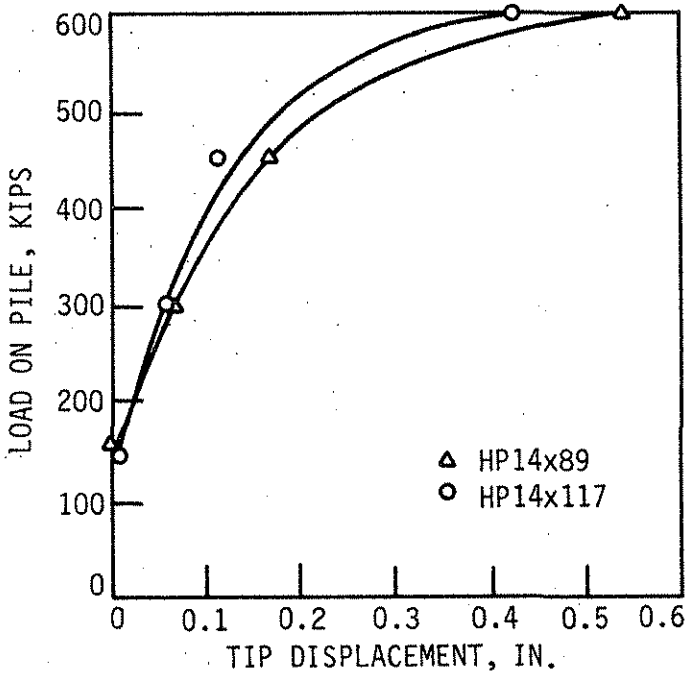


Fig. 4.24. Relationship between tip movement and load.

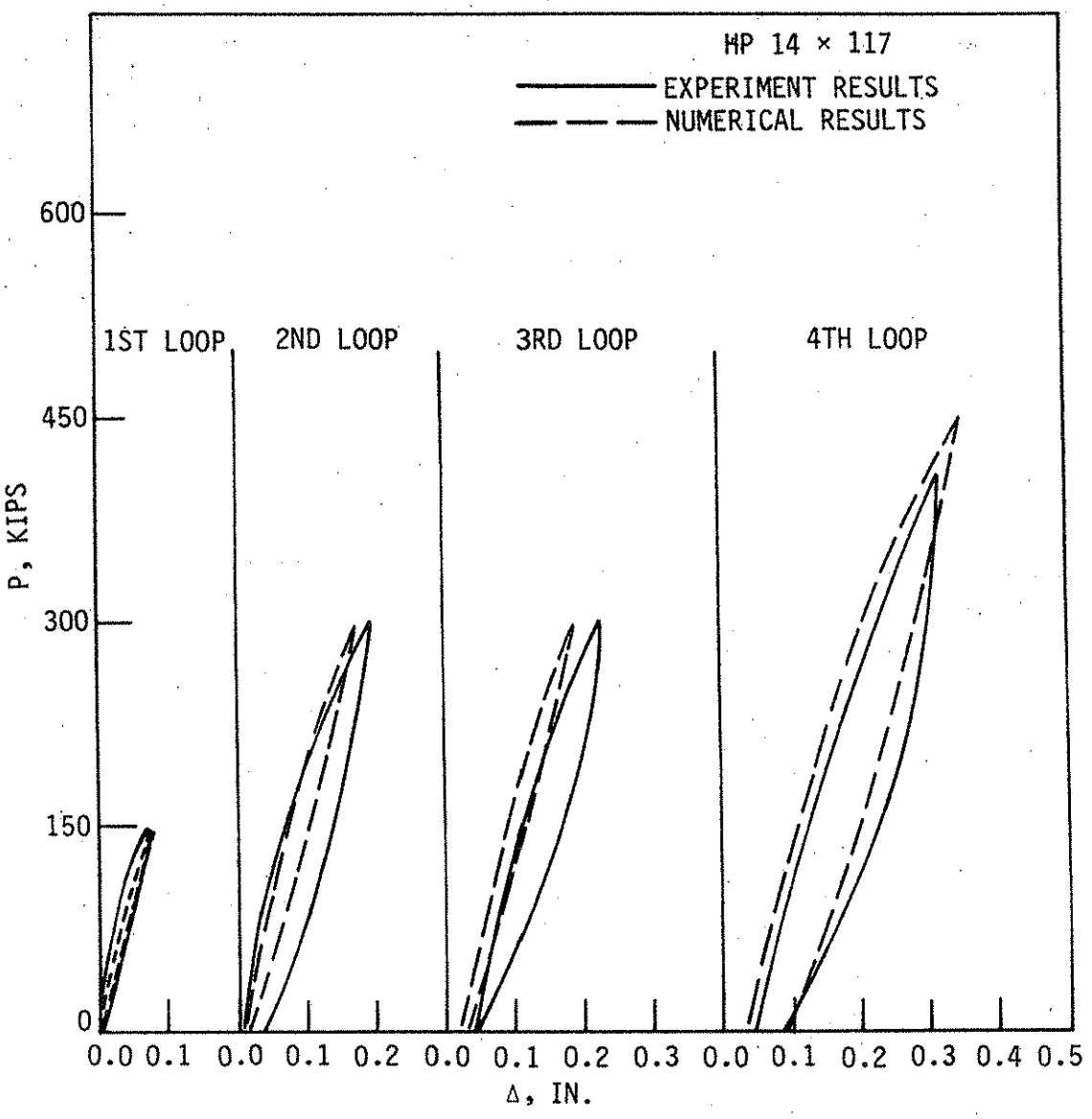


Fig. 4.25. Load-settlement curve for HP14x117 test pile.

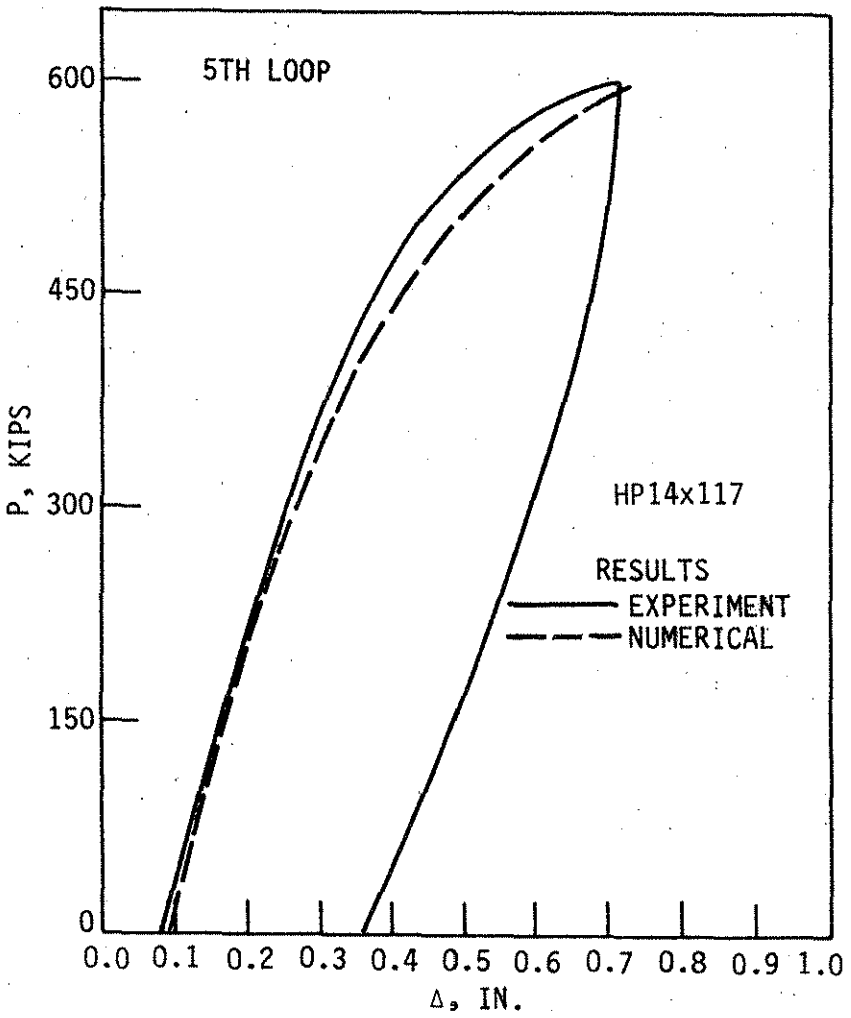


Fig. 4.25. continued.

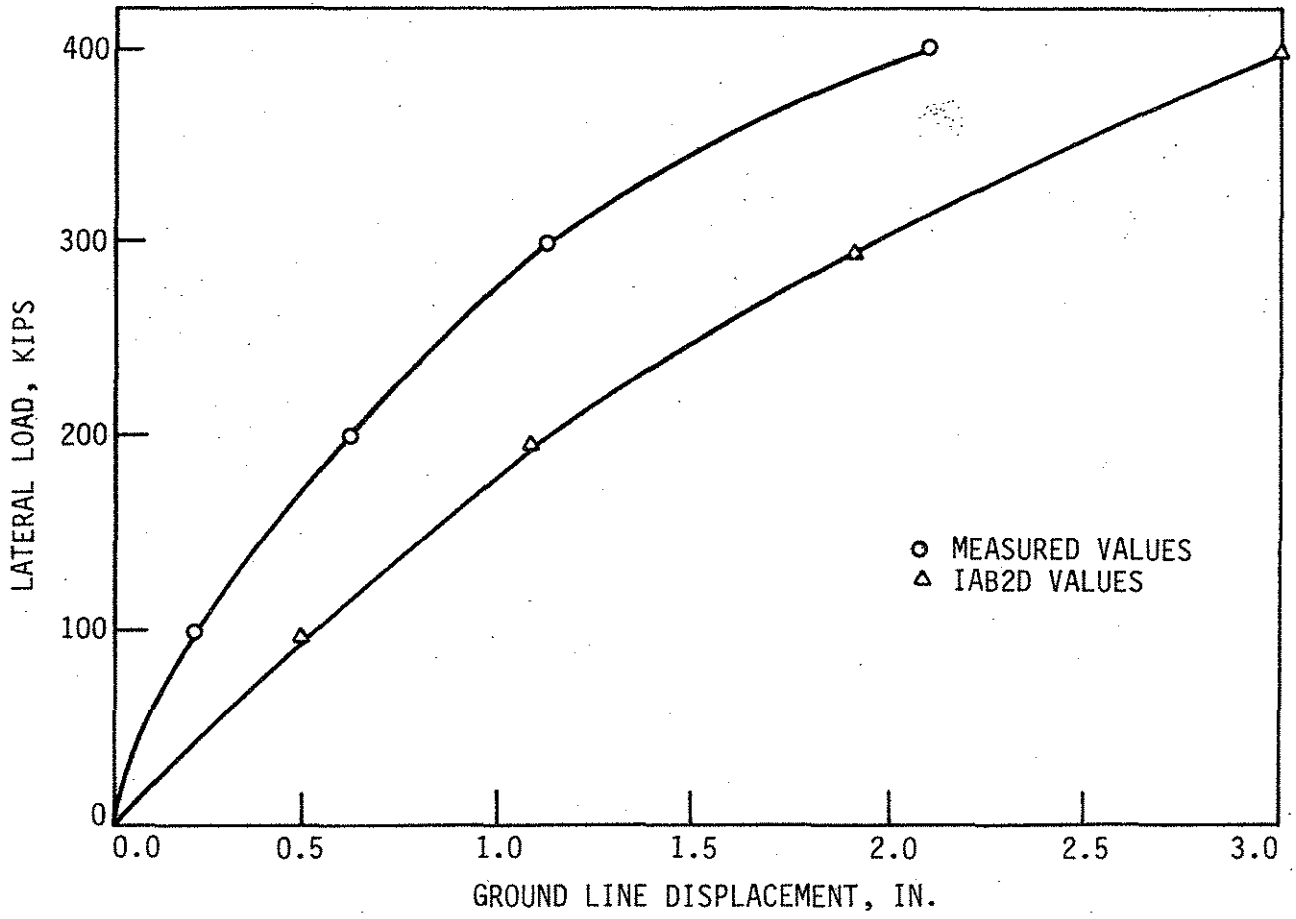


Fig. 4.26. Load-displacement curves, pier 1.

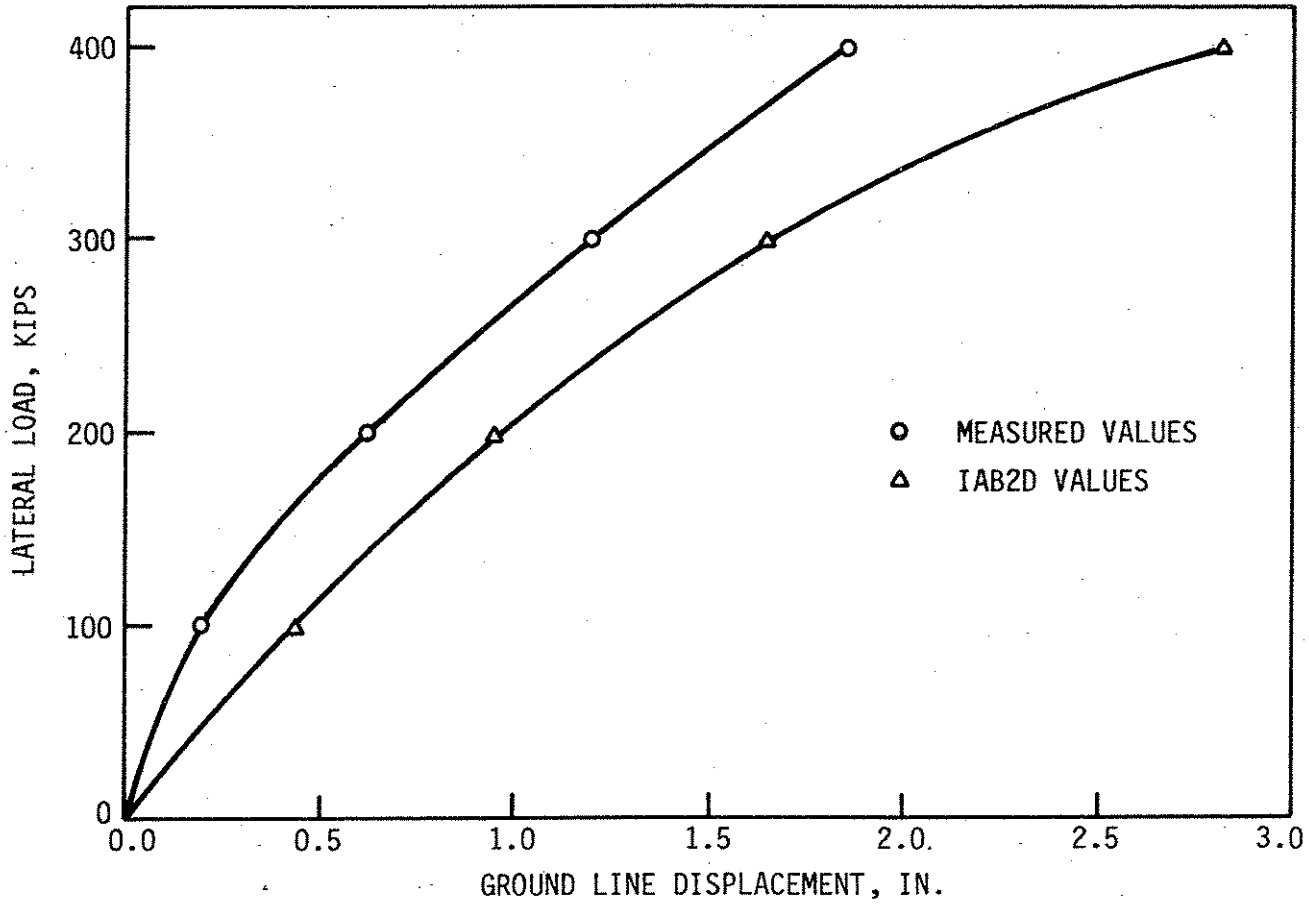


Fig. 4.27. Load-displacement curves, pier 2.

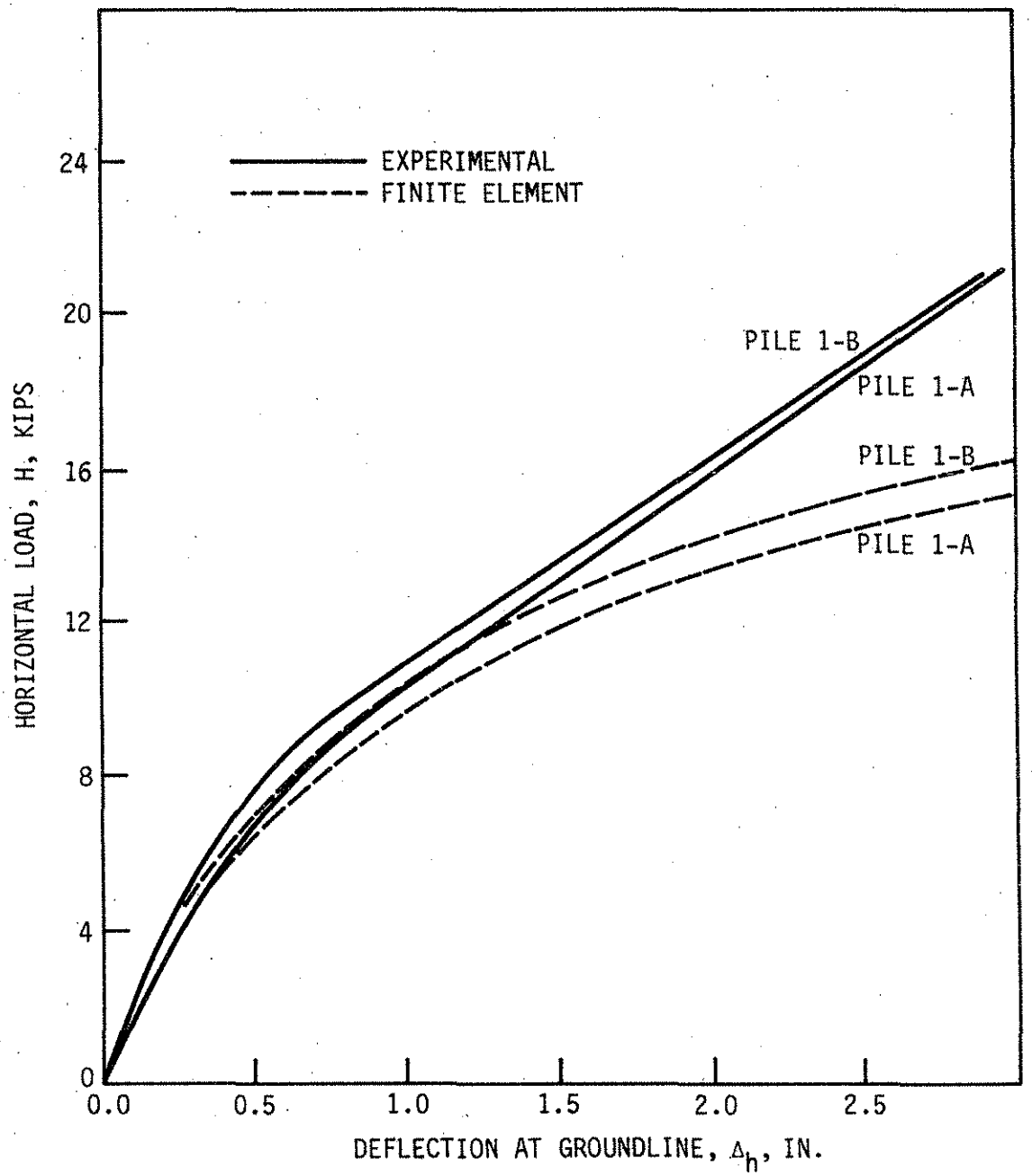


Fig. 4.28. Load-deflection curve for piles 1-A and 1-B.

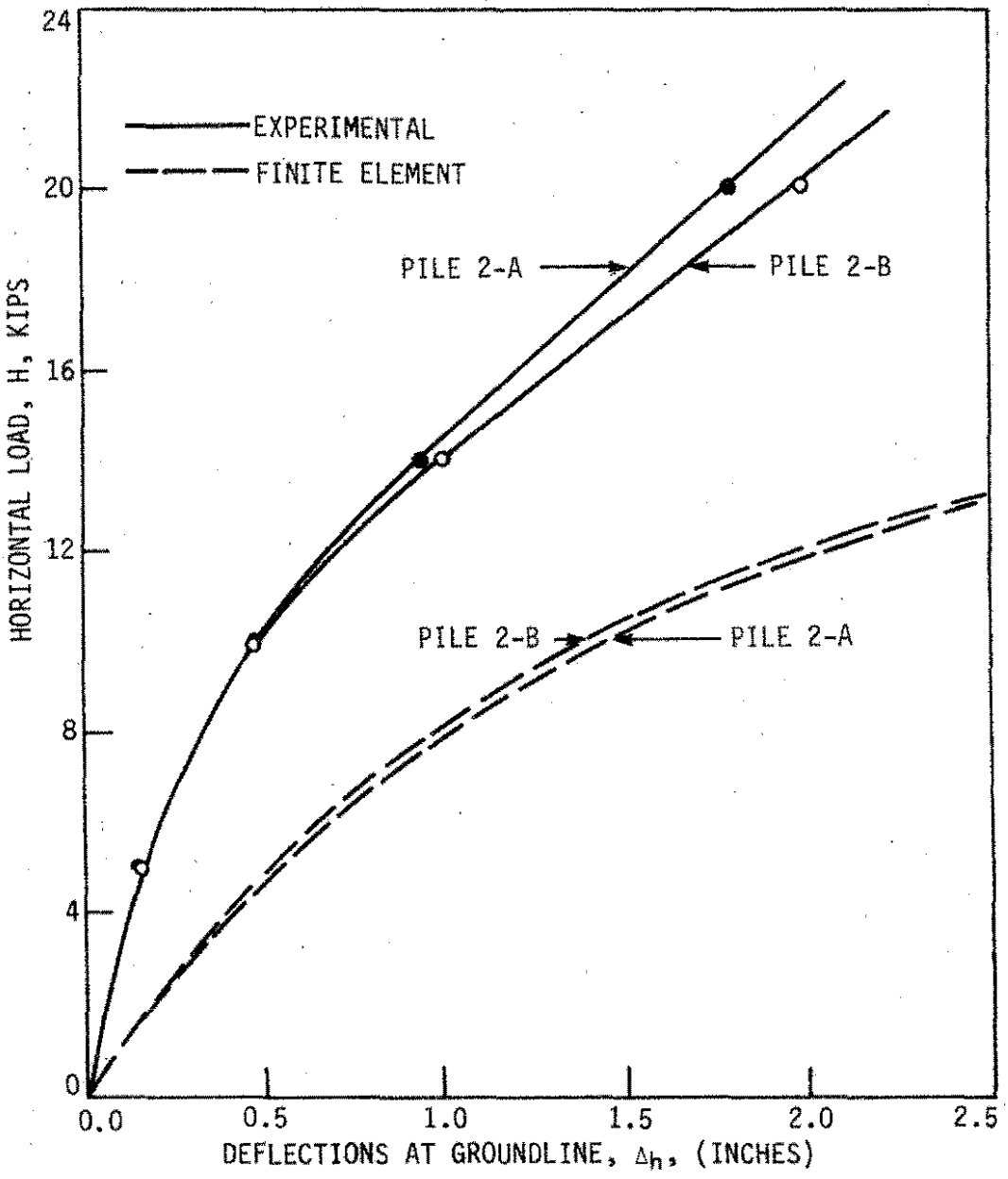


Fig. 4.29. Load-deflection curve for piles 2-A and 2-B.

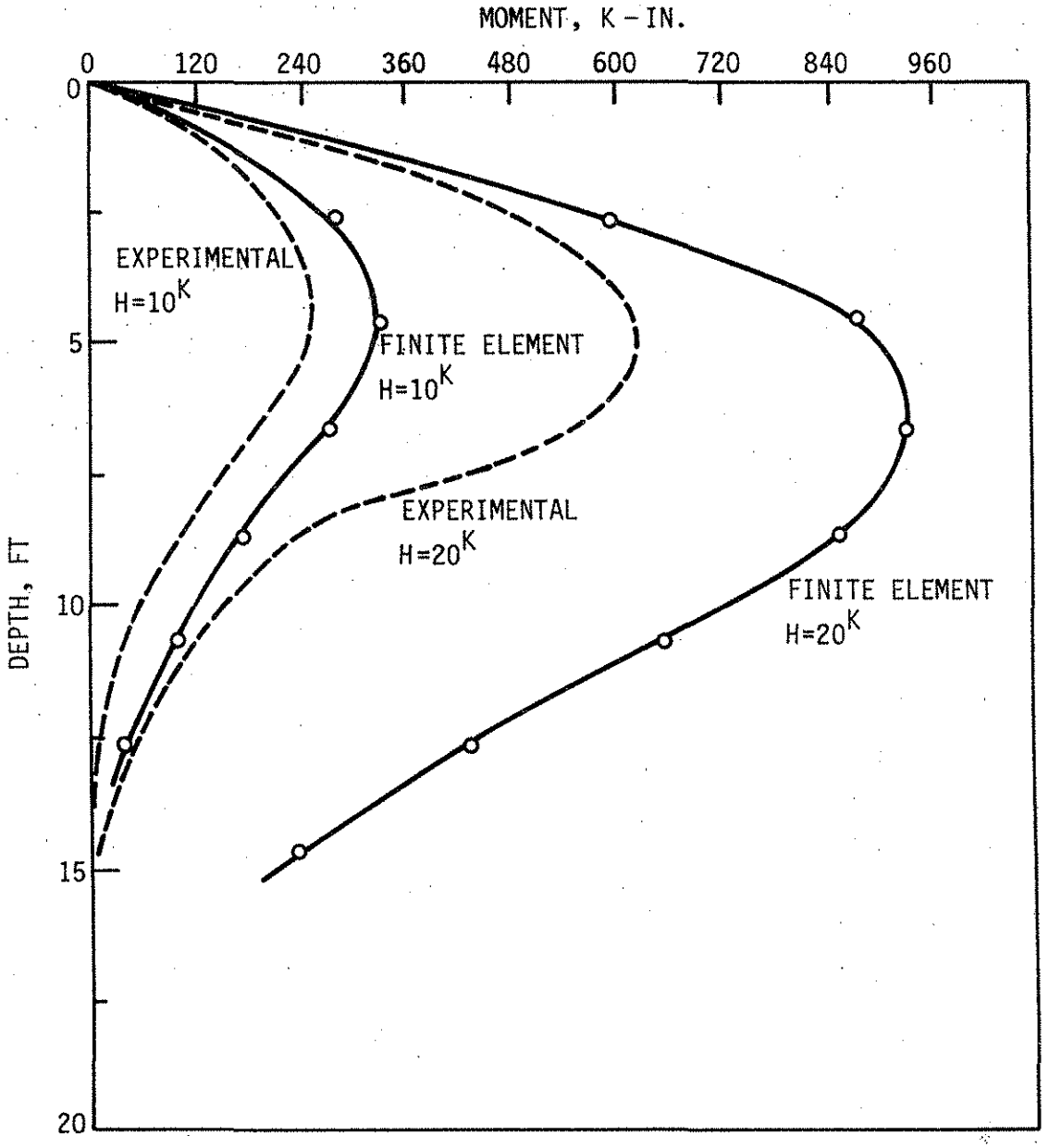


Fig. 4.30. Moment versus depth diagram for pile 1-A.

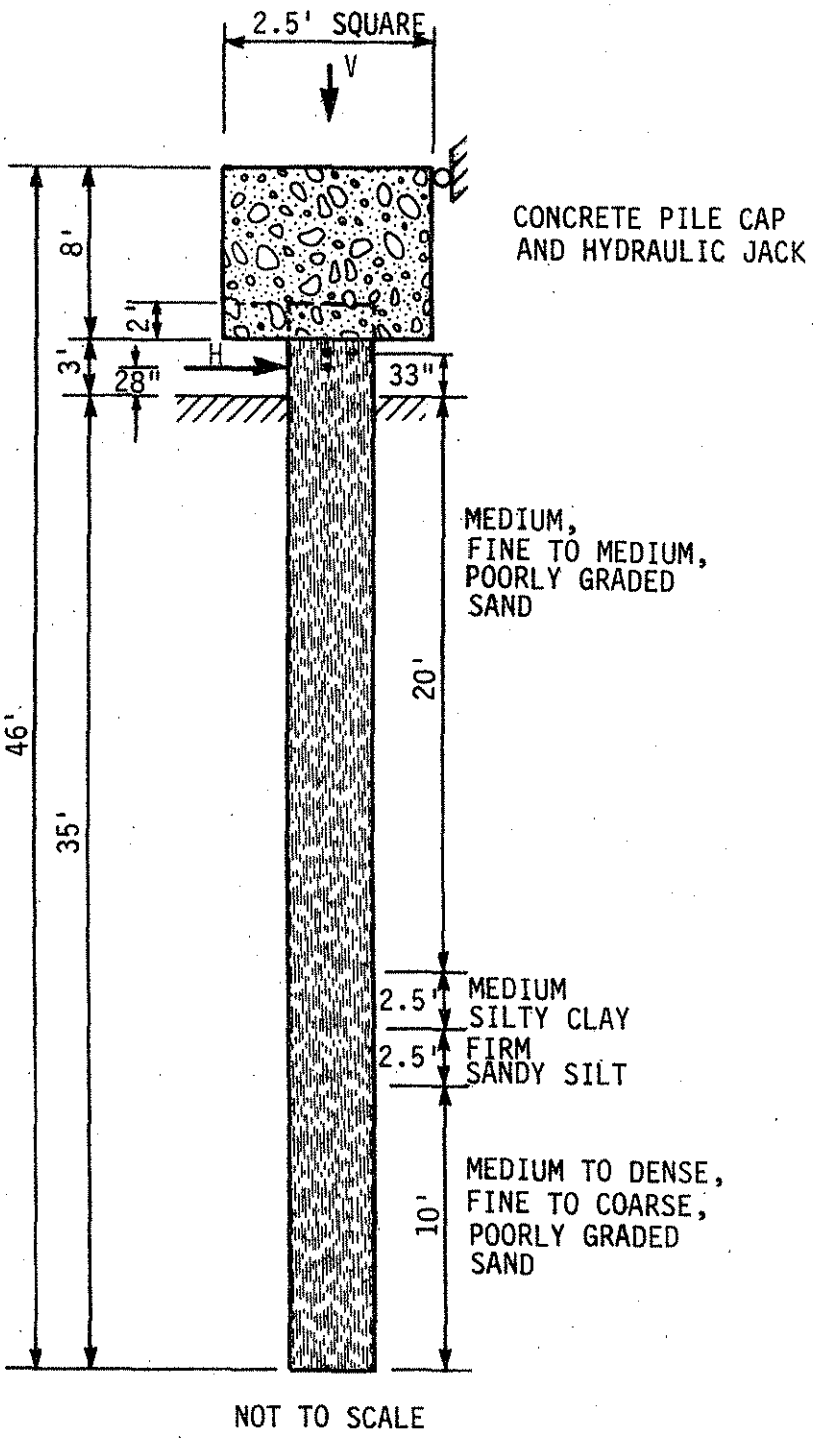


Fig. 4.31. Schematic diagram of the pile and generalized soil profile.

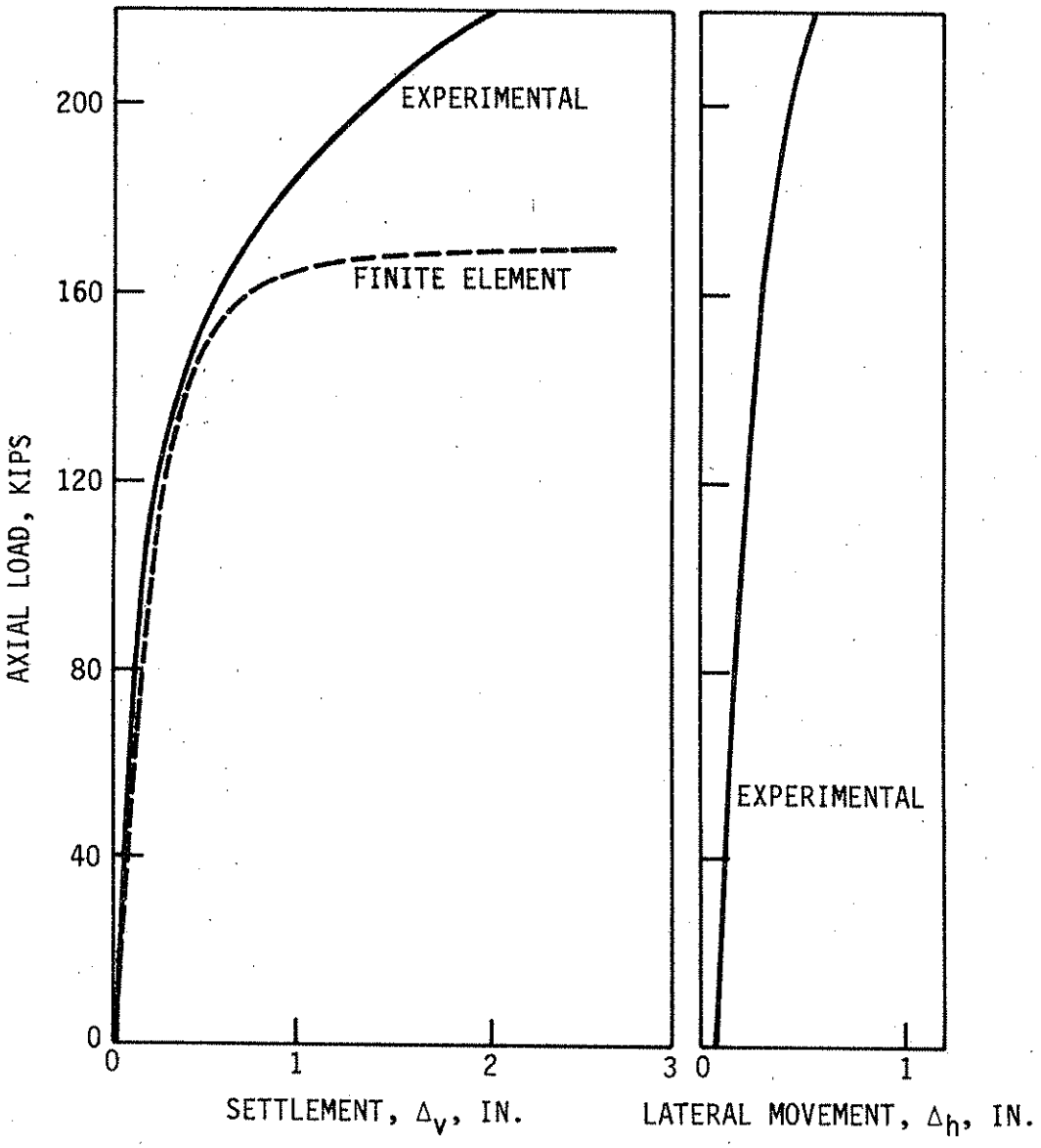


Fig. 4.32. Load versus settlement for the axial load test.

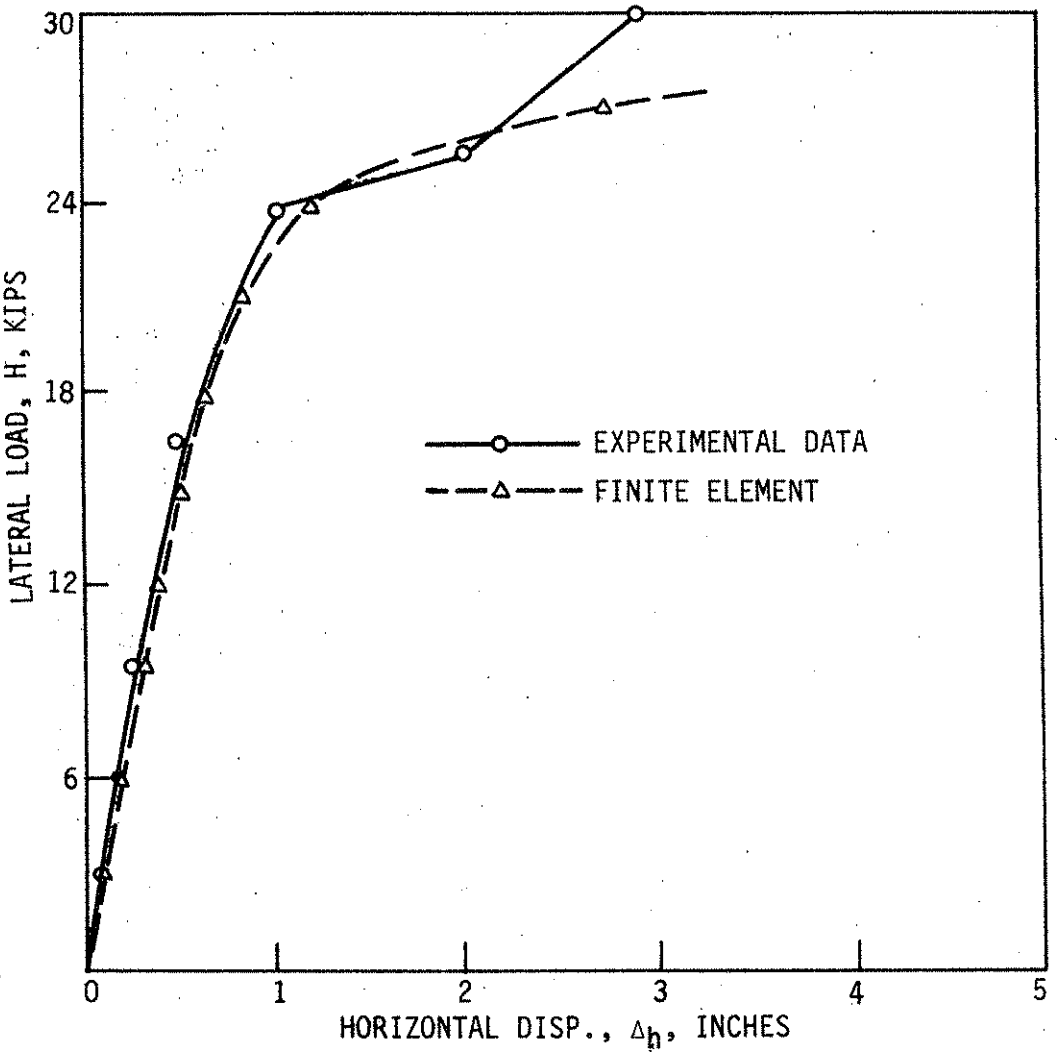


Fig. 4.33. Lateral load versus displacement for the combined load test (with a 60-kip axial load).

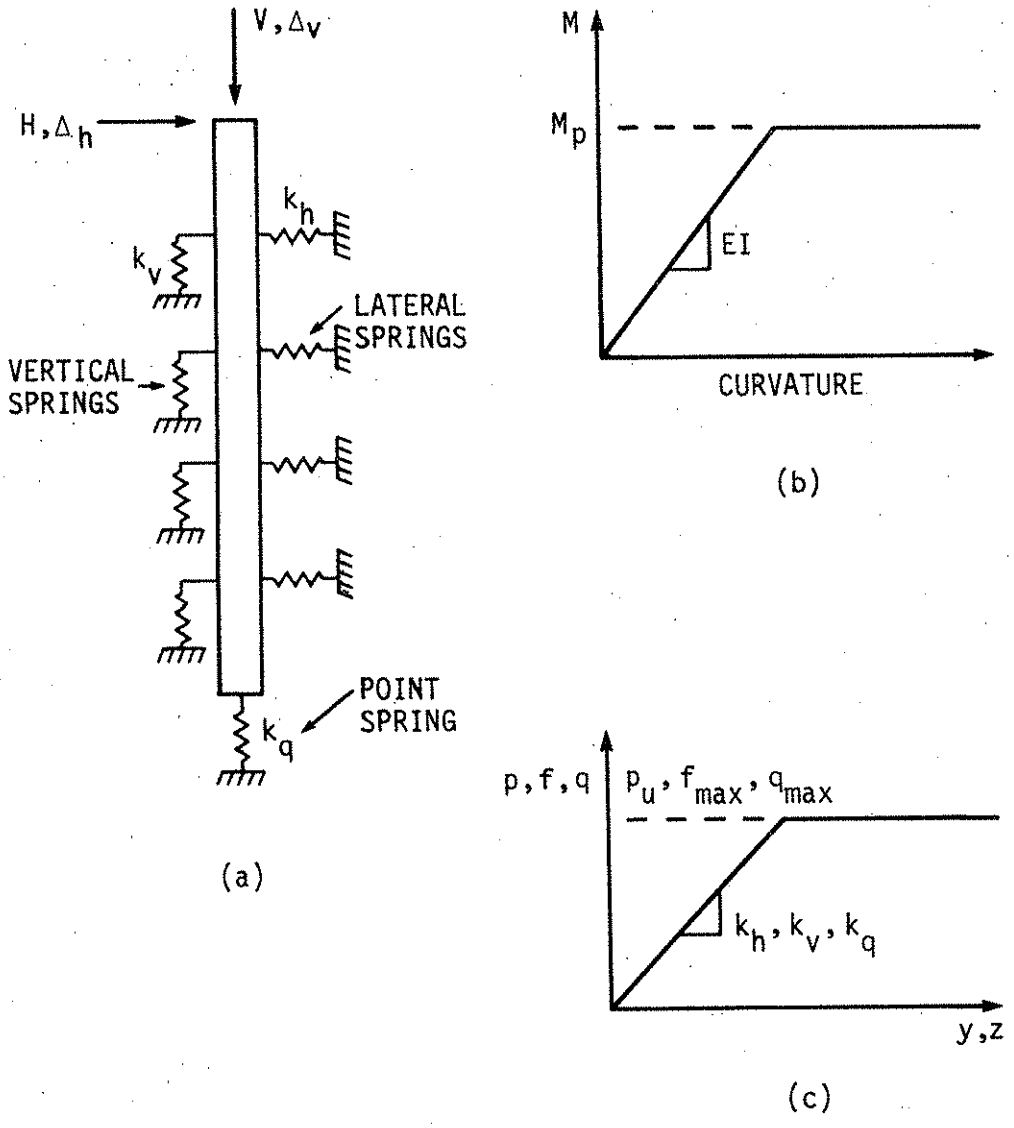


Fig. 5.1. Design model: (a) model of soil-pile system, (b) elastic,perfectly plastic moment-curvature relationship for the pile, (c) bilinear soil resistance-displacement relationships for the soil springs.

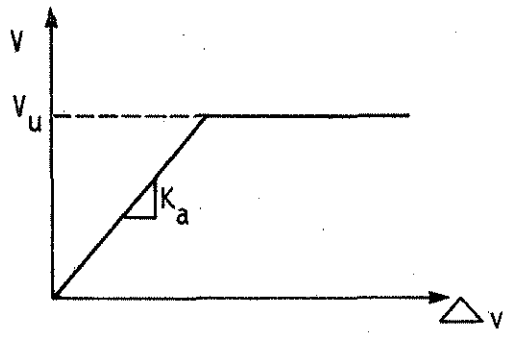


Fig. 5.2. Axial load-displacement curve for the design model.

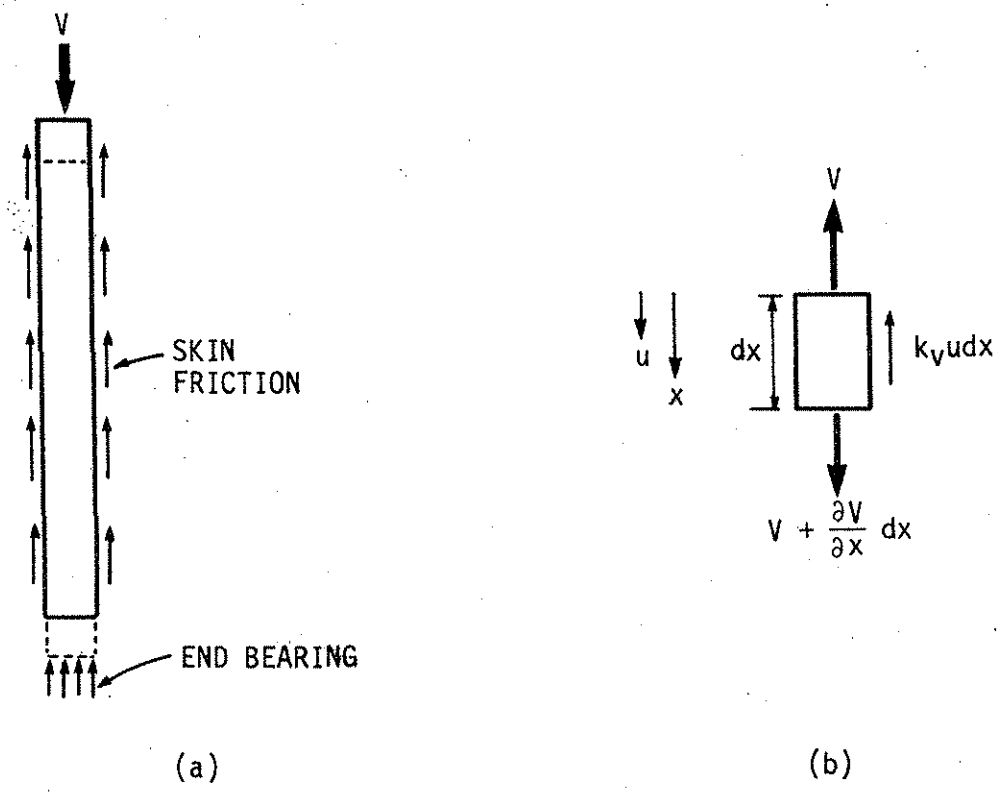


Fig. 5.3. (a) Vertical load on the pile is carried by skin friction and end bearing, (b) Element of pile under axial loading.

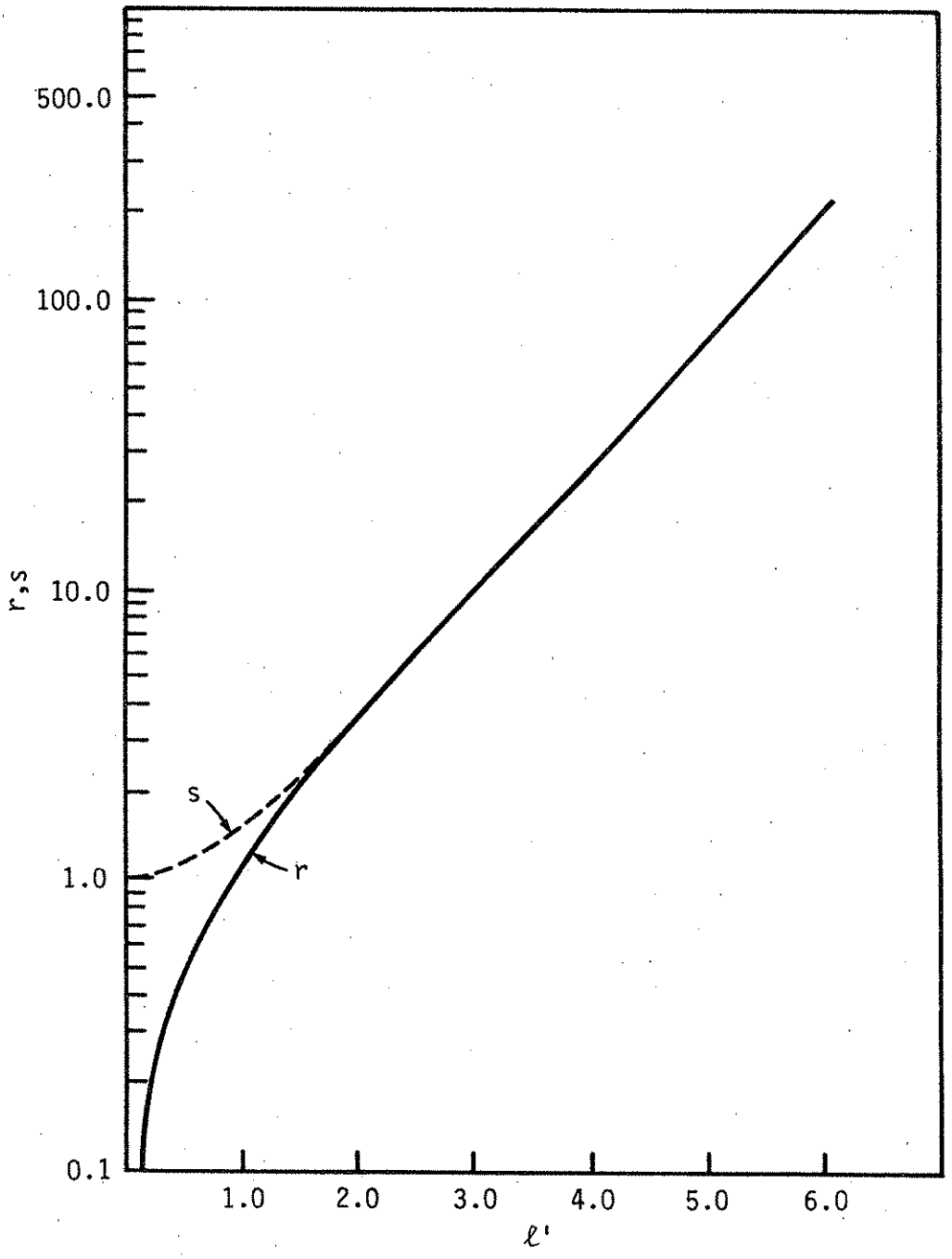


Fig. 5.4. Coefficients r and s versus ℓ', for use in axial stiffness equations.

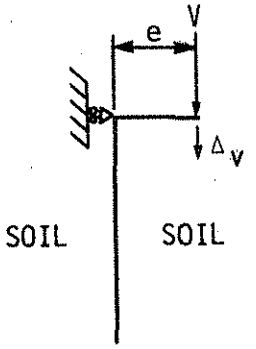


(a)

PERFECTLY ELASTIC CASE

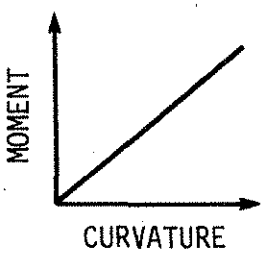


RIGID, PERFECTLY PLASTIC CASE

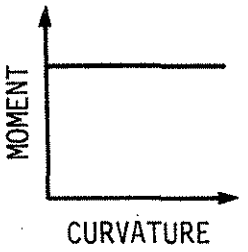


(b)

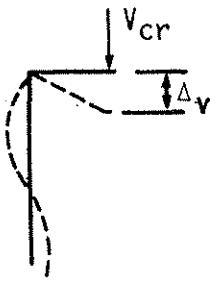


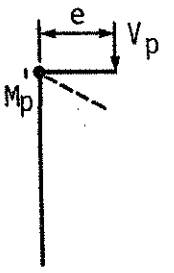


(c)

Fig. 5.5. Example illustrating lateral mechanism: (a) schematic drawing of the pile and soil, (b) material properties, (c) failure modes.

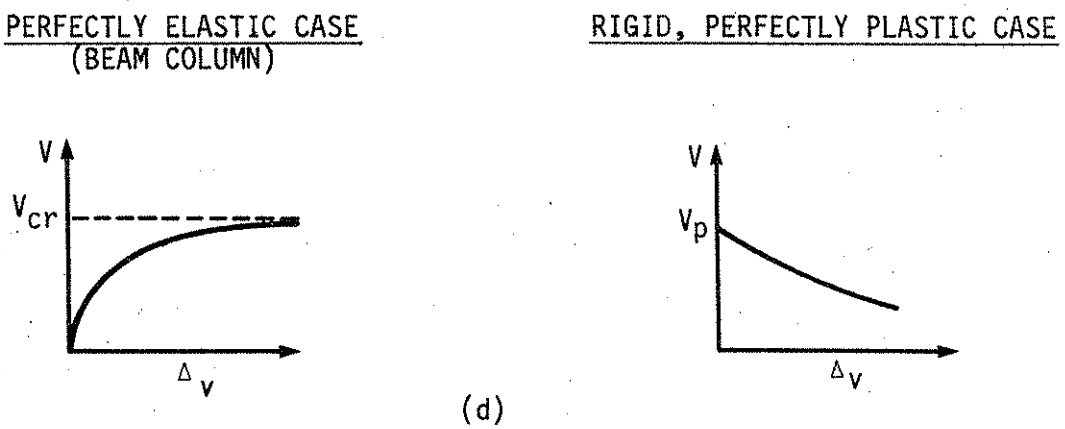


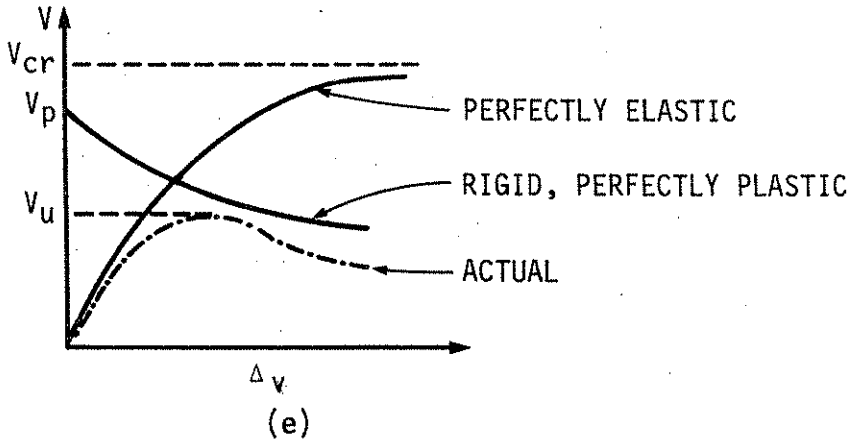


Fig. 5.5. Example illustrating lateral mechanism (con't): (d) load-displacement curves for each case, (e) load-displacement curves for the pile.

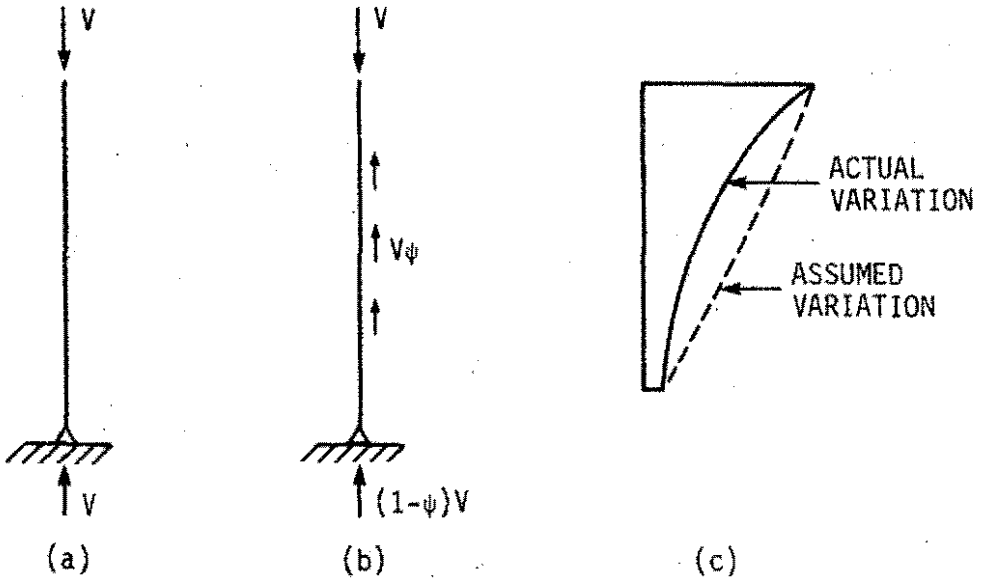


Fig. 5.6. Design model used for calculating the elastic buckling load: (a) pile with constant axial load, (b) pile with vertical load transfer, (c) variation of axial load with depth. Note: lateral soil support is not shown.

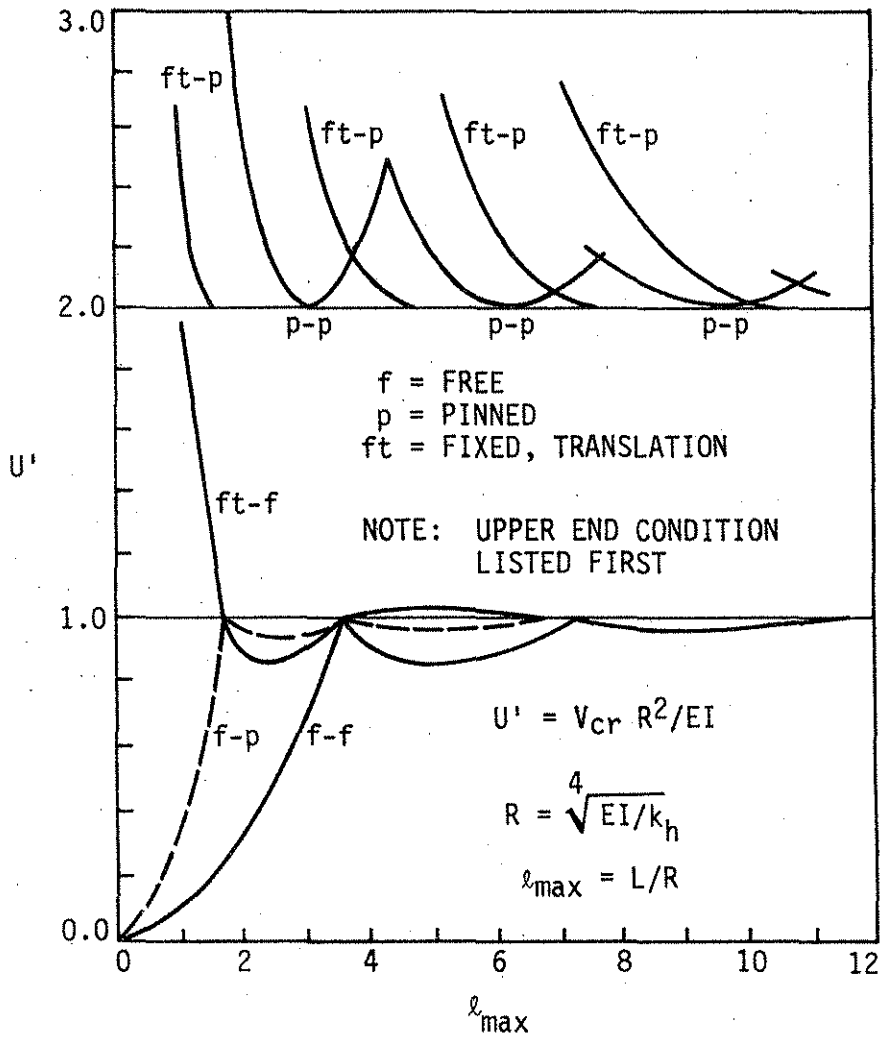


Fig. 5.7. Nondimensional buckling coefficient versus length for constant $k_h$ [5.5] (see Fig. 5.9 for boundary conditions).

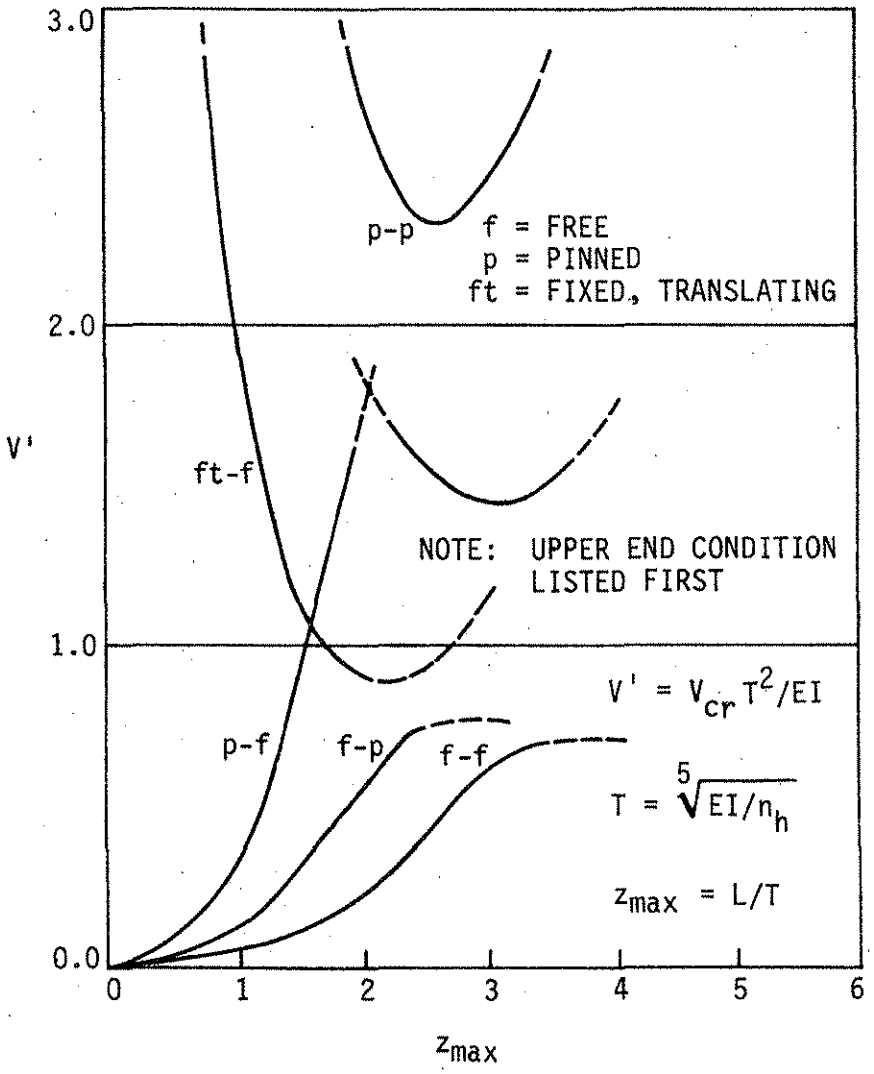


Fig. 5.8. Nondimensional coefficients versus length for linearly varying $k_h$ [5.5] (see Fig. 5.9 for boundary conditions).

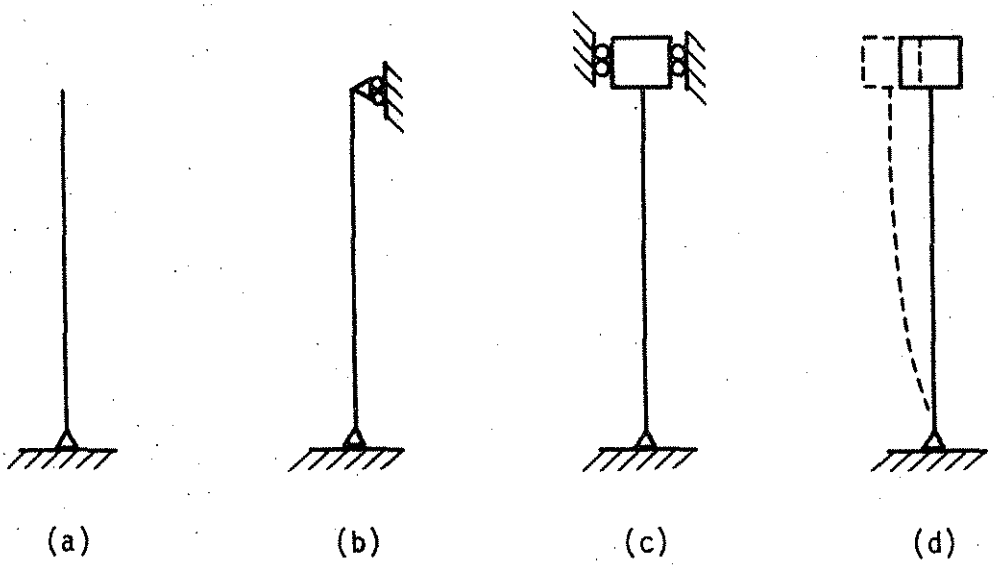


Fig. 5.9. Boundary conditions for elastic buckling load $V_{cr}$. For all cases the lower boundary condition is pinned. The upper boundary condition for each case is (a) free, (b) pinned, (c) fixed, no translation, (d) fixed, translating.

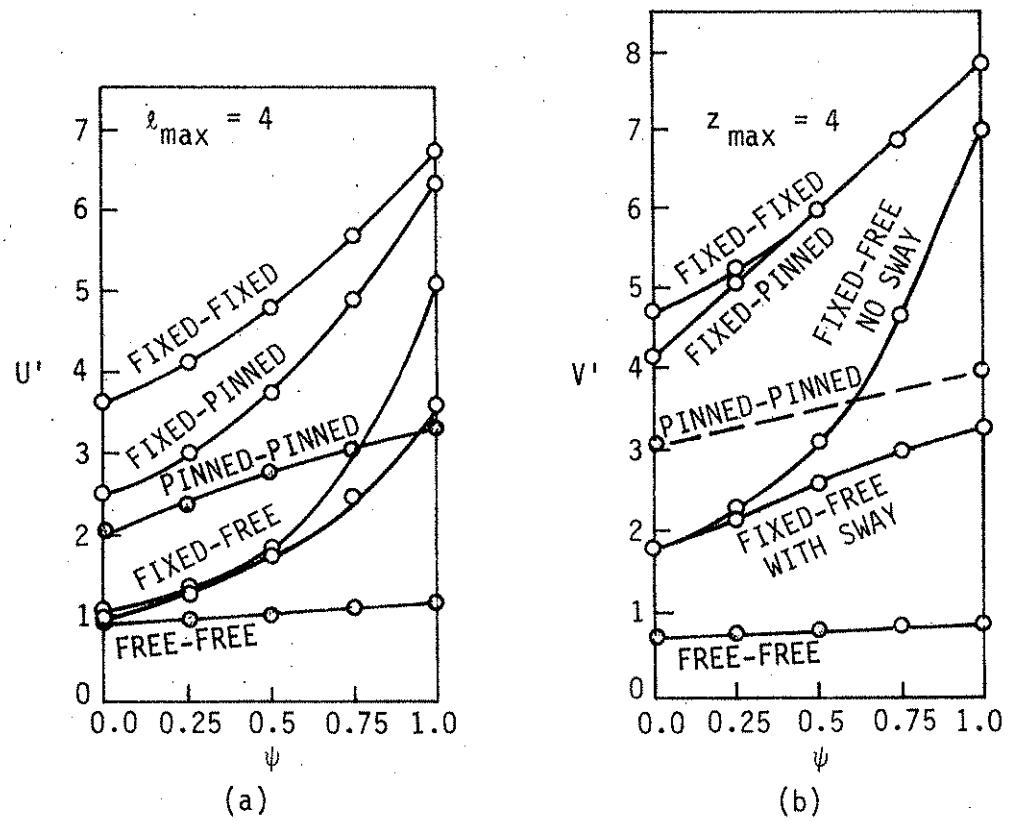


Fig. 5.10. Effect of skin friction on the buckling load for (a) constant lateral soil stiffness, (b) linearly varying lateral soil stiffness [5.6, 5.7] (see Fig. 5.9 for boundary conditions).

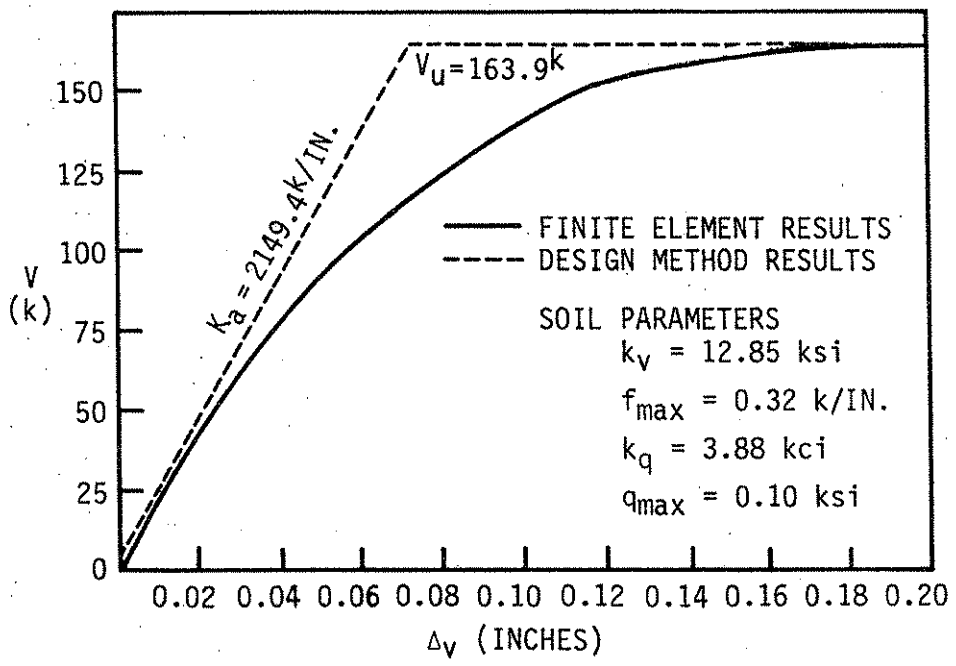


Fig. 5.11. Load-displacement curve for 40-ft-long HP10x42 pile in stiff clay illustrating the slip mechanism.

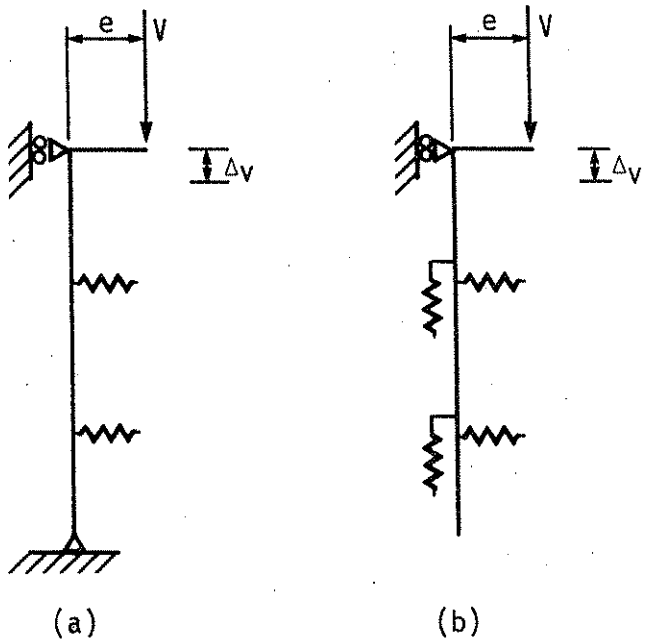


Fig. 5.12. Diagram of pile configurations used to illustrate the lateral mechanism.

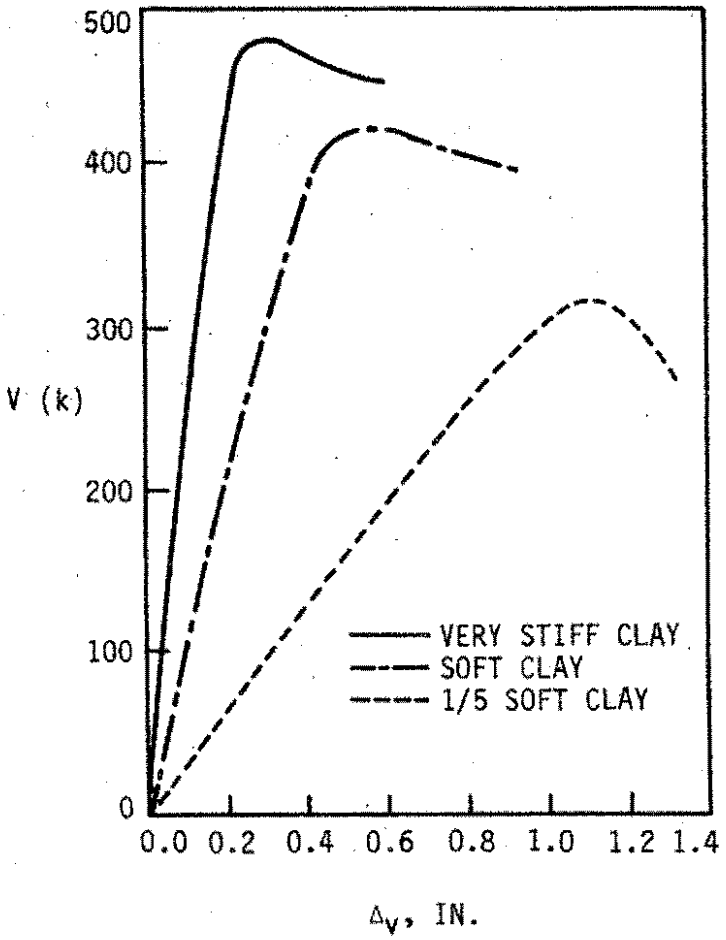


Fig. 5.13. Load-displacement curves for the pile configuration shown in Fig. 5.12(b).

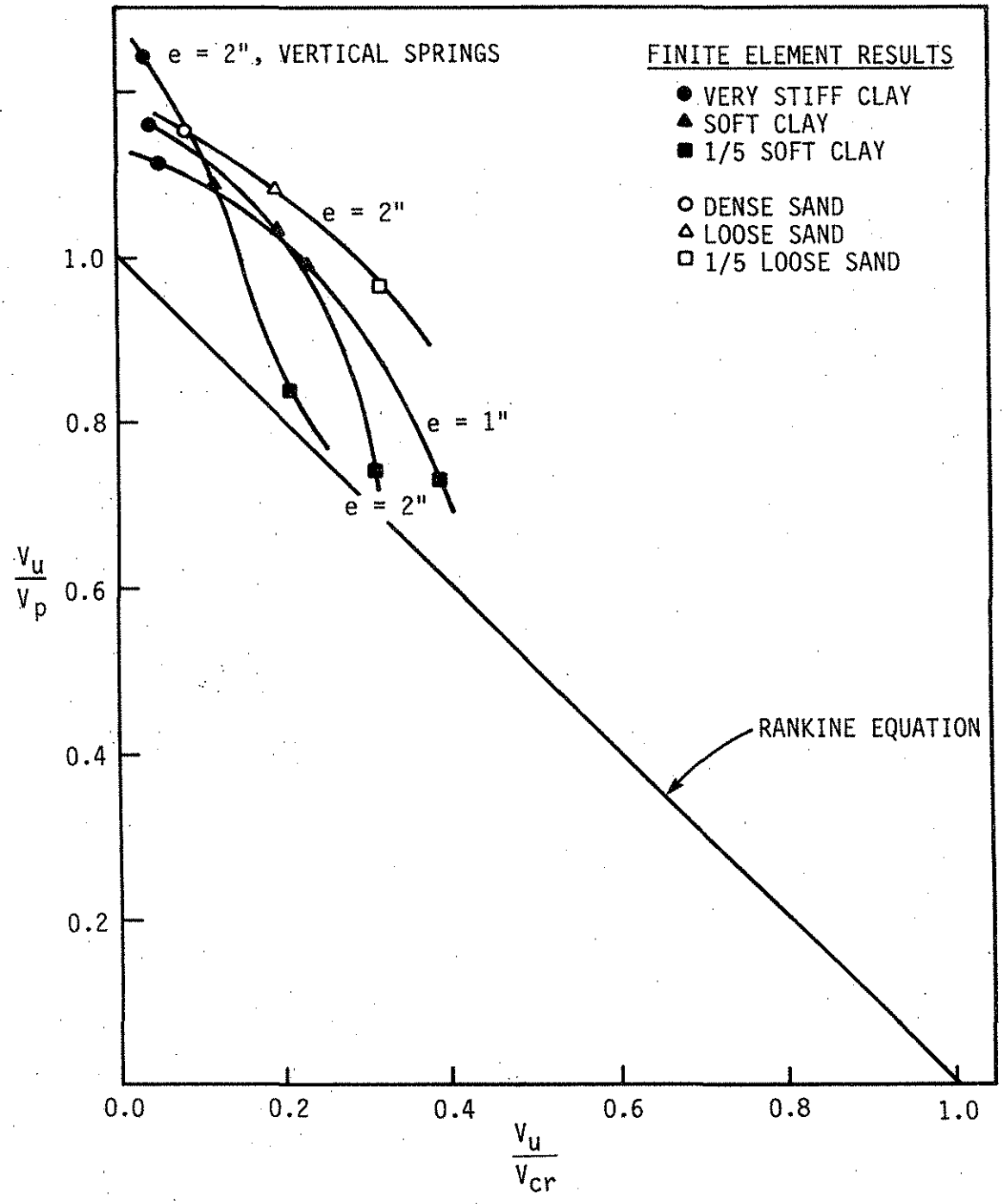


Fig. 5.14. Comparison of Rankine equation and finite element results for various soils.

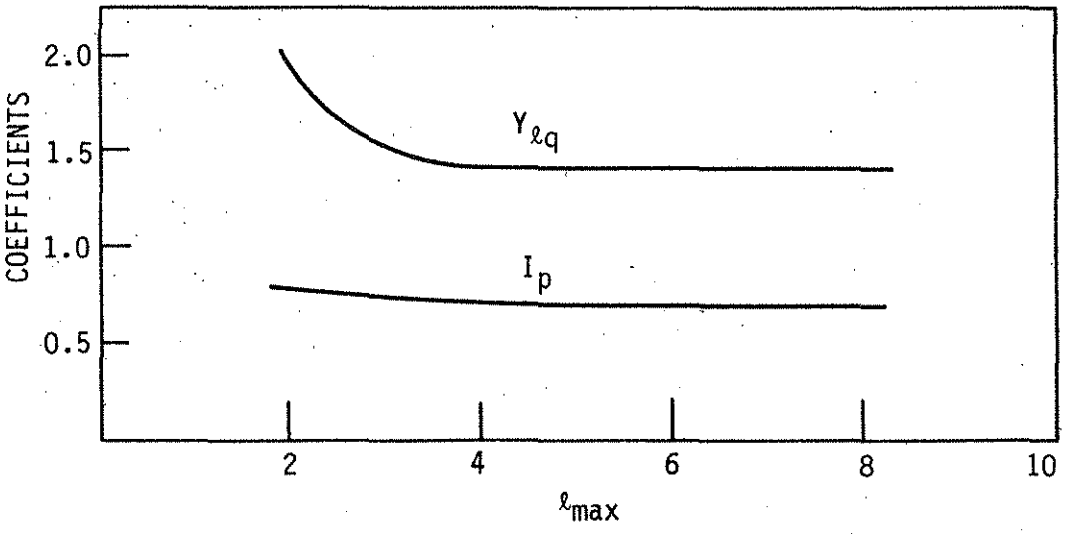


Fig. 5.15. Nondimensional coefficients versus $\ell_{max}$ for constant $k_h$.

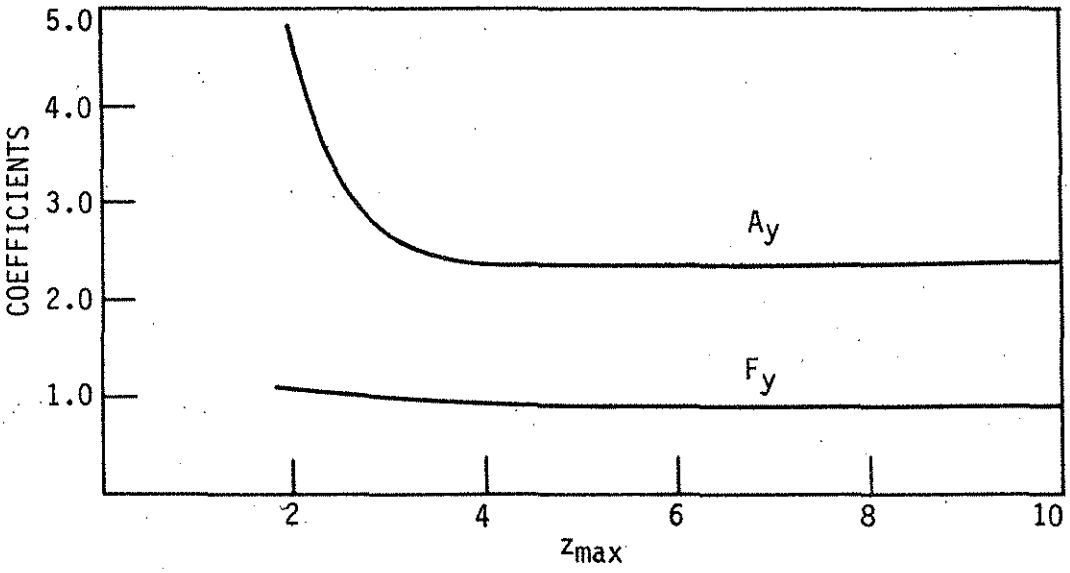


Fig. 5.16. Nondimensional coefficients versus $z_{max}$ for linearly varying $k_h$.

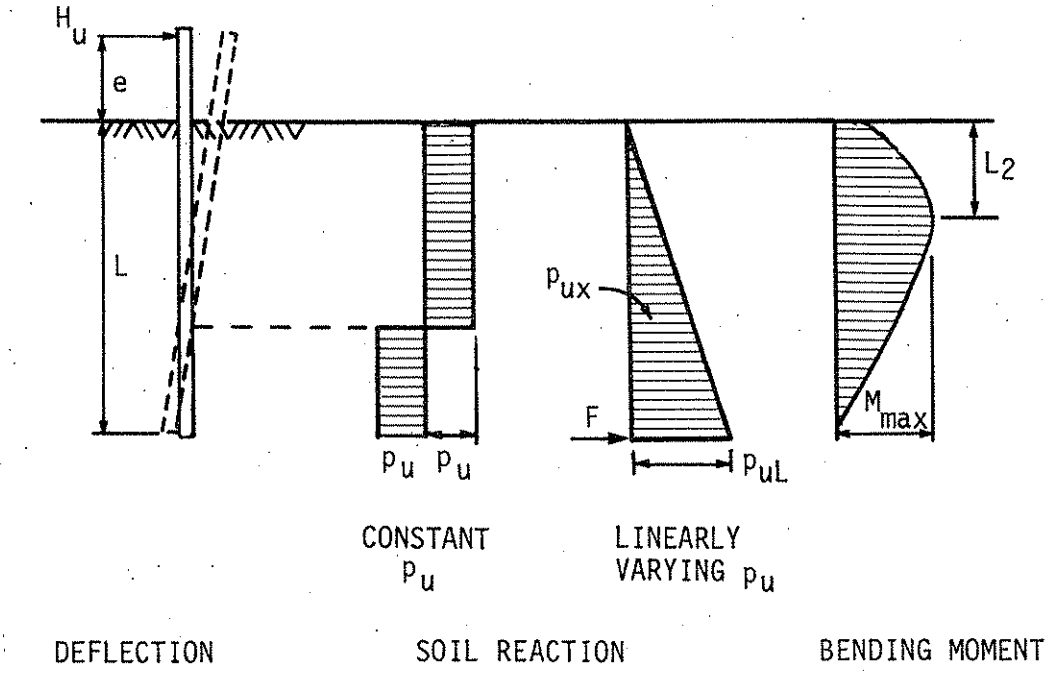


(a)

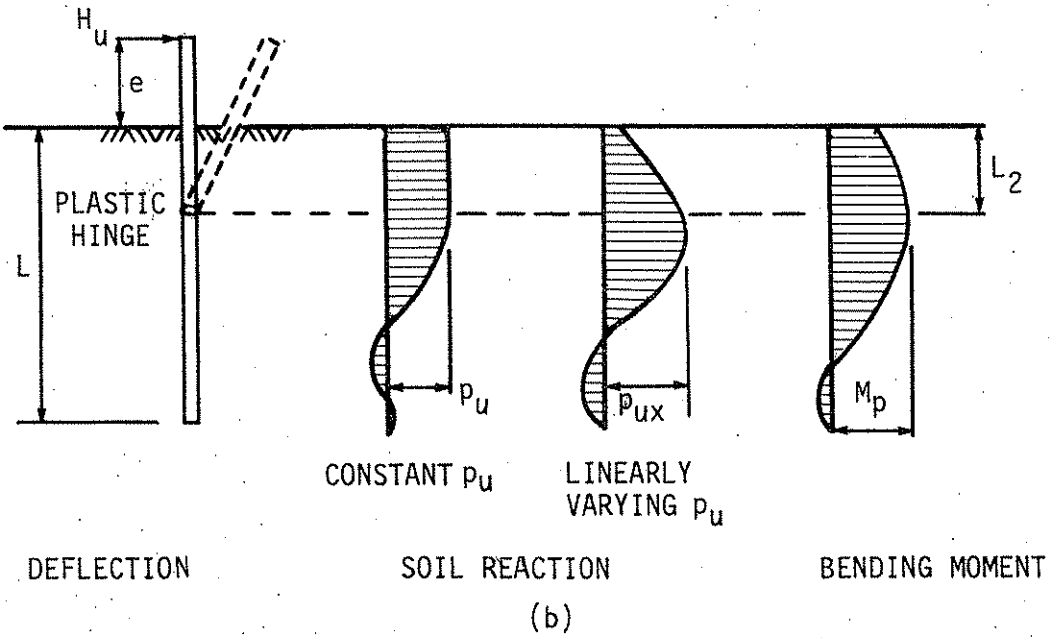


(b)

Fig. 5.17. Lateral failure modes and assumed soil reaction and bending moment distributions for free-headed piles: (a) soil failure (b) pile failure [5.15, 5.16].

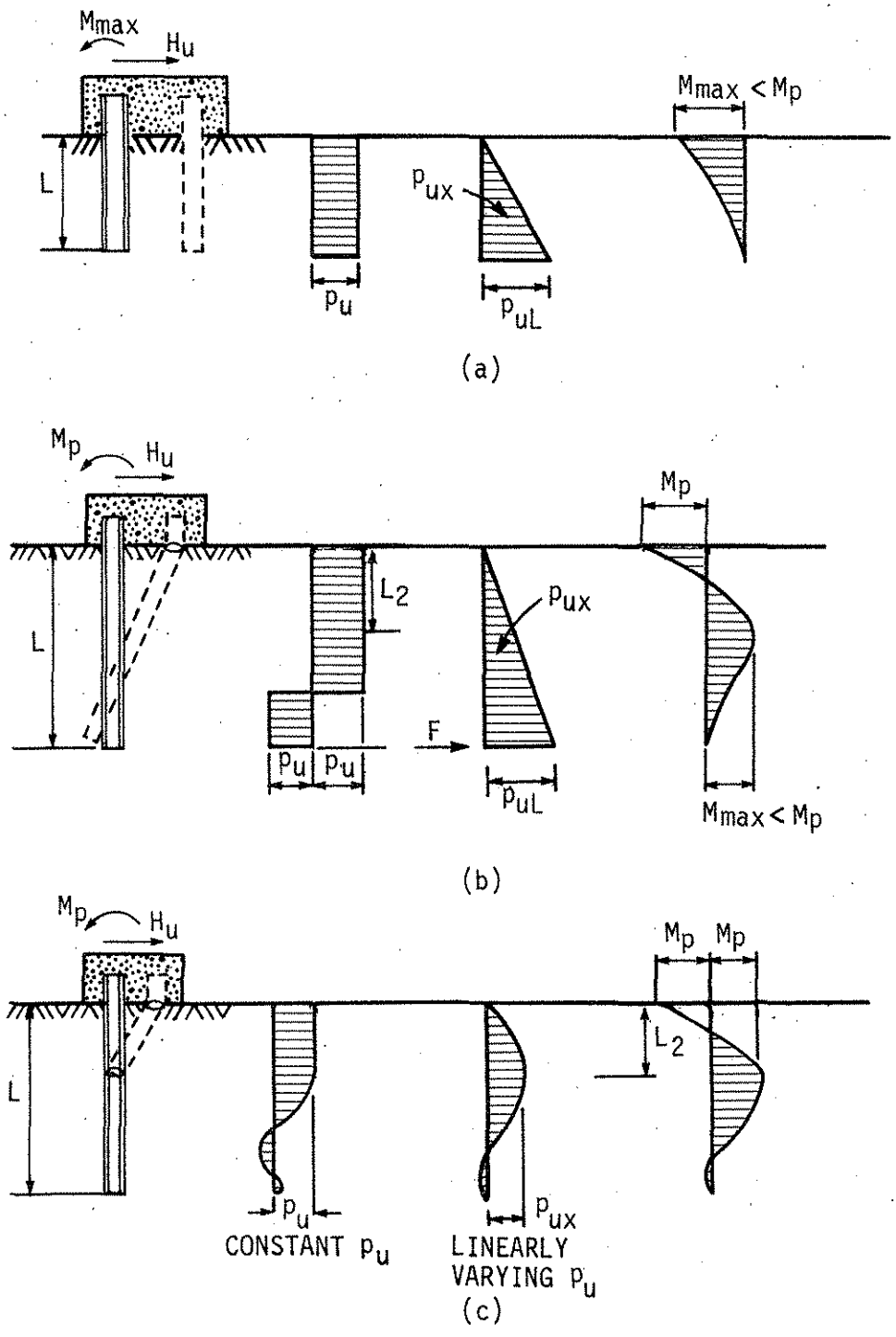


Fig. 5.18. Lateral failure modes and assumed soil reaction and bending moment distributions for fixed-headed piles: (a) soil failure (b) soil and pile failure; (c) pile failure [5.15, 5.16]

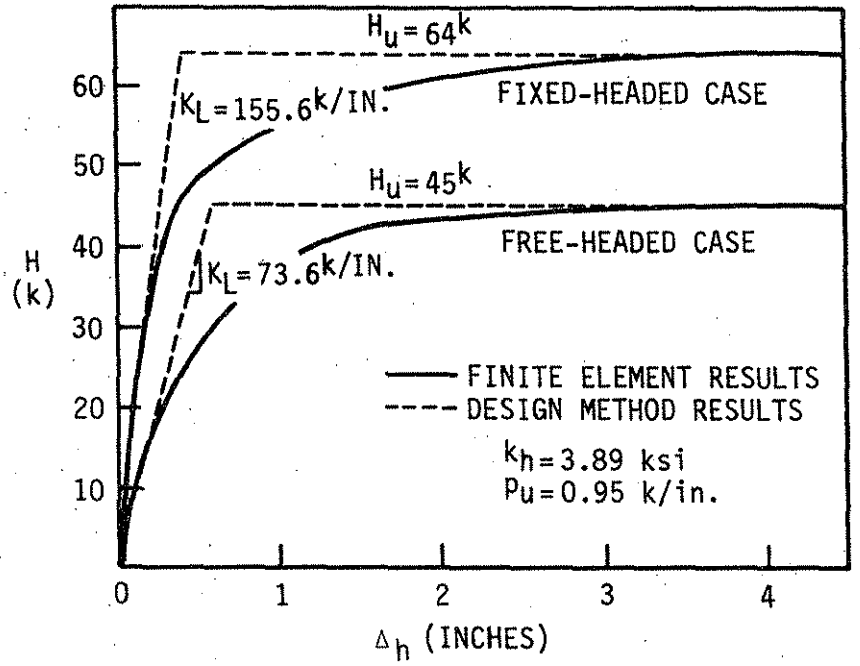


Fig. 5.19. Lateral load-displacement curves for pile failure modes with constant $p_u$.

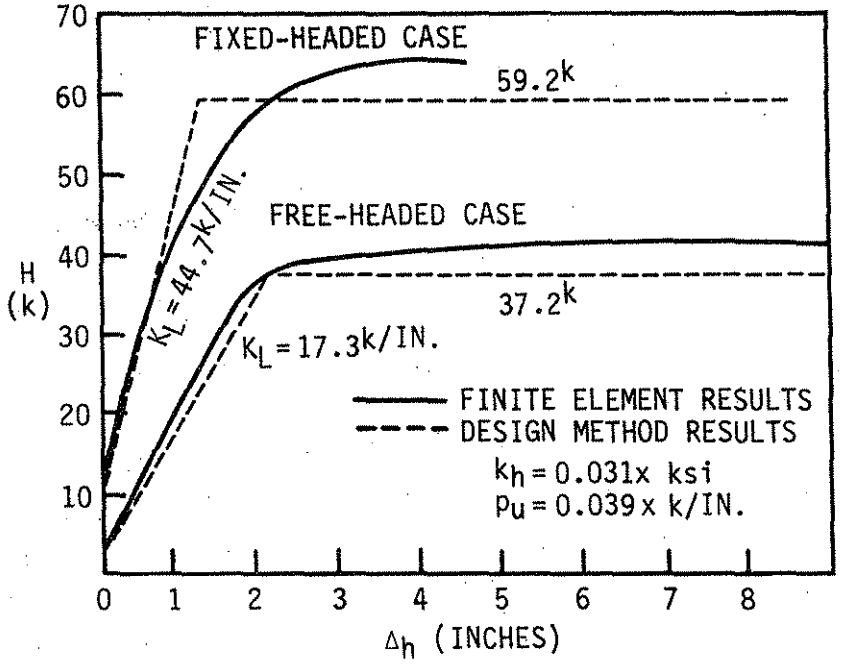


Fig. 5.20. Lateral load-displacement curves for pile failure modes with linearly varying $p_u$.

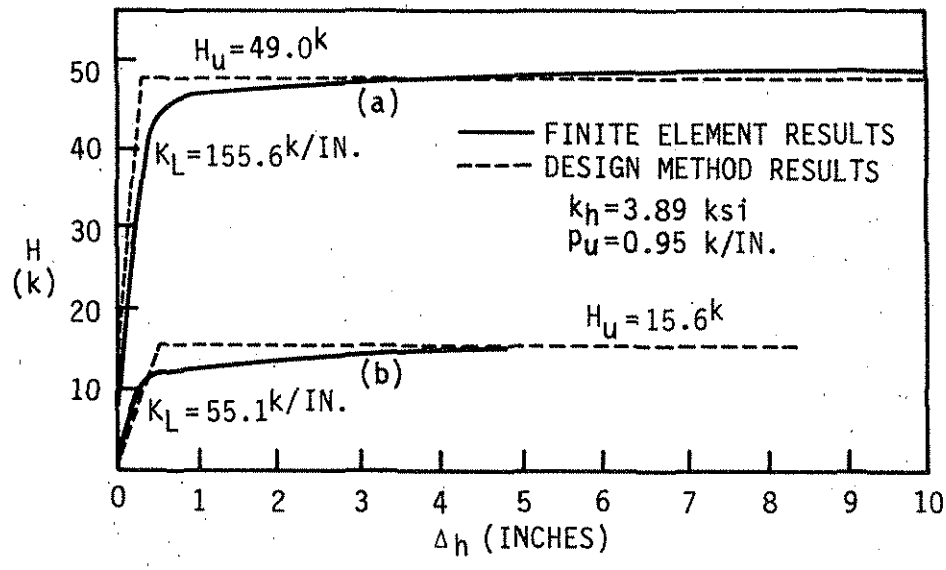


Fig. 5.21. Load-displacement curves representing (a) soil and pile failure mode, (b) soil failure mode for free-headed pile (constant $p_u$).

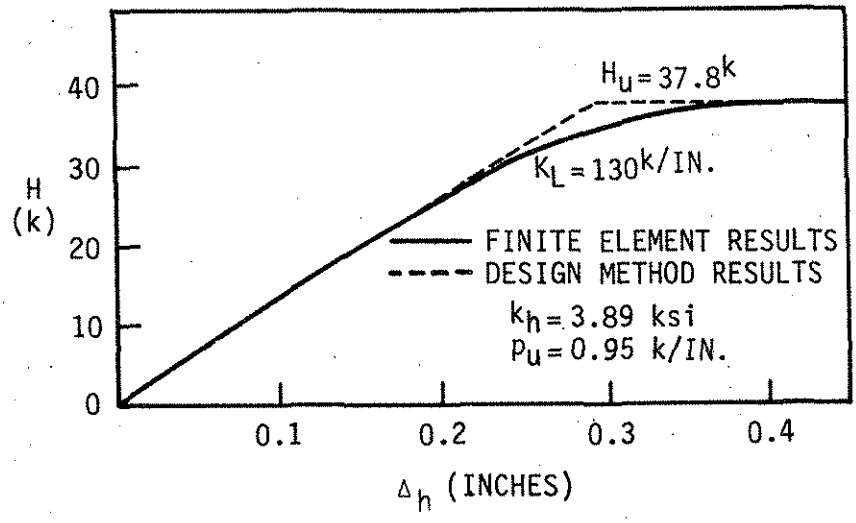


Fig. 5.22. Load-displacement curve representing the soil failure mode for a fixed-headed pile (constant $p_u$).

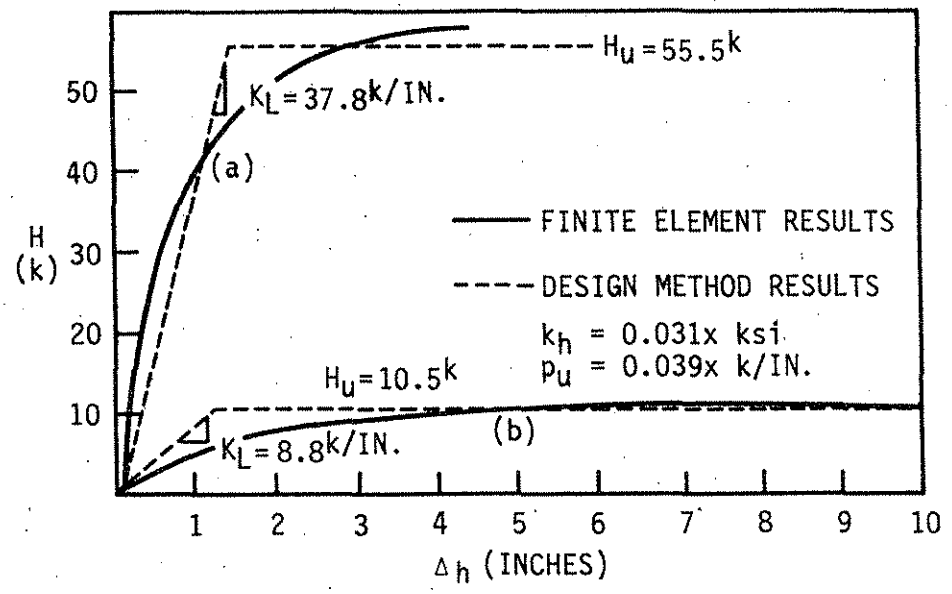


Fig. 5.23. Load-displacement curves representing (a) soil and pile failure mode, (b) soil failure mode for a free-headed pile (linearly varying $p_u$).

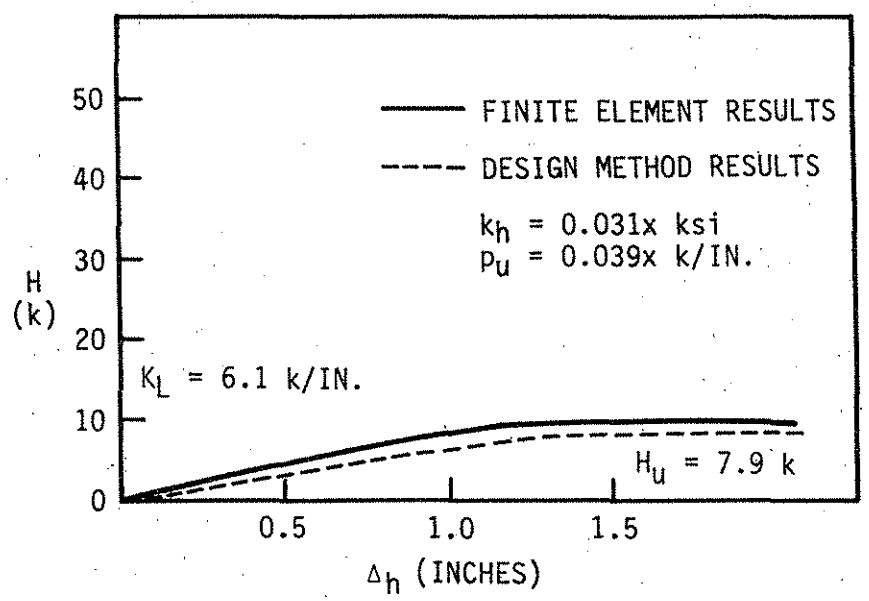


Fig. 5.24. Load-displacement curve representing the soil failure mode for a fixed-headed pile (linearly varying $p_u$).

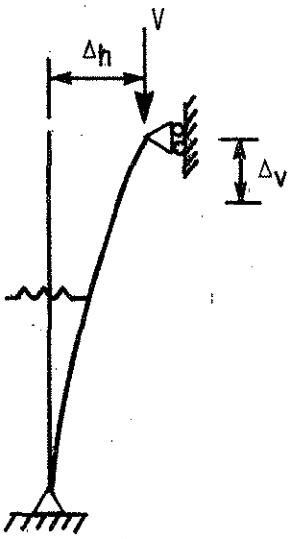


Fig. 5.25. Example of a pile with a lateral displacement and vertical load at the pile head.

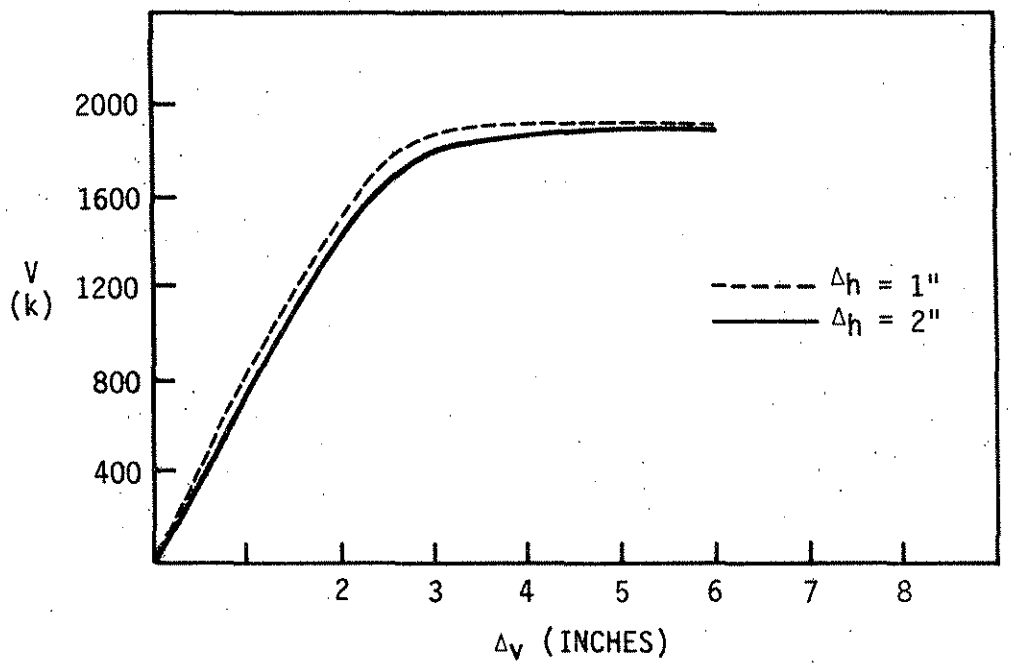


Fig. 5.26. Comparison of elastic buckling loads for piles with different $\Delta_h$ values.

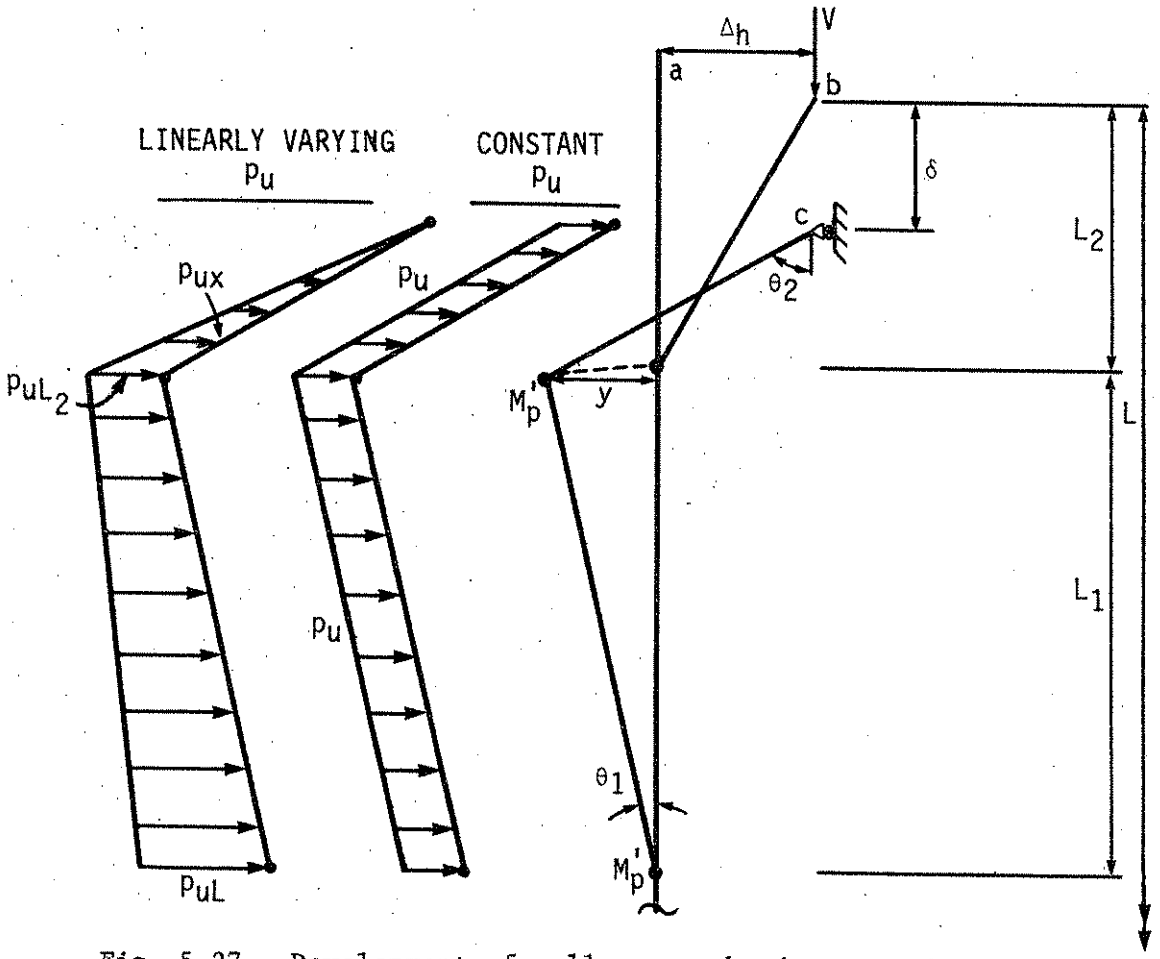


Fig. 5.27. Development of collapse mechanism assuming rigid, perfectly plastic behavior.

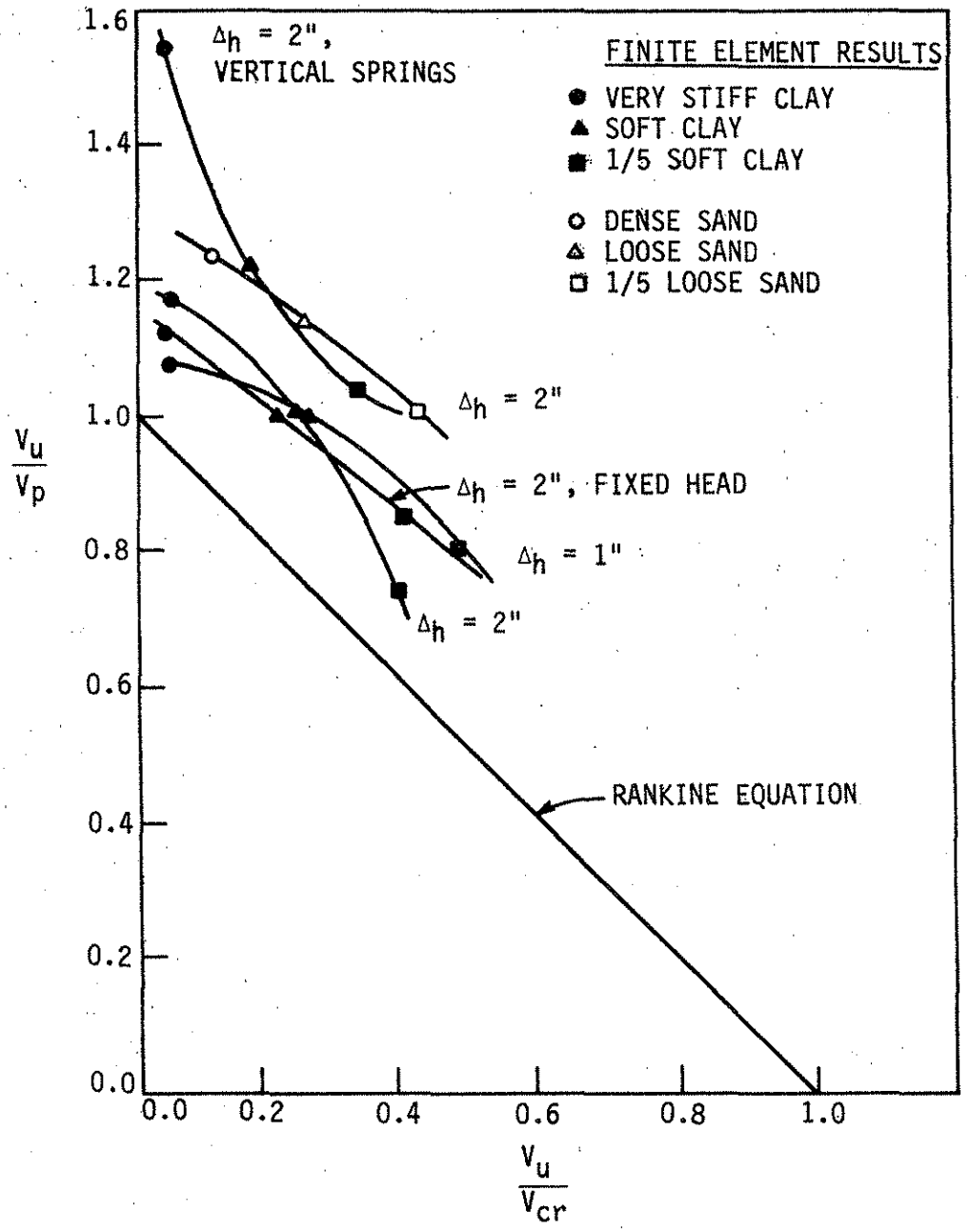


Fig. 5.28. Comparison of Rankine equation and finite element results.

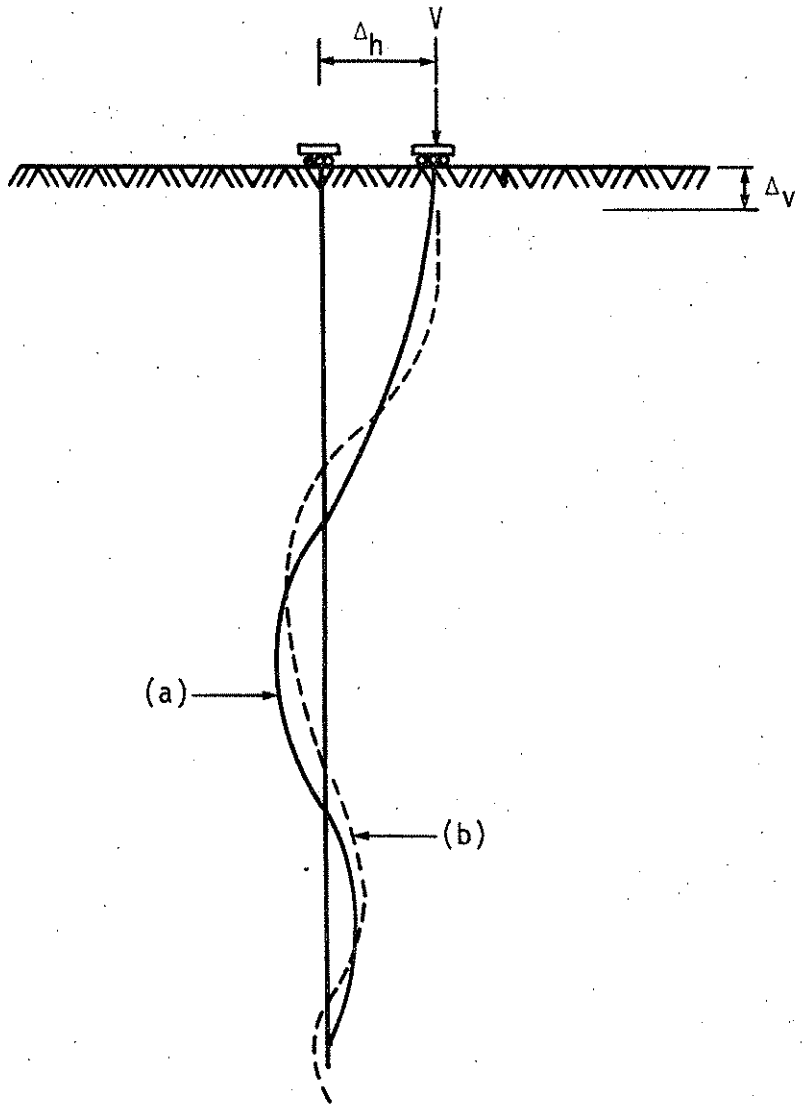


Fig. 6.1. Pile deflected shapes (a) after a specified displacement $\Delta_h$ (solid line), (b) applied vertical load V in case (a) (dashed line).

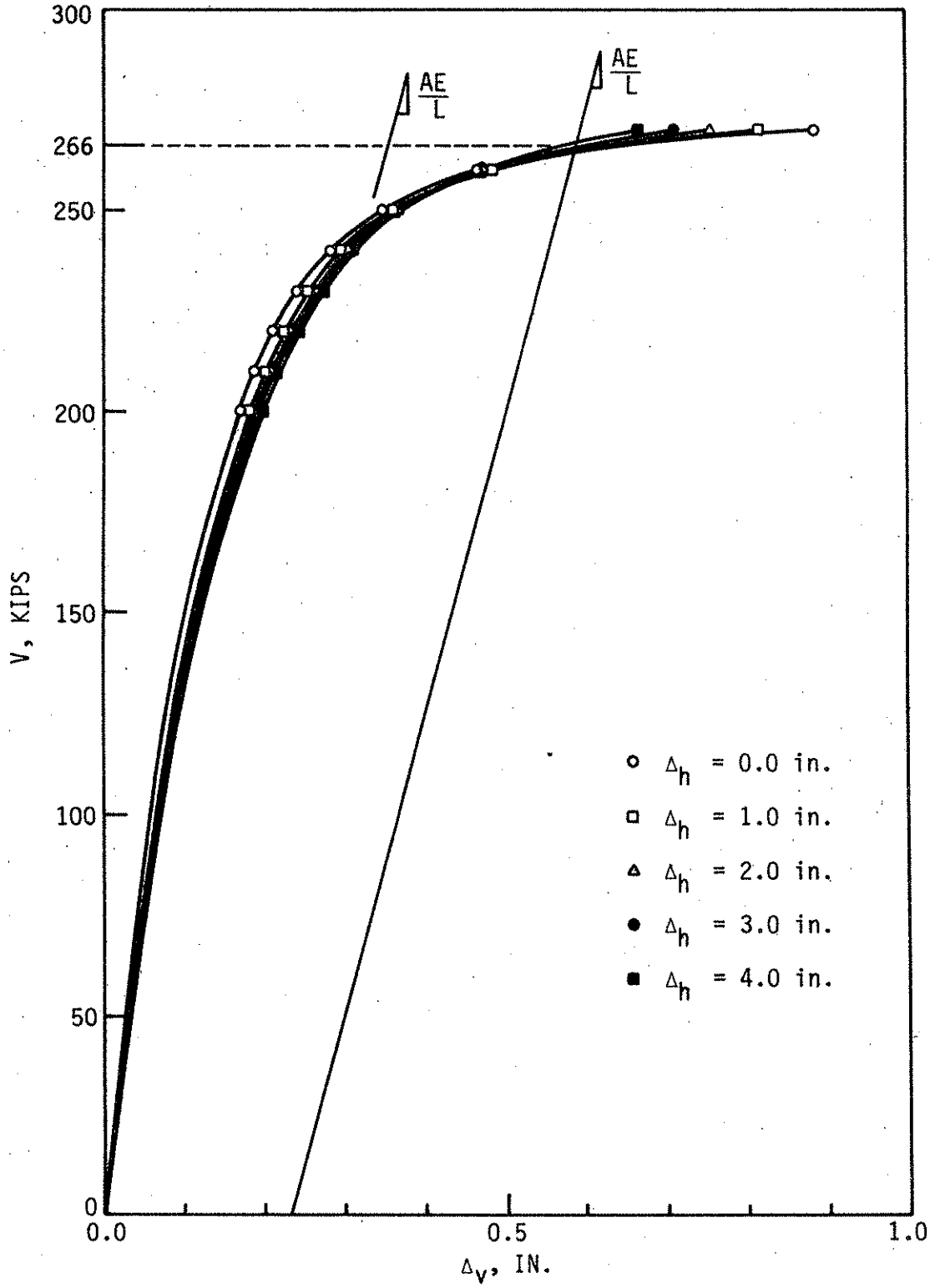


Fig. 6.2. Vertical load-settlement curves with specified lateral displacements, $\Delta_h$ (0, 1, 2, 3, 4 in.) for very stiff clay (friction pile).

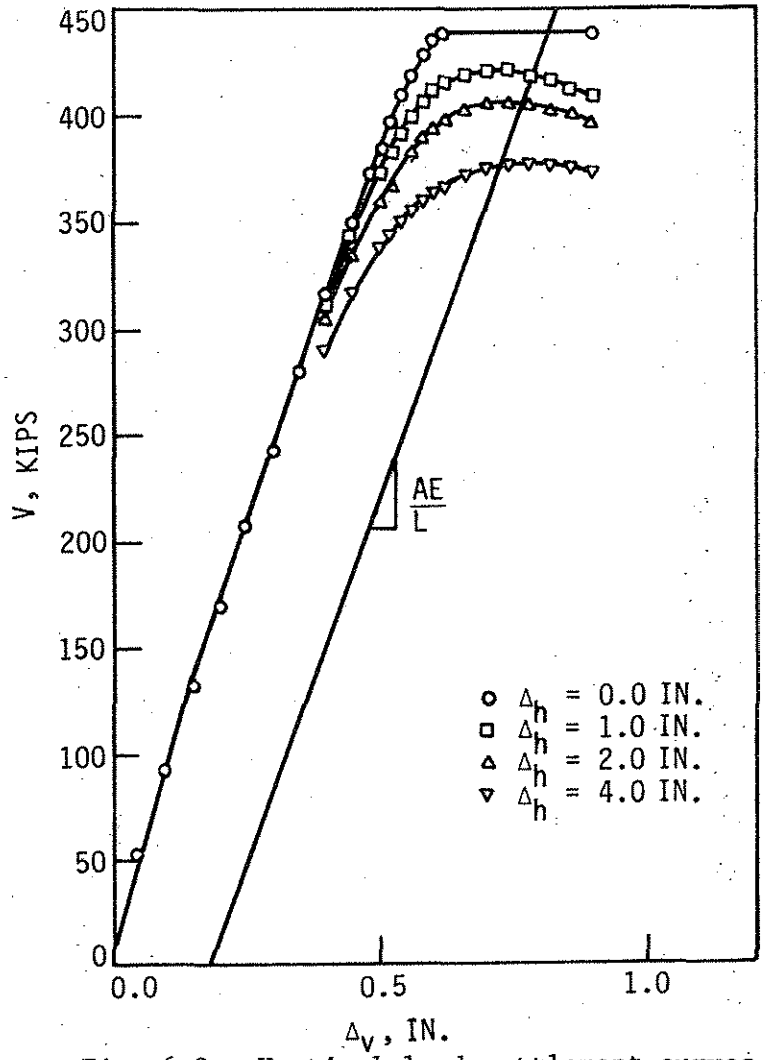


Fig. 6.3. Vertical load-settlement curves with specified displacements, $\Delta_h$ (0, 1, 2, 4 in.) for soft clay (end-bearing pile).

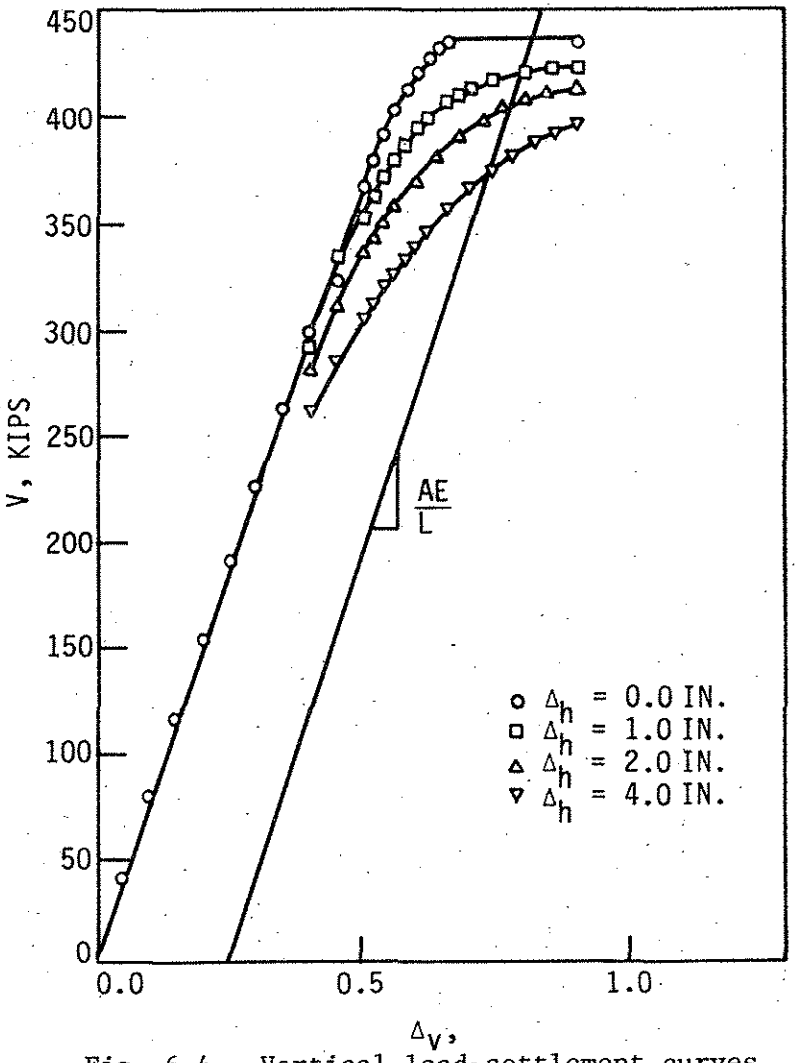


Fig. 6.4. Vertical load-settlement curves with specified displacements, $\Delta_h$ (0, 1, 2, 4 in.) for loose sand (end-bearing pile).

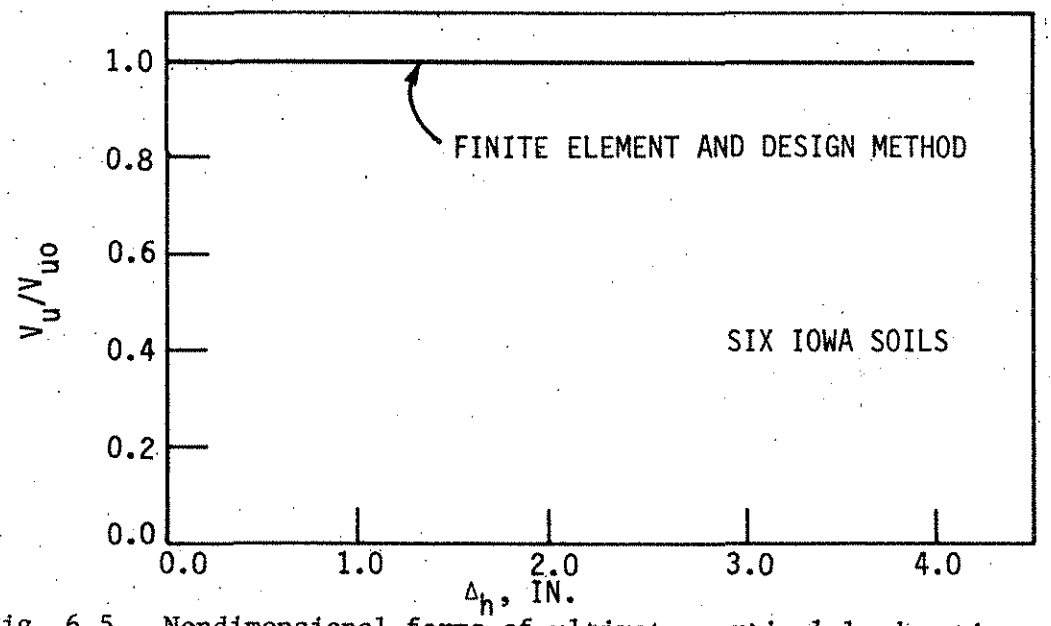


Fig. 6.5. Nondimensional forms of ultimate vertical load ratio versus specified lateral displacements $\Delta_h$, in Iowa soils (friction pile).

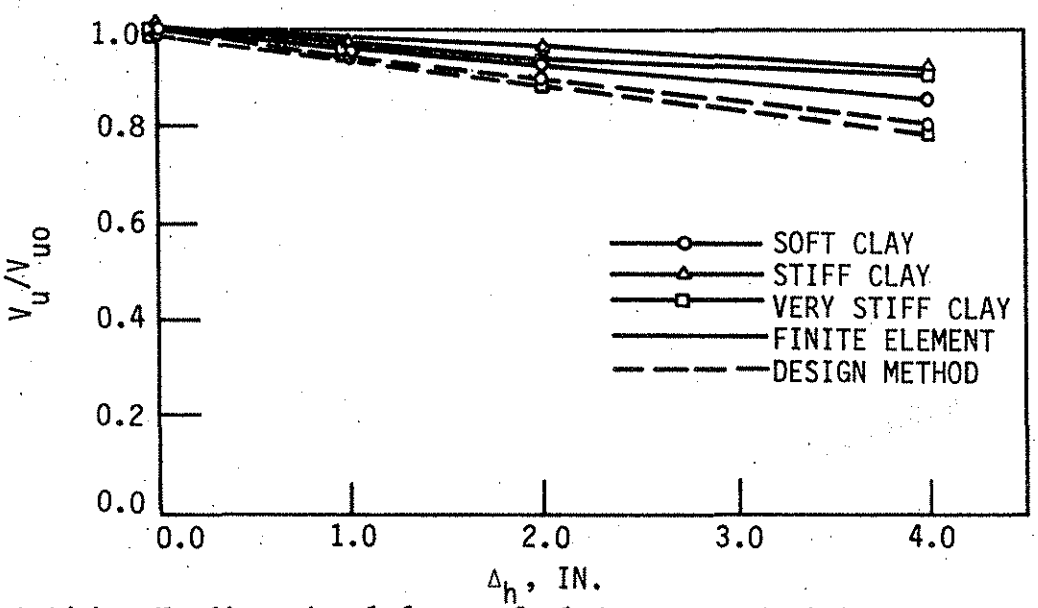


Fig. 6.6(a). Nondimensional forms of ultimate vertical load ratio versus specified lateral displacements $\Delta_h$, in Iowa soils (end-bearing pile).

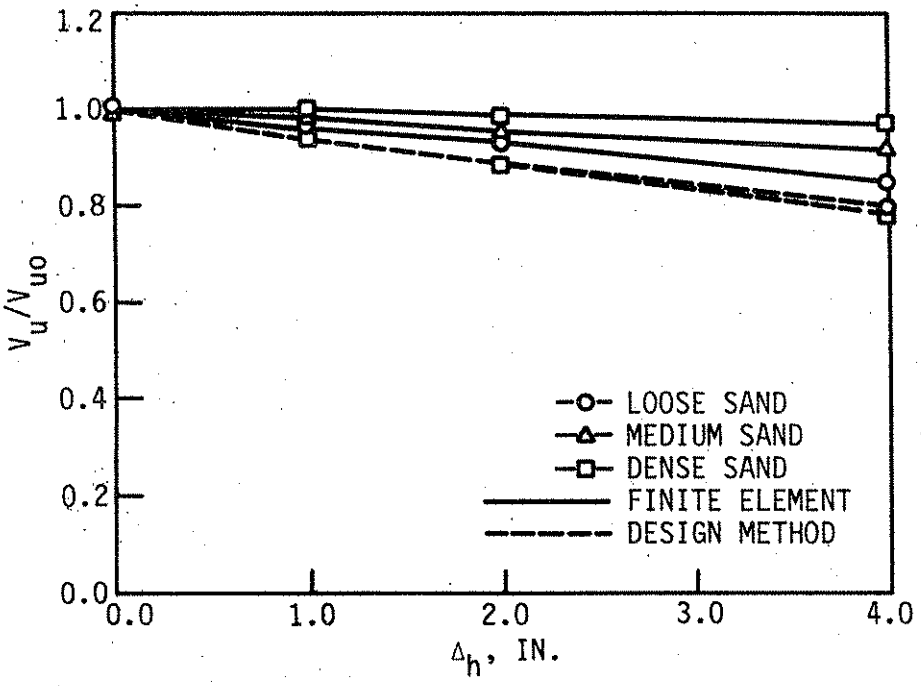


Fig. 6.6.(b). Nondimensional forms of ultimate vertical load ratio versus specified lateral displacements $\Delta_h$, in Iowa soils (end-bearing pile).

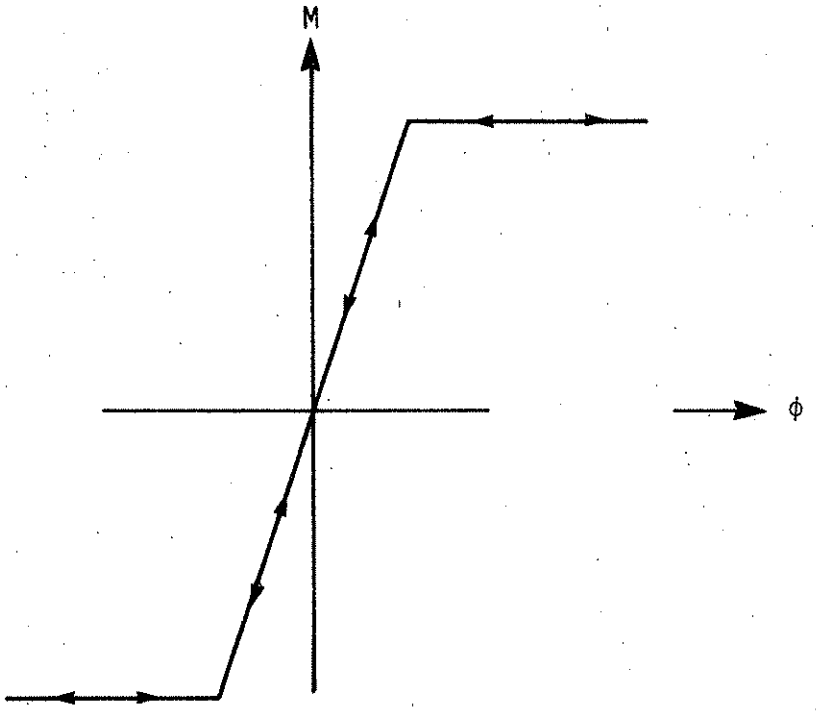


Fig. 6.7(a). Idealized moment-curvature relation and path for noncyclic model.

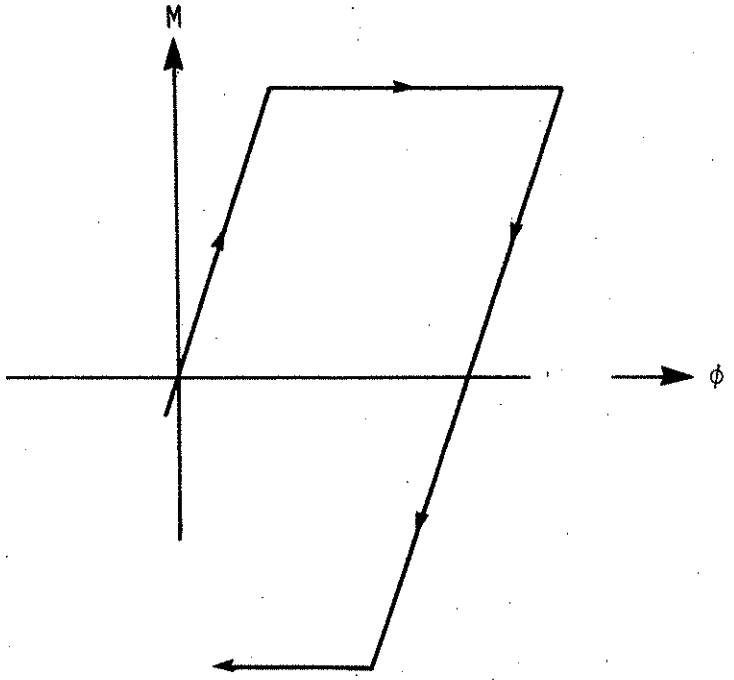


Fig. 6.7(b). Idealized moment-curvature relation and path for cyclic model.

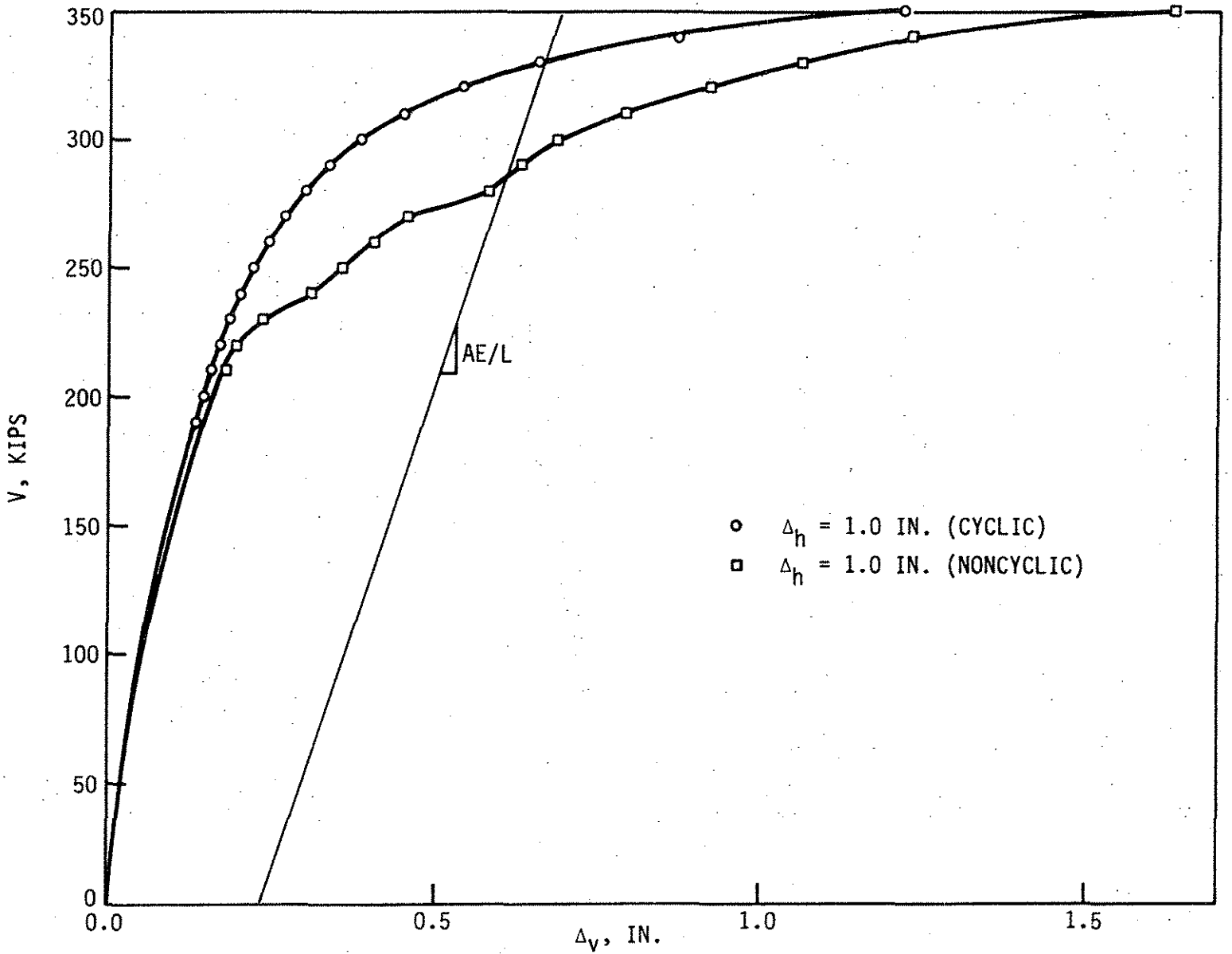


Fig. 6.8. Vertical load-settlement curves with specified lateral displacement $\Delta_h$ (1 in.), for very stiff clay with cyclic and noncyclic models.

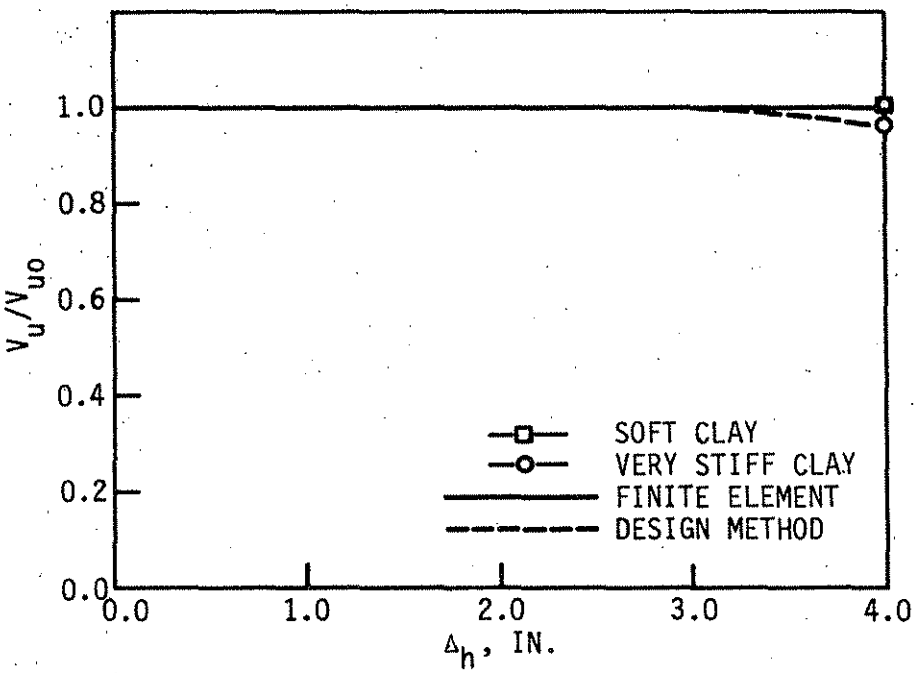


(a) FRICTION PILE WITH PINNED PILE HEAD

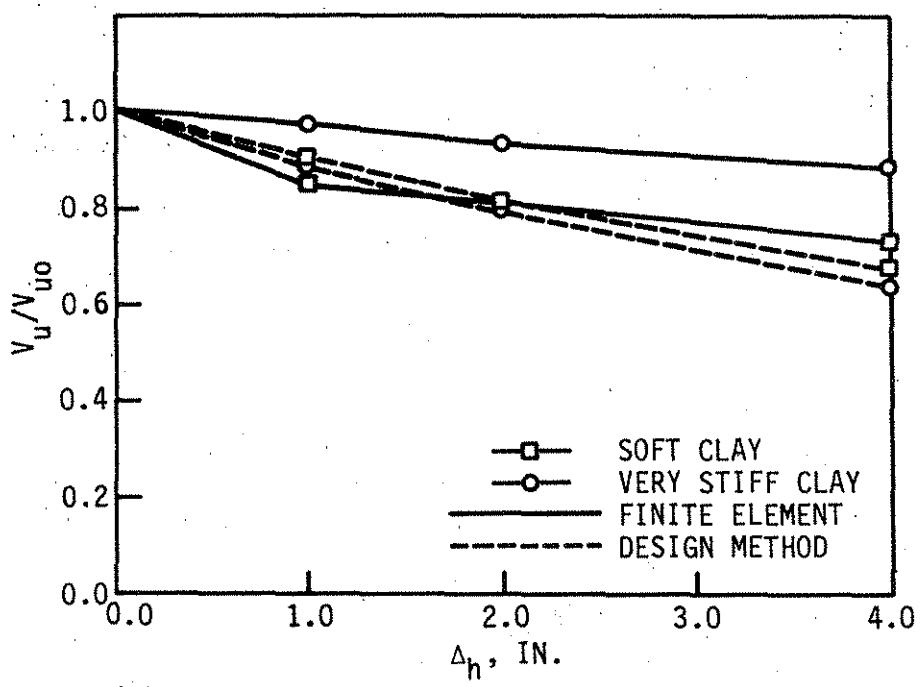


(b) END-BEARING PILE WITH PINNED PILE HEAD

Fig. 6.9. Nondimensional forms of ultimate vertical load ratio.

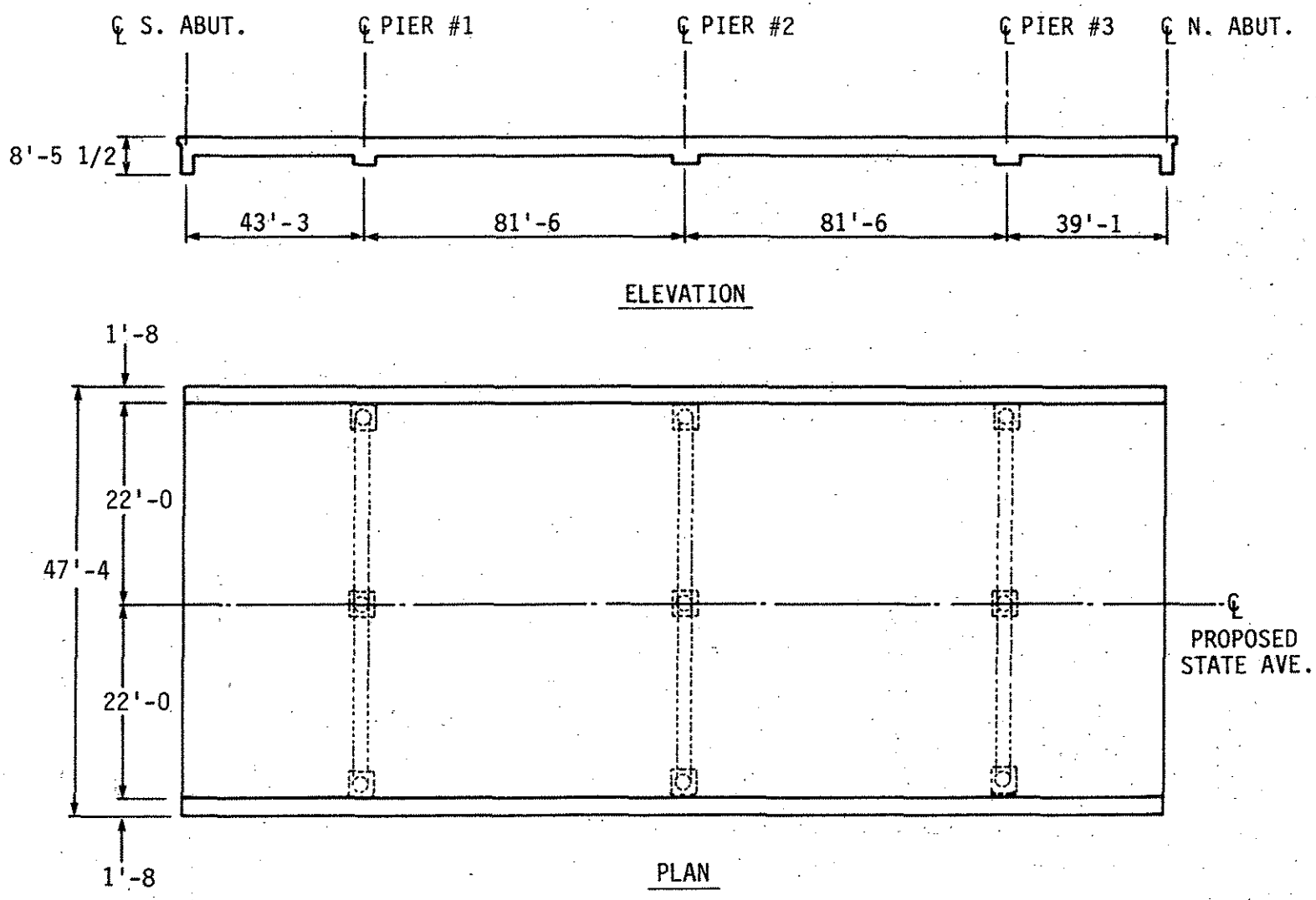


Fig. 6.10. Plan and elevation of bridge.

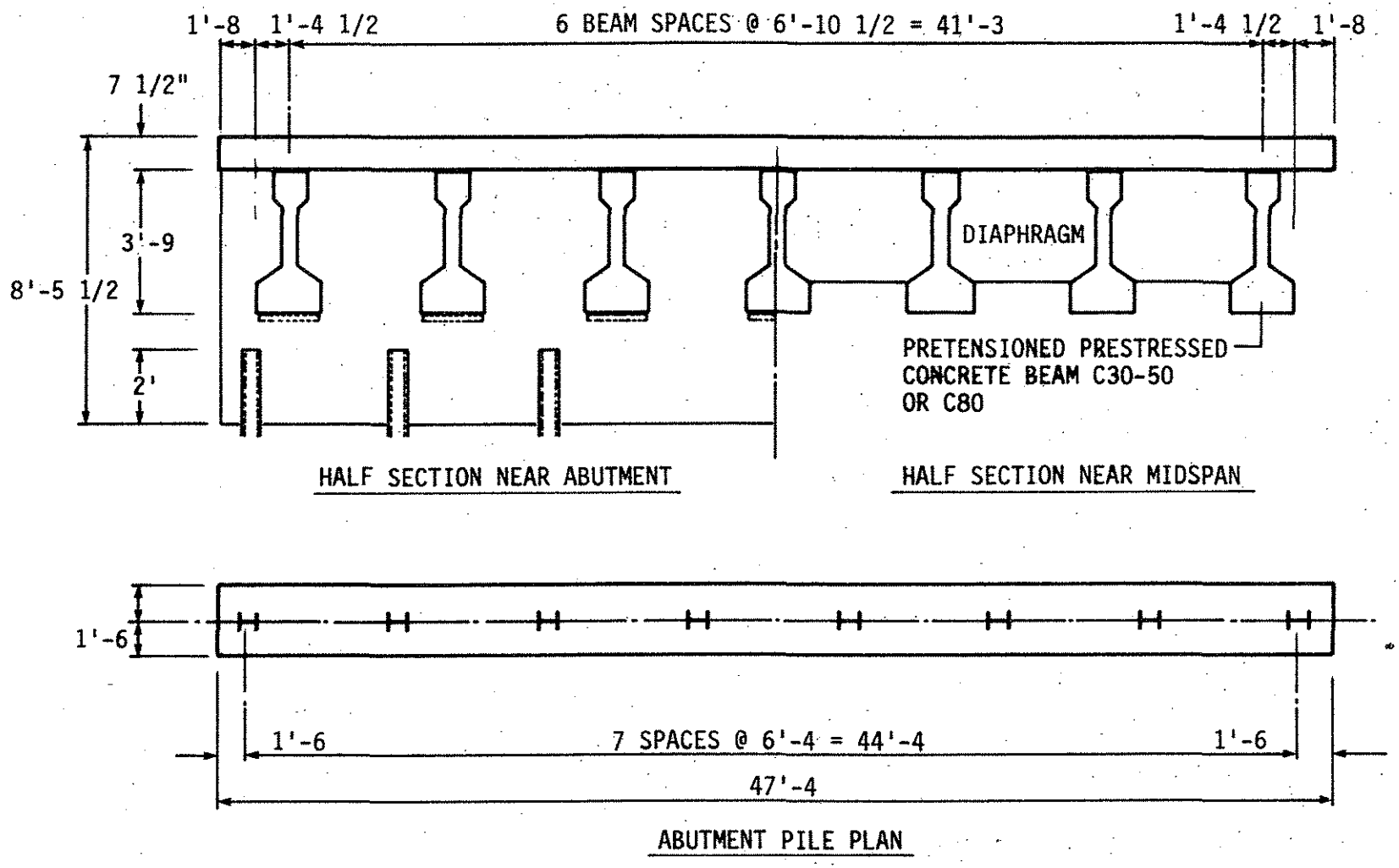


Fig. 6.11. Transverse section through deck.

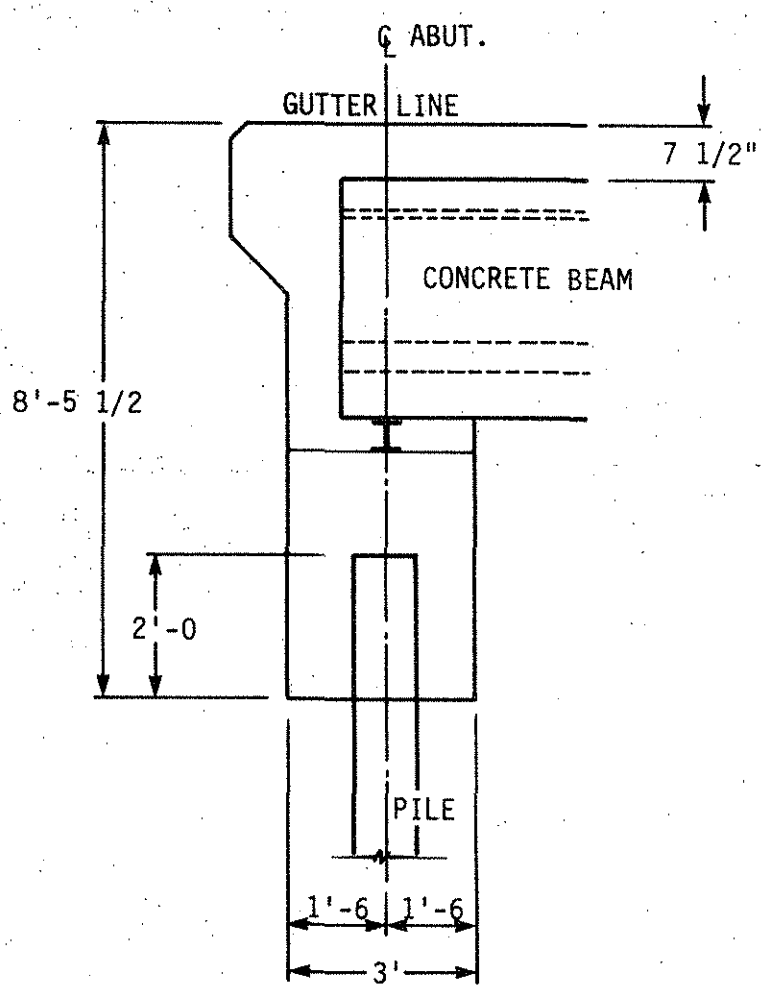


Fig. 6.12. Section through abutment.

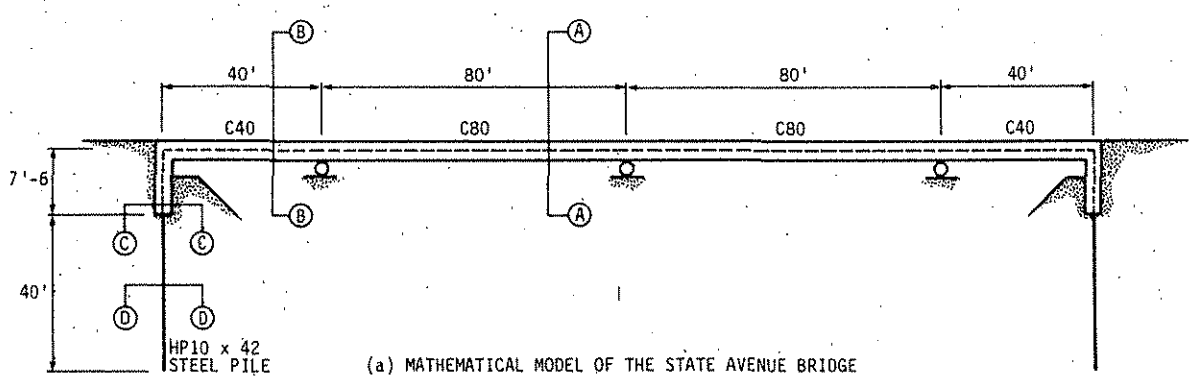


(a) MATHEMATICAL MODEL OF THE STATE AVENUE BRIDGE

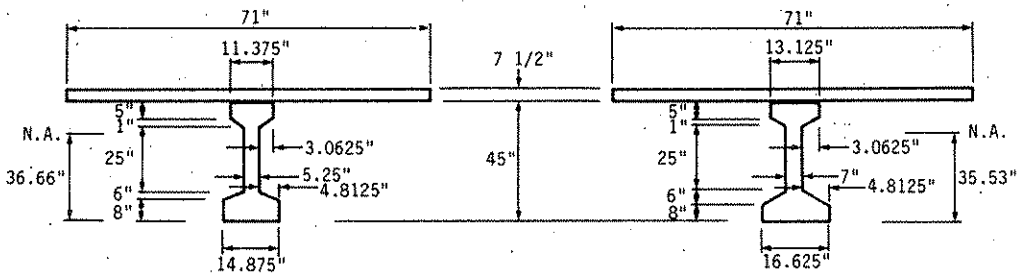


CROSS SECTION B-B

CROSS SECTION A-A

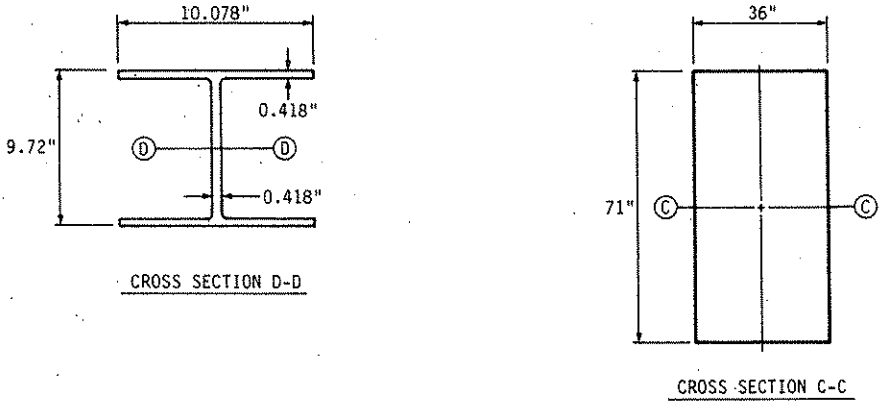


CROSS SECTION D-D

CROSS SECTION C-C

(b) EQUIVALENT CROSS-SECTIONAL PROPERTIES

Fig. 6.13. Mathematical model of the State Avenue bridge and equivalent cross-sectional properties.

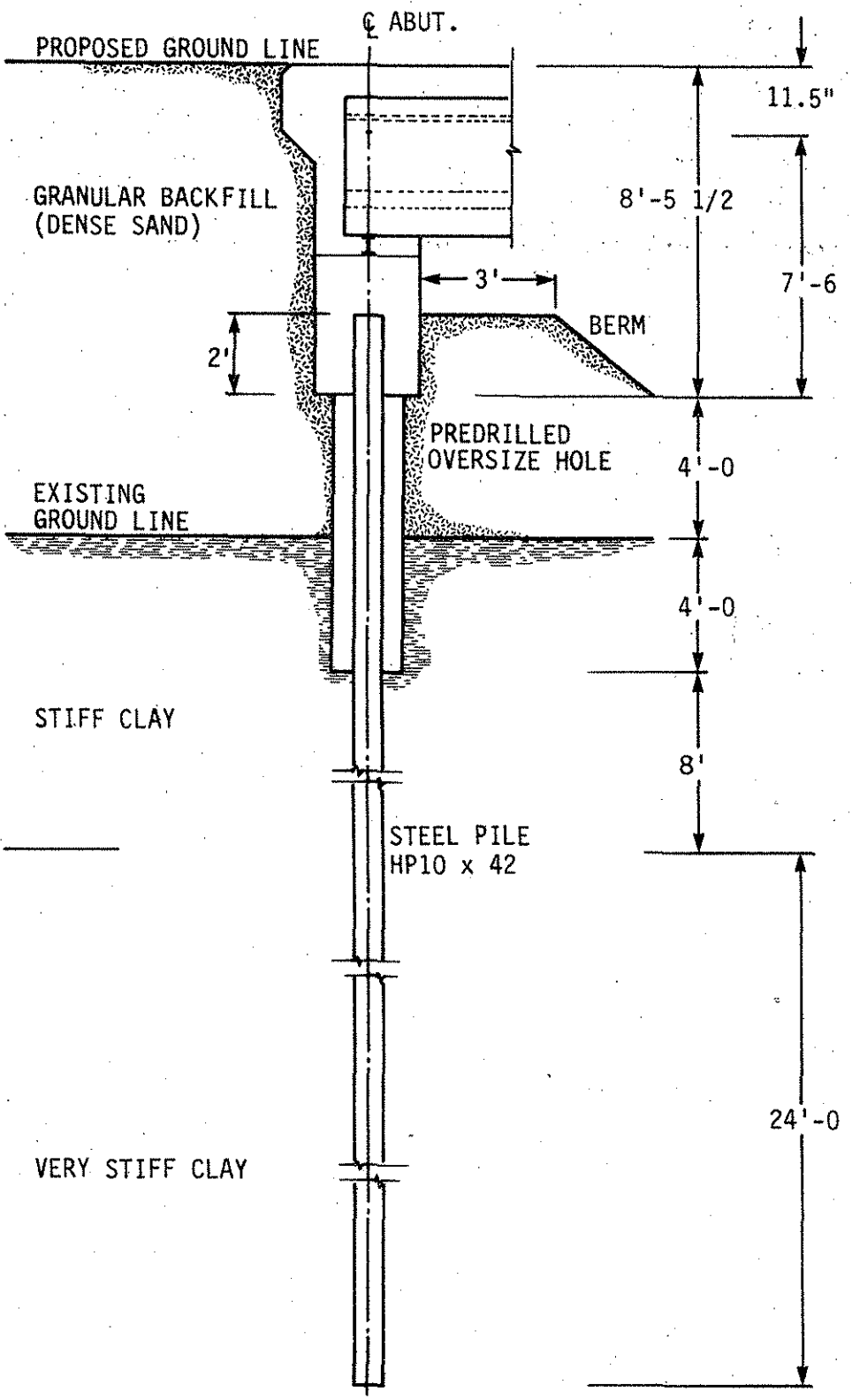


Fig. 6.14. Section through abutment and soil profile.

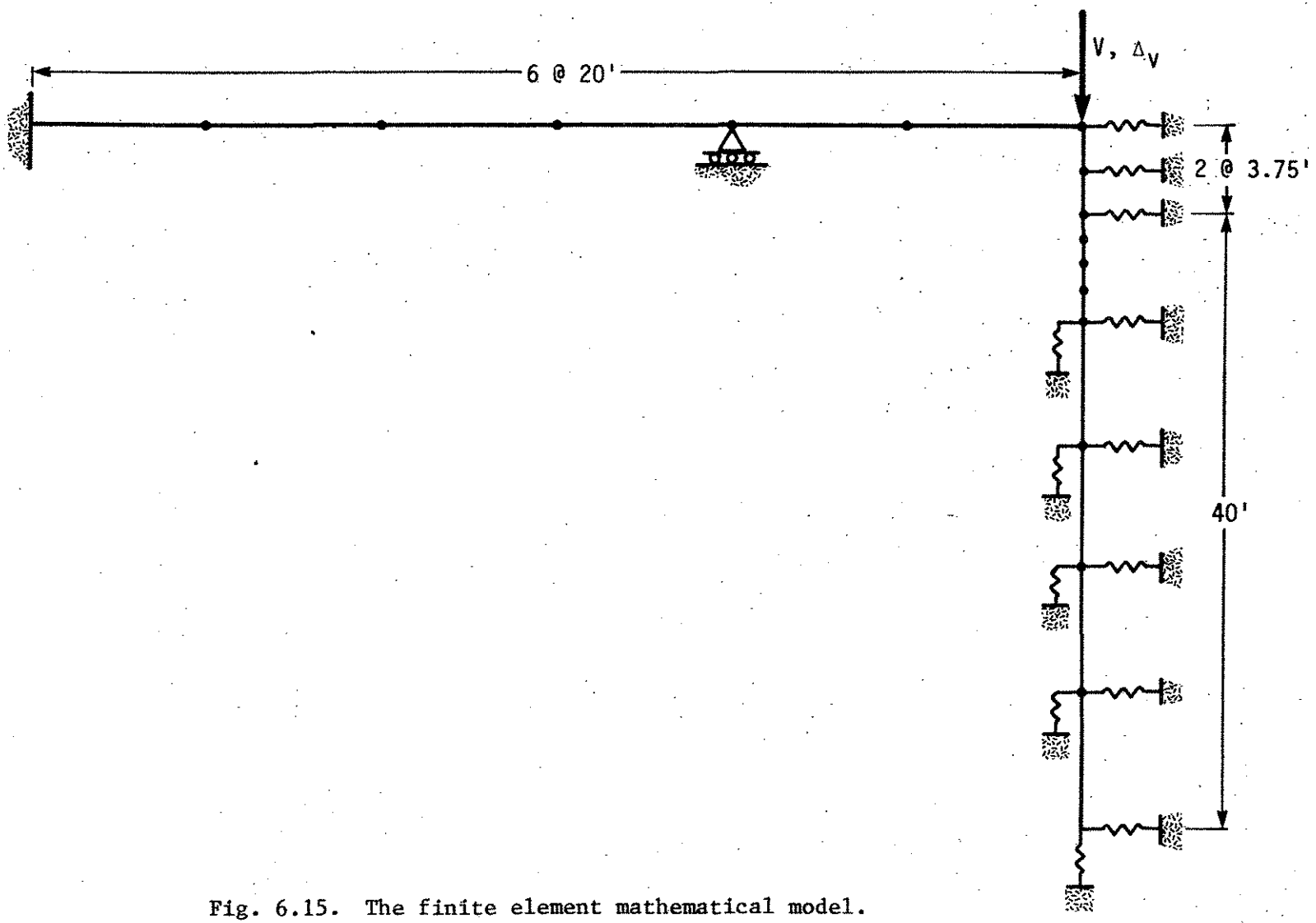


Fig. 6.15. The finite element mathematical model.

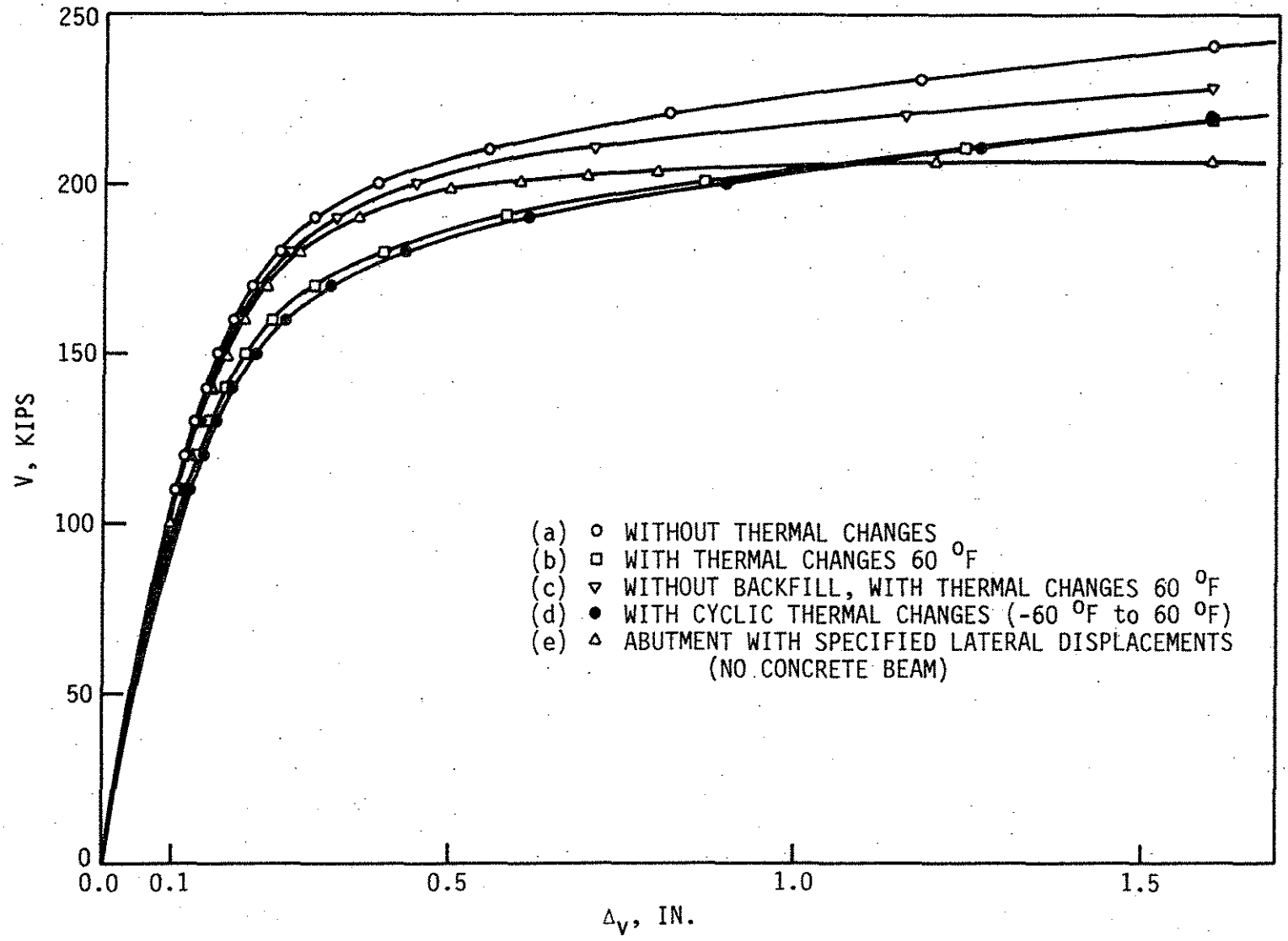


Fig. 6.16. Vertical load-settlement curves for nonskewed bridge.

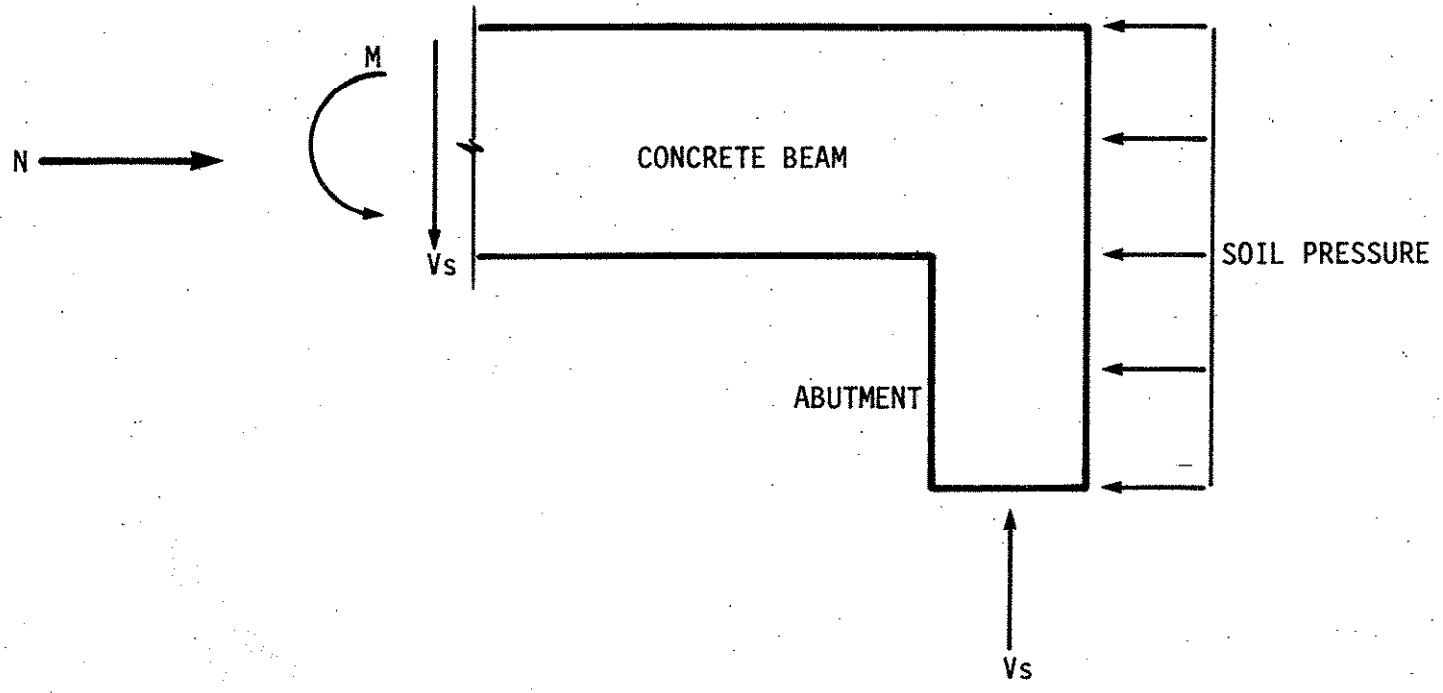


Fig. 6.17. Free body diagram of the concrete beam and abutment.

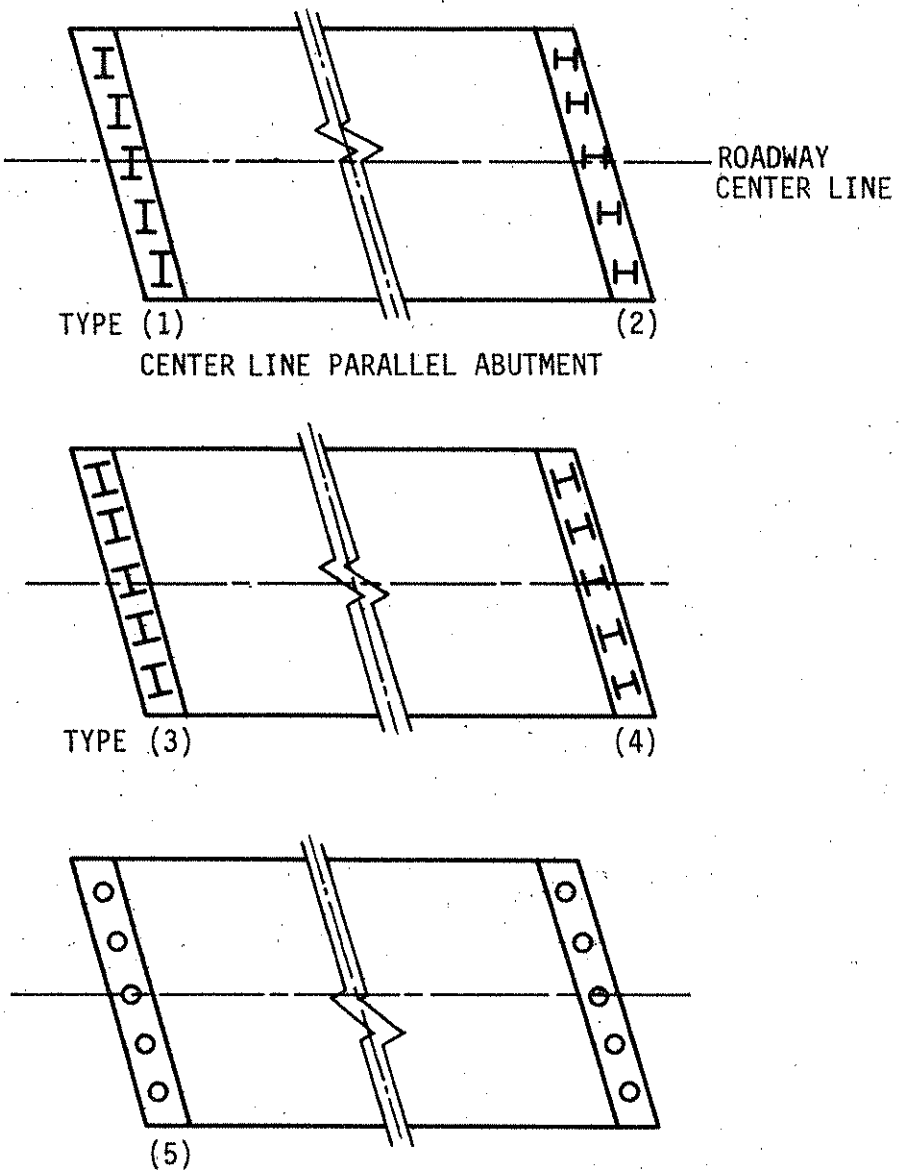


Fig. 6.18. Pile orientations in the integral abutment on skewed bridge.

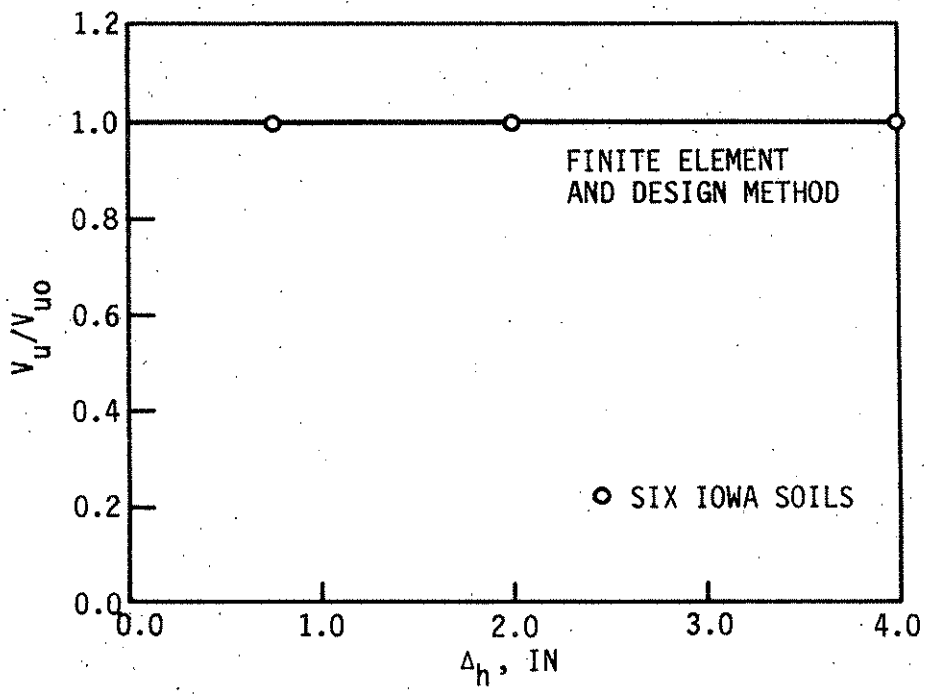


Fig. 6.19. Ultimate vertical load ratio (friction piles about strong axis).

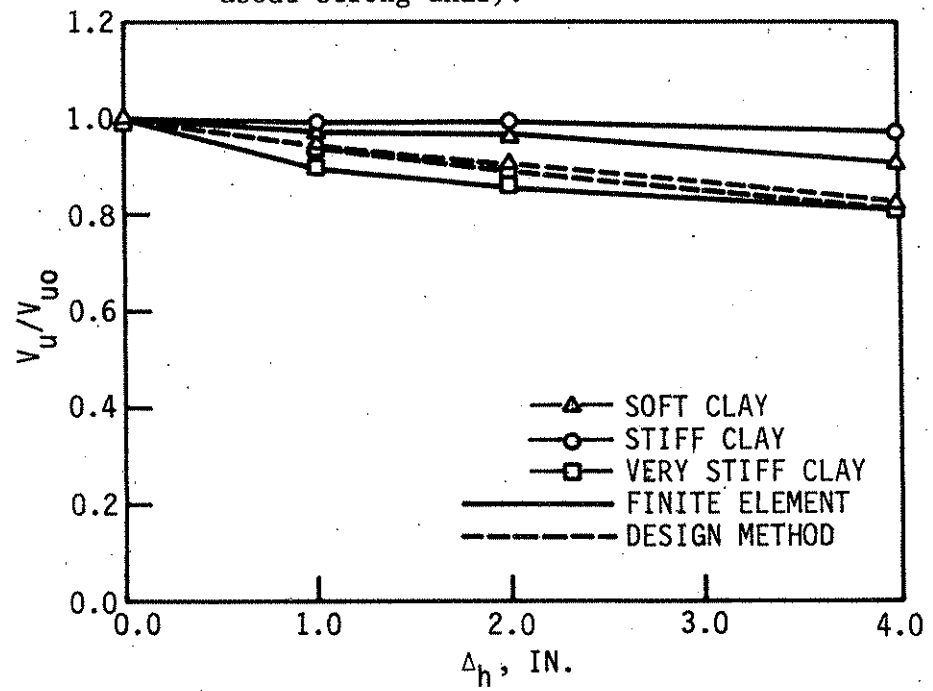


Fig. 6.20(a). Ultimate vertical load ratio (end-bearing piles about strong axis).

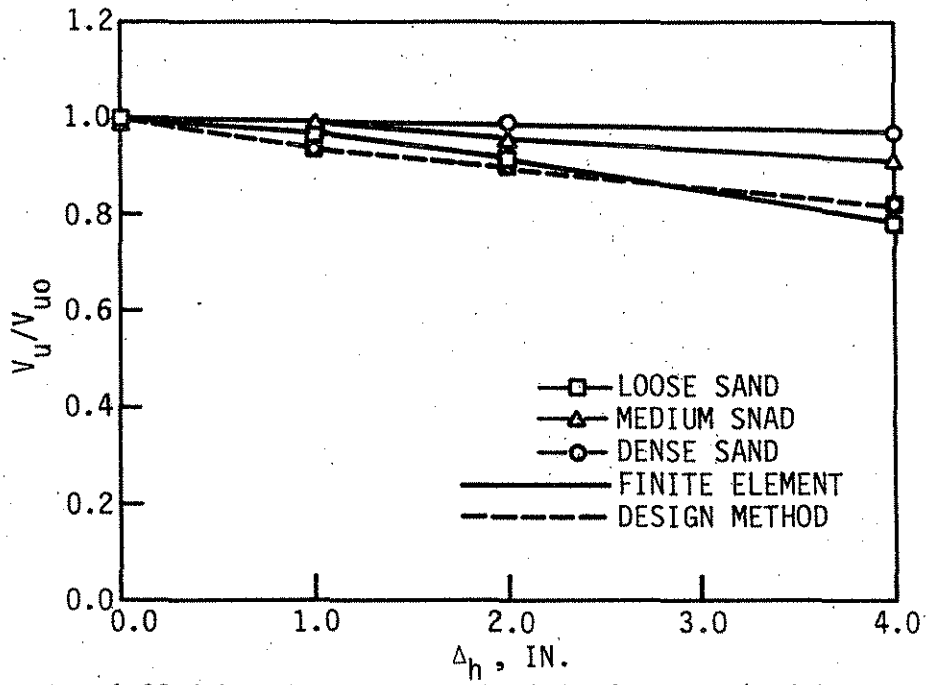


Fig. 6.20.(b) Ultimate vertical load ratio (end-bearing pile about strong axis).

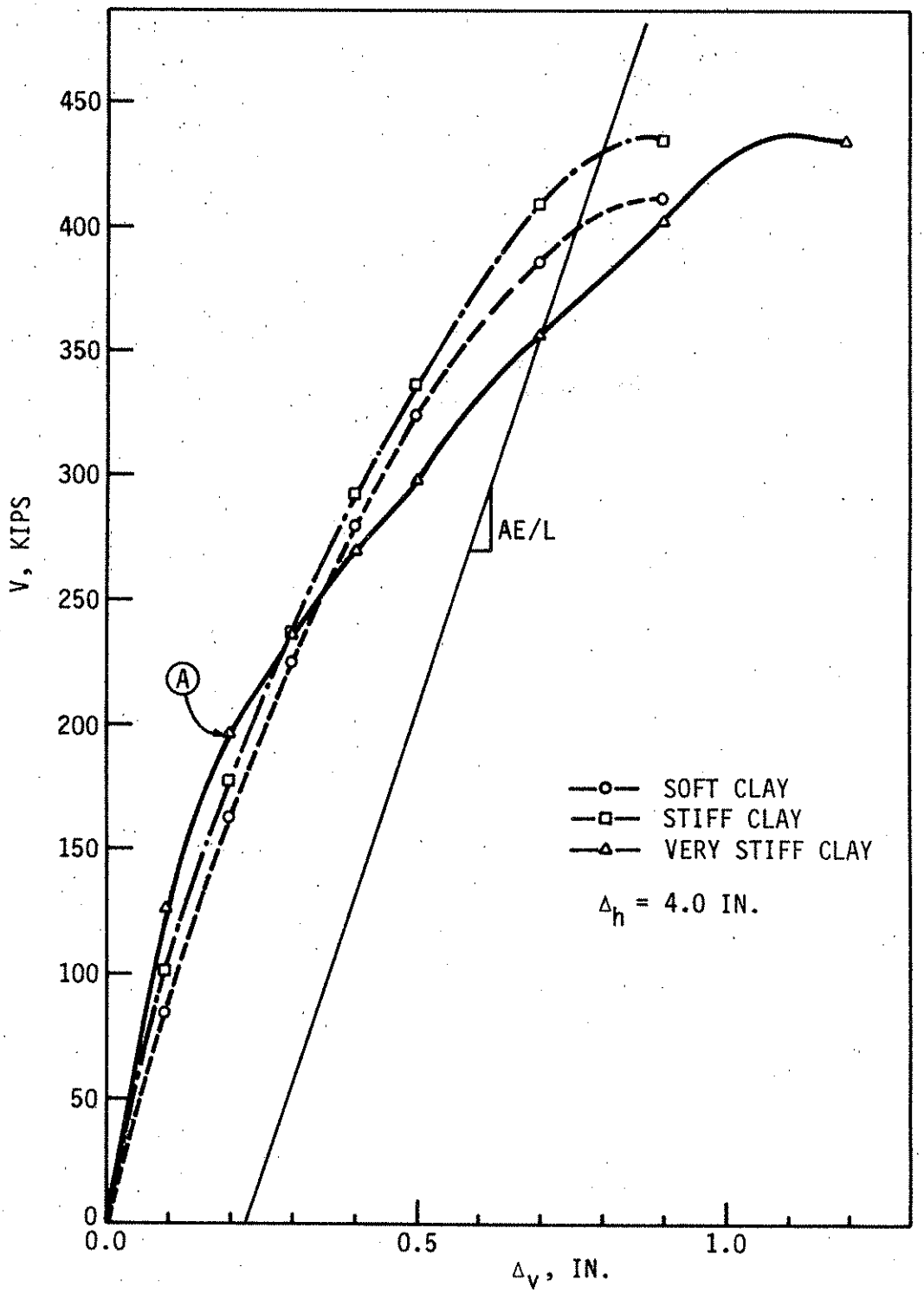


Fig. 6.21. Load-settlement curve for soft clay, stiff clay, and very stiff clay (end-bearing piles with fixed pile heads bending about strong axis).

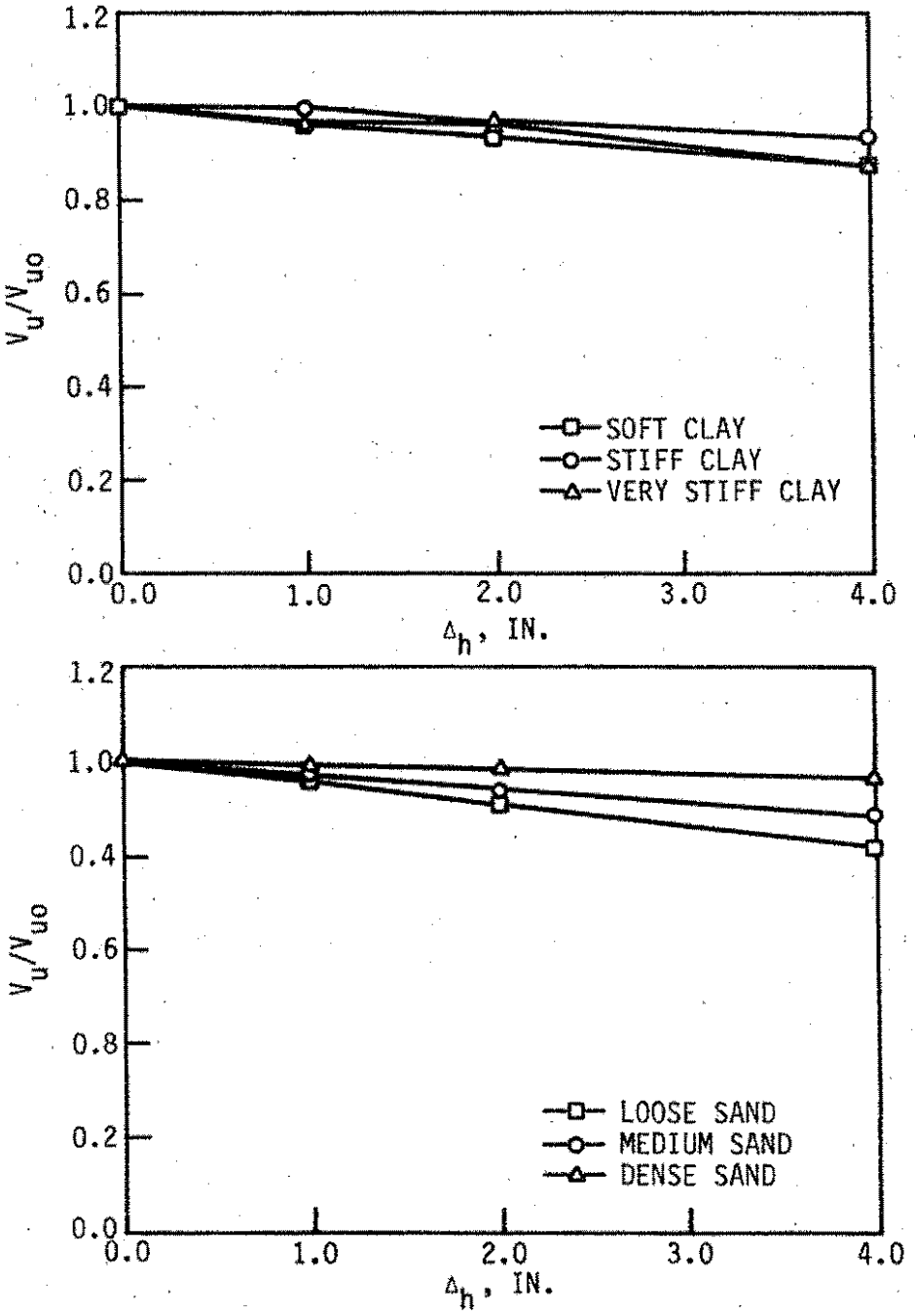


Fig. 6.22. Ultimate vertical load ratio (end-bearing piles about 45° axis) in Iowa soils.

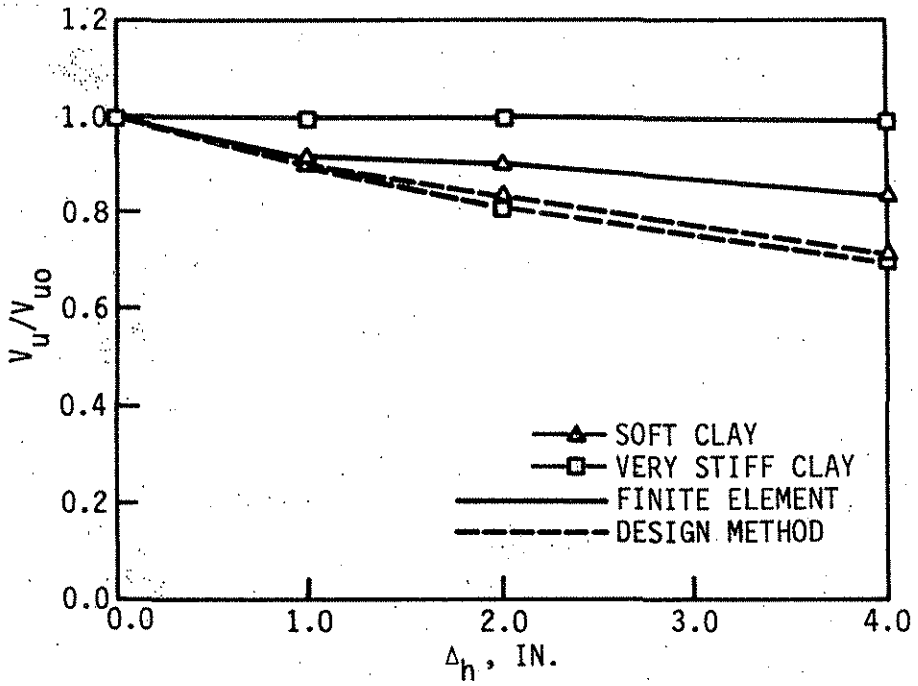


Fig. 6.23. Ultimate vertical load ratio (end-bearing piles with pinned pile heads bending about the strong axis).

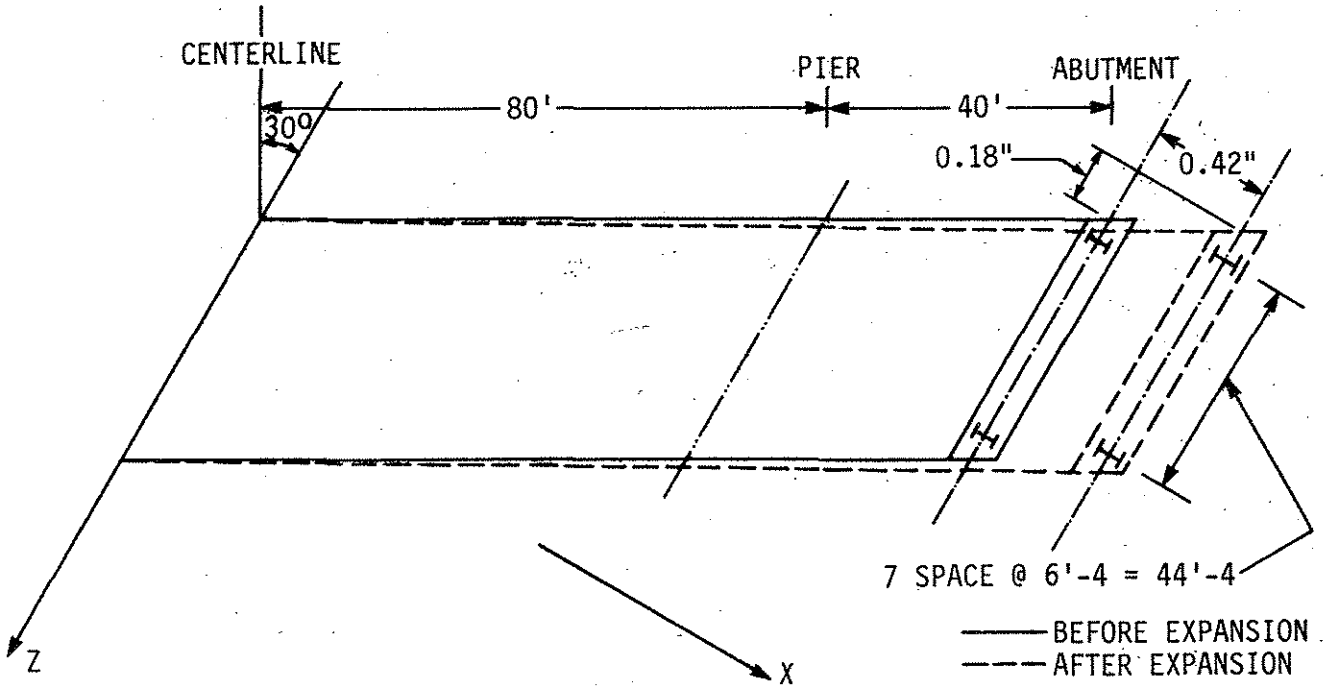


Fig. 6.24. Plan view of skewed bridge and its global coordinates, before and after thermal expansion (see Fig. 6.18 for bridge cross section).

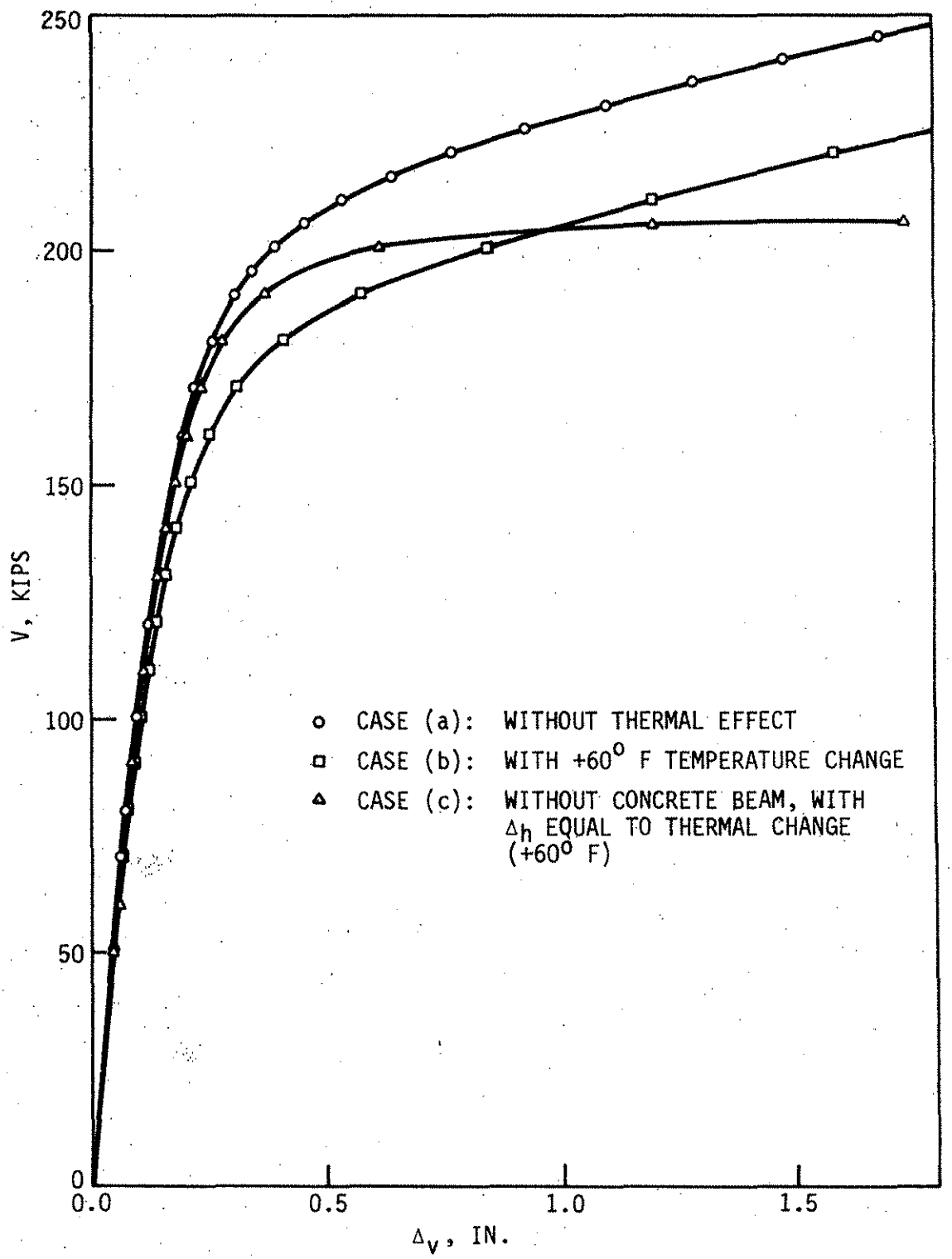


Fig. 6.25. Load-settlement curve for all pile orientations.